UNIVERSITÉ DE STRASBOURG

ÉCOLE DOCTORALE DES SCIENCES CHIMIQUES

[unité de recherche]

THÈSE

présentée par

Andrea CADEDDU

soutenue le : **17 Décembre 2012**

pour obtenir le grade de

Docteur de l'université de Strasbourg

Discipline / Spécialité : Chimie-physique

Supramolecular scaffolding at the nanoscale :

Functional architectures as a step towards Organic Electronics

THÈSE dirigée par :

[Pr. Samorì Paolo]	Professeur, université de Strasbourg

RAPPORTEURS :

[Pr. Giuseppone Nicolas]	Professeur, université de Strasbourg

---

MEMBRES DU JURY :

[Pr. Surin Mathieu]	Professeur, University of Mons, Belgium
[Pr. Palermo Vincenzo]	Professeur, ISOF CNR Italie

To Carlo

"Our comforting conviction that the world makes sense
rest on a secure foundation:
our almost unlimited ability to ignore our ignorance."
- Kahneman, D.

INDEX

Table of abbreviations:

1D – mono–dimensional

2D – bi–dimensional

3D – tri–dimensional

ABNR – Adopted Basis Newton–Raphson Method

ACMod – Alternate Current Modulation

AFM – Atomic Force Microscope

CA – Contact Angle (water)

CHARMM – Chemistry at HARvard Macromolecular Mechanics, toolbox.

DFT – Density Functional Theory

DMSO – Dimethylsulfoxide

DOX – Dioxane

DSC – Differential Scanning Calorimetry

EtOH – ethanol

Gwy – Gwyddion

HA – Heptanoic Acid

HB – Hydrogen Bond

HCP – Hexagonal Close Packed

HOPG – Highly Oriented Pyrolytic Graphite

Ig – Integral Gain

Ill – Adobe illustrator

Ind – Adobe Indesign

IR – InfraRed spectroscopy

It – Tunneling Current

MASPEC – Mass Spectrometer

MC – Monte–Carlo

MD – Molecular Dynamics

Mel – Melamine

MES – Mesitylene

MMFF – Merk molecular force field

NA – Nonanoic Acid

NCG – NanoCrystalline Graphene

NMR – Nuclear magnetic resonance

OA – Octanoic Acid

Pc – Phthalocyanine

PO – 1–phenyloctane

Porph – Porphyrin

Ps – Adobe Photoshop

PSD – Phase Sensitive Detector (Lock–In amplifier)

Py – Pyridine

RT – Room Temperature (25˚C)

SAM(s) – Self Assembled Monolayer

SD – Steepest Descent Algorithm

SPIP – SPIP 6 software metrology

STM – Scanning Tunneling Microscope

STS – Scanning Tunneling Spectroscopy

TCA(s) – Tetracarboxylic Acid(s)

TCB – 1,2,4– Trichlorobenzene

TD – Tetradecane

Tf – Triflate

TFA – trifluoroacetic–acid

TGA – Thermogravimetric Analysis

UHV – Ultra High Vacuum

UPS – UV Photoelectron Spectroscopy

Ut – Tunneling Bias

UV – Ultra Violet

VdW – Van der Waals

VMD – Visual Molecular Dynamics

Forewords:

Equilibrium: - is the state of rest due to the equal action of opposing forces. Is a concept equally valid in literature and science, in arts and nature, in the eastern cultures as in the occidental ones; the blind-folded roman divinity Justitia was represented carrying a scale, which has become the symbol of law and justice, the interface of Society between order and chaos. The concept of Equilibrium permeates our social lives, and equally percolate from stars to our selves, to every small piece of matter: Cells, molecules, atoms and nuclei all may be observed from the same perspective. Shifting equilibriums may fall a tree or produce a new chemical compound. Understanding how to use the balance between forces allowed trough history the humanity to design and build architectural wonders, and allows today, the supramolecular architect to design and produce self-assembled materials in the dawn of nanotechnology;

Of paramount importance is unraveling the entanglement of forces affecting the self assembly: understanding how hydrogen bonds, van der Waals, metal-ligand weak forces and interactions between molecules, substrate and the system, are interweaved pave the way to controlling nano-architectures, and finely draw each connection in two, or three dimensions.

Such knowledge can then be equally applied to all fields of the nanotechnology, ranging from controlled growth of 3d systems, to the synthesis of new materials;

Today, many have confronted the challenges raised by the controlling the self-assembly, and in the last decades have contributed to leap toward the understanding of equilibriums at the nanoscale; Nano-architectural wonders are nowadays object of research in almost all of the fields of technology: In organic optoelectronics self-assembled monolayers are throughtfully employed ranging from the production of renewable energy, to nano-wires to new multi-responsive devices; in Medicine & Biology, weak forces interactions and the functionalization of nano-objects permeates micro-fluidics, tissue regeneration, and drug release; The importance and the research in self-assembled materials definitely spans from Quantum Informatics to new building materials.

Even if the weak forces controlling the assemblies, and their regulation have been object of profound investigation, the list of open challenges is overwhelming. Among all, we individuate three main directions for the research in this field, where providing a(n humble) contribution was general aim of this work, and his context:

- 2D-3D transition, i.e. growing a pre-programmed architecture, layer by layer, in a rigidly restrained fashion;
- Reactivity on the surface, which besides the obvious industrial appeal in the development of new more efficient catalyst, promises to disclose the synthesis of 2D-conjugated polymers.
- Responsive assemblies, i.e. molecular networks capable responds to external stimuli, as light, pH, or specific analytes by rearranging themselves in a different packing, have monumental interest in the preparation of new sensors or responsive devices.

Three strands (threads – braids) are intertwined and constitute the canvas (fabric) of this work: Simulations, Scanning Tunneling Microscopy, and instrumental and software development:

Scanning tunneling Microscopy is the appropriate window to observe the phenomena at the nanoscale, Simulations are a great aid in understanding and designing, and the advancement of both is necessary for a continuous progress.

In chapter 1 we discuss briefly the status-of-the-art in the research and we give a brief introduction over the self-assembly concepts

In chapter 2 we dug deeper into the theory and the computational and experimental methods. This allows to dissect the scanning tunneling microscope to rationalize the components.

In chapter 3 we discuss about the bi-dimensional self-assembly at the solid-liquid interface. There are four principal blocks which are consequential.

In chapter 4 we apply scanning tunneling microscopy and molecular dynamics to unravel the mechanism of bi-layer formation of a simple tetra-carboxylic acid.

In chapter 5, we report of the synthetic attempts in the realization of 2D covalent frameworks

In Chapter 6, we summarize

In Appendix 1, we report about the development and application of a modified scanning tunneling microscope

In appendix 2, we gather all the "software" details, ranging from a brief elementary introduction for the non-programmer to the details of the algorithms and softwares produced.

Finally in the annexes are reported the synthetic procedures, and the other details which were somehow distracting from the discussion inside the respective chapters, but are a useful support.

Chapter 1: Introduction

This chapter contains a brief summary of the core concepts on which this work is based, and a brief but exhaustive picture of the state-of-the-art of the research done in the field of self-assembly as seen through Scanning Tunneling Microscopy.

Scanning Probe Microscopy

Scanning Probe Microscopy has changed the way to investigate the properties of the matter in science. It has given the opportunity (possibility) to many groups around the world to investigate the nanoscale with reasonable expenses and small equipment[i]. It has also allowed for the first time actual manipulation of the matter at the atomic level, as shown by the unforgettable IBM logo written by positioning single atoms.[1]

Above all it has permitted to study at the molecular level the interface between liquid and solid, or between solid and air. It is one of the key instruments for unveiling the secrets of complex phenomenon such as the self-assembly. The scanning probe microscopy has proven to be an invaluable and necessary tool for nanoscience: without the possiblility of observing and manipulating the nanoscale, the whole field would probably not exist.

Among the different types of SPM techniques, we focused our attention on the Scanning Tunneling Microscopy, which historically is the "oldest" one, since it has been developed in 1980-81.[ii] Nevertheless it is still remarkably useful, and used, as shown by the number of publications in the last years: 624 publications[iii] in peer reviewed journals between January 1st and September 14th 2012.

A description of the instrument, the technique, methods and the theories will be given in the next chapter, whereas here we'll focus on it *qualitatively* as a window to observe the auto-organization of matter at the solid-liquid interface[2].

---

[i] The price might range 4 orders of magnitude between *homebrew STMs* which DIY (do it yourself) communities claim to build with 100$ (http://www.ilovephysics.com/2007/10/15/building-a-scanning-tunneling-microscope-for-less-than-100/), to millions of dollars for *state-of-the-art* ultra high vacuum setups.

[ii] According to Gerd Binnig's Nobel lecture.

[iii] Value calculated from Reuters - Web Of Science (Topic=(STM) Timespan=2012-01-01 - 2012-09-14. Databases=SCI-EXPANDED, SSCI, A&HCI, CPCI-S, CPCI-SSH, IC)

Self-Assembly:

The subtle use of interatomic and intermolecular forces at the nanoscale can lead to the formation of new structures. This is what makes the molecular self-assembly an appealing topic and a promising field in science. Self-assembly implies that a structure will construct itself from the spontaneous interconnection of his modular components, forming an ordered pattern from a disordered state. The forces acting *between* the construction units rather than the bonding interactions within them are what conduct the assembly. Among the suitable forces are counted hydrogen bonding, van der Waals forces, electrostatic, and generally all the non-covalent interactions. The ability to construct an ordered structure is dramatically affected by the ability to control all the properties of the building block. The first objective is therefore to consciously exploit all the interactions of the *tectons* in order to allow them to form spontaneously the target architecture across multiple length scales.

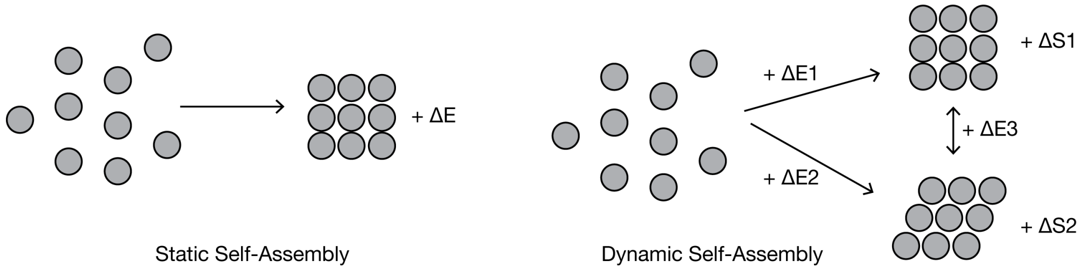

Figure 1: Mechanisms of self-assembly

The matter is driven by energy minimization to form equilibrium structures, but clearly in presence of *external* influences a different outcome may prevail: the system can occupy a temporary minimum energetic state depending on the energy influx in the system, in which his self-assembled structure is *dynamic*. Once the external energy source is removed, the minimum cease existing, and the structure disassemble. This has palpable resemblances to the living process, and in a way explains why mastering the self-assembly is part of unveiling the secret of life.

In both the dynamic and static cases, it is possible to recognize three limiting mechanisms of self-assembly: co-assembly, hierarchical self-assembly and directed self-assembly. Often the distinction between those modes is very labile as clearly there are many mixed occurrences, especially in complex biological systems. The core principles of the three are shown in Figure 2.

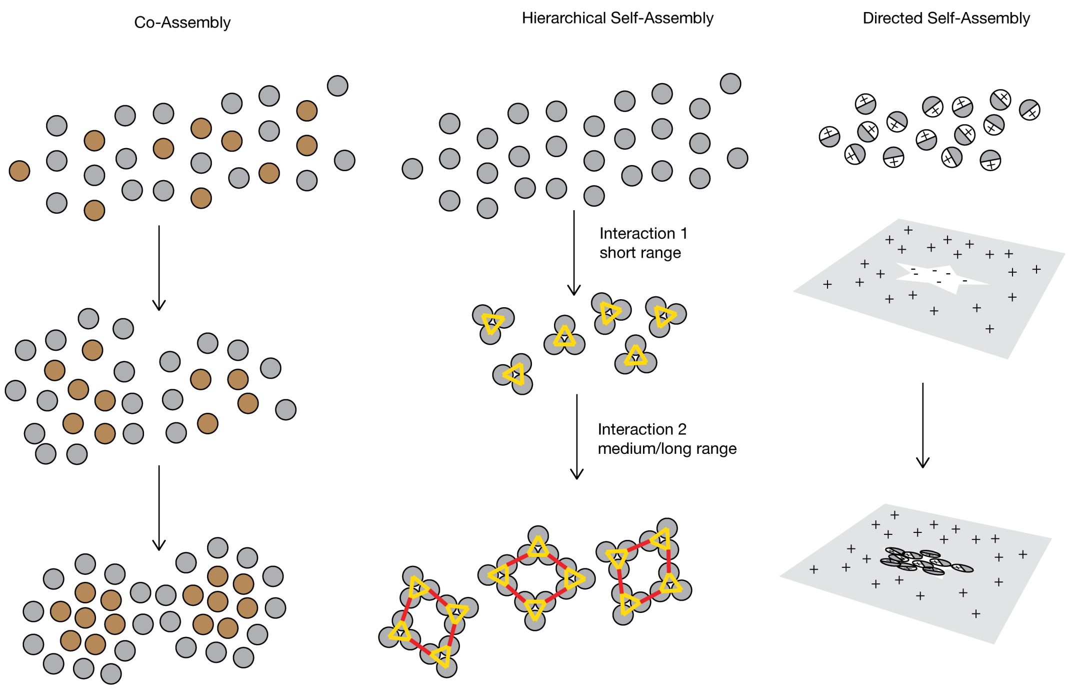

Figure 2: Schematic representation of co-assembly concept, hierarchical and directed self-assembly.

Hierarchical self-assembly represents cases in which a single building block organizes across multiple length scales, through different orders of interactions. Co-assembly is a case where the packing is directed by the simultaneous interactions of different building blocks, leading to a structure which could not have been produced by the isolated assembly of either. Finally, directed assembly is characterized by the influence of external forces that have been purportedly designed.

Equilibrium

The core concept of the self-assembly relies on the chemical equilibrium – all the steps contributing in the assembly of a supramolecular architecture have to be reversible and be driven by moderate ΔGs.

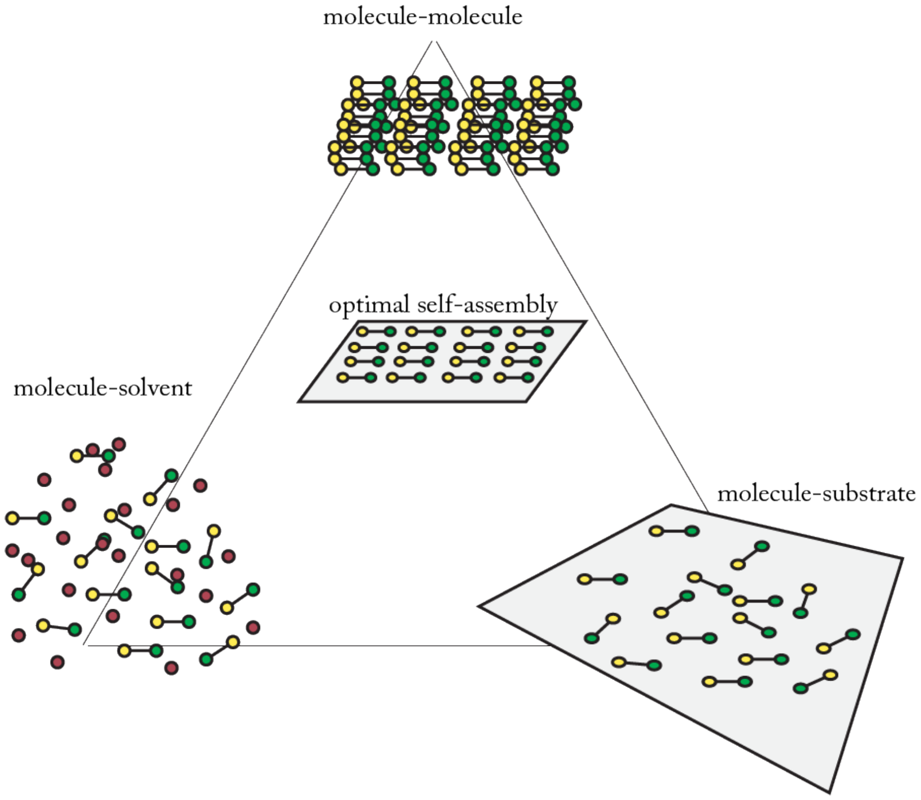

Figure 3: the self-assembly triangle summarizes the equilibrium concept. In order to achieve optimal self-assembly, all the interactions must be balanced;

Furthermore all the multiple interactions must be balanced: the "self-assembly" triangle in figure is a scheme which summarize the concept: in order to achieve the "optimal" architecture, the molecule-molecule, molecule-substrate, and the molecule-solvent interactions must be similar. This may be seen as the first principle of the self-assembly.

Recognition and Supramolecular Chemistry

The concept of recognition it's complementary to the equilibrium one. In order to assembly a controlled structure, is necessary that the synthons will interact selectively one with the other. The idea has been a great achievement for the biochemistry, it arises from Emil Fischer *lock and key* concept.[3] The thought that some interactions occurs preferentially between properly designed structures, dictates the reactivity between proteins and enzymes. The main idea is to pair complementary weak interactions, in an array with specific positioning. Again, one example in nature is the pairing between the azo-bases in DNA. With the correct combination, the thermodynamic resultant is favored, and finally result as the major (and often the only) product. The same concept is also employed in combinatorial chemistry. In the specific case of 2D architectures on surfaces, the approach is *simplified* due to the loss of degrees of freedom, and many examples based on different interaction have been showed.[4]

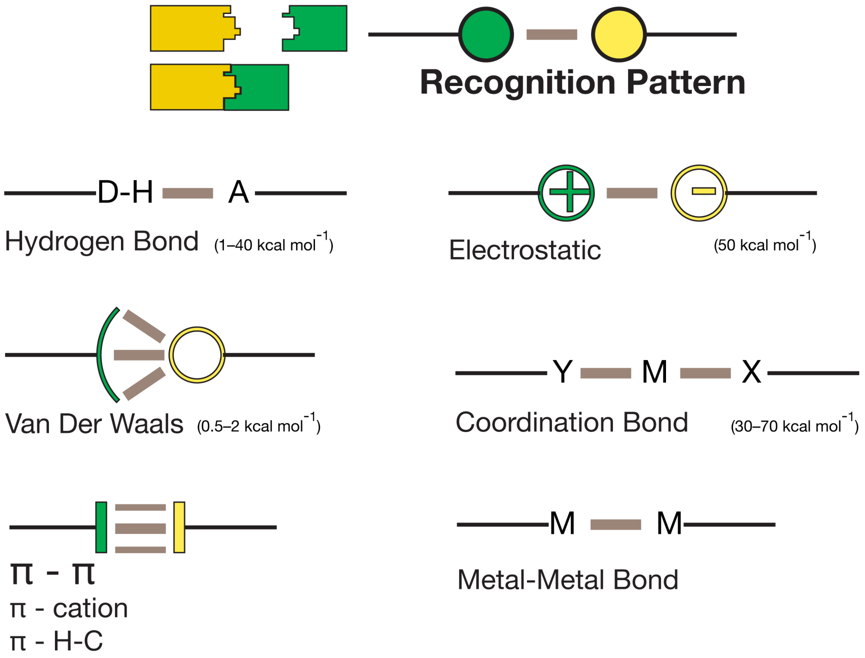

Figure 4: recognition patterns that can be combined in forming self-recognition events.

In his lecture, the Nobel laureate J.-M. Lehn, defines supramolecular chemistry as the "*chemistry beyond the molecule,*"[5] since is based on the association of two or more molecules into organized entities of greater complexity via intermolecular forces. To underline the concept, his definition is usually summarized with *"supermolecules are to molecules and the intermolecular bond what molecules are to atoms and the covalent bond."*. [5]

Non-covalent interactions:

The crystallization of molecules in 2D at surfaces, and especially the formation of self-assembled structures at the solid-liquid interface, relies not only on a delicate balance of intra-molecular, inter-molecular and interfacial interactions. The self-assembly also relies on the recognition events between designed building blocks capable of associating into programmed architectures, gathering from intermolecular interactions, such as hydrogen bonds, van der Waals forces and metallo-ligand interactions which feature a high geometrical control. It is mandatory to consider the mutual interplay of all those interactions, together with the properties of the molecule and of the system in order to understand and predict the self-assembly properties.

The supramolecular chemistry is built around "*non-covalent*" interactions: the term non-covalent includes a wide range of attractive and repulsive forces, which will be briefly discussed. Is it possible to divide the non-covalent interactions in two categories, with similar arguments to the derivation of the klopmann-salem equation:[6]

If the synthons have a dense and localized charge the coulombic term is prevalent and we consider the interactions Electrostatic forces, *hard forces*. In the opposite case, if the force acting on the synthon depends on the polarizability of the electron cloud, it might be useful to discuss in terms of frontier orbitals (FMO), therefore we consider it a *soft* force.

This distinction will come useful for intuitively rationalize the various architectures and recognize what forces dominated the assembly process.

Ion-Ion interaction (100-350kJ/mol, hard):

Ionic bonds have comparable strength to the covalent bonds, i.e. (100 – 350kJ/mol). A tipical ionic material is NaCl, which clearly don't fall inside the "supramolecular" definition, unlike systems such tris-DABO and Fe(CN6)3- .

Ion-Ion interactions are very strong, non-directional, and tend to minimize the structure maximizing the contact.

Ion-ion interactions are vastly used in layer-by-layer deposition,[7] where in general a sequence of positively and negatively charged materials are assembled in series, usually via drop-casting, spin-coating or dip-casting. Another interesting "new" application of ion-ion interaction are the "nanoions" developed by Grzybowski group at Northwestern University – they coated nanoparticles with charged species, which interacts and self-assemble in unforeseen ways.[8] Since ion-ion interactions are non-directional and long-range, very few examples of structures visualized with STM are reported in literature,[9] and they usually couple the ion-ion interaction with complementary hydrogen bonds. This should not surprise, since being the interaction very strong, it breaks the equilibrium rule. For instance carboxylates on metallic surfaces usually prefer to bind to the substrate and adopt a standing geometry as shown by *Li et Al.*[9a, b]

Ion Dipole (50-200 kJ/mol, hard):

The coordination of sodium ions by water, is a typical example of such interaction. Ion-Dipole interactions are observed in both solid state and solution, in supramolecular chemistry a good example are the complexes formed by metallic cations with crown ethers. Among those interactions are the coordination bonds, between metals and ligands with “hard” character. Again, very few examples of 2D ordered architectures which exploits this interaction as the recognition event for the self-assembly are reported.

Dipole-Dipole (5-50kJ/mol, hard)

The alignment of electric dipoles may generate considerable attractive interactions. In general those interactions have a long range dependence, here included a dramatic effect in crystals, and especially in the distribution, shape and size of the domains. However they can also affect the preference towards a particular polymorph. Their effect on the self-assembly will be further presented in chapter 3. Some successful examples of exploitation of dipole-dipole interaction as a recognition event and driving force for patterning a surface are reported in literature. [10]

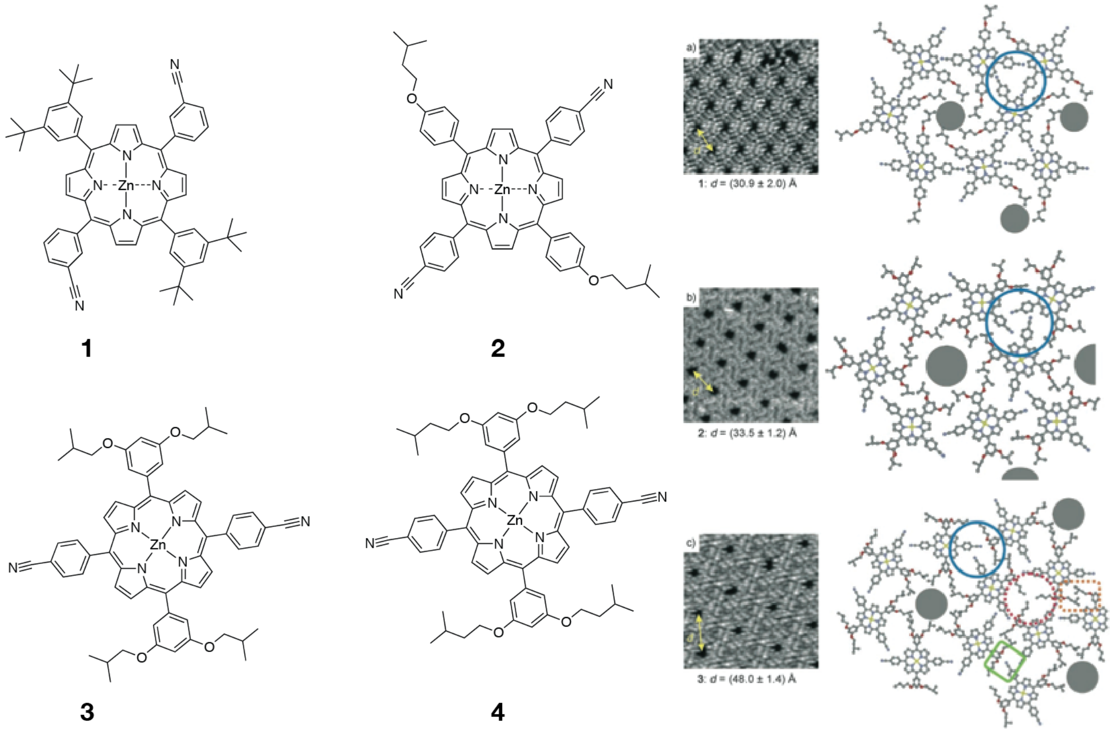

Figure 5:

One excellent example is the work performed by *Spillmann et al.* where the zinc-porphyrins **1-4**,[11] are functionalized with two cyano-phenyl moieties, in order to drive the auto-organization via dipole-dipole interaction. They show how the system pack forming a porous phase capable of hosting C60, and in a subsequent work how changing the length of the other functionalization on the meso position is possible to trim the distance between the pores.

Hydrogen Bond (4-120kJ/mol, hard)

It is definitely one of the most studied and interesting weak interactions. Examples range from amines,[12] to water to the proteins, to the connections among pairs of nucleobases in DNA.[13] It features directionality and can easily be designed into recognition patterns.[14] It is presented in almost all chemistry textbooks, therefore the discussion is kept at a really basic level. Usually it is described to occur between two highly electronegative elements (O, N, F, Cl) via an hydrogen atom, however throughout this work a broader definition where no restrictions about atom identity will be considered. The general structure is –A---H-D- where a hydrogen bond donor (D) forms a polar σ bond with hydrogen that carries a partial positive charge. The group D-H has an attractive interaction with at least one acceptor atom (or group) A, thanks to the accumulation of the electron density on the acceptor. The examples of hydrogen bonded structures are multiple,[15] and it is probably the most used recognition event. The only drawback is that it negatively affect the solubility – often the molecules capable of multiple hydrogen bonds aggregates in insoluble species which are almost unprocessable.

While there's a multitude of different recognition patterns, ranging from lactams[16] to quadruple bonds,[17] the most used is probably the di-hapto recognition between carboxylic acids. Exploiting the directionality of the interaction, is it possible to generate almost all kind of structures, as recently reviewed by Ivasenko and Perepichka.[18] Architectures range from glass phases,[19] to complicate semi-regular topologies,[20] such as the "flower"[21] or the "kagomé"[22] packing.

The hydrogen bond also allows to build multi-component networks, as shown by Beton et al, with the mixed formation of PDCI and melamine porous phases. Their work was one of the first examples, and since 2003 has been extended by many.[23]

The rule of the thumb in multi-components HB networks comes from the crystallographers: "*The best proton donors and acceptors remaining after intramolecular hydrogen-bond formation form intermolecular hydrogen bonds to one another*",[24] which in other words may be stated as "*the best-donors are paired with the best acceptors*".

π-π (0-50kJ/mol, soft)

The π-π interactions are interactions between π conjugated systems, usually aromatics. In general the geometries are controlled by electrostatic interactions, but the major energetic contributions usually comes from other factors.[25] They can be seen as the resultant of the electrostatic and van der Waals interactions between extended aromatic systems.

Examples of π-π interactions on the self-assembly of bidimensional architectures are quite common,[26] despite the general preference for edge-on structures.
In a recent work, *Gesquière et al*,[27] showed how to exploit a smart design of the building block to induce the stacking of oligotiophenes on the graphite surface. In their manuscript, they notice how the adsorption on the surface is induced by the interplay of the van der Waals forces of the alkylic chains plus the hydrogen bonding between bisurea moieties. The thiophene bridge is then free to rotate and assume the edge on orientation, which maximize the π-π interaction.

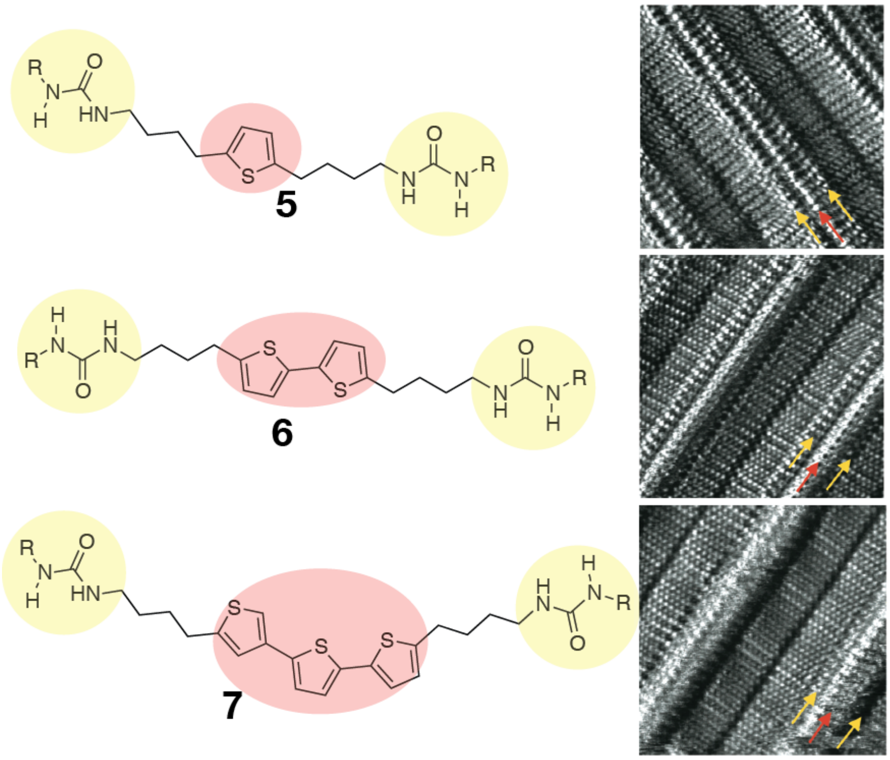

Figure 6, self-assembled structures of the molecules 5-7 at the 1-octanol-HOPG interface. The yellow arrows indicate the position of the urea groups, and the red arrows the position of the thiophene rings within the lamella. In the sketches, R=$C_{12}H_{25}$. ; reproduced from [27]

VdW(<5kJ/mol, soft)

Van der Waals force is a broad definition which usually includes all the non-covalent interactions that scale with the distance as $1/r^6$. Commonly, these forces have their origin on London dispersion forces,[28] which arise from the attraction of the instantaneous dipoles generated by the polarization of the atomic electron clouds, but the van der Waals also comprehends terms from the interaction between dipoles and induced dipoles (Debye),[29] and dipole-dipole interactions between freely rotating molecules (Keesom).[30] Those terms are generally somehow marginal with respect to London dispersion forces.

Despite the relative weakness, VdW forces are very useful in designing supramolecular structures and 2D structures, they present an easily recognition strategy: the interdigitation of alkyl chains, i.e. the trapping of a chain between other two. There are two different useful aspects to describe from the alkyl chains stand point: their contribution to the adsorption energy, by almost 2 kCal/mol per methylene unit,[31] and their mutual interaction with ca. 0.7 kCal/mol per methylene.[32] This implies that they tend to aggregate in parallel fashion,[33] as demonstrated by *Rabe et al.* It is the interdigitation wich makes it possible to form crystalline patterns. Nowadays, interdigitation presents one of the best strategy in design of 2D architectures on the surface, as reviewed recently by *Tahara et al.*[34] One of the most remarkable examples, is probably the work of Adisoejoso and coworkers: they realized the first example of a four component 2D crystal.[35]

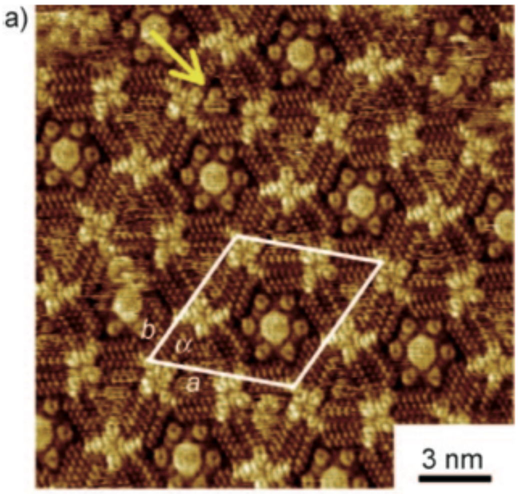

Figure 7: the four component 2D crystal realized by Adisoejoso and coworkers, a remarkable example of crystal engineering via vdW forces. Reproduced from [35]

Simulations and STM:

In order to unfold the mechanisms of the assembly a possibility is to apply a numerical simulation to self-assembly.[36] The two approaches are complementary: simulation helps in predicting and designing a system according to the concepts previously presented, or after achieving the experimental structure calculations helps unraveling the subtleties of the interactions.

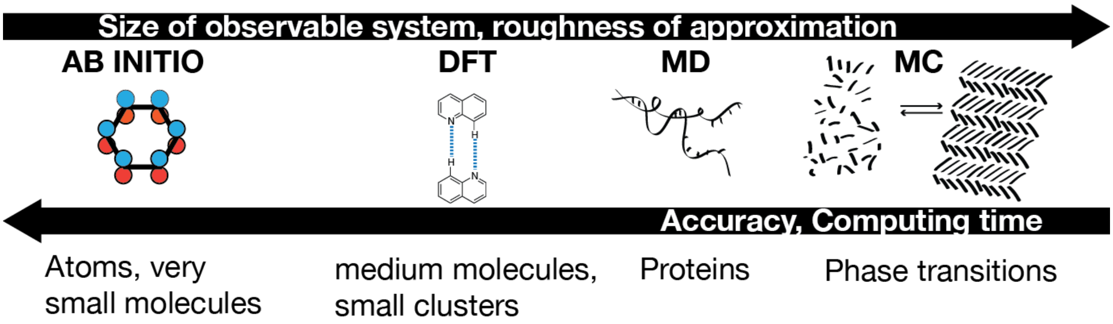

Figure 8: Comparison of the various families of computer simulation methods.

Depending on the family of the simulations, the approach on the self-assembly is different: where ab-initio and dft are mostly employed to analyze the experiment in vacuum conditions, or the geometry of the synthons, at the solid-liquid interface Molecular Dynamics and MonteCarlo methods are prevalent. The contribution are briefly discussed in the following section.

Ab initio

Ab initio methods,[37] in its modern meaning, are calculation from first principles of quantum mechanics.[38] In general they utilize a basis set built form a linear combination of atomic orbitals (LCAO) to solve the Schrödinger equation associated to the system under study. In the most basic methods, such as Hartree-Fock or configuration interaction, this approach allows to reduce the problem to an eigenvalue equation of the electronic molecular Hamiltonian, with a finite number of solutions. Ab initio methods have the great advantage that they can converge to the exact solution, but since the eigenvalue problem usually scales exponentially with the number of atoms are often impossible to use in reasonable times at the appropriate level of approximation for bigger molecules.

Some successful applications of ab initio methods for explaining the self-assembly in 2D and their visualization with STM, have been reported. In their pioneristic work, *Chan et al*,[39] exploited Ab initio calculations to confirm the molecular orientation obtained by EELS, to show that the amino nitrogen atom possess an sp(3) hybridization, and that is directly bonded to the substrate. Another application, this time to discern the limited response to geometrical stimuli between chains and 2D architectures has been showed by Clair and coworkers.[40] A more “classical” but very recent work performed by Makoudi et al,[41] has used a theoretical investigation at the ab initio level to confirms the different binding energies of two coupling motifs and rationalizes the network formation and the diffusion pathway of a hierarchical, bimolecular network of sexiphenyl dicarbonitrile and N,N'-diphenyl oxalic amide molecules on the Ag(111) surface.

Density functional theory (DFT)

Dft methods use the electron density functional to investigate the property of many electron systems. DFT derives from the theoretical grounds of the two Hohenberg-Kohn theorems[42] : The first H–K theorem demonstrates that the ground state properties of a many-electron systems are uniquely determined by an electron density that depends on only 3 spatial coordinates. The second H–K theorem defines an energy functional for the system and proves that the correct ground state electron density minimizes this energy functional.

Computational costs (also know as *machine time*) are relatively low when compared to ab-initio methods, such as Hartree–Fock theory, but DFT sometimes has limited accuracy over the intermolecular interactions, especially the vdW, and other strongly correlated systems.

Despite so, dft is definitely more frequently used in the analysis of self-assembled structures, especially when the interactions with the substrate become important. In the work of Kelly, Lukas et al,[43] two different polymorph of adenine were observed on the Au (111) surface, and their properties thoughtfully studied via DFT. Other applications have been the investigation of the role of gold adatoms in the formation of SAMs of alkanethiols,[44] the analysis of the molecular structure, adsorption geometry, and adsorption energy of linear dicarboxylic acids,[45] and many more.[46]

Molecular Dynamics (MD)

The molecular dynamics is based on the numerical solution of the Newton equation of motion in a system of interacting particles. The forces between the particles, and the potential energies are defined by the Force Field. In general the force field is *empirical* and it consist in a summation over different contribution such as bonds, dihedrals, etc.

MD is by far the most used type of simulation when analyzing the self assembly on a substrate. Almost twenty years ago, a work of Rabe et al, paved the way to the use of molecular dynamics to investigate the packing of alkyl chains on HOPG.[47]

Since then most of the proposed structures pass trough a molecular dynamics minimization. However also other uses have been developed: *Palma et al*, conducted a study of the phase diagram of bi-component porous networks of Melamine and uracyl,[48] Lackinger and coworkers used MD to study the dynamics of the grain boundaries in hydrogen bonded assemblies,[49] and many more examples can be found[50] in literature.

Monte Carlo (MC)

Monte Carlo methods are based on a random sampling to compute their results. This is a profound difference from the other simulations so far presented, which are *deterministic.* MC are based on *stochastic* processes, i.e. are statistic methods. This is extremely useful when solving numerical integrals, but for being applied to real solid-state problems they usually require strong approximations. On the other side, MC methods allow the interplay of thousands and eventually millions of particles, which is practically impossible using deterministic simulations. They have been employed successfully by Szabelski et al to unravel the self-assembly of tripods on triangular lattices compared to the assembly of triangulenes, describing the thermodynamic polymorph as a function of the arm lenght.[51] The studies were further extended by predicting the miscibility of building blocks which differ for the length of the alkyl chains,[52] and to explain polymorphism and the formation of chiral phases.[53]

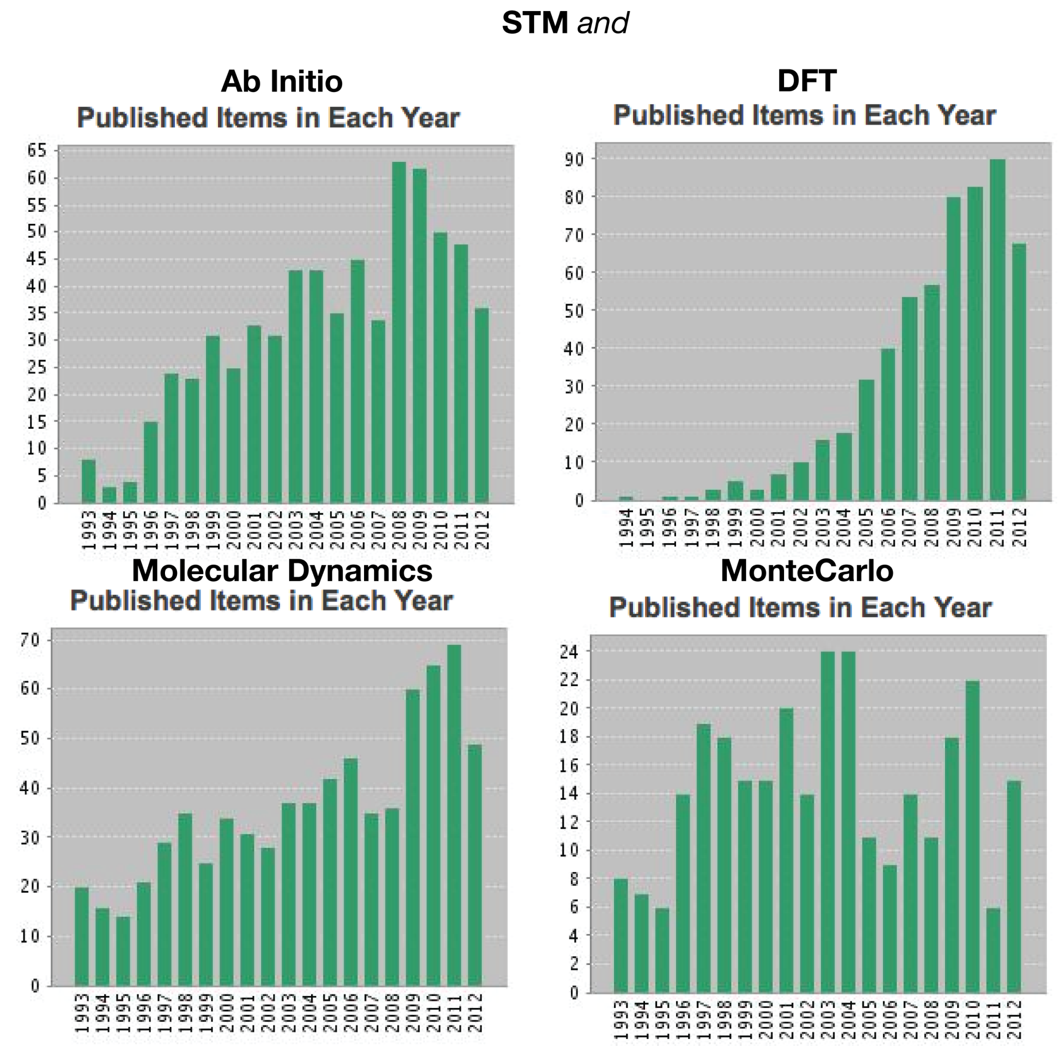

Figure 9: ISI Web of Knowledge publication reports for the key STM and the various numerical methods.

So far, the applications of numerical methods to the self-assembly are still growing, as can be observed from the plots of the publications in the last twenty years reported in figure 9.

Towards 3 Dimensions

The ultimate objective of studying the surfaces is being able to functionalize them in order to direct the growth towards real three-dimensional objects. There's clearly the requirement of the self-assembly; the idea is to have hierarchical growth of multi layered structures, departing from an accurate 2D positioning. One example of such approach has been demonstrated by *Charra et al*: they show the assembly of nano-pillars based on [2,2] paracyclophanes, which can be effectively positioned on top of 2D platforms, forming an highly crystalline 3D pattern.[54]

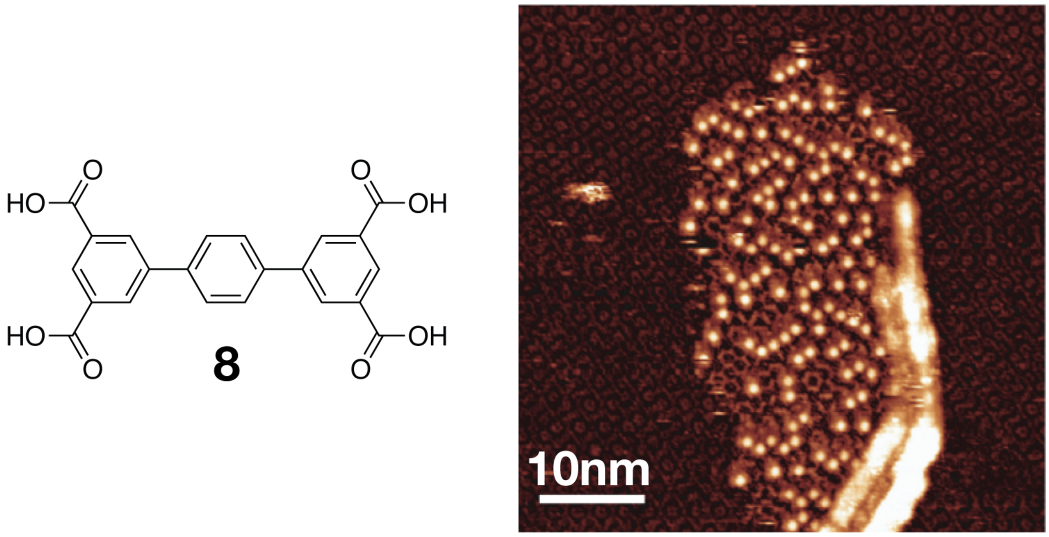

Figure 10: a)the tetracarboxylic acid derivative used to grow templated bi-layers (in b)) after the addition of C60.

Another approach has been finally showed by *Beton et al*,[55] where they showed that the addition of C60 to a preadsorbed monolayer of TCAs induced the activation of the growth of a second layer.

In conclusion, we have shown how from the interplay between Scanning Tunneling Microscopy and computer simulation, is it possible to unravel the mechanisms which direct the self-assembly. Two are the possible approaches, one where the computations are aimed to the design of a structure with selected properties, which has to be subsequently proved experimentally, or vice-versa, a deductive process, where from the experimental evidences the insight is obtained through the computer modeling and simulations.

References:

1. Eigler, D. M.; Schweizer, E. K., Positioning Single Atoms with a Scanning Tunneling Microscope. *Nature* **1990,** *344* (6266), 524-526.

2. (a) Cyr, D. M.; Venkataraman, B.; Flynn, G. W., STM investigations of organic molecules physisorbed at the liquid-solid interface. *Chemistry of Materials* **1996,** *8* (8), 1600-1615; (b) De Feyter, S.; De Schryver, F. C., Two-dimensional supramolecular self-assembly probed by scanning tunneling microscopy. *Chemical Society Reviews* **2003,** *32* (3), 139-150.

3. Fischer, E., *Berichte der deutschen physikalischen gesellschaft* **1894,** *27*, 2985-2993.

4. Theobald, J.; Oxtoby, N.; Phillips, M.; Champness, N.; BETON, P., Controlling molecular deposition and layer structure with supramolecular surface assemblies. *Nature* **2003,** *424* (6952), 1029-1031.

5. Lehn, J. M., Supramolecular Chemistry - Scope and Perspectives Molecules, Supermolecules, and Molecular Devices. *Angewandte Chemie-International Edition In English* **1988,** *27* (1), 89-112.

6. Klopman, G., Chemical reactivity and the concept of charge- and frontier-controlled reactions. *Journal Of The American Chemical Society* **1968,** *90* (2), 223-234.

7. Decher, G., Fuzzy Nanoassemblies: Toward Layered Polymeric Multicomposites. *Science* **1997,** *277* (5330), 1232-1237.

8. (a) Kalsin, A. M.; Fialkowski, M.; Paszewski, M.; Smoukov, S. K.; Bishop, K. J. M.; Grzybowski, B. A., Electrostatic Self-Assembly of Binary Nanoparticle Crystals with a Diamond-Like Lattice. *Science* **2006,** *312* (5772), 420-424; (b) Kalsin, A. M.; Kowalczyk, B.; Smoukov, S. K.; Klajn, R.; Grzybowski, B. A., Ionic-like Behavior of Oppositely Charged Nanoparticles. *Journal Of The American Chemical Society* **2006,** *128* (47), 15046-15047.

9. (a) Li, Z.; Han, B.; Wan, L. J.; Wandlowski, T., Supramolecular nanostructures of 1,3,5-benzene-tricarboxylic acid at electrified au(111)/0.05 M H2SO4 interfaces: An in situ scanning tunneling microscopy study. *Langmuir* **2005,** *21* (15), 6915-6928; (b) Li, Z.; Wandlowski, T., Structure Formation and Annealing of Isophthalic Acid at the Electrochemical Au(111)-Electrolyte Interface. *Journal of Physical Chemistry C* **2009,** *113* (18), 7821-7825; (c) Sasahara, A.; Uetsuka, H.; Ishibashi, T.; Onishi, H., The dependence of scanning tunneling microscope topography of carboxylates on their terminal groups. *Journal Of Physical Chemistry B* **2003,** *107* (50), 13925-13928.

10. (a) Kong, L. M.; Chesneau, F.; Zhang, Z. Z.; Staier, F.; Terfort, A.; Dowben, P. A.; Zharnikov, M., Electronic Structure of Aromatic Monomolecular Films: The Effect of Molecular Spacers and Interfacial Dipoles. *Journal of Physical Chemistry C* **2011,** *115* (45), 22422-22428; (b) Kunkel, D. A.; Simpson, S.; Nitz, J.; Rojas, G. A.; Zurek, E.; Routaboul, L.; Doudin, B.; Braunstein, P.; Dowben, P. A.; Enders, A., Dipole driven bonding schemes of quinonoid zwitterions on surfaces. *Chemical Communications* **2012,** *48* (57), 7143-7145; (c) Niu, T. C.; Zhou, C. G.; Zhang, J. L.; Zhong, S.; Cheng, H. S.; Chen, W., Substrate Reconstruction Mediated Unidirectionally Aligned Molecular Dipole Dot Arrays. *Journal of Physical Chemistry C* **2012,** *116* (21), 11565-11569; (d) Wei, Y. H.; Tong, W. J.; Zimmt, M. B., Self-assembly of patterned monolayers with nanometer features: Molecular selection based on dipole interactions and chain length. *Journal Of The American Chemical Society* **2008,** *130* (11), 3399-3405; (e) Xu, L.; Miao, X. R.; Ying, X.; Deng, W. L., Two-Dimensional Self-Assembled Molecular Structures Formed by the Competition of van der Waals Forces and Dipole-Dipole Interactions. *Journal of Physical Chemistry C* **2012,** *116* (1), 1061-1069.

11. (a) Spillmann, H.; Kiebele, A.; Stohr, M.; Jung, T. A.; Bonifazi, D.; Cheng, F. Y.; Diederich, F., A two-dimensional porphyrin-based porous network featuring communicating cavities for the templated complexation of fullerenes. *Adv Mater* **2006,** *18* (3), 275-+; (b) Wintjes, N.; Hornung, J.; Lobo-Checa, J.; Voigt, T.; Samuely, T.; Thilgen, C.; Stohr, M.; Diederich, F.; Jung, T. A., Supramolecular synthons on surfaces: Controlling dimensionality and periodicity of tetraarylporphyrin assemblies by the interplay of cyano and alkoxy substituents. *Chemistry-a European Journal* **2008,** *14* (19), 5794-5802.

12. Moore, T. S.; Winmill, T. F., CLXXVII.-The state of amines in aqueous solution. *Journal of the Chemical Society, Transactions* **1912,** *101*, 1635-1676.

13. Watson, J. D.; Crick, F. H. C., Molecular Structure of Nucleic Acids: A Structure for Deoxyribose Nucleic Acid. *Nature* **1953,** *171* (4356), 737-738.

14. (a) Desiraju, G. R., Hydrogen bridges in crystal engineering: Interactions without borders. *Accounts Chem Res* **2002,** *35* (7), 565-573; (b) Desiraju, G. R., *Crystal design*. John Wiley & Sons Inc.: 2003.

15. (a) Ciesielski, A.; Perone, R.; Pieraccini, S.; Spada, G. P.; Samori, P., Nanopatterning the surface with ordered supramolecular architectures of N-9-alkylated guanines: STM reveals. *Chemical Communications* **2010,** *46* (25), 4493-4495; (b) Ciesielski, A.; Schaeffer, G.; Petitjean, A.; Lehn, J.-M.; Samori, P., STM Insight into Hydrogen-Bonded Bicomponent 1D Supramolecular Polymers with Controlled Geometries at the Liquid-Solid Interface. *Angew Chem Int Edit* **2009,** *48* (11), 2039-2043; (c) Lackinger, M.; Griessl, S.; Heckl, W. A.; Hietschold, M.; Flynn, G. W., Self-assembly of trimesic acid at the liquid-solid interface - a study of solvent-induced polymorphism. *Langmuir* **2005,** *21* (11), 4984-4988.

16. Mourran, A.; Ziener, U.; Moller, M.; Suarez, M.; Lehn, J. M., Homo- and heteroassemblies of lactim/lactam recognition patterns on highly ordered pyrolytic graphite: An STM investigation. *Langmuir* **2006,** *22* (18), 7579-7586.

17. Gesquiere, A.; Jonkheijm, P.; Hoeben, F. J. M.; Schenning, A. P. H. J.; De Feyter, S.; De Schryver, F. C.; Meijer, E. W., 2D-Structures of quadruple hydrogen bonded oligo(p-phenylenevinylene)s on graphite: Self-assembly behavior and expression of chirality. *Nano Lett* **2004,** *4* (7), 1175-1179.

18. Ivasenko, O.; Perepichka, D. F., Mastering fundamentals of supramolecular design with carboxylic acids. Common lessons from X-ray crystallography and scanning tunneling microscopy. *Chemical Society Reviews* **2011,** *40* (1), 191-206.

19. Garrahan, J. P.; Stannard, A.; Blunt, M. O.; Beton, P. H., Molecular random tilings as glasses. *P Natl Acad Sci USA* **2009,** *106* (36), 15209-15213.

20. Cadeddu, A.; Ciesielski, A.; El Malah, T.; Hecht, S.; Samori, P., Modulating the self-assembly of rigid "clicked" dendrimers at the solid-liquid interface by tuning non-covalent interactions between side groups. *Chemical Communications* **2011,** *47* (38), 10578-10580.

21. (a) Gutzler, R.; Sirtl, T.; Dienstmaier, J. F.; Mahata, K.; Heckl, W. M.; Schmittel, M.; Lackinger, M., Reversible Phase Transitions in Self-Assembled Mono layers at the Liquid-Solid Interface: Temperature-Controlled Opening and Closing of Nanopores. *Journal Of The American Chemical Society* **2010,** *132* (14), 5084-5090; (b) Lackinger, M.; Heckl, W. M., Carboxylic Acids: Versatile Building Blocks and Mediators for Two-Dimensional Supramolecular Self-Assembly. *Langmuir* **2009,** *25* (19), 11307-11321; (c) Shen, Y.-t.; Deng, K.; Zhang, X.-m.; Lei, D.; Xia, Y.; Zeng, Q.-d.; Wang, C., Selective and Competitive Adsorptions of Guest Molecules in

Phase-Separated Networks. *Journal of physical Chemistry C* **2011,** *40* (115), 19696–19701.

22. (a) Ciesielski, A.; Cadeddu, A.; Palma, C.-A.; Gorczynski, A.; Patroniak, V.; Cecchini, M.; Samori, P., Self-templating 2D supramolecular networks: a new avenue to reach control over a bilayer formation. *Nanoscale* **2011,** *3* (10), 4125-4129; (b) Lu, C.; Wei, Y.; Zhu, E.; Reutt-Robey, J. E.; Xu, B., Polymorphism in Self-Assembled Structures of 9-Anthracene Carboxylic Acid on Ag(111). *International Journal of Molecular Sciences* **2012,** *13* (6), 6836-6848; (c) Nath, K. G.; Ivasenko, O.; MacLeod, J. M.; Miwa, J. A.; Wuest, J. D.; Nanci, A.; Perepichka, D. F.; Rosei, F., Crystal engineering in two dimensions: An approach to molecular nanopatterning. *Journal of Physical Chemistry C* **2007,** *111* (45), 16996-17007; (d) Zhao, J.-F.; Li, Y.-B.; Lin, Z.-Q.; Xie, L.-H.; Shi, N.-E.; Wu, X.-K.; Wang, C.; Huang, W., Molecule Length Directed Self-Assembly Behavior of Tetratopic Oligomeric Phenylene-Ethynylenes End-Capped with Carboxylic Groups by Scanning Tunneling Microscopy. *Journal of Physical Chemistry C* **2010,** *114* (21), 9931-9937; (e) Zhou, H.; Dang, H.; Yi, J.-H.; Nanci, A.; Rochefort, A.; Wuest, J. D., Frustrated 2D molecular crystallization. *Journal Of The American Chemical Society* **2007,** *129* (45), 13774-+.

23. (a) Gardener, J. A.; Shvarova, O. Y.; Briggs, G. A. D.; Castell, M. R., Intricate Hydrogen-Bonded Networks: Binary and Ternary Combinations of Uracil, PTCDI, and Melamine. *Journal of Physical Chemistry C* **2010,** *114* (13), 5859-5866; (b) Hoeben, F. J. M.; Zhang, J.; Lee, C. C.; Pouderoijen, M. J.; Wolffs, M.; Wuerthner, F.; Schenning, A. P. H. J.; Meijer, E. W.; De Feyter, S., Visualization of Various Supramolecular Assemblies of Oligo(para-phenylenevinylene)-Melamine and Perylene Bisimide. *Chemistry-a European Journal* **2008,** *14* (28), 8579-8589; (c) Palma, C.-A.; Bjork, J.; Bonini, M.; Dyer, M. S.; Llanes-Pallas, A.; Bonifazi, D.; Persson, M.; Samori, P., Tailoring Bicomponent Supramolecular Nanoporous Networks: Phase Segregation, Polymorphism, and Glasses at the Solid-Liquid Interface. *Journal Of The American Chemical Society* **2009,** *131* (36), 13062-13071; (d) Thalacker, C.; Miura, A.; De Feyter, S.; De Schryver, F. C.; Wurthner, F., Hydrogen bond directed self-assembly of core-substituted naphthalene bisimides with melamines in solution and at the graphite interface. *Organic & Biomolecular Chemistry* **2005,** *3* (3), 414-422; (e) Zhang, H.-M.; Xie, Z.-X.; Long, L.-S.; Zhong, H.-P.; Zhao, W.; Mao, B.-W.; Xu, X.; Zheng, L.-S., One-step preparation of large-scale self-assembled monolayers of cyanuric acid and melamine supramolecular species on Au(111) surfaces. *Journal of Physical Chemistry C* **2008,** *112* (11), 4209-4218; (f) Zhang, X.; Chen, T.; Chen, Q.; Wang, L.; Wan, L.-J., Self-assembly and aggregation of melamine and melamine-uric/cyanuric acid investigated by STM and AFM on solid surfaces. *Phys Chem Chem Phys* **2009,** *11* (35), 7708-7712.

24. Etter, M. C., Encoding and Decoding Hydrogen-Bond Patterns of Organic-Compounds. *Accounts Chem Res* **1990,** *23* (4), 120-126.

25. HUNTER, C. A.; SANDERS, J., The Nature of Pi-Pi Interactions. *Journal Of The American Chemical Society* **1990,** *112* (14), 5525-5534.

26. (a) Ichihara, S.; Yoshinobu, J.; Ogasawara, H.; Nantoh, M.; Kawai, M.; Domen, K., Adsorption of pi-bonded ethylene and ethynyl on Pd(110): an STM study. *Journal of Electron Spectroscopy and Related Phenomena* **1998,** *88*, 1003-1007; (b) Lee, S. L.; Lin, N. T.; Liao, W. C.; Chen, C. H.; Yang, H. C.; Luh, T. Y., Oligomeric Tectonics: Supramolecular Assembly of Double-Stranded Oligobisnorbornene through pi-pi Stacking. *Chemistry-a European Journal* **2009,** *15*

(43), 11594-11600; (c) Saettel, N.; Katsonis, N.; Marchenko, A.; Teulade-Fichou, M. P.; Fichou, D., Triazatrinaphthylene, a three-fold symmetry planar conjugated system with two-dimensional self-assembly properties. *Journal of Materials Chemistry* **2005,** *15* (31), 3175-3180; (d) Samori, P.; Francke, V.; Enkelmann, V.; Mullen, K.; Rabe, J. P., Synthesis and solid state structures of functionalized phenyleneethynylene trimers in 2D and 3D. *Chemistry of Materials* **2003,** *15* (5), 1032-1039; (e) Yoosaf, K.; James, P. V.; Ramesh, A. R.; Suresh, C. H.; Thomas, K. G., Self-organization of phenyleneethynylene into wire-like molecular materials on surfaces. *Journal of Physical Chemistry C* **2007,** *111* (41), 14933-14936; (f) Bauerle, P.; Fischer, T.; Bidlingmeier, B.; Stabel, A.; Rabe, J. P., Oligothiophenes - yet Longer - Synthesis, Characterization, and Scanning-Tunneling-Microscopy Images of Homologous, Isomerically Pure Oligo(Alkylthiophene)S. *Angewandte Chemie-International Edition In English* **1995,** *34* (3), 303-307; (g) Fukunaga, T.; Harada, K.; Takashima, W.; Kaneto, K., *Jpn. J. Appl. Phys.* **1997,** (36), 4466-4467; (h) Stabel, A.; Rabe, J. P., Scanning-Tunneling-Microscopy of Alkylated Oligothiophenes at Interfaces with Graphite. *Synthetic Met* **1994,** *67* (1-3), 47-53.

27. Gesquière, A.; Abdel-Mottaleb, M. M. S.; De Feyter, S.; De Schryver, F. C.; Schoonbeek, F.; van Esch, J.; Kellogg, R. M.; Feringa, B. L.; Calderone, A.; Lazzaroni, R.; Br√©das, J. L., Molecular Organization of Bis-urea Substituted Thiophene Derivatives at the Liquid/Solid Interface Studied by Scanning Tunneling Microscopy. *Langmuir* **2000,** *16* (26), 10385-10391.

28. London, F., The general theory of molecular forces. *Transactions of the Faraday Society* **1937,** *33*, 8b-26.

29. (a) Debye, P. J. W., Zur Theorie der anomalen Dispersion im Gebiete der langwelligen elektrischen Strahlung,. *Berichte der Deutschen physikalischen Gesellschaft* **1913,** *15* 777-793; (b) Onsager, L., Electric Moments of Molecules in Liquids. *Journal of the American Chemical Society* **1936,** *58* (8), 1486-1493.

30. keesom, W. H., *Physikalische Zeitschrift* **1921,** *22*, 129.

31. (a) Gellman, A.; Paserba, K., Kinetics and mechanism of oligomer desorption from surfaces: n-alkanes on graphite. *Journal Of Physical Chemistry B* **2002,** *106* (51), 13231-13241; (b) Gellman, A.; Paserba, K.; Vaidyanathan, N., A comparative study of the kinetics and energetics of oligomer desorption from graphite. *Journal Of Molecular Catalysis A-Chemical* **2005,** *228* (1-2), 67-75; (c) Paserba, K.; Vaidyanathan, N.; Gellman, A., Conformational entropy effects on the desorption kinetics of polyethers from graphite. *Langmuir* **2002,** *18* (25), 9799-9809.

32. Samori, P.; Fechtenkotter, A.; Jackel, F.; Bohme, T.; Mullen, K.; Rabe, J. P., Supramolecular staircase via self-assembly of disklike molecules at the solid-liquid interface. *Journal Of The American Chemical Society* **2001,** *123* (46), 11462-11467.

33. Rabe, J. P.; Buchholz, S., Commensurability and Mobility in 2-Dimensional Molecular-Patterns on Graphite. *Science* **1991,** *253* (5018), 424-427.

34. Tahara, K.; Furukawa, S.; Uji-I, H.; Uchino, T.; Ichikawa, T.; Zhang, J.; Mamdouh, W.; Sonoda, M.; De Schryver, F. C.; De Feyter, S.; Tobe, Y., Two-dimensional porous molecular networks of dehydrobenzo 12 annulene derivatives via alkyl chain interdigitation. *Journal Of The American Chemical Society* **2006,** *128* (51), 16613-16625.

35. Adisoejoso, J.; Tahara, K.; Okuhata, S.; Lei, S.; Tobe, Y.; De Feyter, S., Two-Dimensional Crystal Engineering: A Four-Component Architecture at a Liquid-Solid Interface. *Angew Chem Int Edit* **2009,** *48* (40), 7353-7357.

36. Hallmark, V. M.; Chiang, S., PREDICTING STM IMAGES OF MOLECULAR ADSORBATES. *Surface Science* **1995,** *329* (3), 255-268.

37. (a) Parr, R. G.; Craig, D. P.; Ross, I. G., Molecular Orbital Calculations of the Lower Excited Electronic Levels of Benzene, Configuration Interaction Included. *The Journal of Chemical Physics* **1950,** *18* (12), 1561-1563; (b) Parr, R. G., On the genesis of a theory. *International Journal of Quantum Chemistry* **1990,** *37* (4), 327-347; (c) Chen, T. C., Expansion of Electronic Wave Functions of Molecules in Terms of ``United-Atom'' Wave Functions. *The Journal of Chemical Physics* **1955,** *23* (11), 2200-2201; (d) Roothaan, C. C. J., Evaluation of Molecular Integrals by Digital Computer. *The Journal of Chemical Physics* **1958,** *28* (5), 982-983.

38. Allen, L. C.; Karo, A. M., Basis Functions for Ab Initio Calculations. *Reviews of Modern Physics* **1960,** *32* (2), 275-285.

39. Chen, Q.; Frankel, D. J.; Richardson, N. V., Self-assembly of adenine on Cu(110) surfaces. *Langmuir* **2002,** *18* (8), 3219-3225.

40. Clair, S.; Pons, S.; Seitsonen, A. P.; Brune, H.; Kern, K.; Barth, J. V., STM study of terephthalic acid self-assembly on Au(III): Hydrogen-bonded sheets on an inhomogeneous substrate. *Journal Of Physical Chemistry B* **2004,** *108* (38), 14585-14590.

41. Makoudi, Y.; Arras, E.; Kepcija, N.; Krenner, W.; Klyatskaya, S.; Klappenberger, F.; Ruben, M.; Seitsonen, A. P.; Barth, J. V., Hierarchically Organized Bimolecular Ladder Network Exhibiting Guided One-Dimensional Diffusion. *Acs Nano* **2012,** *6* (1), 549-556.

42. Kohn, W.; Sham, L. J., Self-Consistent Equations Including Exchange and Correlation Effects. *Physical Review* **1965,** *140* (4A), A1133-A1138.

43. (a) Kelly, R. E. A.; Xu, W.; Lukas, M.; Otero, R.; Mura, M.; Lee, Y.-J.; Laegsgaard, E.; Stensgaard, I.; Kantorovich, L. N.; Besenbacher, F., An investigation into the interactions between self-assembled adenine molecules and a Au(111) surface. *Small* **2008,** *4* (9), 1494-1500; (b) Lukas, M.; Kelly, R. E. A.; Kantorovich, L. N.; Otero, R.; Xu, W.; Laegsgaard, E.; Stensgaard, I.; Besenbacher, F., Adenine monolayers on the Au(111) surface: Structure identification by scanning tunneling microscopy experiment and ab initio calculations. *Journal Of Chemical Physics* **2009,** *130* (2).

44. Voznyy, O.; Dubowski, J. J.; Yates, J. T., Jr.; Maksymovych, P., The Role of Gold Adatoms and Stereochemistry in Self-Assembly of Methylthiolate on Au(111). *Journal Of The American Chemical Society* **2009,** *131* (36), 12989-12993.

45. Heininger, C.; Kampschulte, L.; Heckl, W. A.; Lackinger, M., Distinct Differences in Self-Assembly of Aromatic Linear Dicarboxylic Acids. *Langmuir* **2009,** *25* (2), 968-972.

46. (a) Bald, I.; Wang, Y.-g.; Dong, M.; Rosen, C. B.; Ravnsbaek, J. B.; Zhuang, G.-l.; Gothelf, K. V.; Wang, J.-g.; Besenbacher, F., Control of Self-Assembled 2D Nanostructures by Methylation of Guanine. *Small* **2011,** *7* (7), 939-949; (b) Dmitriev, A.; Spillmann, H.; Stepanow, S.; Strunskus, T.; Woell, C.; Seitsonen, A. P.; Lingenfelder, M.; Lin, N.; Barth, J. V.; Kern, K., Asymmetry induction by cooperative intermolecular hydrogen bonds in surface-anchored layers of achiral molecules. *Chemphyschem* **2006,** *7* (10), 2197-2204; (c) Oison, V.; Koudia, M.; Abel, M.; Porte, L., Influence of stress on hydrogen-bond formation in a halogenated phthalocyanine network. *Physical Review B* **2007,** *75* (3); (d) Yu, M.; Wang, J.; Mura, M.; Meng, Q.-q.; Xu, W.; Gersen, H.; Laegsgaard, E.; Stensgaard, I.; Kelly, R. E.

A.; Kjems, J.; Linderoth, T. R.; Kantorovich, L. N.; Besenbacher, F., Homochiral Xanthine Quintet Networks Self-Assembled on Au(111) Surfaces. *Acs Nano* **2011,** *5* (8), 6651-6660.
47. HENTSCHKE, R.; SCHURMANN, B.; RABE, J., MOLECULAR-DYNAMICS SIMULATIONS OF ORDERED ALKANE CHAINS PHYSISORBED ON GRAPHITE. *Journal Of Chemical Physics* **1992,** *96* (8), 6213-6221.
48. Palma, C. A.; Samori, P.; Cecchini, M., Atomistic Simulations of 2D Bicomponent Self-Assembly: From Molecular Recognition to Self-Healing. *Journal Of The American Chemical Society* **2010,** *132* (50), 17880-17885.
49. Lackinger, M.; Griessl, S.; Kampschulte, L.; Jamitzky, F.; Heckl, W. M., Dynamics of grain boundaries in two-dimensional hydrogen-bonded molecular networks. *Small* **2005,** *1* (5), 532-539.
50. (a) Saiz-Poseu, J.; Faraudo, J.; Figueras, A.; Alibes, R.; Busque, F.; Ruiz-Molina, D., Switchable Self-Assembly of a Bioinspired Alkyl Catechol at a Solid/Liquid Interface: Competitive Interfacial, Noncovalent, and Solvent Interactions. *Chemistry-a European Journal* **2012,** *18* (10), 3056-3063; (b) Huang, Y. L.; Li, H.; Ma, J.; Huang, H.; Chen, W.; Wee, A. T. S., Scanning Tunneling Microscopy Investigation of Self-Assembled CuPc/F16CUPc Binary Superstructures on Graphite. *Langmuir* **2010,** *26* (5), 3329-3334; (c) Llanes-Pallas, A.; Yoosaf, K.; Traboulsi, H.; Mohanraj, J.; Seldrum, T.; Dumont, J.; Minoia, A.; Lazzaroni, R.; Armaroli, N.; Bonifazi, D., Modular Engineering of H-Bonded Supramolecular Polymers for Reversible Functionalization of Carbon Nanotubes. *Journal Of The American Chemical Society* **2011,** *133* (39), 15412-15424; (d) Muller, T.; Flynn, G. W.; Mathauser, A. T.; Teplyakov, A. V., Temperature-programmed desorption studies of n-alkane derivatives on graphite: Desorption energetics and the influence of functional groups on adsorbate self-assembly. *Langmuir* **2003,** *19* (7), 2812-2821; (e) Tomba, G.; Stengel, M.; Schneider, W.-D.; Baldereschi, A.; De Vita, A., Supramolecular Self-Assembly Driven by Electrostatic Repulsion: The 1D Aggregation of Rubrene Pentagons on Au(111). *Acs Nano* **2010,** *4* (12), 7545-7551.
51. Szabelski, P.; De Feyter, S.; Drach, M.; Lei, S. B., Computer Simulation of Chiral Nanoporous Networks on Solid Surfaces. *Langmuir* **2010,** *26* (12), 9506-9515.
52. Lei, S. B.; Tahara, K.; Mullen, K.; Szabelski, P.; Tobe, Y.; De Feyter, S., Mixing Behavior of Alkoxylated Dehydrobenzo 12 annulenes at the Solid-Liquid Interface: Scanning Tunneling Microscopy and Monte Carlo Simulations. *Acs Nano* **2011,** *5* (5), 4145-4157.
53. Adisoejoso, J.; Tahara, K.; Lei, S. B.; Szabelski, P.; Rzysko, W.; Inukai, K.; Blunt, M. O.; Tobe, Y.; De Feyter, S., One Building Block, Two Different Nanoporous Self-Assembled Mono layers: A Combined STM and Monte Carlo Study. *Acs Nano* **2012,** *6* (1), 897-903.
54. Bleger, D.; Kreher, D.; Mathevet, F.; Attias, A. J.; Arfaoui, I.; Metge, G.; Douillard, L.; Fiorini-Debuisschert, C.; Charra, F., Periodic Positioning of Multilayered [2.2]Paracyclophane-Based Nanopillars. *Angew Chem Int Edit* **2008,** *47* (44), 8412-8415.
55. Blunt, M. O.; Russell, J. C.; Gimenez-Lopez, M. d. C.; Taleb, N.; Lin, X.; Schroder, M.; Champness, N. R.; Beton, P. H., Guest-induced growth of a surface-based supramolecular bilayer. *Nature Chemistry* **2011,** *3* (1), 74-78.

Chapter 2: Background and Methods

In this chapter, a review of the technical and theoretical background, and the experimental methods are reviewed in details.

Part 1: Instrumentation

Scanning Tunneling Microscopy

The *tunneling-effect* is definitely one of the most fascinating quantum phenomena, and sadly, one of the most abused scientific concepts. The misuse range from new-age philosophies to sixties Sci-fi Z-movies, probably reaching the third place after the relativity and the UFOs. However, most of the fanciness derives from misconceptions. The theory and the first real applications have been devised since long time, such as diodes, but it is in 1981 that our story begins: science-fiction and reality finally merged when in the IBM laboratories in Zurich, Gerd Binnig and Heinrich Rohrer, developed the first scanning tunneling microscope. After thousands of years, we were able to easily observe and manipulate single atoms.
The *probing* in Scanning tunneling microscopy relies on the dependence between the distance between two metallic electrodes and the associated tunneling current.

Theoretical background

Tunneling effect

Expanding from the solutions of a particle in a box, in presence of a thin barrier is it possible to calculate from the Schrödinger equation the probability for the particle to tunnel trough the barrier. The simple derivation[1] brings to the results reported in figure 1: a particle with energy E is described by a wavefunction which spans the entire box, and the $||\Psi||^2$ has a decaying exponential behavior in region 2, i.e. inside the barrier.

$$\Psi_d = 2\Psi_0 e^{-Ad\sqrt{(U-E)/2}}$$

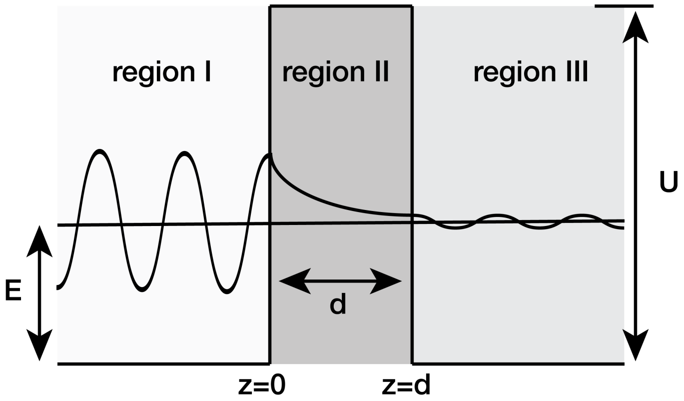

Figure 1: Sketch picturing the real part of the wavefunction for a traveling particle impinging on a potential barrier of width d and height U.

The transmission coefficient, i.e. the ratio between the square modulus of the reflected vs. transmitted wave, results in

$$T = \{1 + \frac{(e^{\kappa L} - e^{-\kappa L})^2}{16\varepsilon(1-\varepsilon)}\}^{-1}$$

Where ε= E/U.

In the case of STM the situation is a little more complicate. The one-dimensional tunneling is described by the formalism introduced by Lang,[2] joining the works of *Nicol et al*[3] and of the two times Nobel laureate Bardeen.

$$I = \int T(E)\rho_2(E - eV)\rho_1(E)dE$$

Where the current is a function of the tunneling transmission coefficient and of the density of states of the electrodes. Such formula has a *hidden* dependence on the distance (the barrier width) which finally becomes apparent after the experiments of Binnig and Rohrer.[4]

$$I = C_0 e^{-\beta z}$$

Where beta is the constant of tunnel decay.

Instrument Set-up

The instrument requires 5 main components: tip, piezo-drive, controller, substrate and feedback, as shown in Figure 2.

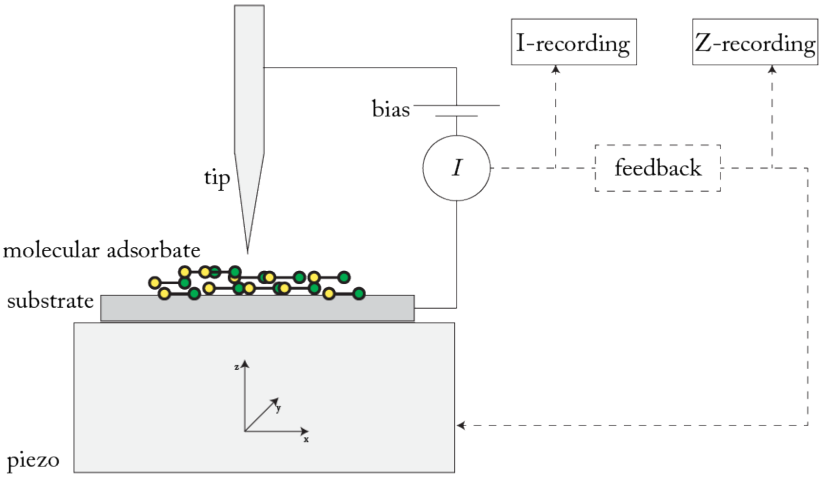

Figure 2: STM Sketch picturing a typical set-up. Between the tip (very close to) and the sample is applied a bias, which induces a tunneling current. Such current is amplified and read by the electronics. The tip is scanned on the substrate by moving one of the two via a piezoelectric drive.

Components

Piezo-drive - it is in general the orthogonal assembly of three piezoelectric crystals capable of displacement in the angstrom range and it is operated under a rigorously controlled voltage. In this way a controlled movement along the three spatial directions is achieved. The most important component is the Z displacement. The scanning procedure consists in sweeping the bias applied to the piezoelectric in order to raster scanning a surface, the details are reported in figure 3b.

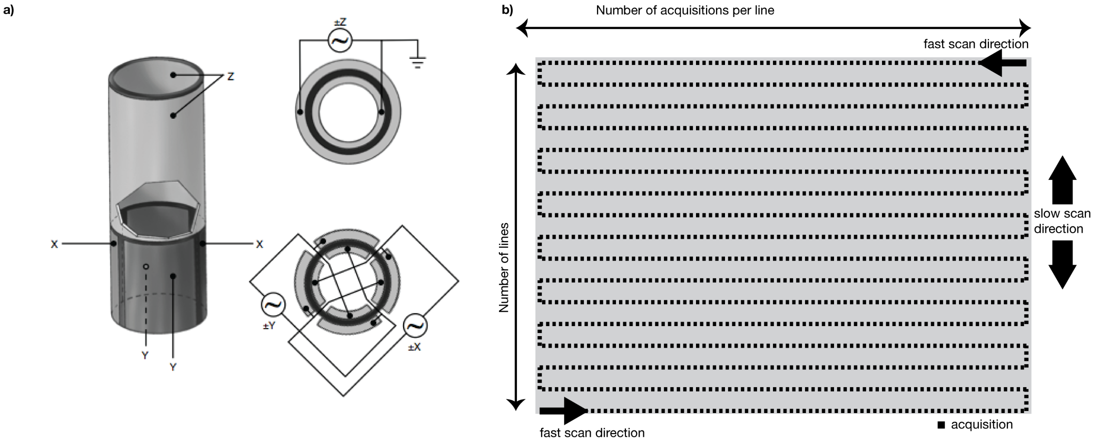

Figure 3: a) Typical Scanner Piezo Tube and X-Y-Z Electrical Configurations, b) raster process and scanning directions. (a) reproduced from Veeco Multimode manual.[5]

Feedback – it is responsible for the control of the tip height in constant current mode. The image obtained is usually called z-error because it is the result of the current applied to the feedback to keep the tip in position.

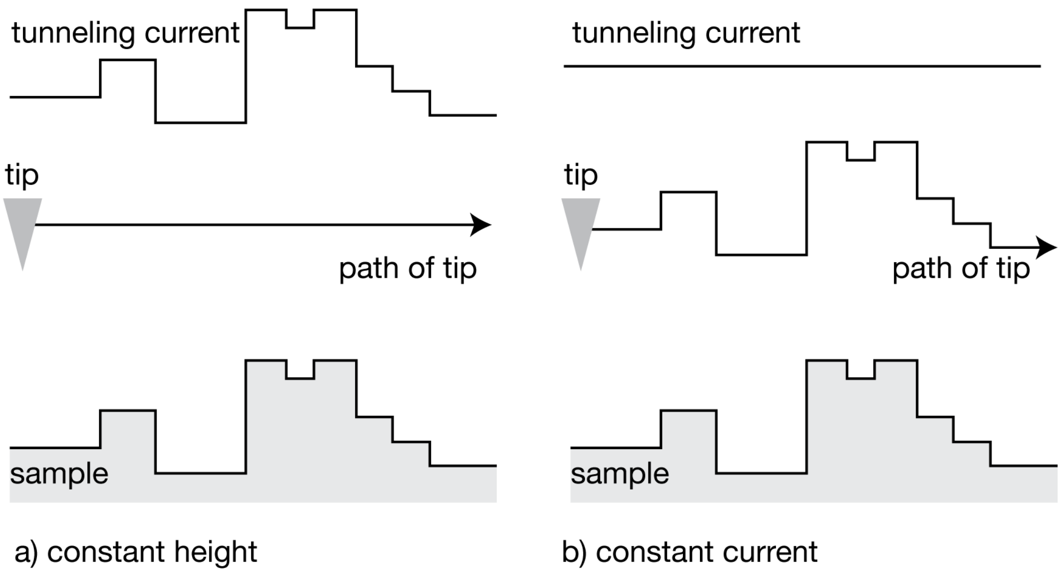

Figure 4: Sketch of the operating modes of STM.

Tip

It consists of a thin metal wire which can be mechanically cut or chemically etched. A sharp tip is a necessary condition for achieving a high resolution, however the reproducibility is very low. The most used materials are a Pt-Ir alloy (80:20) and Tungsten. In general Pt-Ir provides a better resolution due to lower reactivity, and the tungsten gives more reproducible and regular tips. Especially in the case of mechanically cut ones is almost impossible to have two identical. It also clearly depends on the hands of the experimenter: *Cutting tips is still more of an art than a science*. It is important to point out that there are few possible artifacts that depend on the tip: double images due to double tip, the loss of proportion, the differences between scanning directions, and many more.

Substrate

The substrate needs to be conductive and flat; no other important limitations are present. There are many metals used as substrate, especially in ultra-high vacuum setups. However at the solid-liquid interface it is important to take into account their reactivity in air, as formation of insulating oxides or fast absorption of contaminants, therefore at the S/L interface the most used one are Au and HOPG. The differences between the two are:

HOPG (Highly Oriented Pyrolytic Graphite): it is by far the most common substrate for STM. It is cheap, very flat, doesn't react with the adsorbate, and is very easily cleaned. It is the substrate of choice for physisorbed systems and solid-liquid interface experiments.

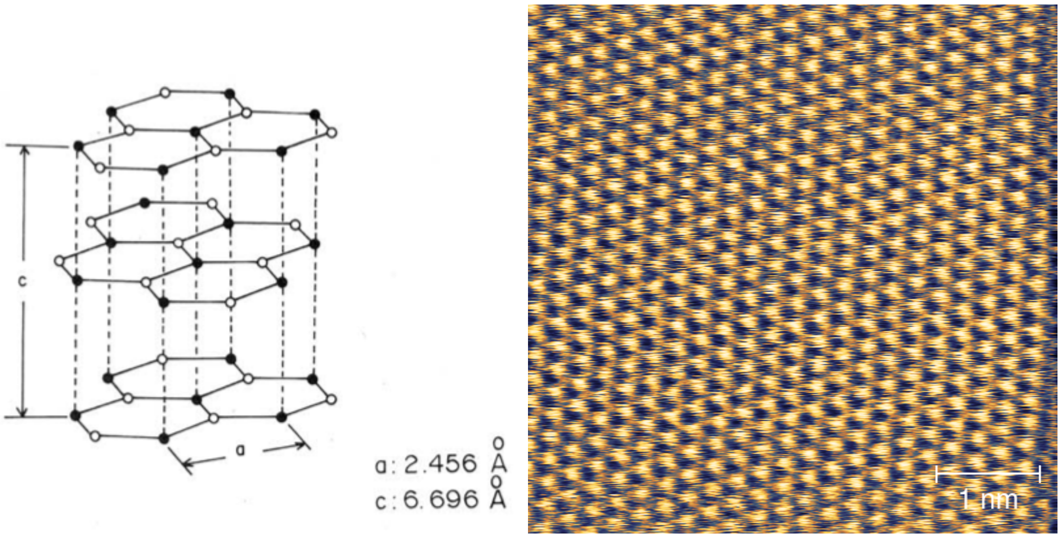

Figure 5: a) Three-dimensional crystal structure of graphite; the nearest-neighbor C-C distance is 1.42 Å. Reproduced from [6] b) 5x5nm STM current image of HOPG. The visible spots corresponds to the atom colored in black in a).

Au: It is reactive and has catalytic properties; it is the most used substrate to study chemisorbed systems. The typical investigated materials are thiols assembled in SAMs, but in general is the substrate of choice for UHV experiments. Unfortunately, it is very hard to achieve a clean surface in air, even immediately after evaporation, therefore it usefulness is limited at the solid-liquid interface.

Controller:

It contains all the hardware necessary for the acquisition, i.e. all the components to transform an analogic signal in input to a digital image, and all the electronics to *drive* the piezo.

Method:

The STM study of the self-assembly in two dimensions was performed using a Veeco scanning tunneling microscope (multimode Nanoscope III, Veeco) at the interface between the chosen substrate and a supernatant solution. Solutions of investigated molecules were applied to the basal plane of the surface. For STM measurements the substrates were glued with cyanoacrylate (Super Attack™) on a magnetic disk (ø = 13mm) and an electric contact was made with silver paint (Aldrich Chemicals). The STM tips were mechanically cut from a Pt/Ir wire (90/10, diameter 0.25 mm, commercially available from Goodfellow). The raw STM data were processed through the application of background flattening (2nd degree least square polynomial fitting on both X and Y directions) and the drift was corrected using the underlying graphite lattice as a reference. The latter lattice was visualized by lowering the bias voltage to 20 mV and raising the current to 65 pA.

Part 2: Simulations

Generalities on molecular modeling and computer simulations

Molecular Dynamics

Molecular dynamics relies on the solution of Newton equation of motion under the assumption of an empirical force field. It means that usually the energy is calculated from the total force obtained as the sum of the contributions of the various interactions acting on a certain atom. Since MD doesn't consider the motion of the electrons, it is absolutely dependent on the validity of the Born-Oppenheimer approximation. The most common terms included in a force field are summarized in Figure 6.

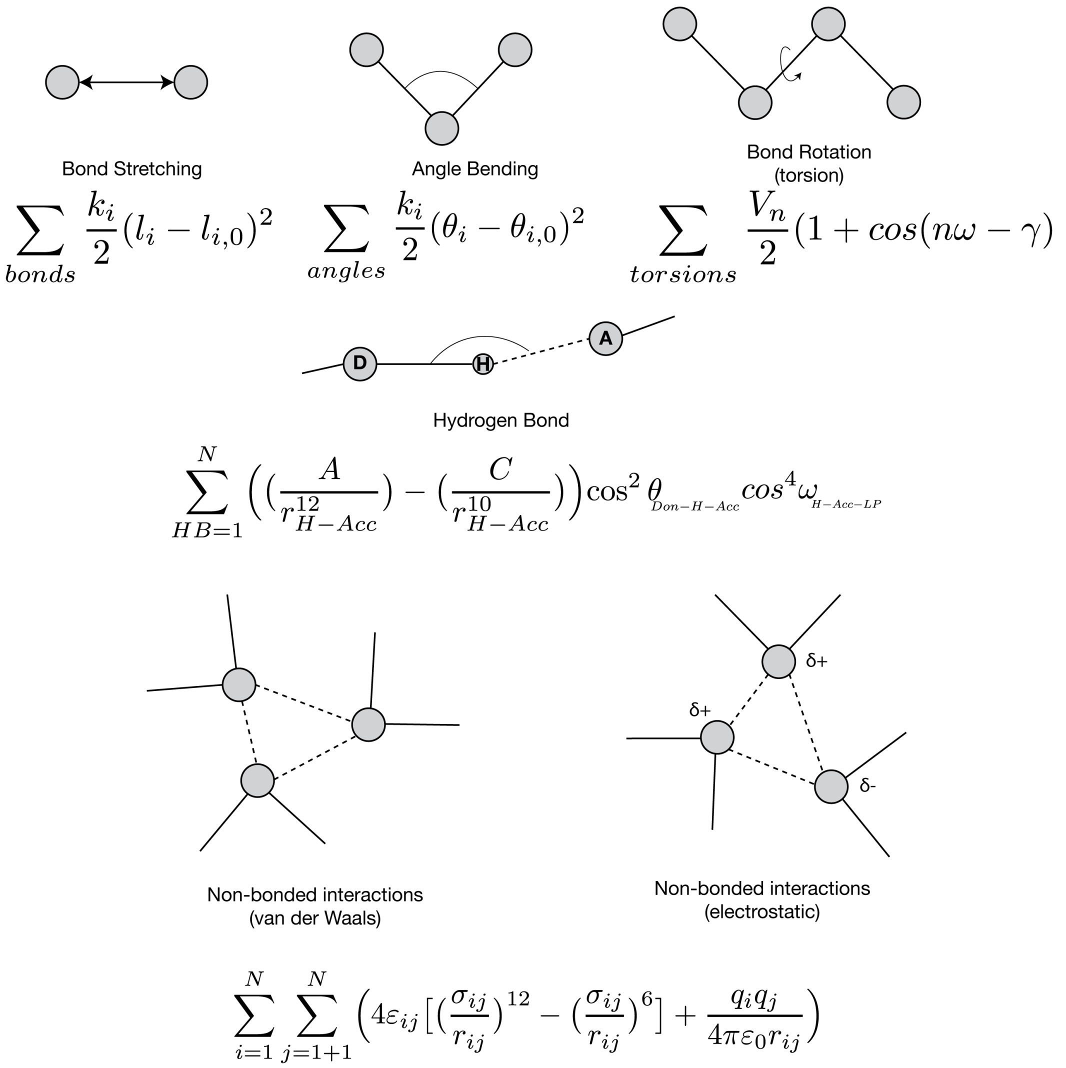

$$\sum_{bonds} \frac{k_i}{2}(l_i - l_{i,0})^2 \quad \sum_{angles} \frac{k_i}{2}(\theta_i - \theta_{i,0})^2 \quad \sum_{torsions} \frac{V_n}{2}(1 + cos(n\omega - \gamma)$$

$$\sum_{HB=1}^{N} \Big((\frac{A}{r^{12}_{H-Acc}}) - (\frac{C}{r^{10}_{H-Acc}}) \Big) \cos^2 \theta_{Don-H-Acc} \, cos^4 \omega_{H-Acc-LP}$$

$$\sum_{i=1}^{N} \sum_{j=1+1}^{N} \Big(4\varepsilon_{ij} [(\frac{\sigma_{ij}}{r_{ij}})^{12} - (\frac{\sigma_{ij}}{r_{ij}})^{6}] + \frac{q_i q_j}{4\pi\varepsilon_0 r_{ij}} \Big)$$

Figure 6: common components of a force field

As can be seen, the first two terms, i.e. bonds and angle stretching, in their simpler form are obtained in an harmonic potential approximation; the torsions on the dihedrals are almost always expressed as a cosine series expansion. For the hydrogen bonds and the non-bonded interactions (NB) the situation is a little more "debated". Definitely for the NB the easiest form uses a Lennard-Jones pairwise for calculation of the VdW contributions, and a Coulomb pairwise functional for the electrostatic part. The hydrogen bond is in its simplest form expressed by a Lennard-Jones potential (usually 12-10, or 6-4) and by an angular cosine expansion. The angular part usually consider two terms: i) the dihedral, defined between the acceptor, his lone pair (LP) , the hydrogen and the donor, and ii) the deviation from the ideal geometry in the angle between donor, hydrogen, and acceptor. To each atom in a simulation is assigned an "atom-type", i.e. a series of parameters for the force field calculations. Such parameters can be either experimentally derived from a set of representative molecules, or computed from ab-initio methods. The choice of the appropriate force field is crucial, therefore often a comparison between different methods is presented.

Molecular dynamics calculates the *real* dynamics of a system, called *trajectory*, allowing extraction of the time averages of the properties. This implies that two other basilar concepts in MD are the *time step* and the total time of the simulation, i.e. the *integration time*. The integration time has to be relevant to the phenomena observed, otherwise it lacks any physical sense: like describing the life of a person by observing just a random day[1]. The time step has the complementary role to make the calculation feasible in a finite amount of real time. In most simulations the time step is around a tenth of femto-seconds, but using algorithms like SHAKE[7] it is possible to extend it.

Density Functional Theory

Hartree-Fock theory uses a Slater determinant built from the N single-electrons wavefunctions to express the multi-electron wavefunction of a molecule. In DFT, the single-electron wavefunction is also used, but only to calculate the total electronic energy and the overall electron density distribution. The idea is that the two are related, as shown in the Hohenberg-Kohn theorem,[8] via a functional:

$$E[\rho(\mathbf{r})] = \int V_{ext}(\mathbf{r})\rho(\mathbf{r})d\mathbf{r} + F[\rho(\mathbf{r})]$$

Where the first term is the interaction with an external potential (e.g. the Coulomb interaction with the nuclei) and the second is the sum of the contribution of the interectronic interactions and the kinetic energy of the electrons. Such term can be approximated as:

$$F[\rho(\mathbf{r})] = E_{KE}[\rho(\mathbf{r})] + E_H[\rho(\mathbf{r})] + E_{\chi C}[\rho(\mathbf{r})]$$

Where the terms are respectively the kinetic energy, the coulombic electron-electron energy, and the exchange and correlation.

After substituting the kinetic energy term and the Hartree electrostatic energy, the full expression of the energy of an N-electron system results in:

$$E[\rho(\mathbf{r})] = \sum_{i=1}^{N} \int \psi(\mathbf{r})\Big(-\frac{\nabla^2}{2}\Big)\psi_i(\mathbf{r})d\mathbf{r} + \frac{1}{2}\int\int \frac{\rho(\mathbf{r_1})\rho(\mathbf{r_2})}{|\mathbf{r_1}-\mathbf{r_2}|}d\mathbf{r}_1 d\mathbf{r}_2 + E_{\chi C}[\rho(\mathbf{r})] - \sum_{A=1}^{M}\int \frac{Z_A}{\mathbf{r}-\mathbf{R}}\rho(\mathbf{r})d\mathbf{r}$$

If as shown by Kohn and Sham we substitute the density with

---

[1] Usually is not even a random day, but something like the first couple of days after the birth!

$$\rho(\mathbf{r}) = \sum_{i=1}^{N} |\psi_i(\mathbf{r})|^2$$

finally we obtain the one electron equations:

$$\{-\frac{\nabla_1^2}{2} - \Big(\sum_{A=1}^{M} \frac{Z_A}{r_{1A}}\Big) + \int \frac{\rho \mathbf{r}_2}{r_{12}} d\mathbf{r}_2 + V_{\chi C}[\mathbf{r}_1]\}\psi_i(\mathbf{r}_1) = \varepsilon_i \psi_i(\mathbf{r}_i)$$

then the total energy is computed from the full expression.
The method to solve the Kohn-Sham equations is *self-consistent*, and the choice of the right exchange-correlation functional is mandatory to the success of the approach.

Monte Carlo

The Monte Carlo method builds a sequence of configurations in a random way. It is by definition a stochastic process, and this aspect is the single most important concept in understanding the mechanics of this simulation. It is also important to point out that in contrary to MD, there's no time dependence between steps. The properties of the system are simply calculated by an average over the number of configurations. It is however possible to use different sampling processes: the only necessary condition is that subsequent configurations have to be part of a Markov chain. It means that the process has to satisfy two conditions: i) the outcome of a trial depends only on the preceding trial, but not on any precedent step, and ii) each trial belongs to a finite set of possible outcomes. The most used importance sampling process is the Metropolis algorithm:

```
If $\Delta E<0$: $P_{acc}=1$
Else: $P_{acc}=\exp(-\Delta E/K_B T)$
If random(x)>$P_{acc}$ : reject configuration
Else: continue
```

As show in the pseudocode snippet, if the difference in energy between two configurations is negative, the move will be accepted. Otherwise the *Boltzmann factor* will be calculated (the probability of acceptation P_{acc} will be a function of the temperature of the system), and will be compared with a random number (which is usually a real generated between 0 and 1). The effect is that if the change in energy is "small" it is possible to accept also steps with a "bad" contribution.

Usually Monte Carlo calculations are performed in the *canonical* ensemble, i.e. number of particles (N), volume(V) and temperature(T) are kept constant during the simulation. It is however possible to change the ensemble in order to calculate different thermodinamical properties, such as the gran canonical (fixed chemical potential (μ) , V, T), or isothermal-isobaric (fixed N, T, pressure (P)).

1. Griffith, D. J., *Introduction to Quantum Mechanics*. Prentice Hall: 1994.
2. Lang, N. D., Spectroscopy of Single Atoms in the Scanning Tunneling Microscope. *Phys Rev B* **1986,** *34* (8), 5947-5950.
3. Nicol, J.; Shapiro, S.; Smith, P. H., Direct Measurement of the Superconducting Energy Gap. *Physical Review Letters* **1960,** *5* (10), 461-464.
4. Binnig, G.; Rohrer, H.; Gerber, C.; Weibel, E., Tunneling through a controllable vacuum gap. *Applied Physics Letters* **1982,** *40* (2), 178-180.
5. Veeco *MultiMode SPM Instruction Manual rev.B* 2004; p 22.
6. Pisanty, A., The Electronic-Structure of Graphite - a Chemists Introduction to Band Theory. *J Chem Educ* **1991,** *68* (10), 804-808.
7. Ryckaert, J. P.; Ciccotti, G.; Berendsen, H. J. C., Numerical-Integration of Cartesian Equations of Motion of a System with Constraints - Molecular-Dynamics of N-Alkanes. *J Comput Phys* **1977,** *23* (3), 327-341.
8. Kohn, W.; Sham, L. J., Self-Consistent Equations Including Exchange and Correlation Effects. *Physical Review* **1965,** *140* (4A), A1133-A1138.

Chapter 3.1: Rotatable arms in simple tripods: conformers, dipole and self-assembly

Unraveling the self-assembly of simple molecular components into larger supramolecular architectures is still a great scientific challenge. Here we study on the nanoscale, the self-assembly at the solid-liquid interface of a tripodal molecular building block, i.e. 1,3,5-tris(pyridin-3-ylethynyl)benzene. The Scanning Tunneling Microscopy measurements, corroborated by both Density Functional Theory and Molecular Dynamic simulations, revealed that due to the low energy barrier for the rotation in solution of the three pyridine rings with respect to the molecular plane of 1,3,5-tris(pyridin-3-ylethynyl)benzene, entropy plays a key role in selecting the most stable conformer, ultimately forming highly-ordered supramolecular assembly.

The self-assembly relies on the recognition events between designed building blocks capable of associating into programmed architectures, gathering from intermolecular interactions, such as hydrogen bonding, van der Waals forces and metallo-ligand interactions which feature a high geometrical control. The crystallization of molecules in two dimensions at surfaces, and especially the formation of self-assembled structures at the solid-liquid interface, relies not only on a delicate balance between intra-and inter-molecular interactions and interfacial forces, but also on a subtle role played by the molecular geometry, the registration on the substrate and the distribution of conformers. The self-assembly of three branch-shaped star molecules in two dimensions at the surface[1] has been thoroughly investigated in the last decade both experimentally and theoretically with a particular attention to the role played by the substrate, and to the effects of the recognition groups. Confining the self-assembly process to two dimensions using a fairly inert crystalline planar surface (e.g. graphite), allows to simplify the contribution of the substrate itself, reducing its influence on the interaction between the molecular building blocks. Despite the increasing interest in the field, the knowledge gathered about the formation of the self-assembled structures, where the lack of conformational rigidity affects the assembly is still relatively poor,[23] and among those, the attention was generally focused on the induction of chirality.[4] Numerous examples of triangular building blocks have been developed and explored so far including, among others, triangulenes,[5] triazatrinaphthylenes,[6] and trimesic acid.[7] Their design principles hinge on either a rigidly planar structure or on the presence of moieties able to assemble under strict triangular symmetry, usually aiming at hexagonal porous networks, relying on the recognition between C_3-symmetric building blocks at the solid–liquid interface.

Here we report a study on the self-assembly of the regio-isomers 1,3,5-tris(pyridin-3-ylethynyl)benzene (**M**) and 1,3,5-tris(pyridin-4-ylethynyl)benzene (**P**) as shown in Figure 1a. We present how the final assembly of the star shaped building block **M** on Highly Oriented Pyrolitic Graphite (HOPG) can be unveiled by a combination of Density Functional Theory (DFT) and Molecular Dynamics (MD). The behavior of **P** has been investigated as control system. The presence of rotational freedom, related to the low energy barrier of rotation around the acetylenic bond of the arms, and the *meta* substitution, makes **M** a suitable system to: i) determine *a priori* how the flexibility (in particular the rotation at the acetylenic groups) breaks the symmetry of the molecule and leads to formation of *"seeds"* for different aggregation patterns, ii) show how the equilibrium between multiple conformations is determinant for the final structure, iii) determine whether the substrate contribution alone is enough to select or stabilize a particular conformer, and iv) test how the presence of long-range dipolar interactions during the self assembly affects the final structure.

Scanning tunneling microscopy was used to probe the self-assembly behavior of **M** at the solution-graphite interface. Figure 1d,f displays STM current images of the physisorbed monolayer on the basal plane of HOPG obtained by applying a drop of a 1 mM warm (80°C) solution in 1-phenyloctane. It reveals highly ordered crystalline structures, consisting of domains extended over hundreds of nm^2 which are stable over several minutes. Defects such as linear defects, grain boundaries and point defects (i.e., vacancies) are observed, (figures 1d,e, Annex 1 S2). The motif exhibits a Moiré pattern, and the registration between the two lattices occurs at a length scale of approximately 4.5 nm and 2 nm along axis b and a, respectively.

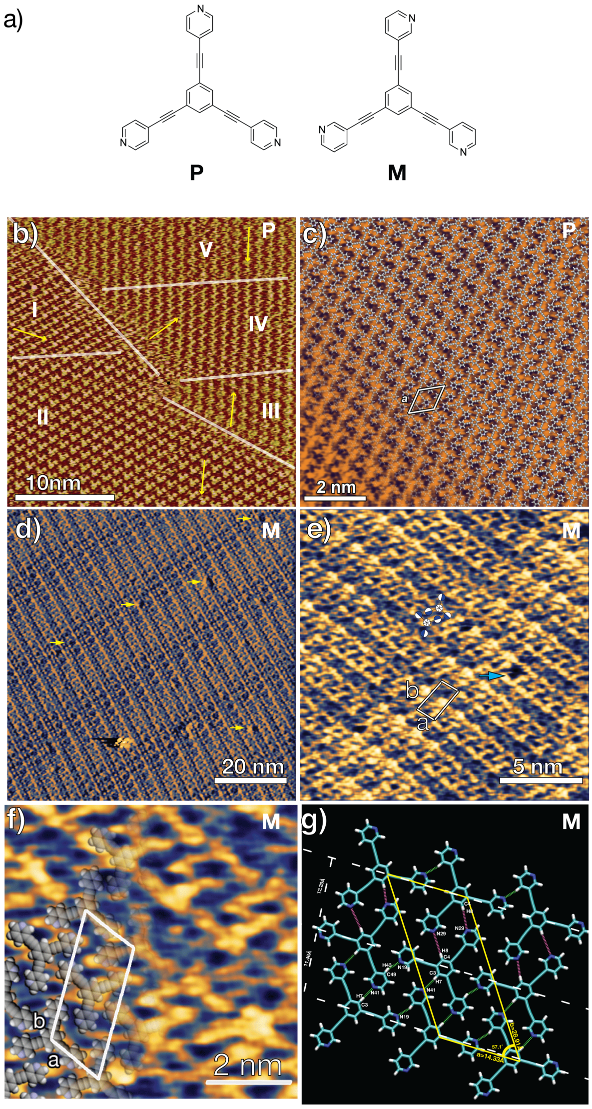

Figure 1: a) Chemical formula of 1,3,5-tris(pyridin-3-ylethynyl)benzene (**M**) and 1,3,5-tris(pyridin-4-ylethynyl)benzene (**P**); b-d) Current and (e, f) height STM images of (b, c) **P** and (d-f,) **M**. (b,c) Survey images highlighting the presence of polycrystalline structures consisting of different domains separated by grain boundaries, and close up with proposed CPK model of **P**. (b-c) Tunneling parameters: It=15pA, Ut=300mV. (d,e) Reveals a Moiré pattern with the presence of point defects (yellow arrows); (d,f) Tunneling parameters: It=25pA, Ut=200mV.

The lamellar structure exhibits a symmetry belonging to the wallpaper group P2, and a unit cell (a=1.3 ± 0.2 nm, b=3.1 ± 0.2 nm, **γ** =91°±2°; A=4.0 ±0.7 nm^2) containing two molecules **M**. The hydrogen bonded network can be described using the graph notation[8] as C(14) [$R_2^2(16)$] [$R_2^2(16)$], i.e. the molecules forms two rings with two donors and two acceptors and a chain with one donor and one acceptor.

No polymorphism was ever observed during the STM experiments, even in low concentration regime. The measurements in high concentration range did not evidence any amorphous phase. Figure 1e exhibits a complex pattern consisting of tripodal features: the charge distribution, and the electrostatic potential maps (Figure 2), are not sufficient to justify lamellar assemblies of **M**, as they do not provide enough geometrical evidence to rigorously exclude a hexagonal phase.

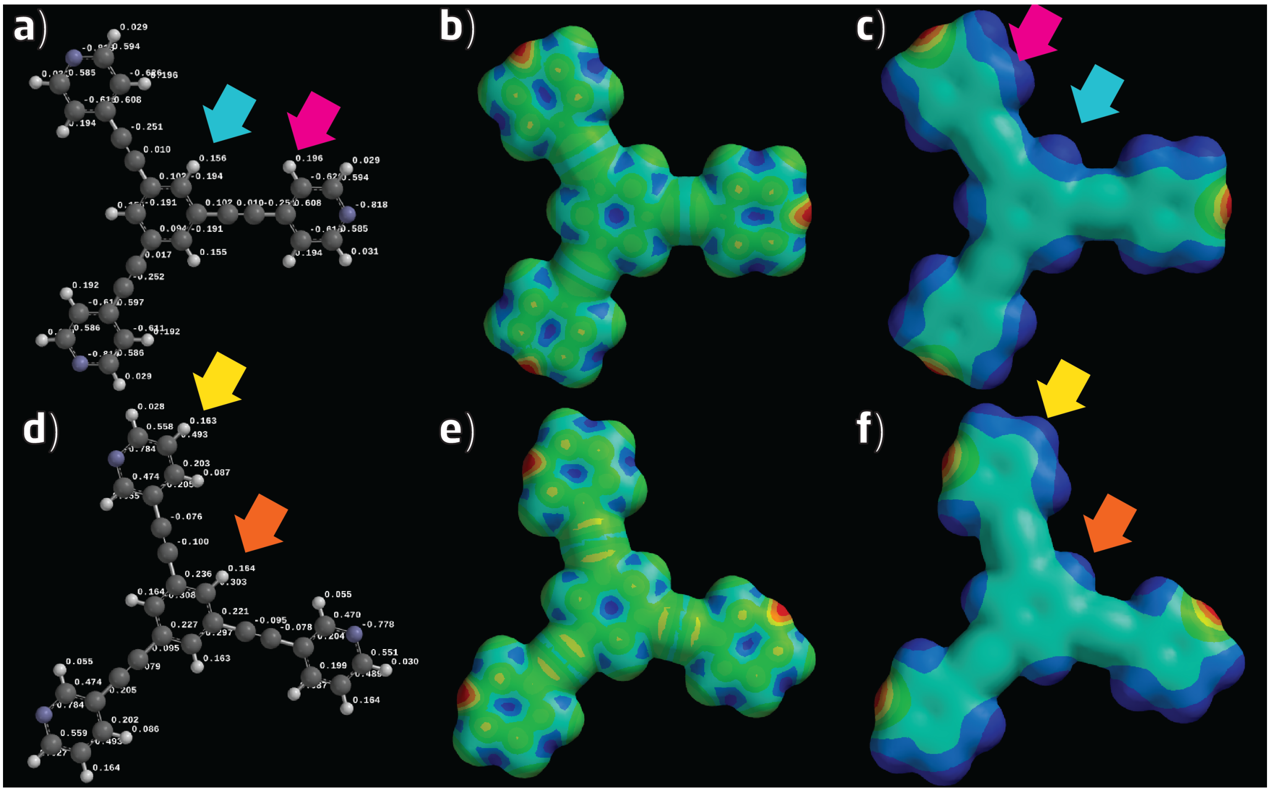

Figure 2: Mulliken charges are showed together with the charge density and electrostatic map of **P** (a-c) and **M** (d-f). The general structure of Hydrogen bond is –A---H-D- where a hydrogen bond donor (D) forms a polar σ bond with hydrogen, and the hydrogen carries a partial positive charge. The group D-H has an attractive interaction with at least one acceptor atom (or group) A, thanks to the accumulation of the electron density on the acceptor.[14] Therefore hydrogen bonds, have a very strong electrostatic component; hence one of the most handful techniques to preview the pattern of connections between molecules is to observe the electrostatic potential and the charge distribution of all the atoms of the molecule, and then pair the best acceptor with the best donor. The simulation shows that: The more positively charged hydrogen are pointed by the arrows – the carbons bearing those hydrogen will act as the HB donor; and the most negative atoms are the three pyridine nitrogens, which will consequently act as HB acceptors. The two possible positions for binding will have consequences on the polymorphism of the system. The calculations were done using DFT b3lyp method and a 631g* basis set.

The control experiment performed with the "classical" star shaped para isomer **P** can be compared with the packing of **M** under the same conditions, i.e. 1mM drop-cast from 1-phenyloctane solution. As evidenced from the STM images in figure 1b-c, in similar high-concentration phases the differences between the two regio-isomers are striking. They can be summarized in 3 main aspects: i) the prevalent defects are grain boundaries for **P** and vacancies for **M**; ii) only **M** presents a Moiré pattern; iii) **P** features parallel arrangements inside the domain, whereas **M** has an antiparallel conformation. The very similar values obtained in the calculated charge distribution for the two isomers proves how such differences are not likely due to variations in the electrostatic contribution (Figure 2). We therefore identify in the symmetry break due to the rotation the major responsible for the appearance of an antiparallel phase.

As first step to unravel the effect of conformational adaptability on the 2D packing, we decided to calculate and study the rotational barriers in vacuum and on the graphite surface, by the means of Density Functional Theory and Molecular Dynamic simulations. The arm rotation barrier of similar star-shaped molecules is strongly related to its chemical structure.[1, 9] Simple systems such as 1,2-di(pyridin-3-yl)ethyne and 3-(phenylethynyl)pyridine exhibited rotational barriers of 46.6 meV and 36.2 meV, respectively.[10]

In case of **M** we should expect a slightly higher rotational barrier, due to the extended conjugation. However, using the restricted Becke three-parameter hybrid exchange functional combined with the Lee–Yang–Parr correlation functional (B3LYP) using 6-31G+(d,p) basis set,[11] the barrier height results 39.8 meV (i.e. 3.75 kJ/mol or 0.896 kcal mol^{-1}) (see **Figure 3**c, and for the details Annex 1). The difference, is probably accounted to I) extended conjugation with respect of 3-(phenylethynyl)pyridine, and II) the meta substitution, which has a smaller hyperconjugative interaction between the nitrogen lone pair and the sp^2 π orbitals. It is important to point out that at room temperature, and after heating at 80°C a simple estimation with the Eyring equation,[12] results in rates of rotation in the range of 1.4 ThZ, making impossible their observation by ^{1}H-NMR.

To compute the rotational barrier on the graphite surface, we performed molecular dynamics calculations using CHARMM[13] and MMFF94[14] force field. Since it has been shown that substituting the graphite surface with a graphene slab dramatically reduce the computational load with marginal error,[15] we decide to utilize this simplification.[16] The results of the calculation shows that the rotational barrier (**Figure 3**c), is almost two orders of magnitude higher for a molecule **M** once physisorbed on a graphene slab: ca 20 meV in vacuum compared to 1.8 eV and 2.8eV once adsorbed. In the physisorbed case, the presence of two values of the energy barrier and their difference depend on the pyridine nitrogen. Since it lacks a hydrogen bonded it encounters a different steric hindrance when facing the graphene slab during rotation. Such barrier height brings the rate to less than 0.56 fHz – (one rotation every 2*10^15seconds!). We can therefore reasonably assume that while the arms rotate in solution, they are almost frozen when the molecule is physisorbed on graphite.

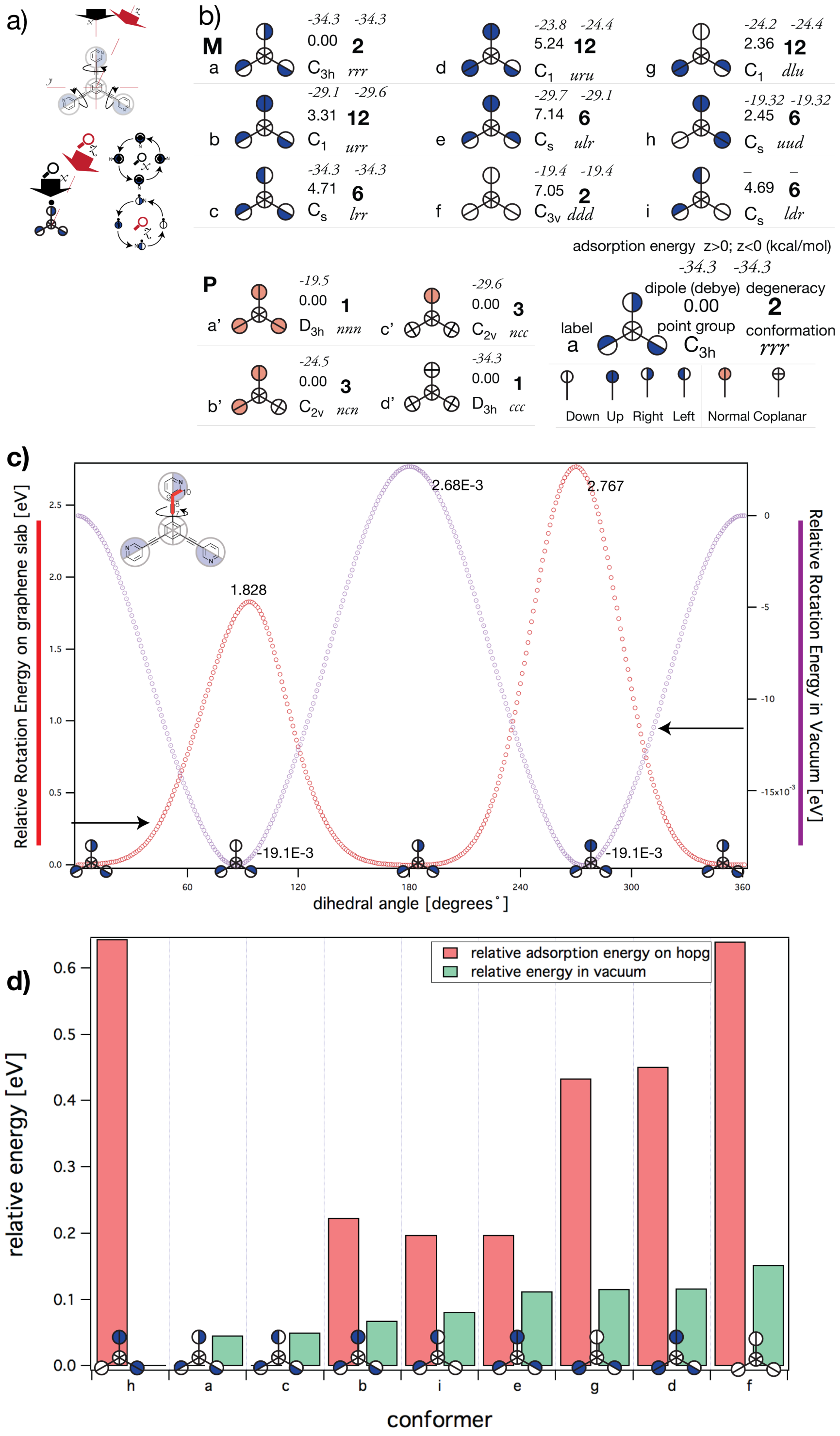

Figure 3: Exploratory scheme of the symbols used to represent different relative geometries in respect of the Cartesian coordinates. The position of each pyridine nitrogen relative to the core may be represented with an half-filled or fully filled circles indicating whether the rings are coplanar (half-filled), or oriented orthogonal pyridine rings, with the nitrogen respectively pointing up (fully filled blue) or down (fully filled white); g) Label, degeneracy, adsorption energies, point group and conformation (r=right, u=up, l=left, d=down) of the limit structures of the conformers used in the calculations. b) Energy profile for the rotation of the dihedral 7-8-9-10 (red bold line in the inset) in vacuum (purple) and on a graphene surface (red); the values reported have been offsetted to report the relative difference in energy from the arbitrarily choosen **Ma** conformer. Except for the dihedral 7-8-9-10, all the others bond angles, length and dihedrals of the molecule were fixed. c) Relative energy of each conformer in vacuum and on the Graphene slab surface;

In solution a multitude of different conformers of **M** is present, due to the fast rotation of the pyridine rings (THz range) around the acetylenic bond. They differ in two key properties used in the self-assembly: the dipole moment and the affinity for the graphite surface, i.e. energy of adsorption.

Under the assumption of a weak energy barrier, and of 4 different rotation states per ring (up, down, right, left – referred to the position of the nitrogen respect to the core, **Figure 3**a,b and Figure 4), we generated the library of conformers reported in **Figure 3**b.

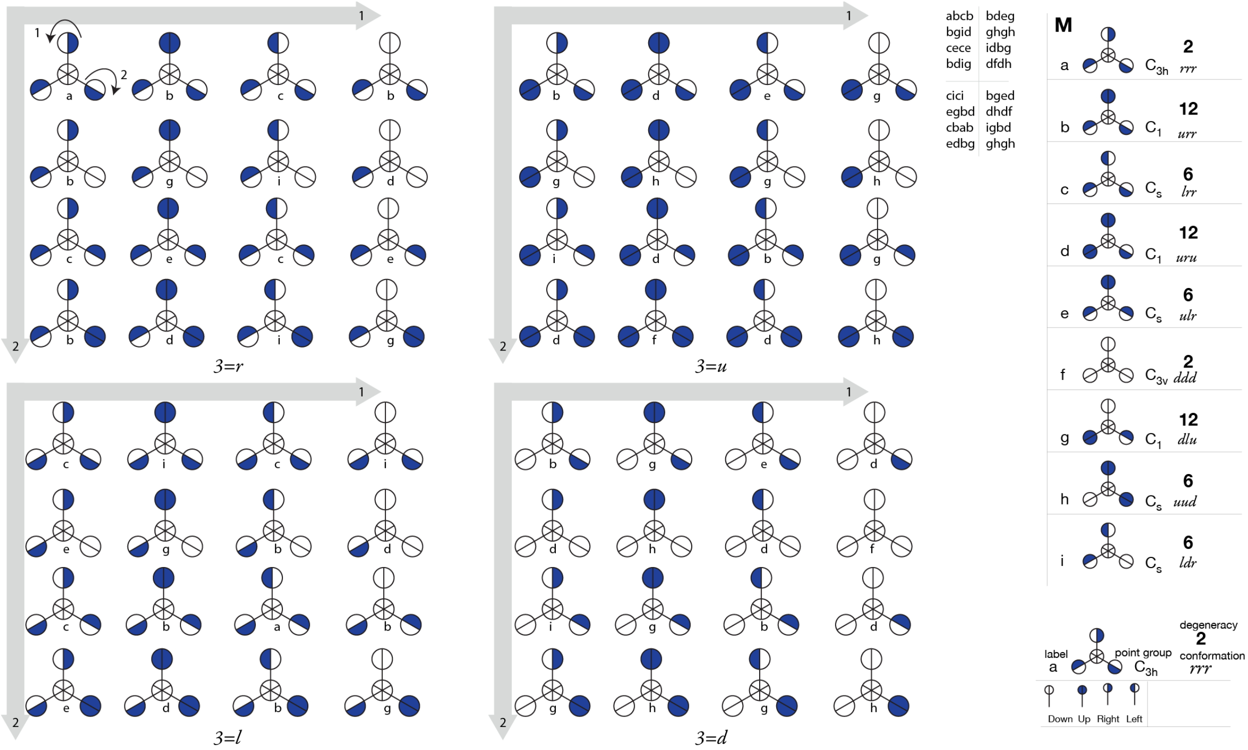

Figure 4**:** all the conformers generated after independent 90° rotation of a pyridine ring, on the right are summarized the irreducible representations the respective symmetry and their degeneracy.

Accordingly, the rate of the rotation in solution has the effect of populating the series of conformational states reported in figure 3 which differs for many fundamental aspects: i) the dipolar moment of each conformation, ii) the point group symmetry, iii) their adsorption energy on the graphite surface, and iv) their degeneracy. We analyzed all the conformers reported in Fig. 3, and computed their energy in vacuum and on the graphite surface. As evident in Fig. 3b, the conformer **Mh** is thermodynamically the most stable in vacuum. The next two conformations, **Ma** and **Mc**, are the only completely flat configurations, and consequently the most stable on graphite. The interaction energy of the two limiting structures **Mc** and **Ma** with the substrate[15b], computed with MMFF exhibit very similar values (E_{Ma}-E_{Mc}< 10^{-5}), allowing us to exclude any *a priori* preference for one or the other conformer due to the affinity for the graphite surface (Annex 1). We would therefore expect to have a distribution of the two on the surface: the probability of observing the conformer **Ma** (P(Ma)) calculated using a Boltzmann distribution results in the 25% at room temperature, following from the higher degeneracy of the state Mc (Figure 5).

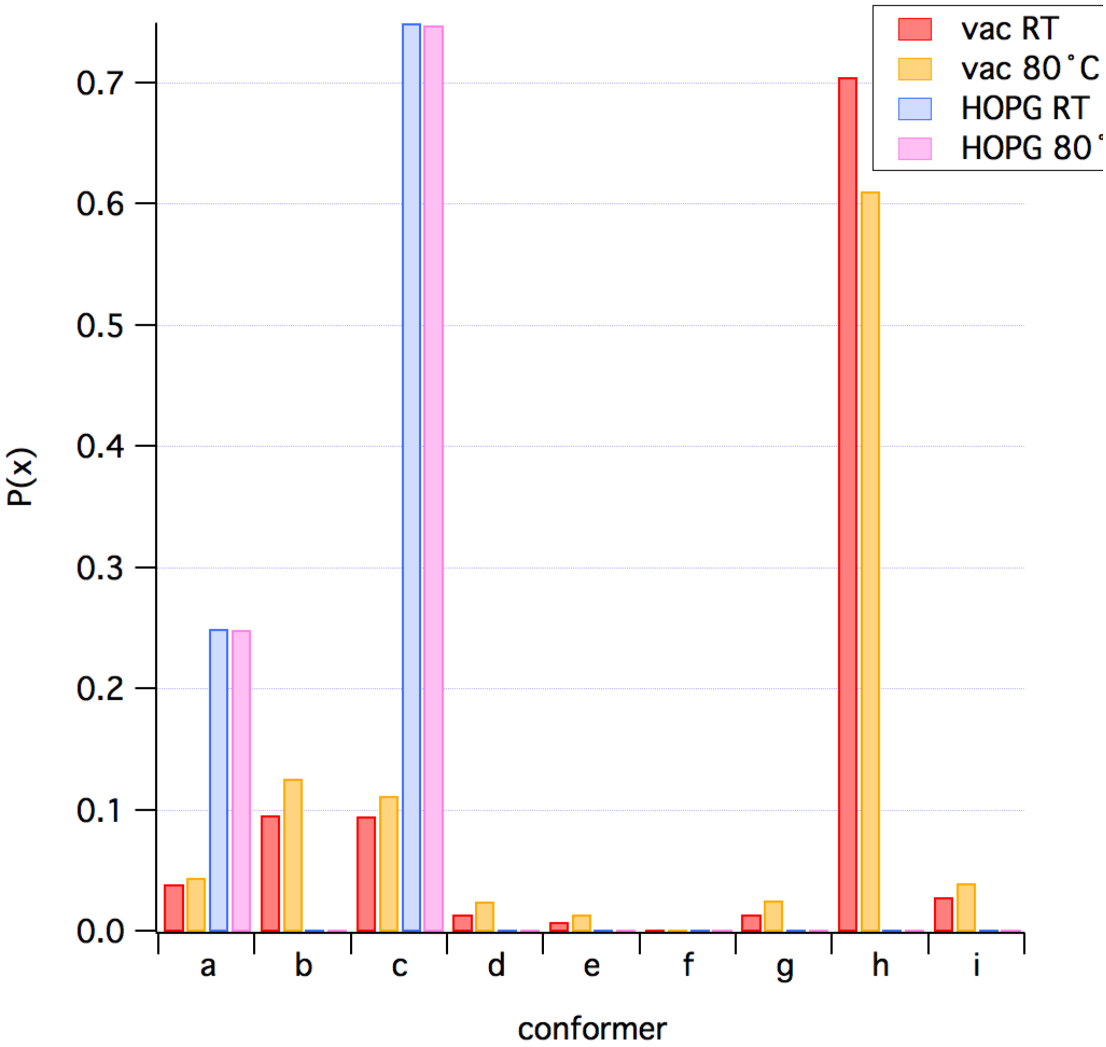

Figure 5: Probability of each configuration in vacuum and on the graphene slab, computed using Boltzmann distribution.

By monitoring the fluctuations of the dihedral angles and of the dipolar moment during 10ns we can further confirm that the rotations are an unlikely event on the surface. The results of a 10ns MD simulation are shown in Figure 6 (details of the calculations are reported in Annex 1) for **M** in vacuum and for the two most probable conformers on HOPG. **Ma** with zero net dipolar moment and symmetry C_{3h} and **Mc,** with a net dipolar moment of 4.9 Debye and C_s symmetry, physisorbed on a graphene surface.

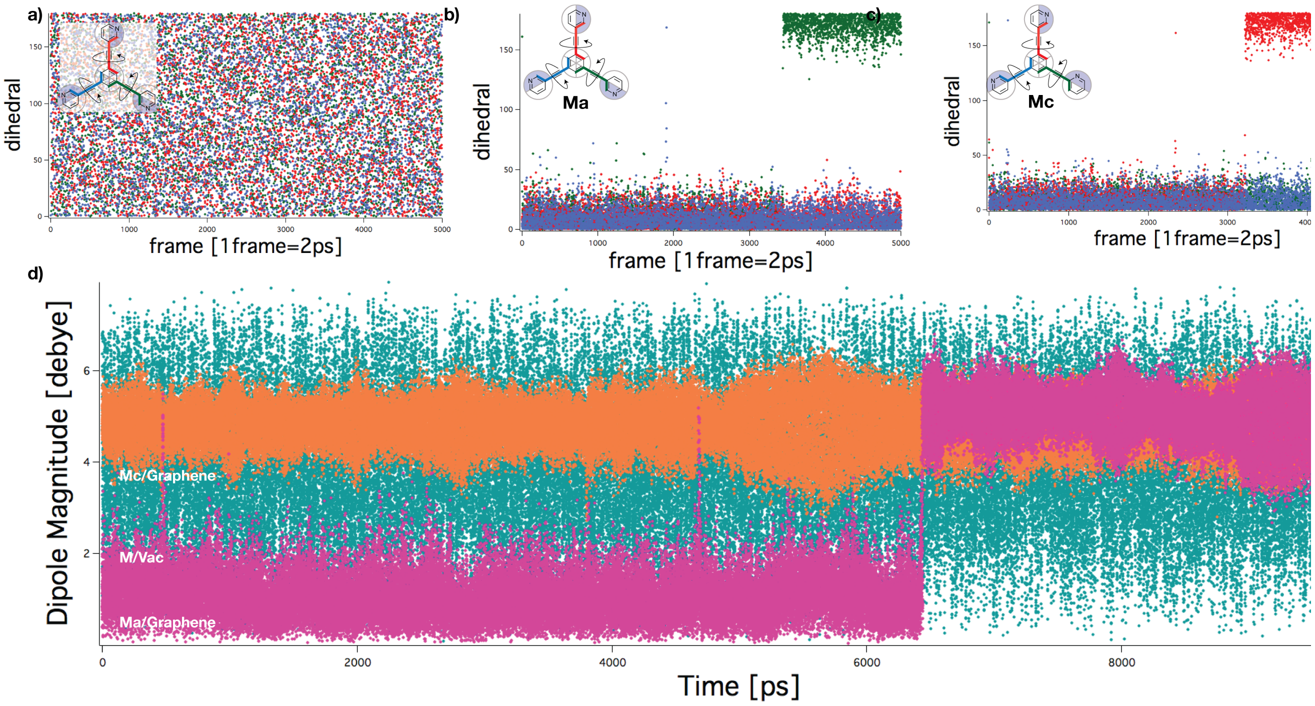

Figure 6: typical plot of the evolution of the dihedrals a-c) and of the dipole moment d) on a graphene slab of the two conformers. The dihedral correspond to the highlighted bonds in the insets. In d) the net dipole moment of Mc (orange) and Ma (purple) is compared with the values of Ma in vacuum (cyan) (NBO charges); It can be noticed that the rotation is almost free in vacuum, and that once adsorbed on the surface the **Ma** conformer is stable for ca 6 ns – after, a rotation of a ring occurs, which statistically hinders the system to going back to the C3h conformation – the simulation also shows that the cs conformer **Mc** on the hopg surface possess a net dipole moment which is uniform along the simulated time frame.

To cast light into the interactions between molecules, we used a low-density simulation with Molecular Dynamics: 36 molecules **M** were randomly dispersed on a graphene slab after thermal equilibration (1ns) and subjected to a Langevin dynamics for 10ns. Such simulations (Figure 7, the details can be found in Annex 1) show that i) hydrogen bonds are formed between the pyridine nitrogen and the *meta*-hydrogen or the core hydrogen, and ii) a glassy arrangement is predominant at room temperature and low coverage in vacuum.

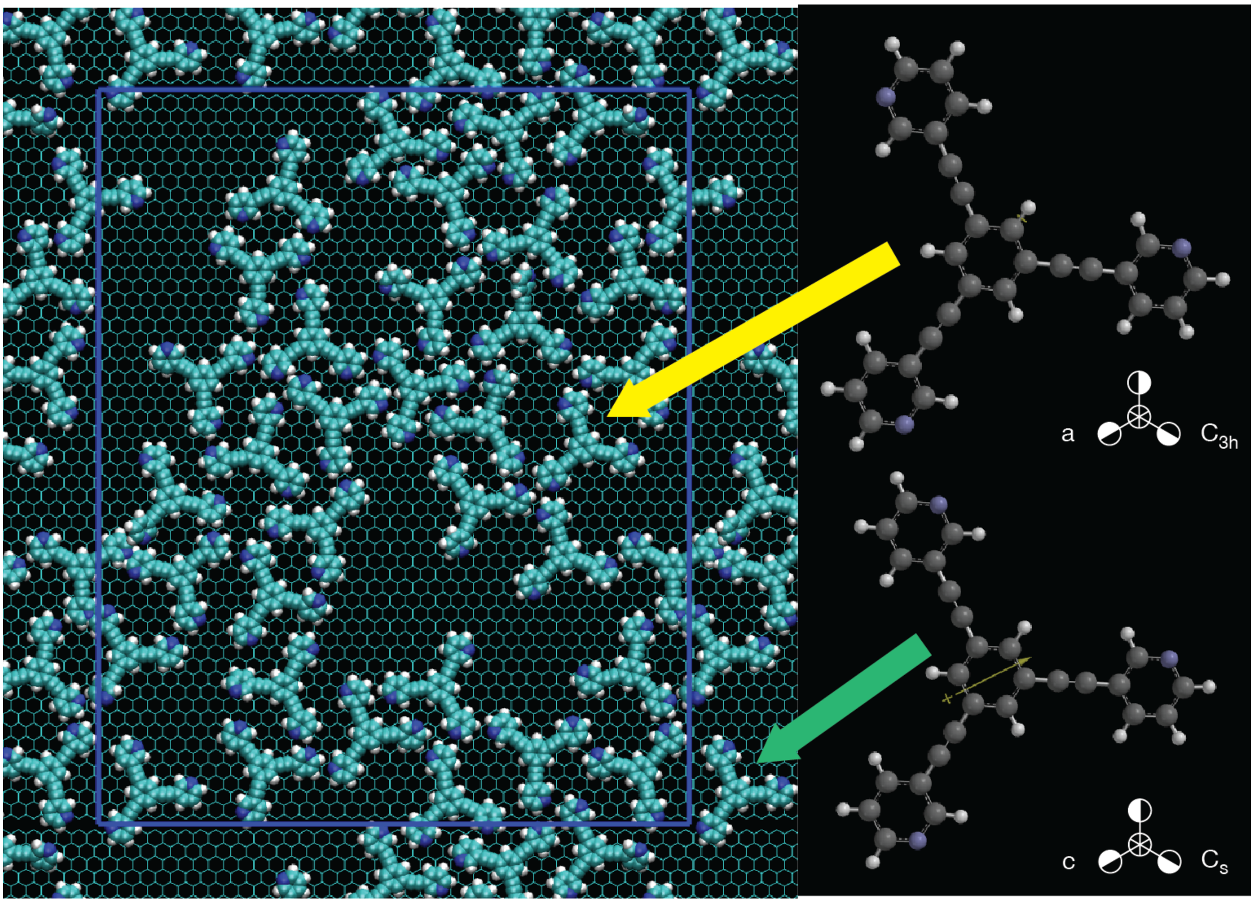

Figure 7: simulation trajectory snapshot imaged with VMD[9] to highlight the typical possible connectivity between molecules. Different hydrogen bond interactions, and two different conformers are present.

Similar behaviors have been recently observed on the regioisomer **P** by UHV-STM[17] and were attributed to the flexibility of the arms. The simulations confirms the presence of weak[18] hydrogen bonds, with a length spanning between 0.38 and 0.24 nm; the connectivity shows as hydrogen-bond acceptor the pyridine nitrogen, and as donors the unsubstituted positions of the core and the meta position of the pyridine rings. This result matches perfectly with the calculated charge distributions (Figure 2) providing evidence that the most likely hydrogens involved are those in the *meta* position and the phenyl hydrogen of the core. Their electrostatic contribution is extremely similar, therefore in order to maximize the number of molecules adsorbed, an high-density phase[19] where the hydrogen bonds are between the core and the pyridine should be the most favorable packing motif.

With a closer look at the simulation results (Figure 7), might be observed the presence on the surface of the two conformers **Ma** and **Mc**, confirming a strong preference for the

Mc conformer (79%). Interestingly, such a conformation has never been investigated in detail in the few reports in literature on molecule **M**. [20]

The absence of polymorphs, amorphous or hexagonal phases in the STM images, and the striking difference among the proportion of the observed pattern and the calculated probabilities of adsorption, suggest a strong role played by the dipolar moment of the predominant conformation. It forces the assembly in order to minimize the total dipolar moment, coupling two molecules per unit cell in opposite directions, in agreement with the model proposed in Fig. 1g.

To confirm the role of the dipolar interaction, we designed another *in silico* experiment: we pre-arranged nine molecules of **M** with a fixed configuration (**Ma** or **Mc)** in a close packing and antiparallel conformations, and then evaluate the energy of the structures, by removing subsequently each of the neighbors of the central molecule. (Figure 8)

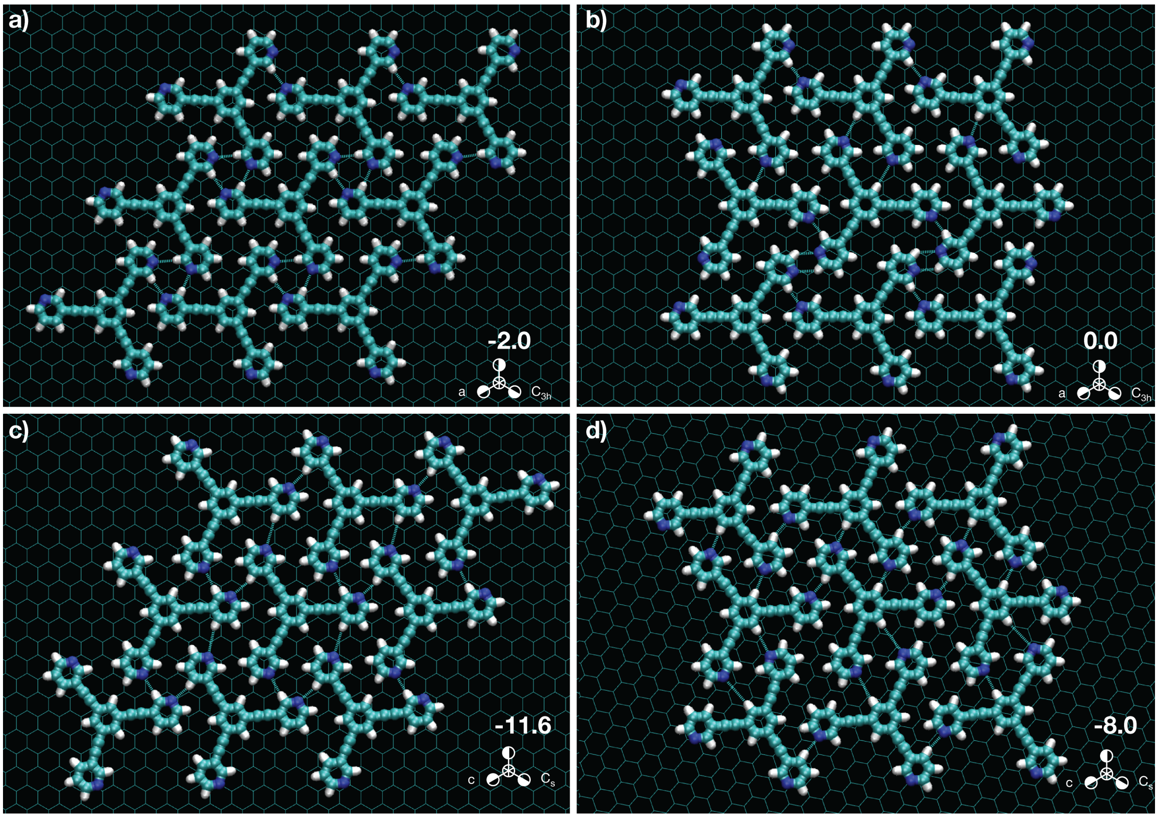

Figure 8: Minimized motifs and relative interaction energies of the four possible polymorphs. The energy value of packed structure has been subtracted to the energy of the structure where the eight outer molecules are moved at a distance of 20nm. a) is composed by a parallel assembly of the Ma conformer, that in b) has an antiparallel arrangement, c) represent the Mc conformer in a parallel structure, and finally d) portraits Mc in antiparallel orientation. The dashed lines corresponds to the weak hydrogen bonds. The energies are relative to a) in kcal/mol.

The calculation shows that for small assemblies (i.e. 9 molecules) the parallel close packed motifs are more stable for both the conformers. For the **Mc** conformer (C_s), the energy difference between the two polymorphs (i.e. parallel and antiparallel) amounts to ca. 0.4 kcal mol^{-1} per molecule (Annex 1), and is due to the presence of one extra weak hydrogen bond per molecule. In the case of Ma both parallel and antiparallel assembly experience no dipolar frustration, but the hydrogen-bonding motif is not optimal. The two patterns of the Ma conformer are destabilized by the formation of geometrically frustrated hydrogen bond motifs such as [$R_3^3(9)$] (Ma parallel) or [$R_2^2(6)$] dimers (Ma antiparallel). Mc parallel results in being the thermodynamic minimum as it possess 6 N---H-C hydrogen bonds per molecule, but such small assembly clearly doesn't fully account for the presence of the net dipole moment. The effect of the dipole in a Mc antiparallel conformation, is clearly more dramatic as the number of shells of neighbours increase: the antiparallel conformation becomes the thermodynamic phase from three neighbouring layers, i.e. from a cluster of 49 molecules (Annex 1). A similar effect, even more interesting, is that the growth of the lamella is probably anisotropic: in Figure 9 are reported the energies of adding neighbours along the lamella axis. It can be seen that after 4 shells, the antiparallel conformation is favoured.

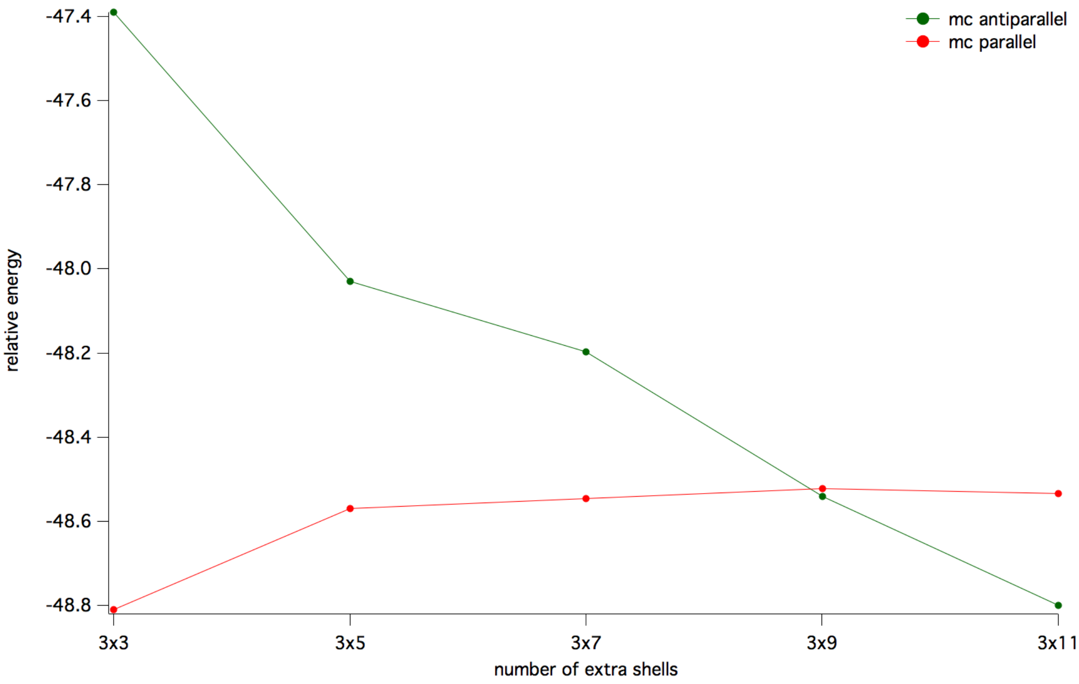

Figure 9: The addition of other molecules along the lamella, i.e. anisotropically, shows that the antiparallel conformation become more stable from for extra neighboring molecules.

Those effects are investigated more in detail in Annex 1, and are still under evaluation. The closure finally arise from the long range scale images reported in figure 1: the relative absence of small domains implies that the system feels no frustration in terms of dipolar moment. A packing of conformer Mc, with a parallel arrangement would give rise to small *Weiss-like* domains or striped phases, which are not observed.

Conclusions

In summary the we have shown that the self-assembly of a rather simple molecular building block such as 1,3,5-tris(pyridin-3-ylethynyl)benzene on the basal plane of graphite has a very complex nature. In particular we have provided in depth analysis of the role of the side arms, which can freely rotate in solution, but are virtually frozen when the molecule is physisorbed on graphite. The rotation causes the existence in solution of different conformers, featuring different symmetries and populations, which regarded under simple Statistical Thermodynamics considerations, suggest the presence of two phases. The reason behind the fact that only one phase is observed, with an evident anti-parallel arrangement, is that the only conformer for whom such assembly is the thermodynamic minimum, has an electric dipole moment of ca. 5 debye. We therefore infer that the dipole itself is responsible for the preferential selection of such phase. Finally we believe that since the dipoles are frozen on the surface in an antiparallel arrangement, and each molecule has a “surface-induced permanent” electric dipole, the final assembly itself presents remarkable similarities to what would be a bi-dimensional antiferroelectric material.

There are some important implications to be underlined: the fact that Entropy selects the dominant phase, is not by itself surprising, what is remarkable is the absence of another polymorph. The fact that the often underestimated dipolar interactions, are probably responsible for the exclusion of a parallel-arranged phase, (which according to the calculations should be the thermodynamic minimum for small clusters), is a striking evidence of the importance of an intimate study of the building block properties before interpreting any STM experiments.

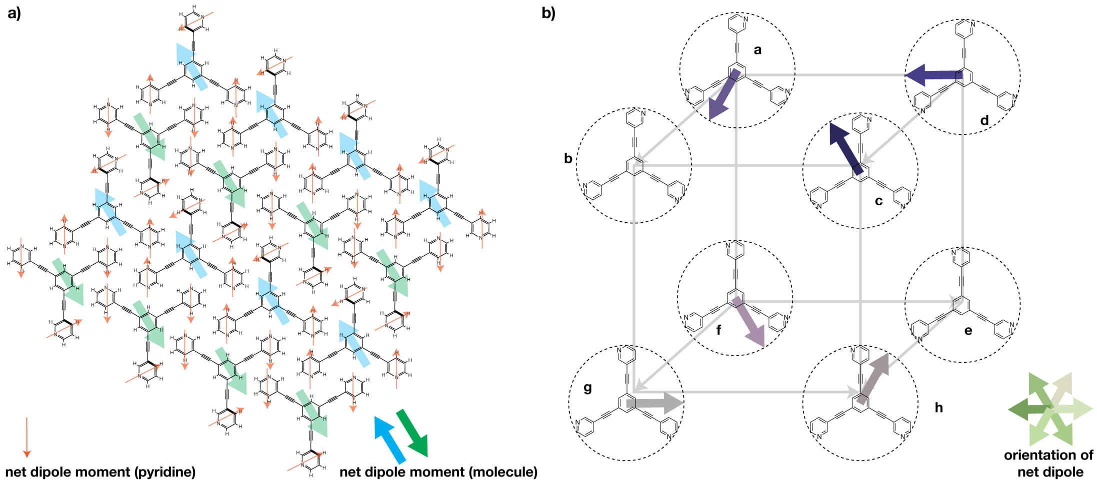

Figure 10: The orientation of the dipoles in the antiparallel packing is reported in a). Assuming to flip a single pyridine ring, is it possible to "switch" the dipole orientation according to the sketch in b). The relationship among the molecules has a cubic topology, i.e. each molecule (vertex) can be converted into the other three connected by an edge.

Finally, the antiparallel phase itself has two remarkable features. The former is that being an antiferroelectric-like 2D arrangement, it raises the question whether it will exhibit other antiferroelectric properties, such as Curie temperature and hysteresis. The latter is that each molecule is trapped in a hydrogen bonded array, which once formed is not dependent on the specific orientation of each arm. Flipping one single pyridine ring[21], will change the orientation of the electric dipole of the molecule, but not affect the H-bodend network, forming an interesting playground to investigate frustration induced by the dipolar mismatching. Furthermore, the possible flipping states of a molecule in the pattern are eight (two with zero – net dipole, and 6 with 60° relative orientation (Figure 4), which can be eventually appealing for development of bi-dimensional multi-state memory elements.

1. Detert, H.; Lehmann, M.; Meier, H., Star-Shaped Conjugated Systems. *Materials* **2010,** *3* (5), 3218-3330.
2. for the effects of conformational changes on different geometries see
3. (a) Linares, M.; Scifo, L.; Demadrille, R.; Brocorens, P.; Beljonne, D.; Lazzaroni, R.; Grevin, B., Two-Dimensional Self-Assemblies of Thiophene,àíFluorenone Conjugated Oligomers on Graphite: A Joint STM and Molecular Modeling Study. *The Journal of Physical Chemistry C* **2008,** *112* (17), 6850-6859; (b) Xu, L.; Miao, X.; Ying, X.; Deng, W., Two-Dimensional Self-Assembled Molecular Structures Formed by the Competition of van der Waals Forces and Dipole,ÄìDipole Interactions. *The Journal of Physical Chemistry C* **2011,** *116* (1), 1061-1069; (c) Takacs, C. J.; Sun, Y.; Welch, G. C.; Perez, L. A.; Liu, X.; Wen, W.; Bazan, G. C.; Heeger, A. J., Solar Cell Efficiency, Self-Assembly, and Dipole,ÄìDipole Interactions of Isomorphic Narrow-Band-Gap Molecules. *Journal of the American Chemical Society* **2012.**
4. Bombis, C.; Weigelt, S.; Knudsen, M. M.; Norgaard, M.; Busse, C.; Laegsgaard, E.; Besenbacher, F.; Gothelf, K. V.; Linderoth, T. R., Steering Organizational and Conformational Surface Chirality by Controlling Molecular Chemical Functionality. *Acs Nano* **2010,** *4* (1), 297-311.

5. (a) Tahara, K.; Yamaga, H.; Ghijsens, E.; Inukai, K.; Adisoejoso, J.; Blunt, M. O.; De Feyter, S.; Tobe, Y., Control and induction of surface-confined homochiral porous molecular networks. *Nat Chem* **2011,** *3* (9), 714-719; (b) Tahara, K.; Lei, S. B.; Adisoejoso, J.; De Feyter, S.; Tobe, Y., Supramolecular surface-confined architectures created by self-assembly of triangular phenylene-ethynylene macrocycles via van der Waals interaction. *Chem Commun* **2010,** *46* (45), 8507-8525.

6. Saettel, N.; Katsonis, N.; Marchenko, A.; Teulade-Fichou, M. P.; Fichou, D., Triazatrinaphthylene, a three-fold symmetry planar conjugated system with two-dimensional self-assembly properties. *Journal of Materials Chemistry* **2005,** *15* (31), 3175-3180.

7. (a) Lackinger, M.; Griessl, S.; Heckl, W. A.; Hietschold, M.; Flynn, G. W., Self-assembly of trimesic acid at the liquid-solid interface - a study of solvent-induced polymorphism. *Langmuir* **2005,** *21* (11), 4984-4988; (b) Nguyen, T. N. H.; Gopakumar, T. G.; Hietschold, M., Polymorphism Driven by Concentration at the Solid-Liquid Interface. *J Phys Chem C* **2011,** *115* (44), 21743-21749.

8. (a) Etter, M. C., Encoding and Decoding Hydrogen-Bond Patterns of Organic-Compounds. *Accounts Chem Res* **1990,** *23* (4), 120-126; (b) Etter, M. C.; Macdonald, J. C.; Bernstein, J., Graph-Set Analysis of Hydrogen-Bond Patterns in Organic-Crystals. *Acta Crystallogr B* **1990,** *46*, 256-262; (c) Ivasenko, O.; Perepichka, D. F., Mastering fundamentals of supramolecular design with carboxylic acids. Common lessons from X-ray crystallography and scanning tunneling microscopy. *Chem Soc Rev* **2011,** *40* (1), 191-206.

9. Kottas, G. S.; Clarke, L. I.; Horinek, D.; Michl, J., Artificial molecular rotors. *Chem Rev* **2005,** *105* (4), 1281-1376.

10. Goller, A.; Klemm, E.; Egbe, D. A. M., Model systems for rod-like polyheteroarylethynylenes. *Int J Quantum Chem* **2001,** *84* (1), 86-98.

11. (a) Becke, A. D., Density-Functional Exchange-Energy Approximation with Correct Asymptotic-Behavior. *Phys Rev A* **1988,** *38* (6), 3098-3100; (b) Lee, C.; Yang, W.; Parr, R. G., Development of the Colle-Salvetti correlation-energy formula into a functional of the electron density. *Physical Review B* **1988,** *37* (2), 785-789.

12. Evans, M. G.; Polanyi, M., Some applications of the transition state method to the calculation of reaction velocities, especially in solution. *Transactions of the Faraday Society* **1935,** *31*, 875-894.

13. Brooks, B. R.; III, C. L. B.; Jr, A. D. M.; Nilsson, L.; Petrella, R. J.; Roux, B.; Won, Y.; Archontis, G.; Bartels, C.; Boresch, S.; Caflisch, A.; Caves, L.; Cui, Q.; Dinner, A. R.; Feig, M.; Fischer, S.; Gao, J.; Hodoscek, M.; Im, W.; Kuczera, K.; Lazaridis, T.; Ma, J.; Ovchinnikov, V.; Paci, E.; Pastor, R. W.; Post, C. B.; Pu, J. Z.; Schaefer, M.; Tidor, B.; Venable, R. M.; Woodcock, H. L.; Wu, X.; Yang, W.; York, D. M.; Karplus, M., CHARMM: The biomolecular simulation program. *Journal of Computational Chemistry* **2009,** *30* (10), 1545-1614.

14. (a) Halgren, T. A., Merck molecular force field .1. Basis, form, scope, parameterization, and performance of MMFF94. *Journal of Computational Chemistry* **1996,** *17* (5-6), 490-519; (b) Halgren, T. A., Merck molecular force field .2. MMFF94 van der Waals and electrostatic parameters for intermolecular interactions. *Journal of Computational Chemistry* **1996,** *17* (5-6), 520-552; (c) Halgren, T. A., Merck molecular force field .3. Molecular geometries and vibrational frequencies for MMFF94. *Journal of Computational Chemistry* **1996,** *17* (5-6), 553-586; (d) Halgren, T. A.; Nachbar, R. B., Merck molecular force field .4. Conformational energies and geometries for MMFF94. *Journal of Computational Chemistry* **1996,** *17* (5-6), 587-615; (e) Halgren, T. A., Merck molecular force field .5. Extension of MMFF94 using experimental data, additional computational data, and empirical rules. *Journal of Computational Chemistry* **1996,** *17* (5-6), 616-641.

15. (a) Palma, C. A.; Samorì, P.; Cecchini, M., Atomistic Simulations of 2D Bicomponent Self-Assembly: From Molecular Recognition to Self-Healing. *J Am Chem Soc* **2010,** *132* (50), 17880-17885; (b) Bjork, J.; Hanke, F.; Palma, C. A.; Samori, P.; Cecchini, M.; Persson, M., Adsorption of Aromatic and Anti-Aromatic Systems on Graphene through pi-pi Stacking. *J Phys Chem Lett* **2010,** *1* (23), 3407-3412.

16. The atom type has been set to vinylic, and the charges manually set to zero. The atomic positions of the carbon atoms inside the slab have been constrained. Please refer to ESI for further details.

17. Ecija, D.; Vijayaraghavan, S.; Auwarter, W.; Joshi, S.; Seufert, K.; Aurisicchio, C.; Bonifazi, D.; Barth, J. V., Two-Dimensional Short-Range Disordered Crystalline Networks from Flexible Molecular Modules. *Acs Nano* **2012,** *6* (5), 4258-4265.

18. Desiraju, G. R., *Crystal design*. John Wiley & Sons Inc.: 2003.

19. Szabelski, P.; De Feyter, S.; Drach, M.; Lei, S. B., Computer Simulation of Chiral Nanoporous Networks on Solid Surfaces. *Langmuir* **2010,** *26* (12), 9506-9515.

20. (a) Brusilowskij, B.; Neubacher, S.; Schalley, C. A., A double intramolecular cage contraction within a self-assembled metallo-supramolecular bowl. *Chem Commun* **2009,** (7), 785-787; (b) Cardoso, C.; Abreu, P. E.; Nogueira, F., Structure Dependence of Hyperpolarizability in Octopolar Molecules. *J Chem Theory Comput* **2009,** *5* (4), 850-858.

21. Henningsen, N.; Franke, K. J.; Torrente, I. F.; Schulze, G.; Priewisch, B.; Rück-Braun, K.; Dokic, J.; Klamroth, T.; Saalfrank, P.; Pascual, J. I., Inducing the Rotation of a Single Phenyl Ring with Tunneling Electrons. *The Journal of Physical Chemistry C* **2007,** *111* (40), 14843-14848.

Chapter 3.2: Modulating the self-assembly of rigid dendrimers by tuning non-covalent interactions between side groups

Intro:

In this chapter we focus on the effect on the assembly induced by different recognition groups, and by their relative position. The work has been done in collaboration with Tamer El Malah, Stefan Hecht (Department of Chemistry, Humboldt-Universität zu Berlin), which are responsible for the synthesis and the spectroscopic characterization of the molecules (copy of the synthesis and the characterization are reported in annex 2).

The self-assembly of molecular components into larger supramolecular architectures is ubiquitous in nature and arguably constitutes the most powerful method to fabricate functional nanomaterials from the bottom up. In the confinement of a solid substrate surface this approach can be exploited to generate periodically ordered two-dimensional structures from suitably designed molecular building blocks.[1] Hence, self-assembly at the interface enables the defined positioning of functional entities with sub-nanometer precision over areas of microns and thereby allows for fine tuning of numerous properties of the resulting hybrid nanomaterials[2] for technological applications, in particular in electronics and optics.[3] To allow for structure formation under thermodynamic control, i.e. to warrant equilibration, the use of weak yet multiple non-covalent interactions has proven advantageous. In particular, the combination of van der Waals and hydrogen-bonding interactions constitutes a successful strategy to generate sophisticated two- and three-dimensional architectures as these interactions enable reversibility, directionality, specificity, and even cooperativity in the self-assembly process.[4] Both, aliphatic residues as well as hydrogen-bonding sites can be attached to suitable molecular building scaffolds to provide either linear, cyclic or branched arrangements. The latter gives rise to dendritic architectures, which can be tailored to self-assemble into a variety of super-structures in solution and in the bulk.[5] However, due to their commonly rather flexible structure and their typically three-dimensional shape the self-assembly of dendrimers on surfaces has less frequently been explored. In fact, hitherto dendrimers[6] have been visualized by Scanning Tunneling Microscopy (STM) only in ultrahigh vacuum,[7] in air forming disordered aggregates,[8] and at the solid-liquid interface as non-planar structures.[9]

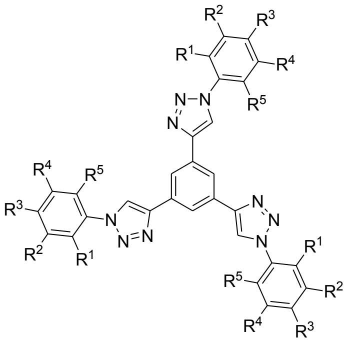

	R^1	R^2	R^3	R^4	R^5
1	H	CO_2H	H	CO_2H	H
2	H	$CO_2C_{18}H_{37}$	H	$CO_2C_{18}H_{37}$	H
3	$OC_{18}H_{37}$	H	H	H	H
4	H	$OC_{18}H_{37}$	H	H	H
5	H	H	$OC_{18}H_{37}$	H	H

Figure 1 : Chemical formulae of the investigated TPTB derivatives.

Here, we report a sub-molecularly resolved STM study of the first generation of a novel type of dendrimer, physisorbed at the solid-liquid interface into highly ordered monolayers. We have focused our attention on five derivatives of rigid and fully planar 1,3,5-tris(1-phenyl-1,2,3-triazol-4-yl)benzenes (TPTB, Figure 1), which constitute the first generation in a series of new shape-persistent poly(triazole-phenylene) dendrimers.

The linking triazole moieties are readily derived via Cu-catalyzed 1,3-cycloadditions, i.e. the so called "click" reaction.[10] The aim of this investigation was to explore the symmetry mismatch between the graphite substrate and the dendrimer scaffold, due to the presence of the five-membered triazole moieties,[11] in combination with different orientations of the self-recognition groups attached in the periphery of the TPTB.

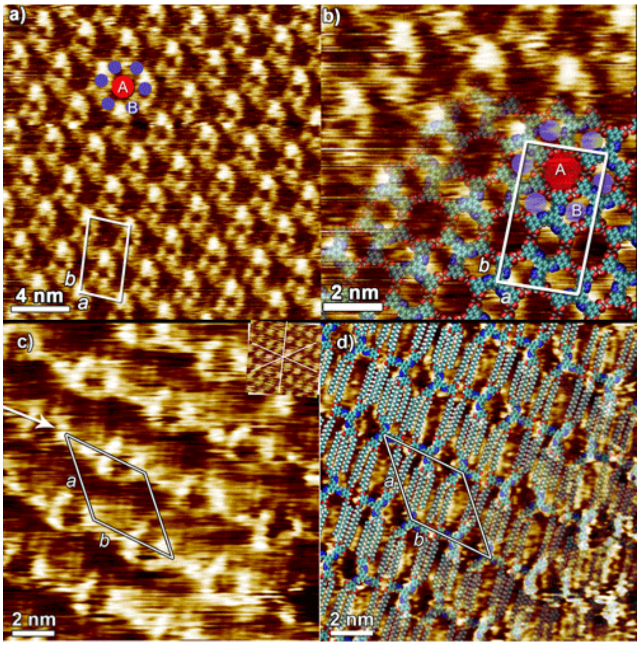

Figure 2: STM images of **1** (a,b) and **2** (c,d) at the solid-liquid interface: (a) survey image, (b-d) small scale image. Images were recorded in (a,b,d) current mode and (c) height mode. Tunneling parameters (a, b): Average tunneling current (I_t) = 18 pA, tip bias voltage (V_t) = 600 mV; (c,d): I_t = 15pA, V_t = 300 mV.

Molecule **1**, equipped with six carboxylic acid moieties in the *meta*-positions of the peripheral phenyl rings, was designed to promote the formation of C6-symmetric self-assembled structures linked via multiple H-bonds, i.e. six carboxylic acid dimers-based on di-hapto O-H···O hydrogen-bonding. To cast light onto the role of such intermolecular hydrogen-bonding pattern, our study was extended to derivative **2**, which exposes six *n*-hexadecylcarbonyloxy side chains in these *meta*-positions. To finally explore the influence of the orientation of the substituents on the peripheral phenyl rings, regioisomers **3-5**, bearing three *n*-octadecyloxy side chains in their *ortho*-, *meta-,* and *para*-positions of the peripheral phenyl moieties, respectively, were investigated. In the case of compounds **2**-**5**, the van der Waals interactions between the alkyl side-side can be expected to play a key role in the self-assembly.

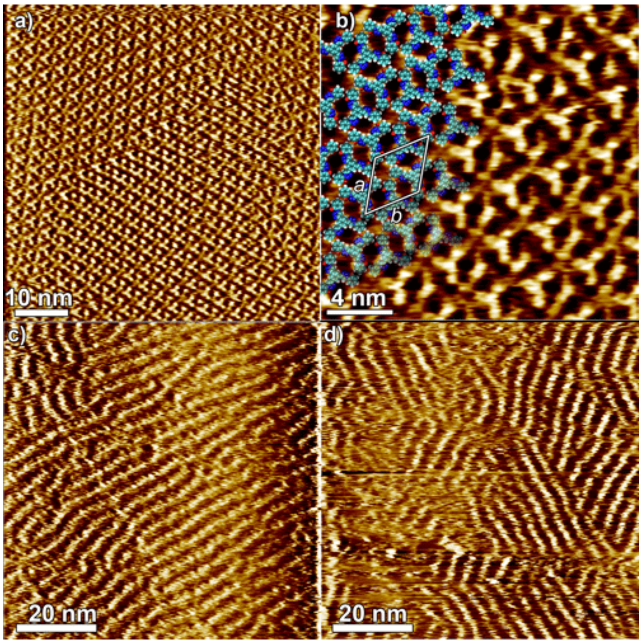

Figure 3**:** STM current images of (a,b) **3**, (c) **4** and (d) **5** recorded at the solid-liquid interface. Tunneling parameters: (a,b) I_t = 15pA, V_t = 900 mV; (c) I_t = 15pA, V_t = 860 mV; (d) I_t = 15pA, V_t = 860 mV.

To allow comparison, all experiments in this study were carried out by applying a drop of solutions of **1-5** in 1-phenyl-octane (concentrations up to 2 mM) to the basal plane of freshly cleaved highly oriented pyrolitic graphite (HOPG) surfaces. Studies of TPTB-based systems using different solvents, 1,2,4-trichlorobenzene, tetradecane and 1-heptanoic acid, did not produce any ordered monolayers. The unit cell parameters of the various crystalline patterns were determined *via* peak detection in the Fast Fourier Transform (FFT) on STM images previously corrected for the thermal drift by using the underlying graphite lattice as reference.

Experimental results:

Density Functional Theory

We recognized the planarity of the core as one of the first requirements to obtain 2D self assembled monolayers of dendrimers. For this reason, a computational study of the conformation of a derivative of **2** has been investigated: we decided to remove long alkyl chains since they shouldn't affect the geometrical preferences of cores. Also the number of atoms (especially number of hetero-atoms) is a crucial point in all *ab initio* calculations.

The time of calculation is proportional to the number of atoms in the investigated structure.

The molecular geometries of TPBTs have been minimized with Chem3D at the MM2 level and fully optimized using the density functional theory (DFT) with restricted Becke three-parameter hybrid exchange functional combined with the Lee–Yang–Parr correlation functional (B3LYP). The standard 6-311G(d,p) basis set was used in all calculations. Literature analysis shows that the geometries, relative stabilities, and frequencies of the structures calculated at the B3LYP/6-311G(d,p) level are in good accord with experimental data.

DFT techniques were used to probe the geometrical preferences of the **TPTB** molecules at room temperature (in vacuum). The investigated structure of **TPTB** slightly differs from the ones investigated with Scanning Tunneling Microscopy. Figure 4 shows the relaxed structure of **TPTB** after B3LYP computation. As shown in the Figure 4b the core of the molecule is almost perfectly flat. Terminal phenyl rings are slightly bended in respect with the core. However, as will be demonstrated with STM measurements, the phenyl rings can rotate in the presence of substrate surface and the molecule can adopt fully planar conformation.

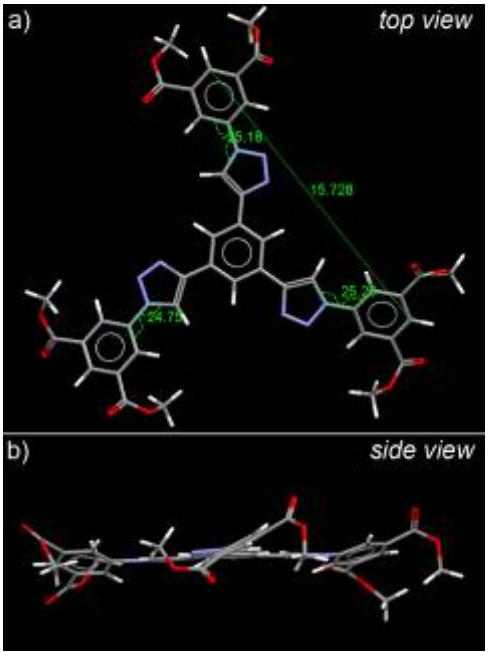

Figure 4: Molecular structures of a hexakis(methyloxy) dendrimer after B3LYP relaxation. Distances are given in Å.

Self-assembly of Hexakis(acid) dendrimer 1.

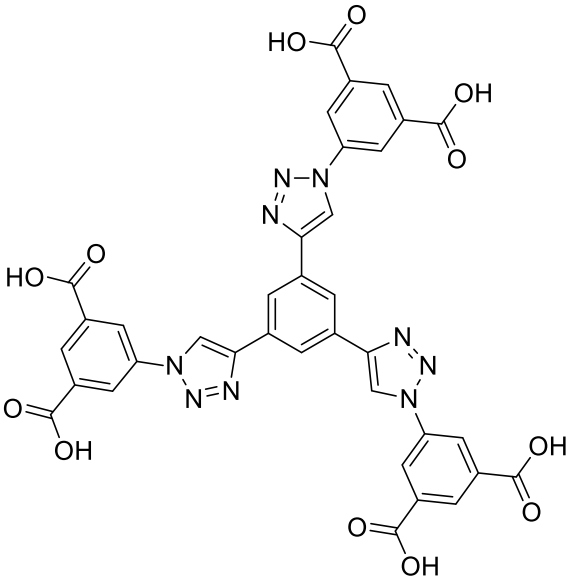

Scanning tunneling microscopy (STM) was used to probe the self-assembly behavior of **1** at the solution-graphite interface. A drop of a highly concentrated solution in 1-phenyloctane was applied to the graphite surface. Figure 5 shows STM current images of the obtained physisorbed monolayer featuring a highly crystalline structure: only domains bigger than hundreds of square nanometers were observed over tens of minutes. These domains exhibit a unit cell: $a = (3.1 \pm 0.2)$ nm, $b = (5.5 \pm 0.2)$ nm, $\alpha = (87 \pm 2)°$ leading to an area $A = (17 \pm 1)$ nm^2, where each unit cell contains four molecules **1** (Figure 5b). We couldn't determine unambiguously the orientation of triazole nitrogen, thus an absolute distinction between P3M1,P6,or P6M in the case of molecules 1 or is not possible. According to our model molecule 1 should have p6. From the experimental data the symmetry is higher and belongs to plane group p6m.

In summary, Hexa-acid **1** forms ordered physisorbed monolayers on HOPG. The respective STM current images (Figure 2a-b) reveal a monocrystalline structure featuring a 2D porous flower-like motif, which topologically coincides with a rhombitrihexagonal tiling. The supramolecular architecture is stabilized by strong (O-H···O) hydrogen-bonds, (Figure 2a,b and Figure 5) where each molecule **1** forms six $R_2^2(8)$[15] homodimeric H-bonds, i.e. twelve strong O-H···O hydrogen-bonds with neighbouring molecules.

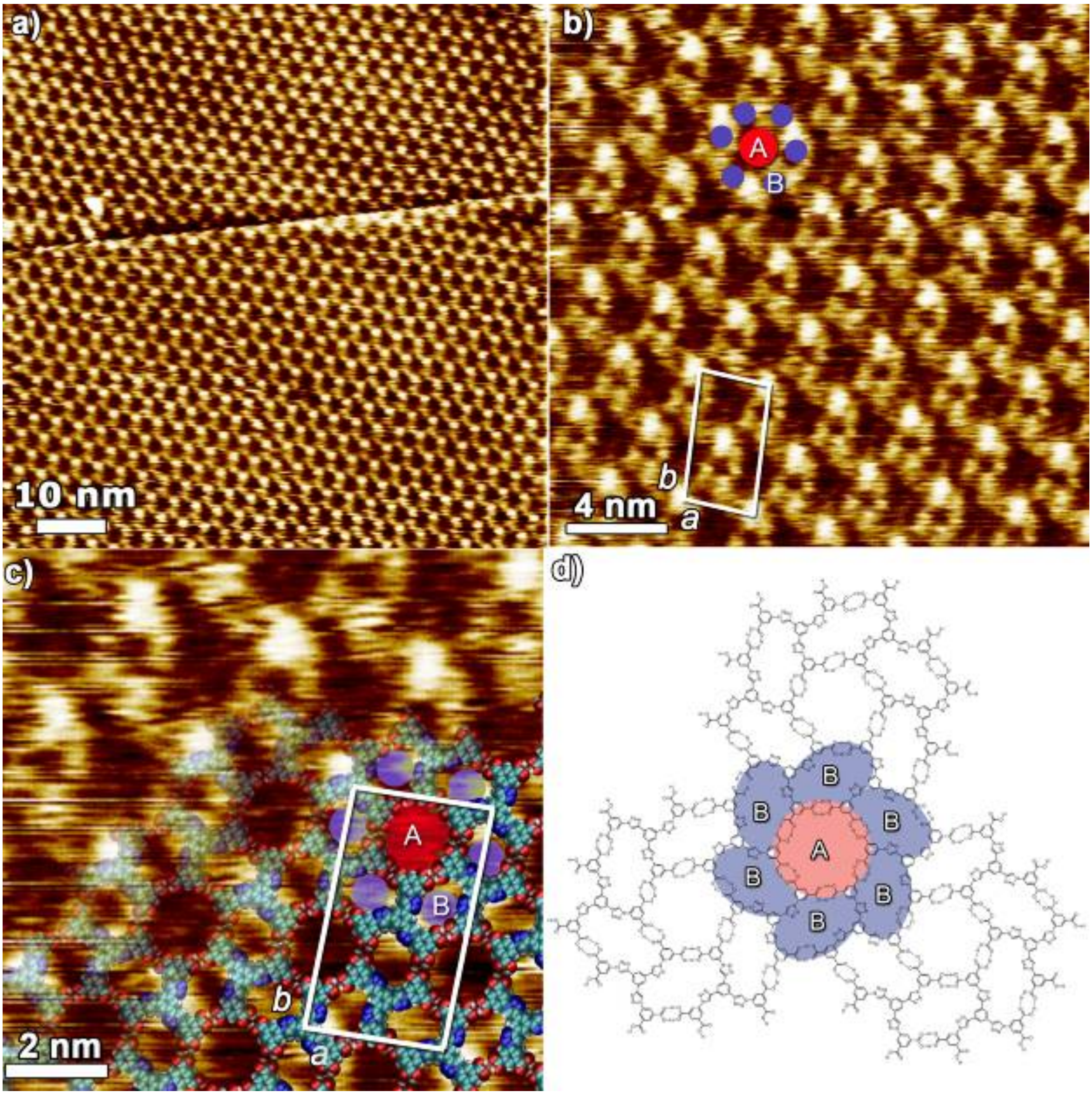

Figure 5 a) Large scale STM current image of 1 at the solid-liquid interface; b) small scale STM height image. c) Proposed CPK model of the 1; (a, b, c) Tunneling parameters: Average tunneling current (It) = 18pA, tip bias voltage (Vt) = 600 mV, d) chemical representation of the proposed packing motif. In green Highlight of the 48 atoms perimeter central pore A, resulting from 6 di-hapto O-H···O H-bonding, and in blue the 42 atoms "smaller" pores B.

Pore size determination

Importantly, this 2D motif incorporates two pore types, i.e. A and B, with inner voids of 1.5 nm^2 and 0.65 nm^2, respectively. The formation of hexameric pores A is a direct consequence of the 120º angle between the two carboxylic functions. Due to the molecular geometry of **1** two of the remaining carboxylic moieties interact via hydrogen-bonds with adjacent molecules, forming the second type of pores, i.e. dimeric pores B of smaller size. From the data it appears that the formed hierarchical pore pattern is dictated by the formation of carboxylic acid dimers via self-complementary hydrogen-bonding interactions.

To evaluate the sizes of the pores we have employed different methods: i.e. they have been calculated using SPIP software via automatic procedure of pixel counting, on different STM images. The values are in good agreement to the ones calculated by the estimated molecular van der Waals volume projected onto the surface.

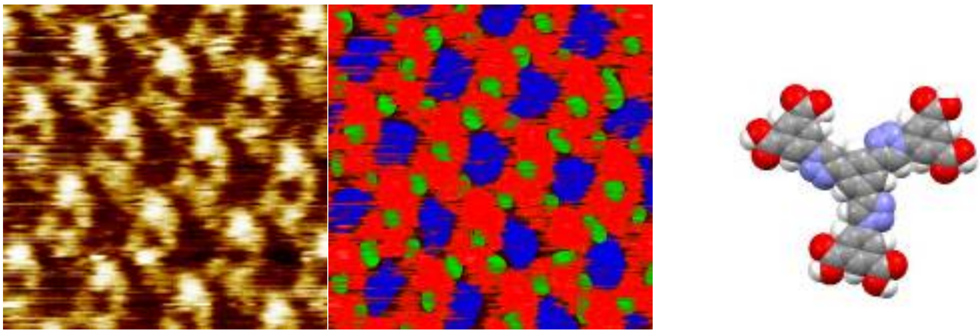

Figure 6: a) as an example we show a zoom into the STM image of 2D crystal of molecule **1** on HOPG (11x11nm); b) the colored domains are those whose area have been estimated trough an automatic procedure of pixel counting; c) estimated projection of the molecular van der Waals volume onto the surface (AvdW)

	Calculated area	Surface Pore A	Surface Pore B	Surface per mol.
Pixel counting	17±2	1.5±0.3	0.5 ± 0.2	2.7±0.5
AvdW	17.36	1.55	0.65	2.75

Table 1: Calculated pore parameters

Therefore it should be possible, and interesting to functionalize the two different pores with other moieties.

Tiling topology determination

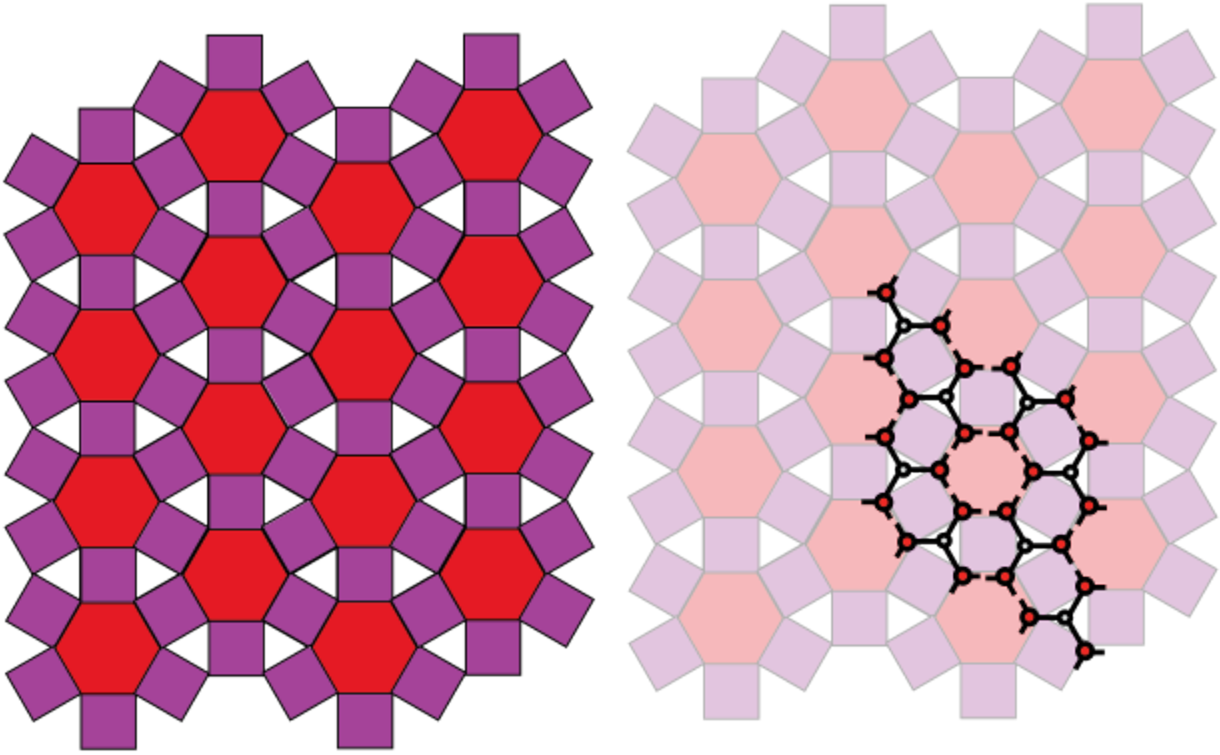

Figure 7: a) Rhombitrihexagonal tiling; b) superposition of a simplified molecular model. The red highlighted nodes are the "isophthalic" rings.

In literature, similar motifs have usually been called "flower"[12] or similar, but interestingly, the obtained pattern is an example of what in topology is called a semi-regular taxellation. Considering the isophthalic moieties as "nodes", the structure is topologically equivalent to the semi-regular rhombitrihexagonal tiling. Each isophthalic node is connected to one molecule (the triangles), two B pores (the squares) and one A pore (the hexagons). Correspondingly, each node contacts one triangle (the molecule), two squares (B pores) (as they involves 4 nodes, are topologically squares) and one hexagon (A pores - six nodes). Schlafli symbol is $t_{0,2}\{ 3 , 6 \}$. [13]

Contrast differences between molecules

Finally, in the image reported in figure 3a,b,c there's an evident difference in contrast between molecules along the fast-scan direction. Such effect can be usually assigned to the following reasons:

a) scanning artifacts, eg: trace-retrace or double tip effects;

b) defects of the molecular packing on the surface or impurities in the material;

c) different number of molecules in a stack filling the tunneling gap between the tip and substrate (eg: A-B multilayers);

d) different conformation of the molecules;

e) different positions of the molecules in the tip-substrate gap;

f) Moiré pattern;

The points (a-c) can be readily excluded: Different images from different experiments, at different angles ruled out hypothesis a); the number of defects in freshly cleaved HOPG is orders of magnitude smaller, and the fact that the materials have been proven by NMR as analytically pure, grant the falsification of hypothesis b); c) can easily be excluded observing the vacancy in Figure 5a; d) and e) aren't in agreement with the planarity of the **1** molecules.

We conclude then that Moiré effect between the self-assembled monolayer and the underlying substrate is the most probable explanation. In an attempt to further prove hypothesis f), Epitaxial registration according to Hooks et Al[14] has been computed: Molecule **1** exhibits a Moiré pattern with a measured azimuthal rotation of the overlayer of 18 ± 2°, as measured from the principal lattice vectors, and a registry between the two lattices at a length scale of approximately 4.5nm; the calculated matrix elements (p=13.0, q=10.6, r=-8.0, s=-18.2) are within the experimental agreement with a Point on Line Coincidence-IA.

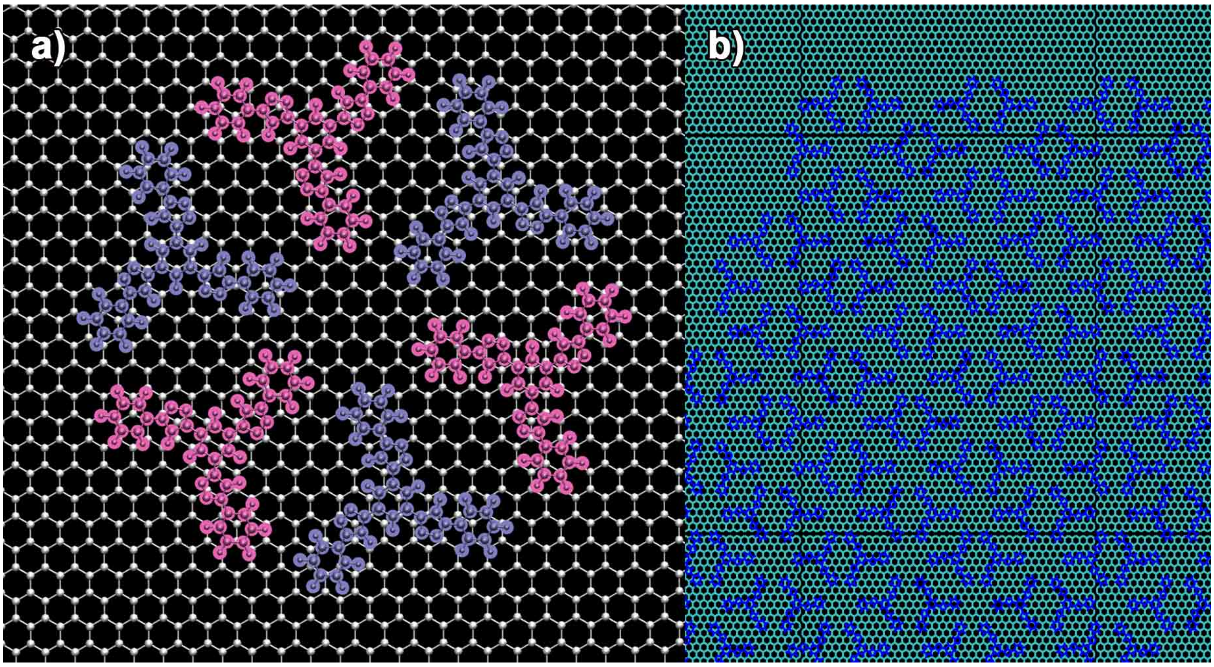

Figure 8: a)Model highlighting the different positions respect to the substrate of the TPTB core in the proposed model Purple and Pink molecules differs by the number of staggered/eclipsed atoms. b) Simple

superposition of the proposed lattice on a model graphene sheet, esemplifiying contrast differences due to moiré effect.

Self-assembly of Hexakis(n-hexahexadecyl) dendrimer 2.

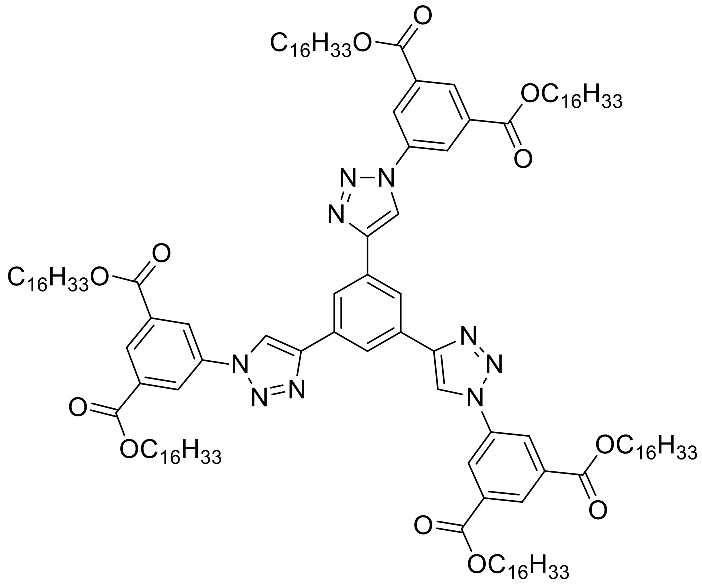

Exchanging the hydrogen-bonding interactions for weaker van der Waals interactions leads to formation of rather different self-assembled monolayers in the case of compound **2**. The associated STM images (Figure 2c,d) show a lamellar structure featuring a nanoscale phase segregation between the TPTB cores and the long alkyl side-chains. The self-assembly behavior of the Hexakis(*n*-hexahexadecyl) dendrimer **2** at the solution-graphite interface shows remarkable differences. Again, a drop of a 1 mM solution in 1-phenyloctane was applied to the graphite surface. In Figure 9 are reported STM current images of the obtained physisorbed monolayer. It features a crystalline structure, which consists of large domains that are stable over several minutes. Within a lamella (marked with white arrow in Figure 2c) the cores are arranged in a "head-to-head" and "tail-to-tail" dimeric motif (Figure 2d). Within the lamella the molecules are physisorbed flat on the surface. One can easily see, especially on the STM height image (Figure 9), molecules forming “head-to-head” and also “tail-to-tail” type of dimers. The domains exhibit a unit cell: $a = b =$ (4.15 ± 0.2) nm, α = (45 ± 3)° leading to an area A = (12.2 ± 0.7) nm^2, where each unit cell contains two molecules **2** (Figure 9b), featuring an Inter-Lamellae distance of 1.60 ±0.2nm.

Study of this system at different concentrations, i.e. at 60μM, 600μM, and 1 mM in 1-phenyloctane, revealed always the same self-assembled structure.

The entire supramolecular architecture is stabilized by the interdigitation of alkyl side chains belonging to adjacent molecules, adsorbed along one of the Miller-Bravais symmetric axes of the underlying HOPG lattice (indicated in the in-set of Figure 2c). For each molecule only four out of six hexadecyl side chains have been detected in the STM image (Figure 2d). However taking the unit cell parameters and the size of the molecule as obtained by Molecular Mechanics simulations into account, it is more likely that the two remaining side chains are also physisorbed on the HOPG surface but are not imaged due to their high conformational dynamics on the time scale of the STM experiments. By comparing structure formation of **1** and **2**, it seems that van der Waals interactions dominate the self-assembly of **2** and lead to a change from a C_6-symmetric rosette pattern to a linear lamellar structure.

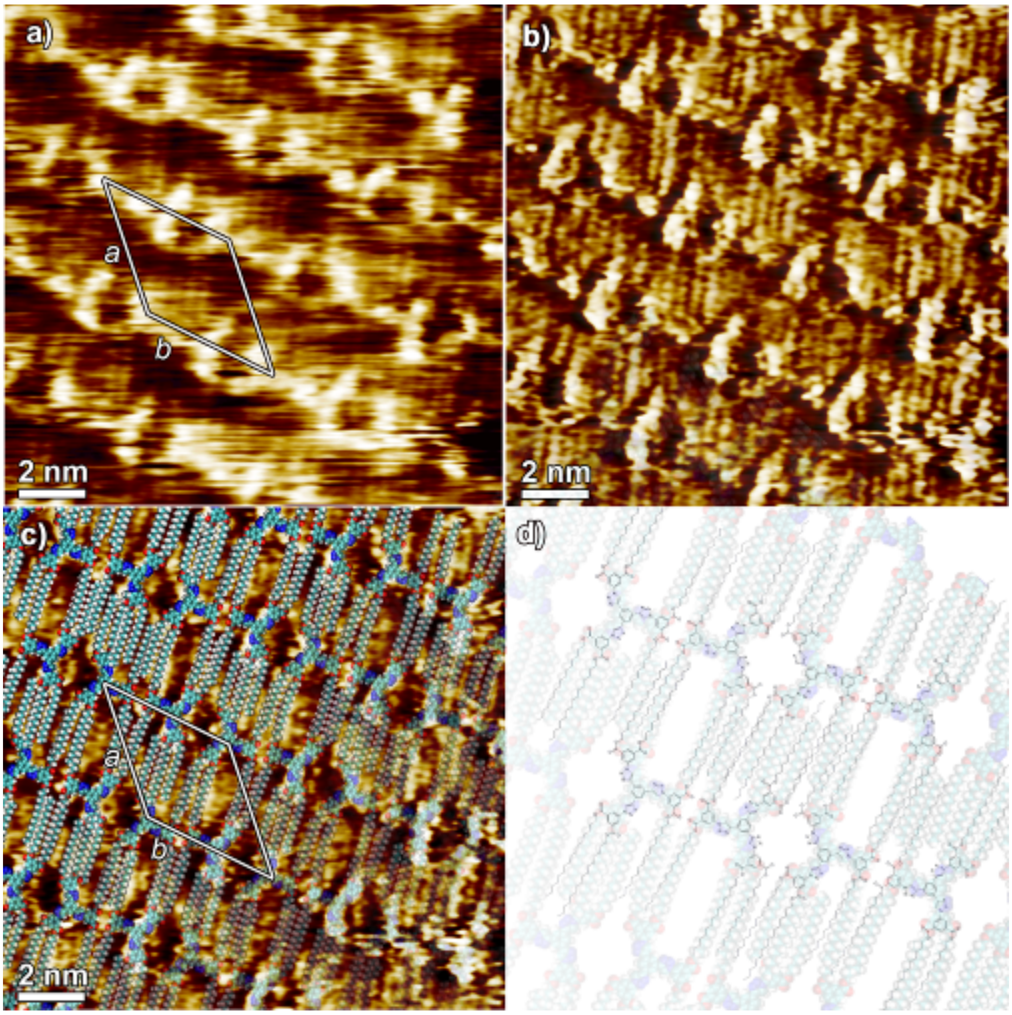

Figure 9: a) Small height image of the monolayer of **2** self assembled at the solid liquid interface, b) small scale STM current image of **2** at the solid-liquid interface; c) Proposed CPK model of the TPTB**2**. Tunneling parameters: Average tunneling current (I_t) = 15pA, tip bias voltage (V_t) = 300 mV. d) chemical representation of the model.

Self-assembly of Tris(ortho-octadecyloxy) dendrimer 3.

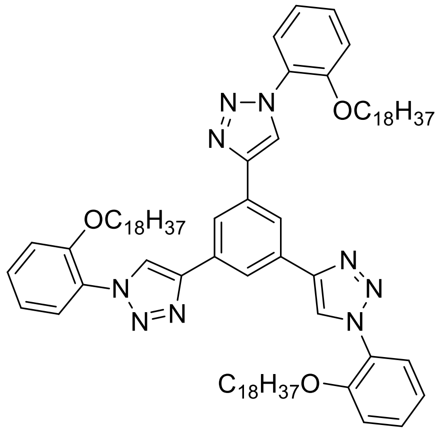

To furthermore discern the effect the of side-chain orientation on self-assembly, high resolution STM images of regioisomers **3**-**5** were obtained (Figure 3).

Scanning tunneling microscopy (STM) was used to probe the self-assembly behavior of **3** at the solution-graphite interface. A drop of a 2mM solution in 1-phenyloctane was applied to the graphite surface. Figure 10 shows STM height images of the obtained physisorbed monolayer featuring a crystalline structure, which consists of hundreds of square nanometers large polycrystalline structures that are stable over several minutes. These domains exhibit a unit cell: $a = (3.7 \pm 0.2)$ nm, $b = (3.7 \pm 0.2)$ nm, $\alpha = (58 \pm 3)°$ leading to an area $A = (11.6 \pm 0.7)$ nm^2, where each unit cell contains two molecules **3** (Figure 10b).

The monolayer of the *ortho*-substituted compound **3** exhibits a crystalline structure with a motif similar to the rhombitrihexagonal tiling observed for **1**, but incorporating only two molecules within the unit cell (Figure 3b). It is most likely that the supramolecular architecture is stabilized by weak van der Waals interactions between adjacent molecules. The proposed molecular packing model as well as the unit cell parameters suggest that all *n*-octadecyloxy side chains of **3** are back-folded into the supernatant solution, which can be ascribed to insufficient van der Waals contacts between the alkoxy chains of adjacent molecules **3**. Importantly, highly ordered self-assembled structures of **3** were observed only upon use of highly concentrated solutions ($c = 2$ mM).

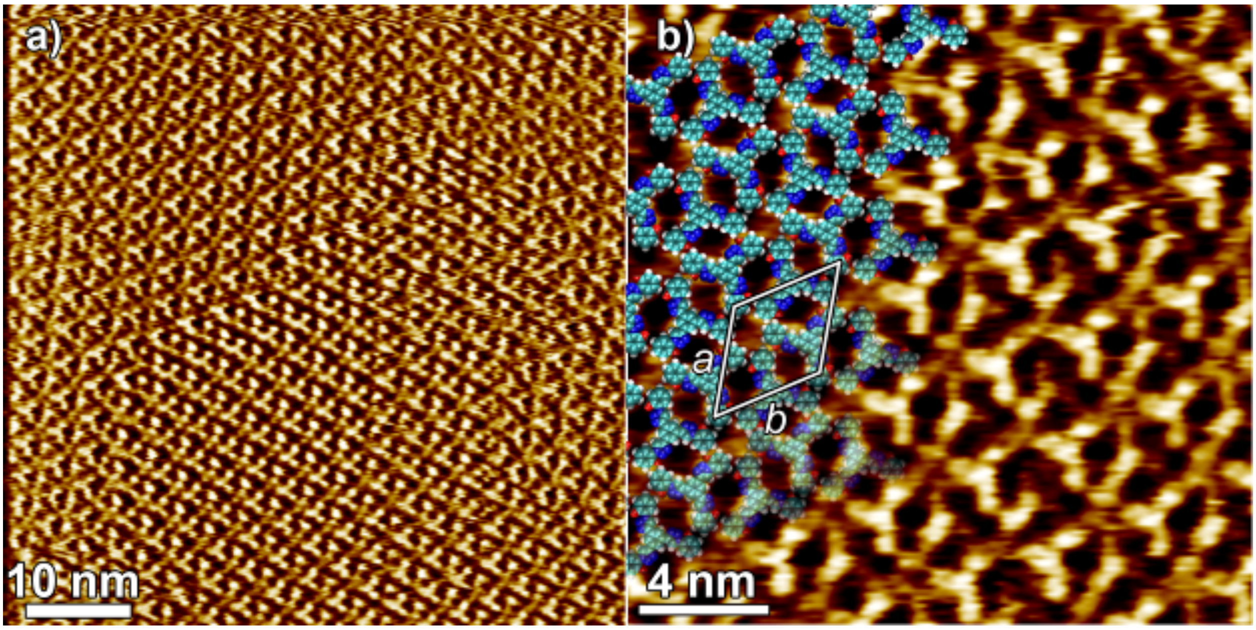

Figure 10**:** a) Large scale STM current image of **3** at the solid-liquid interface; b) small scale STM current image and proposed CPK model of the **3**. Tunneling parameters: Average tunneling current (I_t) = 15pA, tip bias voltage (V_t) = 900 mV.

Self-assembly of:

tris(meta-octadecyloxy) dendrimer 4

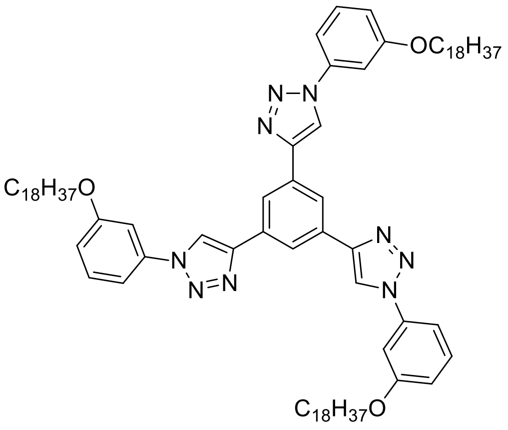

tris(para-octadecyloxy) dendrimer 5

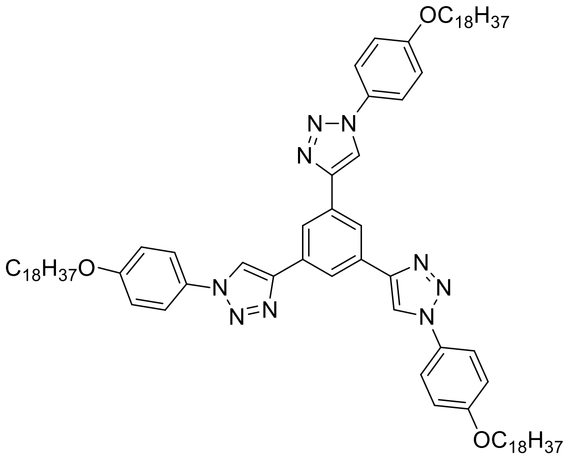

In strong contrast to compound **3**, its *meta-* and *para*-regioisomers **4** and **5**, respectively, form only unstable and poorly ordered lamellar structures on HOPG, highlighting the high molecular mobility on a timescale faster that the tip scan, thereby hindering high resolution STM mapping.

A drop of a 2 mM solution in 1-phenyloctane was applied to the graphite surface. Figure 11 shows STM height images of the obtained physisorbed monolayer featuring a crystalline lamellar structure. In the case of **4**, These domains exhibit a unit cell: a = (4.4 ± 0.2) nm, b = (3.8 ± 0.2) nm, α = (63 ± 3)° leading to an area A = (15.6 ± 0.85) nm^2, where each unit cell contains two molecules **4** (Figure 11b), featuring an Inter-Lamellae distance of 1.6±0.2 nm.

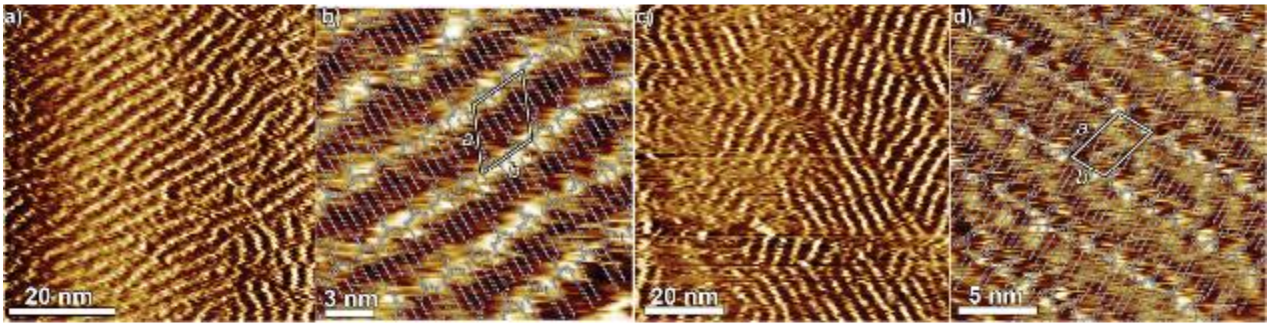

Figure 11: a) Large scale STM current image of **4** at the solid-liquid interface; b) Small scale STM current image and proposed CPK model of the **4**. Tunneling parameters: Average tunneling current (I_t) = 15pA, tip bias voltage (V_t) = 860 mV. c) Large scale STM current image of **5** at the solid-liquid interface; d) Small scale STM current image and proposed CPK model of the **5**. Tunneling parameters: Average tunneling current (I_t) = 15pA, tip bias voltage (V_t) = 860 mV.

In the case of **5**, These domains exhibit a unit cell: a = (4.4 ± 0.2) nm, b = (3.5 ± 0.2) nm, α = (72 ± 3)° leading to an area A = (14.6 ± 0.85) nm^2, where each unit cell contains two molecules **5** (Figure 11d).

The interlamellar distances for the assembly of molecule **4** and **5** amount to (3.0±0.2) nm and (2.75± 0.3) nm, respectively, providing evidence for a tight molecular packing probably caused by interdigitation of alkyl side chains belonging to molecules of adjacent lamellae.

Conclusions

In summary, we have performed a comparative STM study of the self-assembly of various derivatives of the first generation of new poly(triazole-phenylene) dendrimers at the HOPG-solution interface. All molecules were found to physisorb in a flat adsorption geometry on graphite forming 2D supramolecular structures. Different crystalline nanopatterns were observed, ranging from honeycomb-like networks for compounds **1** and **3** to various lamellar structures of different stability in the case of derivatives **2**, **4**, and **5**. Our results provide unambiguous evidence that subtle modification in the substitution pattern of the TPTB scaffold leads to pronounced effects on its 2D self-assembly at the liquid-solid interface. Two factors seem to be responsible for the variation in the observed structures and their stability: (i) due to the presence of the triazole moieties, the TPTB core cannot completely match the six-fold symmetry of the HOPG substrate, i.e. both lattices are not commensurate, and thereby gives rise to an inherent flexibility and thermodynamic instability, and (ii) as a consequence the exact presentation of the alkyl side chains by the TPTB scaffold governs the overall structure formation in the self-assembly process. In general, the capacity of flat dendrimers to pack into highly ordered supramolecular structures at the solid-liquid interface described herein could lead to the design of more complex and multicomponent structures based on dendritic cores.[5]

References

1. (a) Bonifazi, D.; Mohnani, S.; Llanes-Pallas, A., Supramolecular Chemistry at Interfaces: Molecular Recognition on Nanopatterned Porous Surfaces. *Chem-Eur J* **2009,** *15* (29), 7004-7025; (b) Ciesielski, A.; Palma, C.-A.; Bonini, M.; Samorì, P., Towards Supramolecular Engineering of Functional Nanomaterials: Pre-Programming Multi-Component 2D Self-Assembly at Solid-Liquid Interfaces. *Adv. Mater.* **2010,** *22* (32), 3506-3520; (c) De Feyter, S.; De Schryver, F. C., *Chem. Soc. Rev.* **2003,** *32*, 139-150; (d) Palma, C. A.; Bonini, M.; Breiner, T.; Samorì, P., Supramolecular Crystal Engineering at the Solid-Liquid interface from First Principles: Toward Unraveling the Thermodynamics of 2D Self-Assembly. *Adv. Mater.* **2009,** *21* (13), 1383-1386; (e) Elemans, J. A. A. W.; Lei, S.; De Feyter, S., Molecular and Supramolecular Networks on Surfaces: From Two-Dimensional Crystal Engineering to Reactivity. *Angew Chem Int Edit* **2009,** *48* (40), 7298-7332.

2. (a) Kudernac, T.; Lei, S. B.; Elemans, J. A. A. W.; De Feyter, S., Two-dimensional supramolecular self-assembly: nanoporous networks on surfaces. *Chem Soc Rev* **2009,** *38* (2), 402-421; (b) Elemans, J.; Van Hameren, R.; Nolte, R. J. M.; Rowan, A. E., Molecular materials by self-assembly of porphyrins, phthalocyanines, and perylenes. *Adv. Mater.* **2006,** *18* (10), 1251-1266.

3. (a) DiBenedetto, S. A.; Facchetti, A.; Ratner, M. A.; Marks, T. J., Molecular Self-Assembled Monolayers and Multilayers for Organic and Unconventional Inorganic Thin-Film Transistor Applications. *Adv. Mater.* **2009,** *21* (14-15), 1407-1433; (b) Schenning, A. P.; Meijer, E. W., Supramolecular electronics; nanowires from self-assembled pi-conjugated systems. *Chem Commun* **2005,** (26), 3245-3258.

4. (a) Desiraju, G. R., Hydrogen bridges in crystal engineering: Interactions without borders. *Accounts Chem Res* **2002,** *35* (7), 565-573; (b) Ivasenko, O.; Perepichka, D. F., Mastering fundamentals of supramolecular design with carboxylic acids. Common lessons from X-ray crystallography and scanning tunneling microscopy. *Chem. Soc. Rev.* **2011,** *40* (1), 191-206; (c) Tahara, K.; Lei, S.; Adisoejoso, J.; De Feyter, S.; Tobe, Y., Supramolecular surface-confined architectures created by self-assembly of triangular phenylene-ethynylene macrocycles via van der Waals interaction. *Chem Commun* **2010,** *46* (45), 8507-8525.

5. (a) Rosen, B. M.; Wilson, C. J.; Wilson, D. A.; Peterca, M.; Imam, M. R.; Percec, V., Dendron-Mediated Self-Assembly, Disassembly, and Self-Organization of Complex Systems. *Chem Rev* **2009,** *109* (11), 6275-6540; (b) Zeng, F. W.; Zimmerman, S. C., Dendrimers in supramolecular chemistry: From molecular recognition to self-assembly. *Chem Rev* **1997,** *97* (5), 1681-1712.

6. Widmer, I.; Hubler, U.; Stohr, M.; Merz, L.; Guntherodt, H. J.; Hermann, B. A.; Samori, P.; Rabe, J. P.; Rheiner, P. B.; Greiveldinger, G.; Murer, P., Hourglass-shaped dendrimers on surfaces: A comparison of different scanning-tunneling-microscopy approaches. *Helv Chim Acta* **2002,** *85* (12), 4255-4263.

7. Li, W. S.; Kim, K. S.; Jiang, D. L.; Tanaka, H.; Kawai, T.; Kwon, J. H.; Kim, D.; Aida, T., Construction of segregated arrays of multiple donor and acceptor units using a dendritic scaffold: Remarkable dendrimer effects on photoinduced charge separation. *J Am Chem Soc* **2006,** *128* (32), 10527-10532.

8. (a) Fleming, C. J.; Liu, Y. X.; Deng, Z.; Liu, G. Y., Deformation and Hyperfine Structures of Dendrimers Investigated by Scanning Tunneling Microscopy. *J Phys Chem A* **2009,** *113* (16), 4168-4174; (b) Fleming, C. J.; Yin, N. N.; Riechers, S. L.; Chu, G.; Liu, G. Y., High-Resolution Imaging of the Intramolecular Structure of Indomethacin-Carrying Dendrimers by Scanning Tunneling Microscopy. *Acs Nano* **2011,** *5* (3), 1685-1692.

9. Latterini, L.; Pourtois, G.; Moucheron, C.; Lazzaroni, R.; Bredas, J. L.; Kirsch-De Mesmaeker, A.; De Schryver, F. C., STM imaging of a heptanuclear ruthenium(II) dendrimer, mono-add layer on graphite. *Chemistry-a European Journal* **2000,** *6* (8), 1331-1336.

10. (a) Rostovtsev, V. V.; Green, L. G.; Fokin, V. V.; Sharpless, K. B., A stepwise Huisgen cycloaddition process: Copper(I)-catalyzed regioselective "ligation" of azides and terminal alkynes. *Angewandte Chemie-International Edition* **2002,** *41* (14), 2596-+; (b) Meldal, M.; Tornoe, C. W., Cu-catalyzed azide-alkyne cycloaddition. *Chem Rev* **2008,** *108* (8), 2952-3015; (c) Tornoe, C. W.; Christensen, C.; Meldal, M., Peptidotriazoles on solid phase: [1,2,3]-triazoles by regiospecific copper(I)-catalyzed 1,3-dipolar cycloadditions of terminal alkynes to azides. *J Org Chem* **2002,** *67* (9), 3057-3064.

11. (a) Meudtner, R. M.; Ostermeier, M.; Goddard, R.; Limberg, C.; Hecht, S., Multifunctional "Clickates" as versatile extended heteroaromatic building blocks: Efficient synthesis via click chemistry, conformational preferences, and metal coordination. *Chemistry-a European Journal* **2007,** *13* (35), 9834-9840; (b) Ostermeier, M.; Berlin, M. A.; Meudtner, R. M.; Demeshko, S.; Meyer, F.; Limberg, C.; Hecht, S., Complexes of Click-Derived Bistriazolylpyridines: Remarkable Electronic Influence of Remote Substituents on Thermodynamic Stability as well as Electronic and Magnetic Properties. *Chemistry-a European Journal* **2010,** *16* (33), 10202-10213; (c) Piot, L.; Meudtner, R. M.; El Malah, T.; Hecht, S.; Samori, P., Modulating Large-Area Self-Assembly at the Solid-Liquid Interface by pH-Mediated Conformational Switching. *Chemistry-a European Journal* **2009,** *15* (19), 4788-4792; (d) Zornik, D.; Meudtner, R. M.; El Malah, T.; Thiele, C. M.; Hecht, S., Designing Structural Motifs for Clickamers: Exploiting the 1,2,3-Triazole Moiety to Generate Conformationally Restricted Molecular Architectures. *Chemistry-a European Journal* **2011,** *17* (5), 1473-1484.

12. (a) Lackinger, M.; Griessl, S.; Heckl, W. M.; Hietschold, M.; Flynn, G. W., Self-Assembly of Trimesic Acid at the Liquid-Solid Interface a Study of Solvent-Induced Polymorphism. *Langmuir* **2005,** *21* (11), 4984-4988; (b) Thi Ngoc Ha, N.; Gopakumar, T. G.; Hietschold, M., Polymorphism Driven by Concentration at the Solid–Liquid Interface. *Journal Of Physical Chemistry C* **2011,** *115* (44), 21743-21749.

13. Coxeter, H. S. M., *Regular Polytopes*. 1973.

14. Hooks, D. E.; Fritz, T.; Ward, M. D., Epitaxy and molecular organization on solid substrates. *Advanced Materials* **2001,** *13* (4), 227-+.

15. (a) Etter, M. C., Encoding and Decoding Hydrogen-Bond Patterns of Organic-Compounds. *Accounts Chem Res* **1990,** *23* (4), 120-126; (b) Etter, M. C.; Macdonald, J. C.; Bernstein, J., Graph-Set Analysis of Hydrogen-Bond Patterns in Organic-Crystals. *Acta Crystallogr B* **1990,** *46*, 256-262.

Chapter 3.3: Bi-dimensional Self-Assembly of 2amino-pyrimidine derivatives

Intro:

In this section we focus on the analysis of the bi-dimensional assemblies of different building blocks derived from 2amino-pyrimidine, one of the most interesting synthons from a biologically perspective: 3 out of 4 nucleobases are pyrimidine derivatives, and it has been shown that under UV irradiation, pyrimidine degrades into uracil. We focused on two different 2-amino-pyrimidine derivatives, one functionalized with an alkyl chain, and the other with 2-2' bipyridine. The aim of the study was to evaluate the interactions and the competition between multiple recognition groups, (the alkyl chain interdigitation vs. the hydrogen bonding, or hydrogen bonds vs. metal ligand). The investigation was performed in collaboration with Silvia Colella from BASF (ISIS/UMR CNRS 7006 Université de Strasbourg), which synthesized and characterized the compounds (a copy of the procedure and the characterization is reported in annex 3).

One of the requirements for successfully planning supramolecular architectures is a deep understanding of the phenomenology of the relationship between the various interactions. It is important to develop a set of simple rules which would give a basis from which we could build such architectures. It would be very useful to have a simple rule of thumb to determine which interactions would drive the assembly of a given hypothetical synthon, by considering two points: the hierarchy among the recognition groups (RG), and their interrelationship and competition.

The objective is to provide a set of simple empirical rules, similar to the observation of *Etter et Al*,[1] to consider the competition among different RGs.

The first three of *Etter*'s rules, states:

1. All good proton donors and acceptors are used in hydrogen bonding.

2. Six-membered-ring intramolecular hydrogen bonds form in preference to intermolecular hydrogen bonds.

3. The best proton donors and acceptors remaining after intramolecular hydrogen-bond formation form intermolecular hydrogen bonds to one another.

Such a remarkable work of inference is not complete when other competing recognition groups, such as alkyl chains or ligand moieties, are present in a building block.

A collective effort is necessary to gather enough knowledge to build such set of rules, but, as a first small step in that direction we envisaged couple of principles:

1) the system designed should be as simple as possible and possess multiple RGs
2) the competition between groups should be *triggerable* via external stimuli.

There are, as discussed extensively before,[i] a couple of factor to keep in equilibrium in order to generate ordered self-assembled structures, which means that the desired synthon is also automatically in competition with himself and with the solvent for the adsorption/solvation/crystallization;

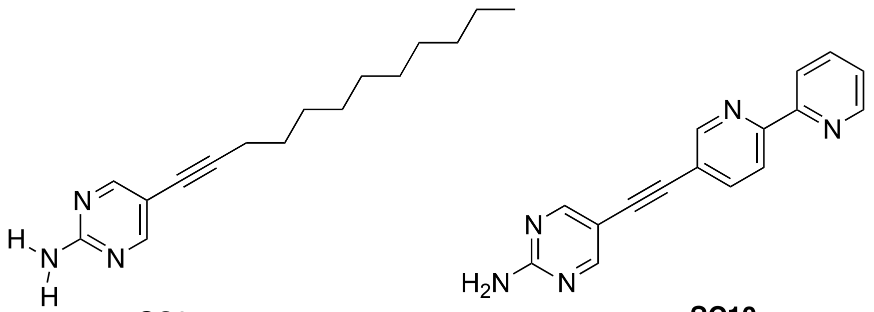

SC9 **SC10**

Figure 1: Investigated molecules.

With this objective in mind we synthesized two building blocks (Figure 1), one possessing an alkyl chain(**SC9**), and one possessing a bipyridine unit(**SC10**). Both possess the pyrimidin-2-amino functionality, which is known to form different crystalline assemblies based on hydrogen bonds upon addition of carboxylic acids. It has been shown[2] that 2-aminopyrimidine has a preference to form an adduct with carboxylic acids trough the formation of eight membered hydrogen bonded dimer $R_2^2(8)$,[1, 3] but an investigation of similar systems, based on poly-aromatics connected to position 4, that was conducted by *Stoll et Al*,[4] also showed some remarkable effects of π-π stacking in the crystalline assembly, adding another actor to the play. To summarize, our aim in using the building block **SC9** was to highlight the competition between hydrogen bonding and alkyl-chain interdigitation, and with **SC10**, to observe the antagonism between HB, π-π, and Metal-ligand interaction. We will see that in the case of **SC9** there was no evidence

---

[i] see equilibrium section in the introduction

of competition, but on the contrary, *only* if associated with a carboxylic acid[5] possessing a long alkyl chain via hydrogen-bond, gave rise to SAMs. In the case of **SC10** the competition is present, and give rise to different polymorphs;

Experimental details:

Sc9

Different solvents and reagent concentrations were tested as reported in the following table.

For each measurement a drop of 4μL of solution was applied on the basal plane of a freshly cleaved HOPG substrate and imaged with a scanning tunneling microscope with manually cut Pt/Ir tip.

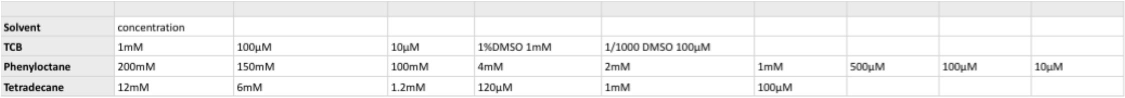

Solvent	concentration								
TCB	1mM	100μM	10μM	1%DMSO 1mM	1/1000 DMSO 100μM				
Phenyloctane	200mM	150mM	100mM	4mM	2mM	1mM	500μM	100μM	10μM
Tetradecane	12mM	6mM	1.2mM	120μM	1mM	100μM			

Table 1: Experimental conditions tested.

No ordered assemblies were observed in any of the experiments.

The **SC9** molecules are amphiphilic, and have a strong interaction with the solvent. Furthermore we expect that the molecule-molecule interaction is higher than the interaction with the substrate which explains the experimental difficulty of forming a SAM, and the fact that **SC9** crystallizes in three dimensions before forming any two-dimensional ordered monolayer. Striking evidence of this behavior is that even after dropcasting from highly concentrated solutions (i.e. 200mM), the smallest addition of solvent dissolves every white crystal formed and there are no observable SAMs on the HOPG/solvent interface.

In order to gain greater insight into this behavior, short MD simulations were performed.

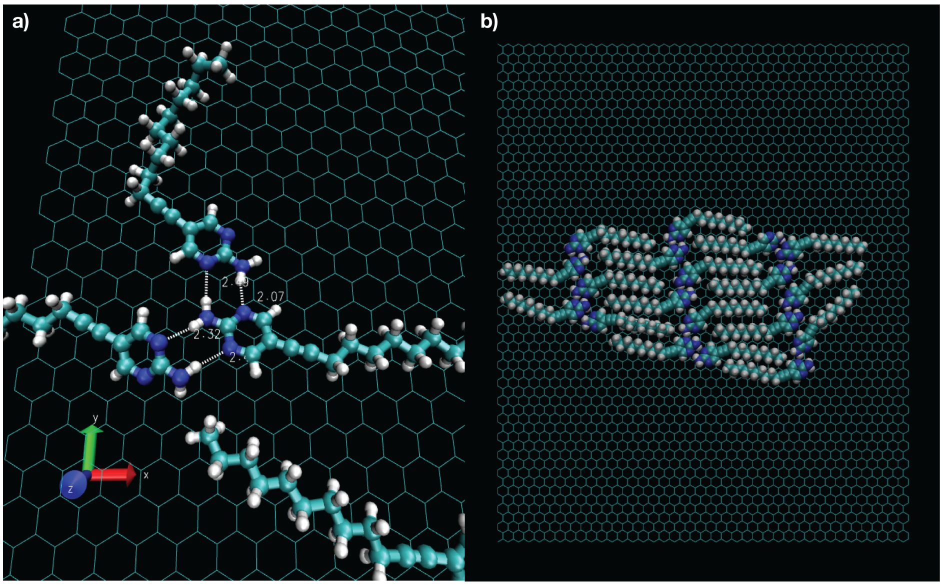

Figure 2: a) tipical HB trimer and bond length from the calculations, b) minimized structure of the expected lamellar packing.

MD Simulations:

Short simulation using MMFF94 and CHARMM confirmed the instability of the self-assembly on the HOPG surface. Simulations were performed with 19 molecules on a monolayer of graphene in vacuum, for 2 ns, at 300K, both starting from the expected model and from random positions; The structure was placed at 5Å from a graphene slab and minimized with 20000 steps of SD, 10000 of ABNR then gradually heated from 100°C to 300°C at 20°C per step, and kept under those conditions for 1ns. Subsequently the sample was subjected to Langevin dynamics with a friction coefficient of 0.05 (standard value) for 10 ns.

MD calculations confirmed the formation of head-to-head HB, and the presence of non-covalent interactions between the tails. However, the proposed lamellar assembly is not stable, and dissolves after few steps of Langevin dynamics. The most stable assemblies are dimers and trimers, such as the one portrayed in fig.2. The system shows the formation of dimers and trimers that are quite stable while bigger "oligomers" are dissolved in a few picoseconds at room temperature. The high speed of diffusion on the graphene slab observed using the standard conditions confirms the expected weak interaction with the HOPG surface.

Sc9: Coprecipitation with carboxylic acids:

The self-assembly behavior of the bi-component network formed with **SC9** and nonanoic acid (NA) at the solution-graphite interface was observed with STM. A drop of a 100 mM solution of **SC9** in NA was applied to the graphite surface. Figure 3 shows STM current and height images of the physisorbed monolayer obtained, featuring a crystalline structure, which consists of large crystalline domains (hundreds of square nanometers) that are stable over several minutes. These domains exhibit a unit cell: a =(1.71 ± 0.2), b= (2.14±0.2) nm, γ = (73 ± 3)° leading to an area A = (3.5 ± 0.5) nm2, where each unit cell contains two sc9 and two NA molecules, arranged in the typical tetrameric pattern D(18) $R_2^2(8)$ $R_2^2(8)$ $R_2^2(8)$, which form extended lamellas through interdigitation of the alkyl chains.

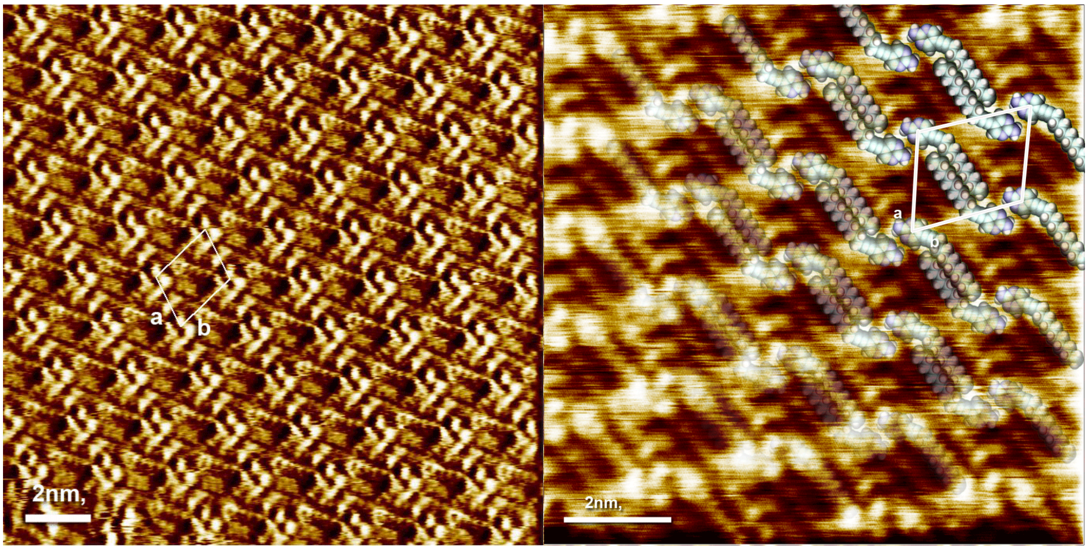

Figure 3: a) Small scale STM current image of sc9 +nonanoic acid at the solid-liquid interface; b) Proposed CPK model. The other contrast features are likely due to the coadsorbed nonanoic acid. Tunneling parameters: Average tunneling current (It) = 10pA, tip bias voltage (Vt) = 350 mV.

The use of other concentrations and solvents, (10, 1mM, 100, 10μM in NA and 100, 10, 1mM 100, 10μM in octanoic and heptanoic acid) did not display any self-assembled structures.

Observations:

Sc9 molecules were found to self-assemble into lamellar structures at the solid-liquid interface only if co-precipitated with NA. NMR experiments will need to be done in order to verify whether there is an HB dimer,[6] as expected, or whether it has dehydrated to an amide. Within the lamellae the molecules are physisorbed flat on the surface. The entire supramolecular architecture is stabilized by interdigitated alkyl side chains from adjacent Sc9-NA dimers.

The absence of an ordered structure with shorter carboxylic acids is somewhat surprising. It may be due to two different reasons: the difference in length of the alkyl chains which don't allows for optimal interdigitation, or the fact that the dimer don't reach a critical adsorption energy. To verify which is the dominant effect, we have designed a series of simulations, to be further tested experimentally. The experiments are best illustrated by the two matrices in Figure 4. In the case in which the SAMs are observed for the grey area in Figure 4a, the major contribution to the adsorption would be due to the number of methylene units in the alkyl chain. Whereas, with a behavior similar to Figure 4b the reason for the formation of SAMs will reside in the difference in length, actually hindering an optimal interdigitation. However, experiments have to be postponed until the requested molecules are synthesized.

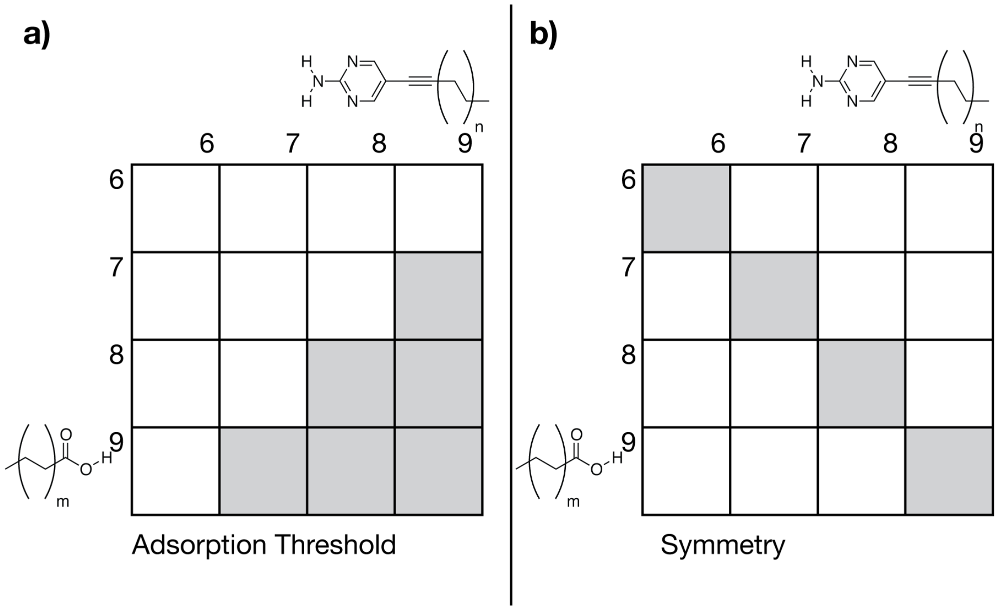

Figure 4: The presence or absence of a SAM of coadsorbed SC and carboxylic acids may relate to two different factors, the necessity to surpass a threshold (in methylene segments) for the adsorption, or due to the symmetry of the two interdigitating moieties.

The adsorption energies of all of the combinations of alkyl chain lengths have been computed via Molecular Dynamics simulation, using CHARMM and MMFF94 force fields, and are reported in Figure 5. In each run a dimer was placed at 5Å from a graphene slab, was minimized using 10000steps of Steepest Descent (SD) algorithm, and subsequently further minimized with 1000 steps of Adopted Basis Newton Rapson (ABNR). After evaluation of the energy, the dimer was raised from the surface by 10nm to calculate the value of the energy of desorption (given by the difference between the two states).

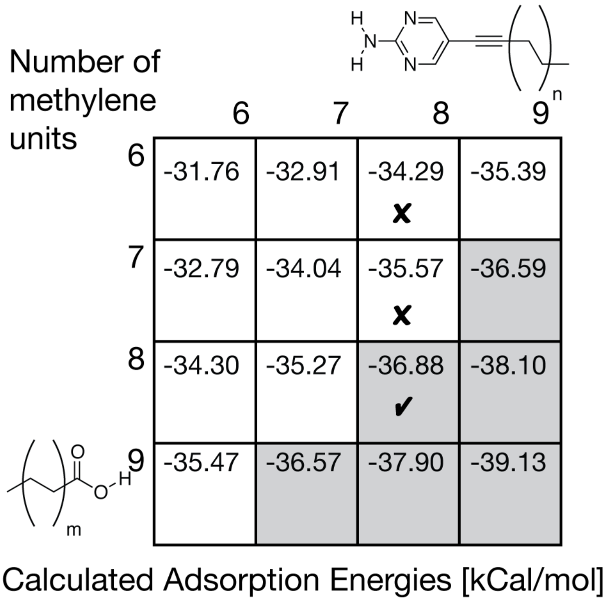

Number of methylene units	6	7	8	9
6	-31.76	-32.91	-34.29 ✗	-35.39
7	-32.79	-34.04	-35.57 ✗	-36.59
8	-34.30	-35.27	-36.88 ✓	-38.10
9	-35.47	-36.57	-37.90	-39.13

Calculated Adsorption Energies [kCal/mol]

Figure 5: Calculated adsorption energies per number of methylene units in the carboxylic acid (rows) and in the 2-pyrimidin-amine derivative (columns). The cell 8,8 corresponds to the dissolution of SC9 in NA. The marks correspond to the observation of a SAM. All the experiments were performed at 1mM concentration.

We calculate a minimal difference between the experimental cases of SC9 + NA (cell 8-8 in the matrix) and the other values. The difference between the adsorption energies in NA and OA is ca 1.3 kCal/mol.

We can conclude that:

1) the SC9 chain is too short to form SAMs without coprecipitation.
2) The length of the associated carboxylic acid chain must be at least 9 methylene units.
3) The system is not optimal for the study of the competition between interdigitation and hydrogen bonds.

However, we can suggest that the study of the combinatorial assembly with long-chain carboxylic acids as a possible direction for further investigation. In this frame it will be necessary to functionalize the 2-amino-pyridine molecule with different alkyl chain lengths and test the different conditions. Szabelski, De Feyter et al, have done a fascinating study of the effect on the phase separation of triangulenes due to different length of the alkyl substituents. We expect remarkable differences in this case due to I) different symmetry, II) the presence of hydrogen bonds, and III) the presence of what appears to be an "adsorption threshold".

Sc10

The molecules were dissolved in TCB with an approximate concentration of 2mM and diluted to the concentrations reported in Table 1. Use of other solvents, i.e. 1-phenyloctane and tetradecane, did not lead to the formation of ordered monolayers. In 1-nonanoic acid, formed very unstable lamellas with a double contrast pattern, which are probably due to coadsorption; the investigation of such pattern is deferred to the next section.

Solvent	*Concentration*
TCB	2mM, **1mM**, 666uM, 500uM, 333uM, 100uM, 10uM
PO	50mM, 10mM, 1mM, 100uM
NA	1mM
TD	1mM

Table 2: Experimental conditions tested.

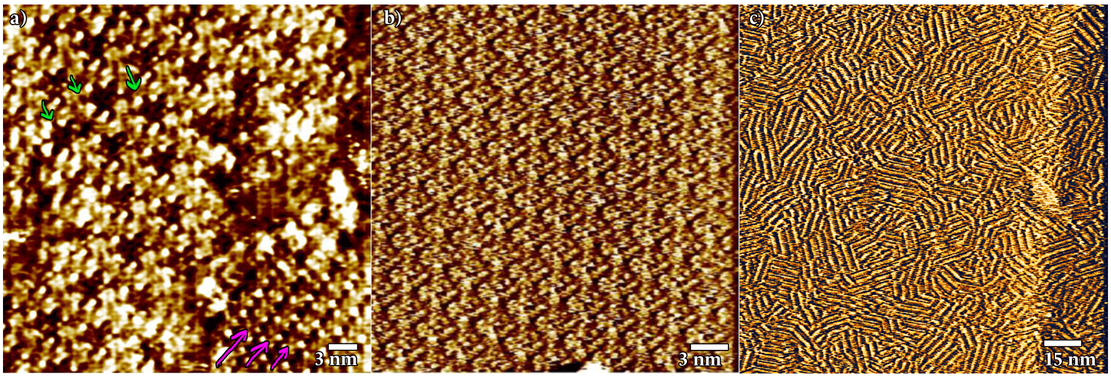

Figure 6: (a,b,c) Current images of the SC10 building block showing the different structures observed: a) coexistence of hexagonal porous phases (green arrows) and lamellar (purple arrows) phases; b) hexagonal close packed c) survey of the lamellar structure after addition of $PdCl_2$.

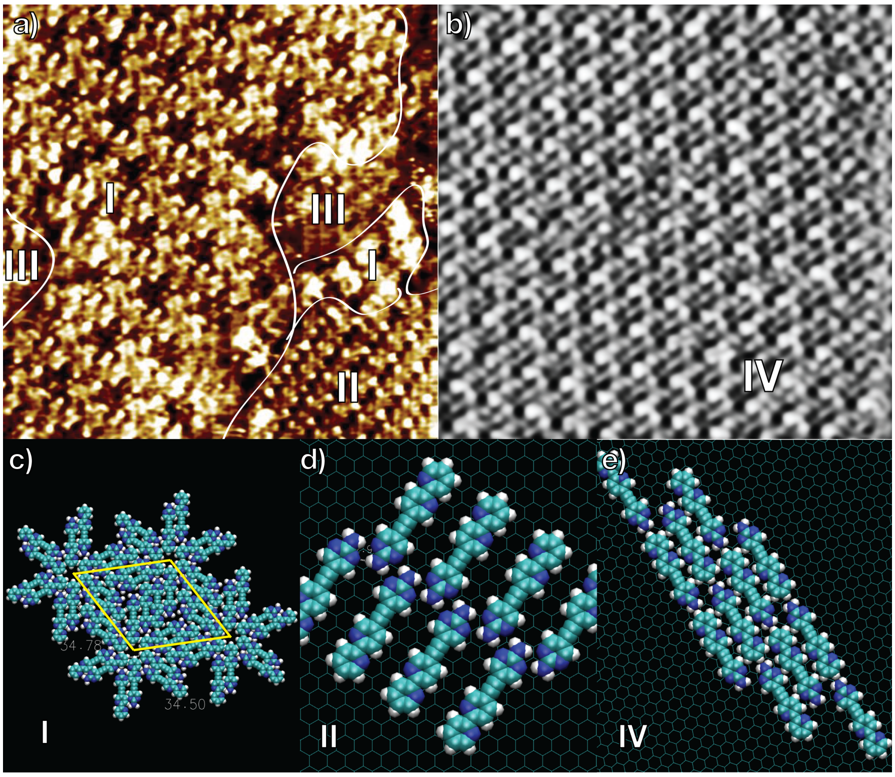

Figure 7: a,b) Polymorphism of the **SC10** building block, c,d,e) suggested packing motifs of the respective polymorphs.

The solubility of SC10 in phenyloctane is remarkably high: even at the highest concentration tested, (50mM!) no adsorbed layers were observed. SC10 deposited from TCB solutions displayed an amorphous phase under all of the concentrations tested, suggesting the potential presence of impurities, which were not visible using ^{1}H-NMR spectroscopy. Another purification was therefore executed, and subsequently an ordered assembly was observed. Such observations were only possible in the 24h immediately following the purification, suggesting that SC10 is susceptible to air/moisture or is somehow degrading, and should purified before use. In the purified samples, three different phases were detected, one porous hexagonal polymorph and a lamellar pattern, domains I and II respectively, in Figure 7a, immersed in a matrix of the glassy amorphous phase III.

After further purification, only the polymorph IV was observed for 24h (Figure 7b). It presents a dense lamellar arrangement, with very extended domains, larger than 200nm^2, with a moderate concentration of 0D defects such as vacancies (Figure 8).

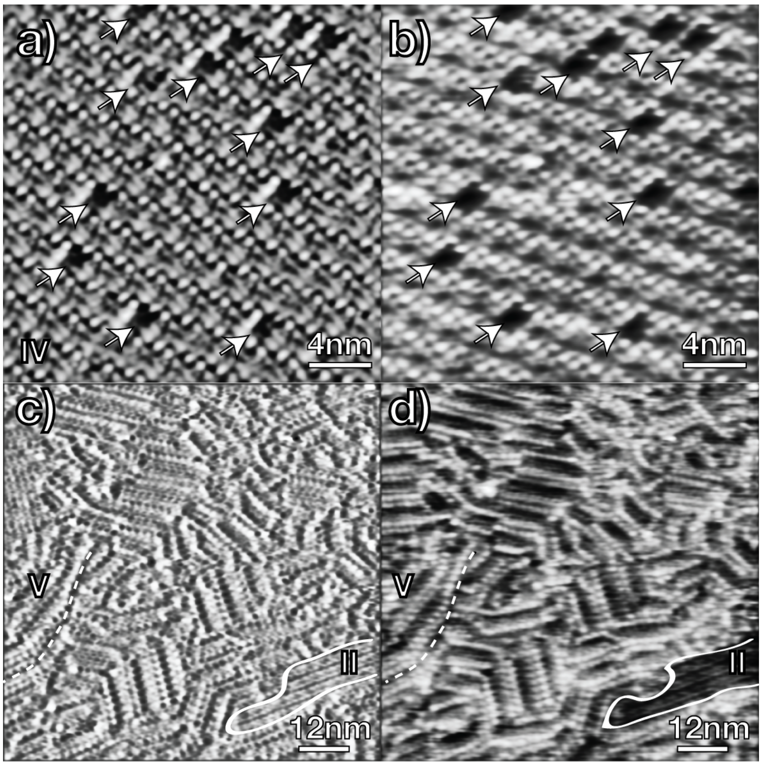

Figure 8: a,b) Current and height images highlighting of the vacancies in polymorph IV; c,d) After in situ addition of PdCl2 the small domains of polymorph V cover almost all of the surface, except for the small domain of II enclosed by a continuous line; the dashed line is an aid to the eye to follow one bended lamellar feature.

I	II	IV	V
3.4 ±0.2	1.5±0.2	2.7 ±0.2	3.2 ±0.2
3.5±0.2	0.8±0.2	2.9±0.2	0.9 ±0.2
61±2	72±2	64 ± 2	75 ±2
10.4±0.9	1.1±0.3	7.0±0.7	2.8 ±0.6

Table 3: Unit cells of the various phases

Upon addition of $PdCl_2$ the lamellar structure V reported in Figure 6c, Figure 8c,d was always observed even for the unpurified solutions. It features a broad distribution of domains, with an average size of roughly $100nm^2$ (a typical example with highlighted domains and the grain statistics is shown in Figure 9) with the characteristic feature of being almost contiguous: the lamellae are not completely linear inside a domain, but are often bended to connect different domains (Figure 8c,d dashed line). For the first minutes after deposition *in-situ* of $PdCl_2$, lamellar domains of polymorph II are still present, as shown in the contoured area in Figure 8c,d. From the height image (Figure 8d) a remarkable difference in the height contrast is evident, suggesting a non-planar character for phase V. The size of the unit cell is almost double that of the one measured in phase II, suggesting a close similarity.

In order to calculate the grain distribution, the grain highlighting Watershed algorithm[7] in Gwyddion[8] (Location steps 18 drop size 4.51%, threshold 15px^2, segmentation steps=129, drop size 15.01%) has been used and the individual grains boundaries were eventually refined manually; The projected areas exported were subsequently analyzed using the 1D statistic toolbox of WaveMetrics IGOR Pro.

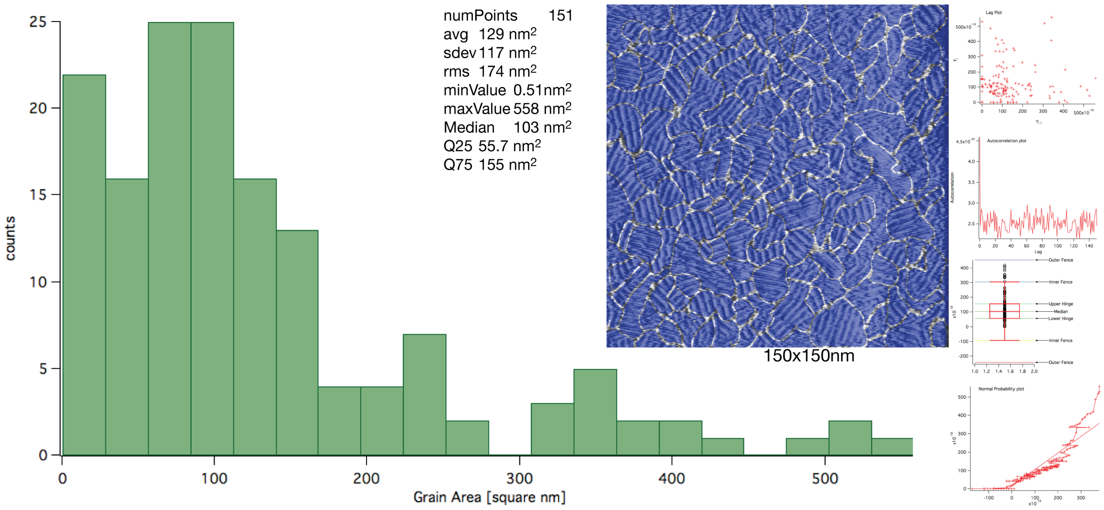

Figure 9: Typical grain distribution of the domain area after addition of PdCl$_2$.

Reverse switching:

Pd has a very high propensity to form cyanide complexes[9], therefore we could expect to shift the equilibrium by the addition of HOCN;

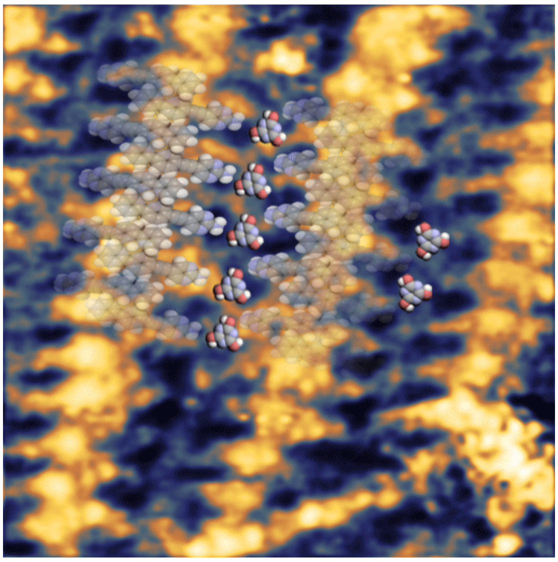

Figure 10: Proposed cpk model of the SC10$_2$-Pd complex, after coadsorption of HOCN.

However, the attempts (performed with *in-situ* addition of 4μL 1mM HOCN) showed the same pattern previously observed, but with a remarkable increase in the resolution. Such a difference can be attributed to the coadsorption of HOCN, which stabilizes the packing and reduces the thermal motion. See Figure 10 for the suggested packing motif.

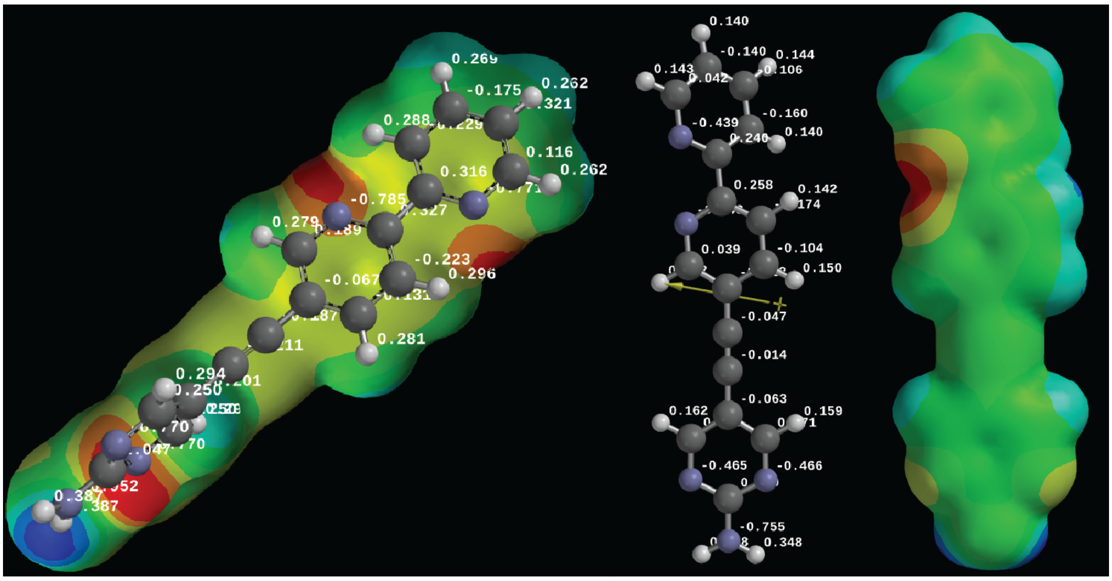

Figure 11: Electrostatic potential maps and charge distribution (Mulliken) of the two conformers, anti (a) and syn (b-c);

Observations and discussion:

Graph analysis[ii] of the different polymorphs, is useful to compare the crystallographic structures and hydrogen bonded networks that exist. Phases II and V, have a graph

---

[ii] The details of the notation are briefly summarized in the annexes, and can also be found in references [1, 3]

description of C(6)[R_2^2(8)], i.e. two hydrogen bonded 8 membered rings, and can form an infinite chain involving 6 atoms per unit cell. Polymorph IV has more complicated features, with a chain graph C(14), and three different rings: [R_2^2(28)] [R_2^2(10)] [R_2^2(8)] (considering the presence of hydrogen bonds between two adjacent bipyridines).

For structure I, the graph of the main ring motif can be resolved into six dimers, (D) and a ring [R_{12}^{12}(42)].

Conclusions:

The system is capable of switching after addition of $PdCl_2$, but the investigation is complicated by the polymorphism that is present. We believe that simpler building blocks are needed in order to fulfill the initial goals of this project. Substituting the 2-aminopirimidine for an isophtalic acid might be a better candidate to successfully unravel the mechanism of the competition between hydrogen bonding and metal-ligand coordination.

In any case, a more complete investigation with molecular simulations, that measure the energy of each polymorph and correlate it with the symmetry of the building block might be really interesting and rewarding and is left for future work.

Competition between multi-component hydrogen bonded patterns and metal coordination.

To investigate the competition and equilibrium of different hydrogen-bonded network in response to different stimuli, a 5μL drop of a 1mM solution of **SC10** was deposited on top of a freshly cleaved HOPG substrate. After imaging, 5μL of an HHTP 1mM solution (commercial, Alfa-Aesar) were added to the system.

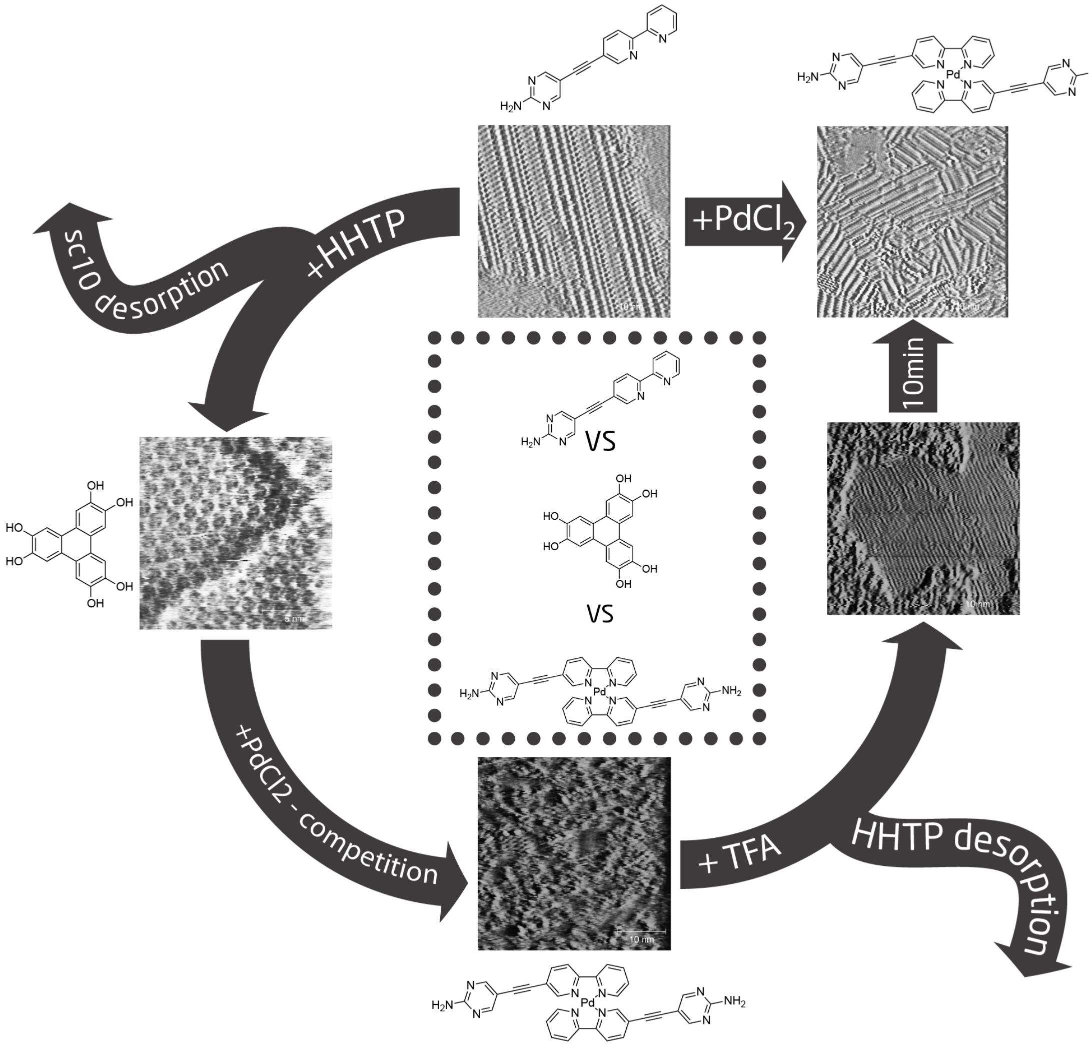

Figure 12**:** scheme reporting the series of modification and the stimuli associated to the variation of the self-assembly

Subsequent addition of $PdCl_2$ (Aldrich, 2.5μL,1mM) and TrifluoroAceticAcid (TFA, Aldrich, 10mM, 2.5μL) were performed in sequence, *in-situ*.

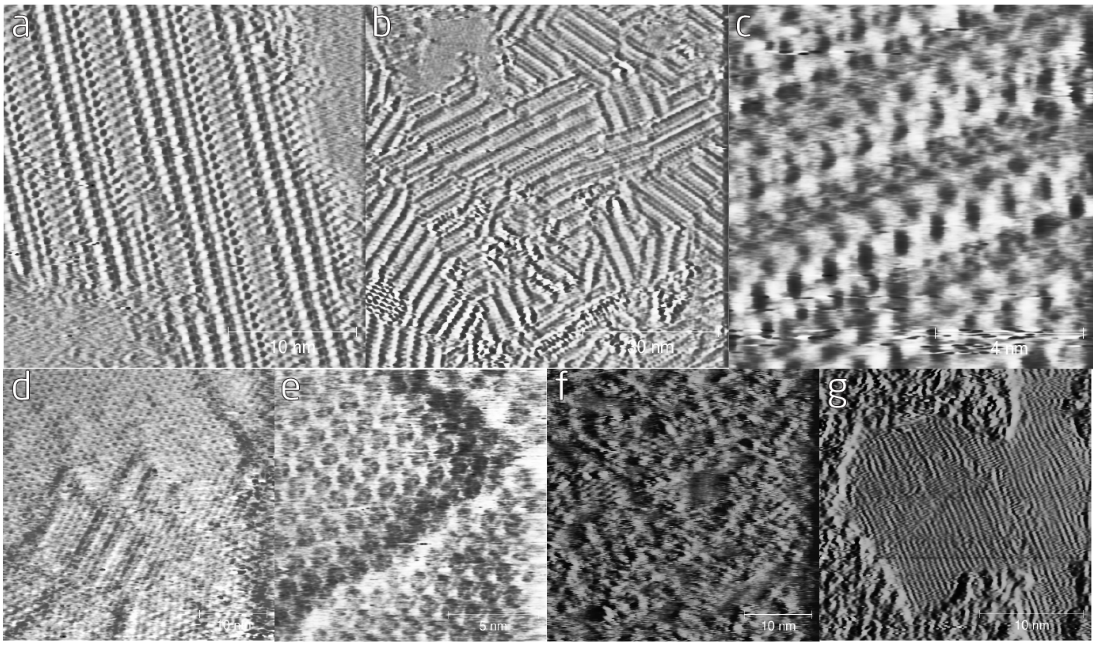

Figure 13: STM images of SC10 and hhtp physisorbed from nonanoic acid: a) sc10 as deposed; b,c) sc10+$PdCl_2$; d,e) hhtp; f) hhtp competing with $(sc10)_2Pd$; g) after the addition of TFA to destroy the hydrogen bonding pattern of HHTP;

The deposition of **SC10** on the HOPG surface produces small lamellar domains featuring a distinctive contrast along the lamella axis as shown in Figure 13a. Such a pattern is remarkably different from the one previously reported and is probably due to coadsorption of nonanoic acid[6]. As expected, after the addition of $PdCl_2$, all of the surface becomes covered in shorter, disordered lamellas with a differing contrasts, as shown in Figure 13b and c, comparable to that shown in the previous section. If HexaHydroxy-Tri-Phenylene (HHTP) is added to the pre-organized SC10 network, the latter desorbs and a full coverage of HHTP in a hexagonal pattern is achieved (Figure 13d,e). The HHTP packing presents a hexagonal motif with relatively small domains, with characteristic grain boundaries, similar in their resemblance (i.e. the difference in contrast) to those observed in SAMs of alkanethiols. In some experiments the typical depressions known as pits were also observed. The subsequent addition of $PdCl_2$ produces amorphous disordered assemblies on the surface, as shown in Figure 13f. Subsequent addition of TFA, induces the formation of lamellar domains (Figure 13g) which rearrange to the assembly shown in Figure 13b and c after ca. 10 minutes.

As showed in Figure 12, after the addition of HHTP to a pre-formed sc10 network, the latter desorbs and the former covers the entire surface. In this case the preferential adsorption of HHTP on the HOPG is evident. This preference might be reduced to give greater competition between the two species, upon the addition of palladium chloride. This means that the formation of a complex with the bypiridine moieties of **SC10** raises the affinity of **SC10** for the surface, to an adsorption energy value comparable to that of HHTP. In fact, if HHTP is present, the system shows no preference for any phase, and an amorphous network with small phase-segregated domains is formed. Subsequently, destroying the hydrogen bonded network via the addition of a competing acid, i.e. TFA, removes the HHTP, and after some time allows the formation of the palladium-**SC10** SAM.

The Pd complex shows a surprisingly higher affinity for the HOPG surface when compared to the simple ligand **SC10**. Focusing our attention to the geometry of such a complex, it is evident that Pd coordination could not be square-planar, due to the steric hindrance of the hydrogen connected to the bipyridine 3,3' positions, but is probably a distorted square-planar. Such coordination implies that the building block is not flat, and is probably distorted: it has been shown possible that two rings separated by a triple bond can have some conformational flexibility, therefore we expect a slight bending of the molecular backbone once physisorbed to i) maximize the interaction with the substrate, ii) minimize the steric hindrance between the bipyridine hydrogen.

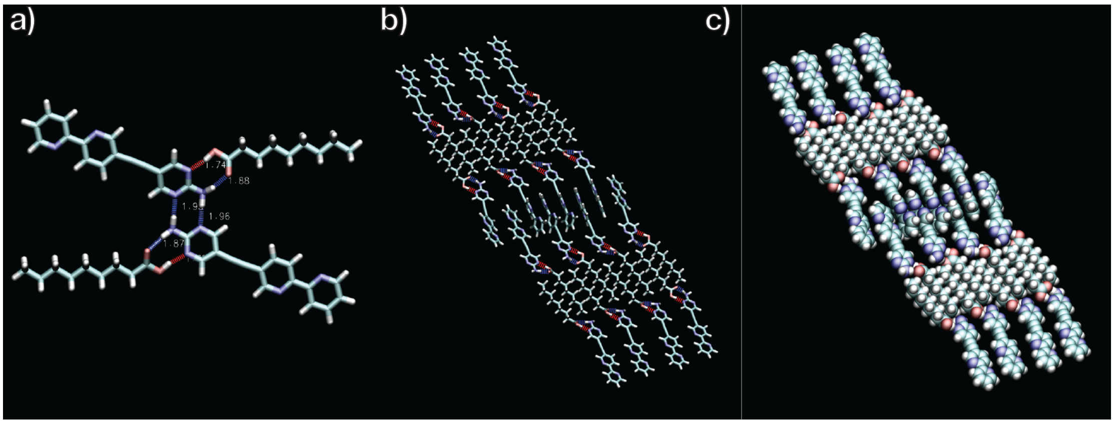

Figure 14 : The minimized structure of the hydrogen bonded dimer between SC10 and nonanoic acid after a steepest descent minimization of 10k steps. Note the presence of different [$R_2^2(8)$] motifs (highlighted in red and blue in a),b)), and the presence of a portion of the molecule which assembles edge-on; It is also surprising that in the center of the structure all of the pyridin nitrogens are pointing in the same direction.

Conclusions:

We have investigated the response of **SC10** in different environments and under a variety of stimuli, and we were able to set up a competitive environment to analyze the self-assembly of the synthon in a qualitative manner. However, we have to underline the fact

that during this work we found that **SC10** was not the optimal building-block for realizing the larger aims of this project, due to the presence of major drawbacks: i) the synthon degrades quickly, impeding our ability to undertake long experiments, and affecting the reproducibility of the measurements; and ii) **SC10** forms a number (>3) of different polymorphs, which complicate the analysis. Besides these problems, we can make a series of interesting remarks: **SC10** physisorption is promoted in long chain carboxylic-acid solvents, in a similar way to **SC9**, probably due to the coadsorption of the solvent. Physisorption is even more prominent in the presence of palladium chloride. Furthermore, the addition of HOCN further increased the stability of the physisorbed species, even if the high affinity of Pd towards the cyanides would have suggested a removal of the Pd from the bipyridines.
The response to the presence of a *competitor* for the adsorption such as HHTP is also interesting: the fact that complete desorption of **SC10** is observed upon addition of HHTP may be due to two main effects. These will be analyzed in more detail below.
We can assume that the adsorption of SC10+NA is described by the sum of two (four if considered separately) contributions, i.e. the free energy of adsorption (ΔGaSC10/NA), and the interaction energy, (or packing energy, ΔGp(SC10/NA)) which we can assume is the sum of all of the hydrogen bonds and other non-covalent interactions. So when we add HHTP, the observation of the complete desorption of **SC10** implies that:

$$\Delta Ga(SC10/NA) + \Delta Gp(SC10/NA) > \Delta Ga(HHTP) + \Delta Gp(HHTP)$$

This is likely the result of a combination of two factors: i) the presence of HHTP somehow hinders the interactions of **SC10** with NA, therefore reducing ΔGp(SC10/NA); or ii) the enthalpy of adsorption and the packing energy of HHTP are much larger than ΔGa(SC10/NA) since **SC10** has to desorb in order for HHTP to pack on the surface.
When palladium chloride is added to the same solution, we have *competition* for the adsorption. This means that the two terms are roughly equal:

$$\Delta Ga((SC10)_2 \cdot PdCl_2 \cdot NA) + \Delta Gp((SC10)_2 \cdot PdCl_2 \cdot NA) \simeq \Delta Ga(HHTP) + \Delta Gp(HHTP)$$

This is very interesting, as it tells us that the energy of formation of the metal-ligand interaction is roughly equal to the difference in the total free energy between HHTP and

SC10/NA alone. Following along those lines, we could develop a system of chemical inequalities, summarized in Figure 15.

$$\Delta G_{abs} = A; \qquad \Delta G_{pack} = P; \qquad \Delta G_{react} = R$$

$$\begin{cases} A_s + P_s > A_h + P_h \\ A_p + P_p \simeq A_h + P_h \\ A_s + P_s + R_p \simeq A_h + P_h \\ A_p + P_p < A_h \end{cases}$$

$$s = SC10/NA; \quad p = PdCl_2/SC10/NA; \quad h = HHTP;$$

Figure 15: System of relationships in the observed experiments.

The system has 7 variables and 4 equations, therefore is it not yet possible to solve. It should be possible to solve experimentally by selectively isolating the terms one by one, and numerically by evaluating the adsorption energies. For that it is necessary to calculate the absorption enthalpies of all the molecules involved. Enthalpies of adsorption can be obtained using other techniques such as isothermal titration calorimetry (ITC) or by studying the kinetics of the process via NMR spectroscopy, but they are yet to be performed. Therefore the solution of the system is deferred to future works.

It is impossible to comment with certainty about the Pd coordination with just the STM experiments, especially regarding the amount of distortion of the square planar coordination. Such information must be obtained from XRD experiments. It has also proven impossible to use our standard MD procedure to model the coordination geometry, due to the limitations of the MMFF force field, which is not designed to take into account the geometry of metal complexes. Suitable force fields do exist, but they aren’t appropriate for the computation of adsorption energies on graphene. To find a suitable technique, should be possible to develop an ad-hoc FF, but unfortunately this is beyond the scope of this work.

Even with all of those omissions, it is possible to develop a rough model. If we assume the presence of a dimer, the pattern formed is comprised of lamellas of wallpaper group P2, with each unit cell containing a dimer with C_2 symmetry. These dimers are connected *inter eos* by hydrogen bonding involving the pyrimidine nitrogen and the amine hydrogen.

References:

1. M. C. Etter, *Accounts Chem Res*, 1990, **23**, 120-126.
2. a) M. C. Etter and D. A. Adsmond, *J Chem Soc Chem Comm*, 1990, 589-591; b) M. C. Etter, D. A. Adsmond and D. Britton, *Acta Crystallographica Section C-Crystal Structure Communications*, 1990, **46**, 933-934.
3. M. C. Etter, J. C. Macdonald and J. Bernstein, *Acta Crystallogr B*, 1990, **46**, 256-262.
4. I. Stoll, R. Brodbeck, B. Neumann, H. G. Stammler and J. Mattay, *CrystEngComm*, 2009, **11**, 306-317.
5. Considerations on the reactivity of amines and carboxylic acids –

One of the most important reactions in polymer chemistry is the polycondensation between carboxylic acid derivatives and diamines. We need to demonstrate that a similar process does not occur in our system. It must be noted that the reaction is catalyzed by aromatic boronic acids, like the one used in this thesis, therefore the highest attention in cleaning everything has been devised. However, to the best of our knowledge, an amino dehydroxylation reaction featuring 2 aminopyrimidine has never been reported before, despite the well-documented coprecipitation of the two species.

6. a) G. He, S. Aitipamula, P. S. Chow and R. B. H. Tan, *Acta Crystallographica Section E-Structure Reports Online*, 2011, **67**, o552-o553; b) D. E. Lynch, T. Latif, G. Smith, K. A. Byriel and C. H. L. Kennard, *Journal of Chemical Crystallography*, 1997, **27**, 567-575; c) D. E. Lynch, M. Singh and S. Parsons, *Crystal engineering*, 2000, **3**, 71-79.
7. a) S. Beucher, in *International workshop on image processing, real-time edge and motion detection*, 1979; b) S. Beucher, *The morphological approach to segmentation: the watershed transformation*, 1993; c) M. Couprie, *Proc. of SPIE Vision Geometry V*, 1997, **3168**, 136-146; d) L. Najman, *Mathematical Morphology*, 1994, **38**, 99-112.
8. D. Necas and P. Klapetek, *Cent Eur J Phys*, 2012, **10**, 181-188.
9. a) R. Hancock and A. EVERS, *Inorganic Chemistry*, 1976, **15**, 995-996; b) J. Harrington, S. Jones and R. Hancock, *Inorganica Chimica Acta*, 2005, **358**, 4473-4480.

Chapter 3.4 porphyrin based tectons

Porphyrins are among the most technologically and biologically relevant molecules because of their exceptional opto-electronic properties, that make them important for technological applications in numerous fields of science and technology.[1] *In collaboration with Dr. F. Sguerra and Prof. W. Hosseini (Laboratoire de tectonique*
Moléculaire du solide, Université de Strasbourg), we have explored the capacity of tailored made porphyrins when combined with a suitable metal to form spatially extended (>100x100nm domains) mono-component bidimensional coordination networks. In particular we focused our attention to: i) unraveling the effect of the metal center in the porphyrin core on the packing in two dimensions, and ii) the formation of 2D networks featuring two different metals precisely organized. Dr. Sguerra synthesized and characterized spectroscopically the molecules. The details are reported in annex 4.

Porphyrin based tectons:

Objectives:

- Design and selection of suitable tectons
- Synthesis of the building blocks
- Physisorption of the ligand in different solvents, analysis of domains sizes and presence of polymorphism, or eventually solvatomorphysm
- Effect of complexation *in-situ* with Ag-Co-Cu-Pd
- Deposition from bulk complexation
- Mixed metals interactions - phase separation or substitution?
- Dynamic Switching of network architecture depending on the metal affinity.

Design and selection:

To realize the supramolecular network it is mandatory to properly control the geometry of the assembly. Successful synthesis of the desired framework relies then on the right choice of the building blocks. It should be designed to assemble in large polymeric arrays by virtue of their functionality and structure, exploiting different non-covalent bonds. New rules and strategies to implement the design of such system are produced almost on daily basis along the guidelines of *crystal engineering*, a discipline which according to

Desiraju, (one of the founders) aims at *"understanding intermolecular interactions in the context of crystal packing and the utilization of such understanding in the design of new solids with desired physical and chemical properties".*[2] In general such principles are meant for the growth of 3D crystalline phases, but clearly they can be adapted to tackle the 2D problem.

In parallel fashion, also the field of coordination polymers has experienced an extreme growth in the last few years, interpenetrating and intermixing on multiple levels with the crystal engineering into the design of the Metal-Organic Frameworks (MOFs).[3] In essence, we have today the opportunity to select the desired functional combination gathering from a vast know-how. We chose to exploit the well-known recognition between the terpyridine and pyridine around a square-planar coordinating metal, which has already been demonstrated capable of forming 2D self-assembled monolayers.[4]

The choice of the recognition group in position 1, 10 on the ring has been therefore straightforward.

However, the design of the porphyrin core has raised an optimization issue. It has been necessary to find a compromise between the "*simplicity* [1]" of the synthesis and the insertion in the two remaining meso position (i.e. 5, 15) of the porphyrin ring of two groups capable of promoting the physisorption. The new porphyrin derivatives (Molecules **1-3**), summarized in Figure 1, didn't produce any suitable bi-dimensional network on a surface, but have been proven capable of forming a coordination polymers via XRD. The inability to form a physisorbed monolayer is likely due to the presence of tosyl groups. Those (the tosylates) are forced by steric hindrance between the methyls and the porphyrin ring to adopt a conformation orthogonal to the porphyrin core. From such conformation there are two likely scenarios after physisorption on flat solid surfaces: i) if the molecule is rigid it reduces the surface contacting the HOPG; ii) if the molecule is somehow flexible it can force a distortion of the core to maximize the surface interaction. The necessity of deformation and/or the lack of contact, will heavily affect the energy of adsorption.

---

[1] With the term simplicity, we desire to summarize the combination of solubility, the number of steps involved, the complexity and yield of the purification procedure, and the availability of the starting materials.

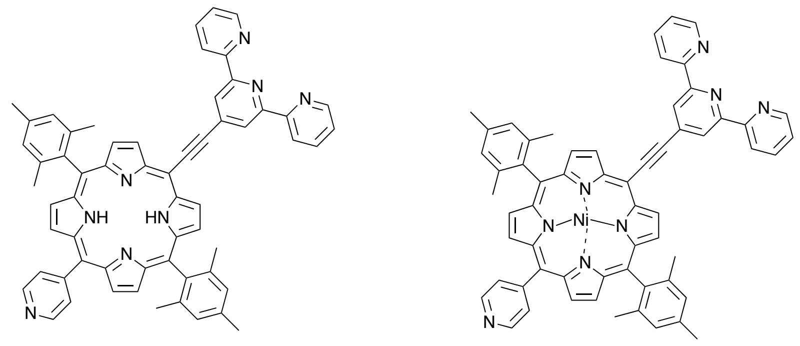

1 Chemical Formula: C60H46N8
Molecular Weight: 879.06

3 Chemical Formula: C60H44N8Ni
Molecular Weight: 935.74

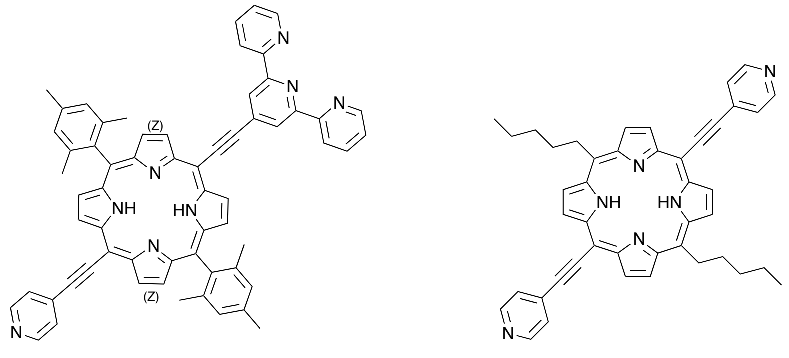

2 Chemical Formula: C62H46N8
Molecular Weight: 903.08

4 Chemical Formula: C44H40N6
Molecular Weight: 652.83

Figure 1 : Investigated molecules.

Being **4** the only molecules bearing alkyl chains in the periphery it will likely be the only one having enough affinity for HOPG. We believe this is the reason why the only system visualized on the graphite surface was **4**.

To confirm such intuition, the energy of adsorption of **1**,**3**,**4** on the graphite surface was computed using a MD simulation via CHARMM[5] and MMFF94[6]. The compound **2** contains Zn, which is not included in the MMFF94 force field, therefore could not be used in the calculations. The aromatic structure of the porphyrin ring is often troublesome to process using the *kekulization* algorithm of CHARMM, therefore a kekulé structure has been assigned manually in accord to Figure 1.

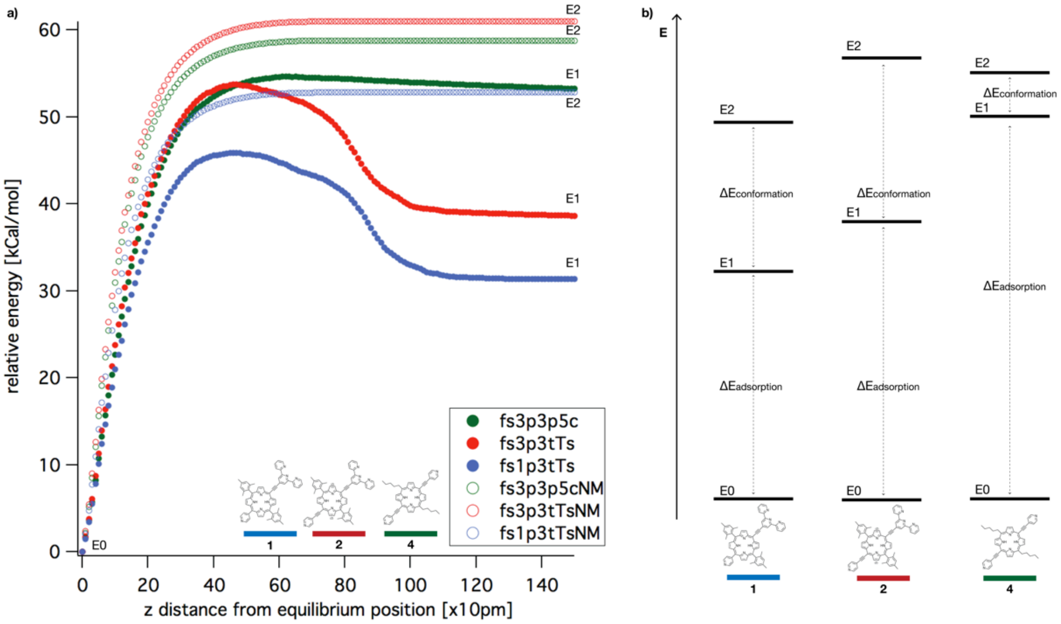

Figure 2: a) Energy profile for desorption of molecules **1**,**2** and **4**, in the first 1.5 nm from the equilibrium position on a graphene slab, following an equilibrium path, i.e. minimized after each step along z (full circles) compared to the pure desorption pathway for the surface minimized structure (empty circles). The Energy differences are reported in b).

Following the procedure developed by Bjork et al.[7] the molecules were deposed on a graphene slab, minimized with 20000 steps of steepest descent (SD) algorithm, and subsequently lifted from the surface to a distance of 20nm. The first 1.5 nm of the profile are shown in Figure 2-a. The molecules were raised from the surface with two different criteria: in one case, (filled curves in a) they were minimized after each step in the z direction, while in the other the same structure was simply raised from the surface without further minimization. Comparing the two curves for each molecule, is it possible to distinguish between the contribution of the adsorption and the one relative to the conformational changes. In Figure 2b such differences are sketched in an energy diagram. Is noteworthy to mention that molecules **1** and **2** undergo to a high conformational change during the adsorption on graphite.

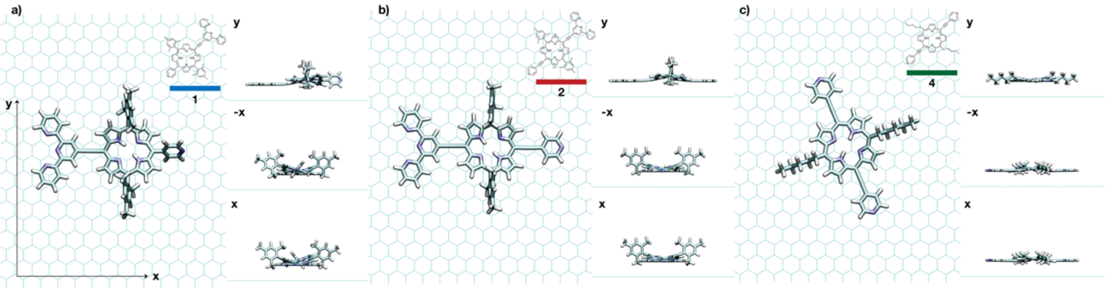

Figure 3: conformational minima (at E0) after adsorption on a graphene slab.

To evidence such conformational change, the physisorbed structures are shown in **Figure 3**. It is important to point out how the porphyrin core adopt a saddle configuration[8] due to the bending of the tosyl groups. The conformation of the terpyridine nitrogen is *syn-syn* on the surface.

The high conformational barrier, and the lower adsorption energy are a rational explanation for the absence of adsorbed phases for molecules **1** and **2**. The experimental details on the investigation of the compounds **1-4** (i.e. the experimental condition tested) are presented in Table 1.

Solvent	**Concentration**	**1**	**2**	**3**	**4**
TCB	1mM	x	x	x	x
	100uM	x	x	x	x
	10uM	x	x	x	x
TCB + sa	1mM		x		
	100uM		x		
PO	1mM	x	x	x	x
	100uM	x	x	x	x
PO + sa	1mM		x		x
NA	1mM	x	x	x	x
	100uM	x	x	x	x
	10uM	x	x	x	x
TD	1mM		x		x
+ CuTf or CuAc	1mM	x	x	x	x
	100uM		x		
+ CoCl2	1mM	x	x	x	x
+ PdCl2	1mM	x	x	x	x
+ AgTf	1mM		x		x
	sa = solubilization agent: IPA, Acetonitrile,Chloroform, DMSO …				

Table 1: experimental condition tested for the different molecules.

The final design choice was to substitute the tosyl groups with an alkyl chain. The compound **4** exhibit such a feature, and for this reason it has been investigated as a model system: The aim is to prove that 1) the core modifications allow formation of ordered SAMs, and 2) to test the reactivity toward different metals. Meanwhile, the asymmetrically functionalized building block possessing the terpyridine and the pyridine groups is being synthesized.

In the following section we will discuss the details of the adsorption of **4** and the modifications induced by *in-situ* and *ex-situ* addition of metals.

SAMs of 5,15-dipentyl-10,20-(pyridin-4-ylethynyl)porphyrin (4) and effect of addition of Cu – Co – Ag - Pd:

A 1mM solution of **4** in acetonitrile/phenyloctane 1:3 or 1-nonanoic acid was used in all the experiments. A drop of 4μL was then drop-casted on a freshly cleaved HOPG substrate. After observation of the SAM of 4 a drop of 1mM solution of metals was added directly on the surface in the *in-situ* experiments. The *ex-situ* experiments were performed by mixing 100μL of the two mother solutions, and after 1h depositing 4μL of the resulting solution.

metal salt	concentration [mM]	Solvent
AgTf	1	ipa/po 1:10
CuAc	1	CH_3CN/po 1:10
$PdCl_2$	1	ipa/po 1:10
$CoCl_2$	1	ipa/po 1:10
$CdCl_2$	1	ipa/po 1:10

Table 2: Metal salts used for complexation. Ipa=isopropyl alcohol, po=phenyloctane.

Neither color change nor any precipitate was observed during the mixing of the solutions for the *ex-situ* experiments.

1: self-assembly of tecton 4 pristine.

The deposition from a mixture of 1-phenyloctane/acetonitrile 1:1, and from 1-nonanoic acid produced the assemblies in **Figure 4**. The pattern presents two polymorphs: a linear phase (I) and a square motif(II).

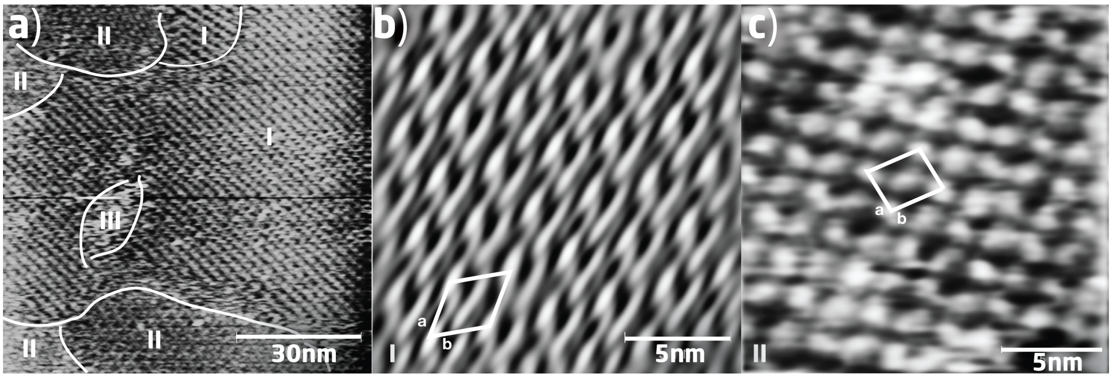

Figure 4: STM images of **4** self assembled at the nonanoic-acid/HOPG interface; a) survey current image; b) high-resolution height image of domain I, c) high resolution height image of domain II.

Sample	**1**	**2**	**3**	**4**	**5**	**6**
a (±0.2 nm)	1.8	1.8	1.8	1.8	2.8	2.1
b (±0.2 nm)	1.8	1.7	1.8	1.7	2.7	1.8
γ (±2°)	75	77	77	77	64	72
A (±0.5 nm^2)	3.2	3.1	3.2	3.1	6.9	3.5

Table 3: Unit cell parameters of polymorph II of molecule **4**, extracted from different STM images. For this and the next samples, the average values are summarized in Figure 16.

The repeating unit of domain I, showed in Figure 4b, is formed by two spots of ovoidal shape with a small hole of different contrast in the middle, with a slight misalignment between the features. In the filtered image in **Figure 4c** is reported a height image of the motif II, evidencing the square lattice.

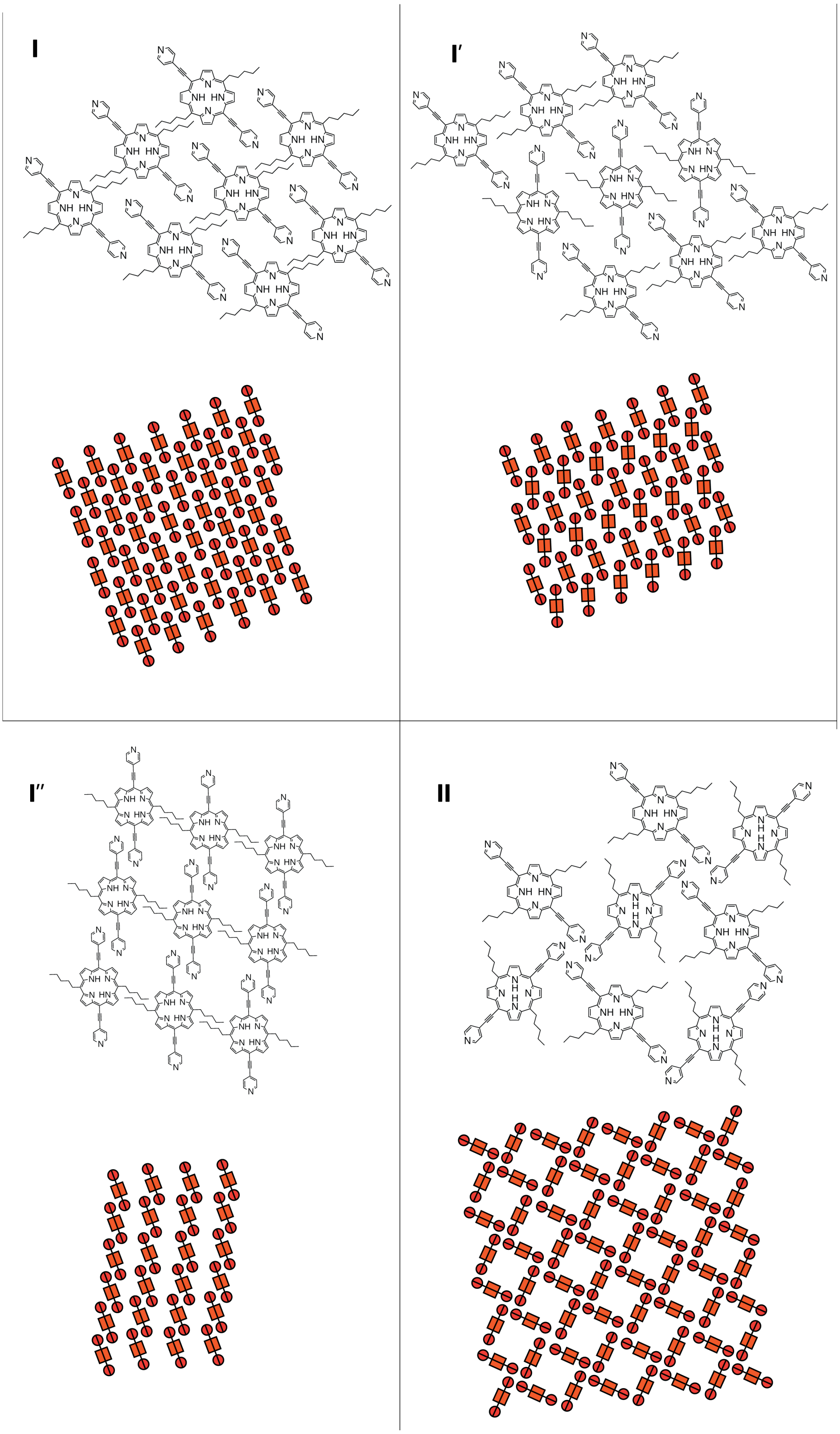

Figure 5: proposed packing models for the different polymorphs.

Two are the proposed models for the assembly (Figure 5), based on the following considerations: (I) is proposed in order to maximize the weak interdigitation of the alkyl chains, together with the surface filling factor. (I') has a little tilting between the layers in order to form two additional weak HB between the pyrrole hydrogen and the pyridine, despite some loss in the density of the assembly. Assembly (I") has again two weak HB per molecule in a non-tilted geometry. The pattern (II) proposes a network of weak hydrogen bonds, featuring again as acceptor the pyridine N, and as donors the *meta*-positions of the pyridine rings.

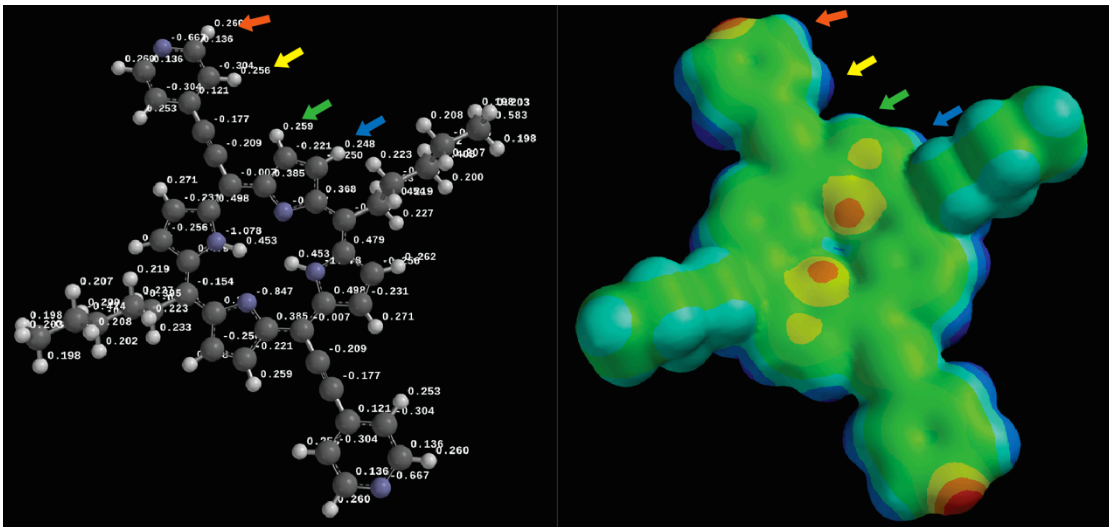

Figure 6: Ab-initio (RHF 321g*) calculated Mulliken charge distribution and electrostatic potential map. The colored arrows point to possible donors. Among them, the *most eligible donors* will satisfy two conditions: the hydrogen has to possess the higher partial positive charge and has to be connected to the higher negative partial charge. We can then identify as the most likely connecting point the hydrogen pointed by the yellow and the green arrows, as the donors, and the pyridine nitrogen as the acceptor.

Both of those assembly models are consistent with the calculated charge distribution (Figure 6), however for steric hindrance reasons and for the HB pattern angles, the most probable polymorphs are I" and II.

2: metal coordination

2.1: AgTf

After *in-situ* addition of one equivalent of Silver Triflate (Aldrich) the previously formed self-assembled monolayer of **4** desorbed. After ca. 15' only unstable lamellar features as in **Figure 7** were observed. The deposition of a solution where the mixing of the metal and the ligand was executed *ex-situ* at room temperature, provided the lamellar assembly that can be observed in **Figure 7**b-c.

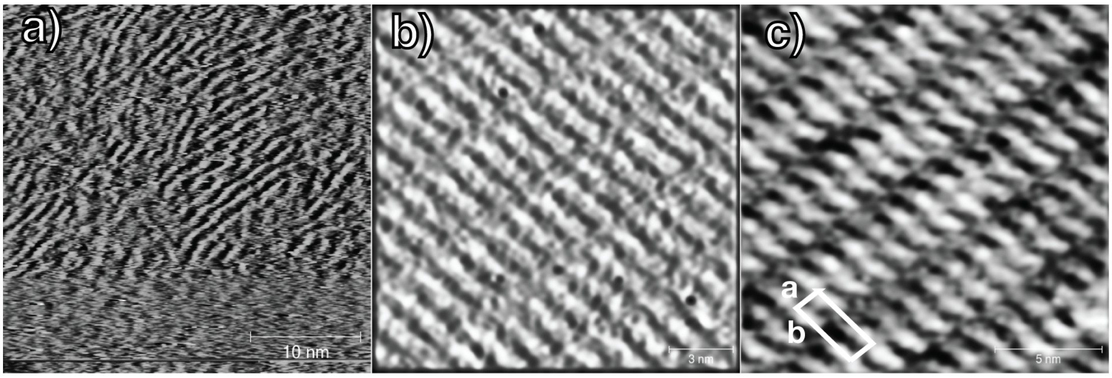

Figure 7: a) current image of the modified assembly of **4** after addition of 1eq of AgTf; b,c) current and height close up images after the deposition of a 1:1 solution of AgTf and **4**.

Sample	1	2	3	4
a (±0.2 nm)	2.5	3.6	3.6	3.6
b (±0.2 nm)	1.8	1.3	1.3	1.3
γ (±2°)	83	82	83	82
A (±0.5 nm^2)	4.4	4.7	4.7	4.7

Table 4: Unit cell parameters of the porphyrin derivative **4**+AgTf obtained from the STM images for the *ex-situ* samples.

The unit cell parameters are compatible to a possible edge on conformation on the surface, but the resolution of the image is not sufficient to unequivocally discern such behavior.

2.2: CuAc

With the *in-situ* deposition of 1eq. of copper acetate, we noticed a sudden improvement of the resolution. No desorption of the previous formed layer was observed. The resulting assembly is shown in Figure 8 and in Figure 9, the stability of such assembly and the dimensions of the domains were notably increased, with dimensions larger than 100 x 100 nm and more than hours of stability.

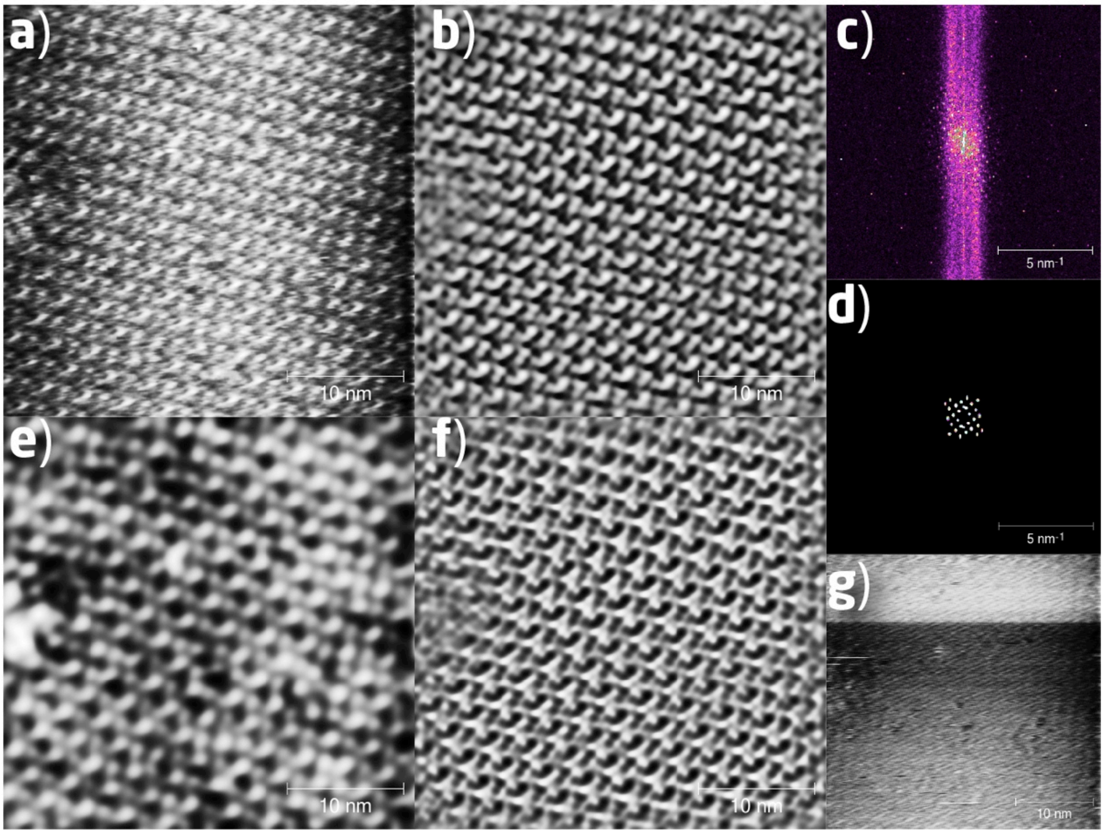

Figure 8: STM height image and filtering. *In-situ* experiment a) raw image; b)FFT filtered, c,d,g)FFT,filter,and difference; e) CWT Filtered[9] (Gaussian wavelets 10px); f) inverted b) image. I_t=20pA, -520mV.

Sample	**1**	**2**	**3**	**4**
a (±0.2 nm)	2.8	1.9	1.9	1.7
b (±0.2 nm)	1.7	1.6	1.6	1.9
γ (±2°)	45	88	87	82
A (±0.5 nm^2)	3.2	2.9	2.9	3.2

Table 5: 4 + CuAc (bulk) unit cell parameters

In Figure 8, the raw and filtered images are reported, to show the effect of the filtering. FFT filtering has the misleading effect of enhancing triangular features (in Figure 8c,f) which are due to the empty spaces between the adsorbed species, as shown by the application of Continuous Wavelet Transform (CWT)[9] filter in Figure 8e. The pattern generated by *ex-situ* deposition still exhibits two polymorphs, as shown in Figure 9. The two seems to possess the same periodicity, but have evident different contrast features. The upper "domain" presents a brighter spot in the center, which may be ascribed to the presence of a coordinated metal in the domain II.

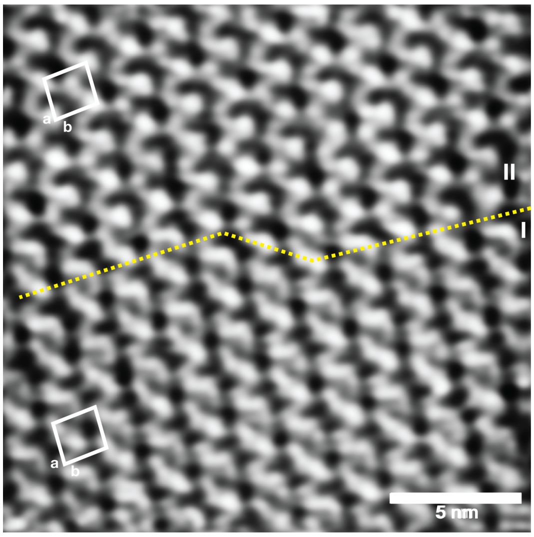

Figure 9 : STM height images of the packing observed during the *ex-situ* experiment.

2.3: $PdCl_2$

The *in-situ* addition of $PdCl_2$ induced desorption and formation of multiple small domains, with a square lattice. The deposition *ex-situ* showed full-coverage of big size (more than $100 nm^2$) domains with a correspondent square lattice. The differences between the current and height images are remarkable, as shown Figure 11a,c. The current image (Figure 11a) presents long periodically modulated continuous linear features, whereas the height image exhibits a square centered motif (similar to the number 5 in a dice). Such effect can be eventually due to continuous conjugation along the stripes: it can be a surface state of the material. Such interesting effect is still under investigation.

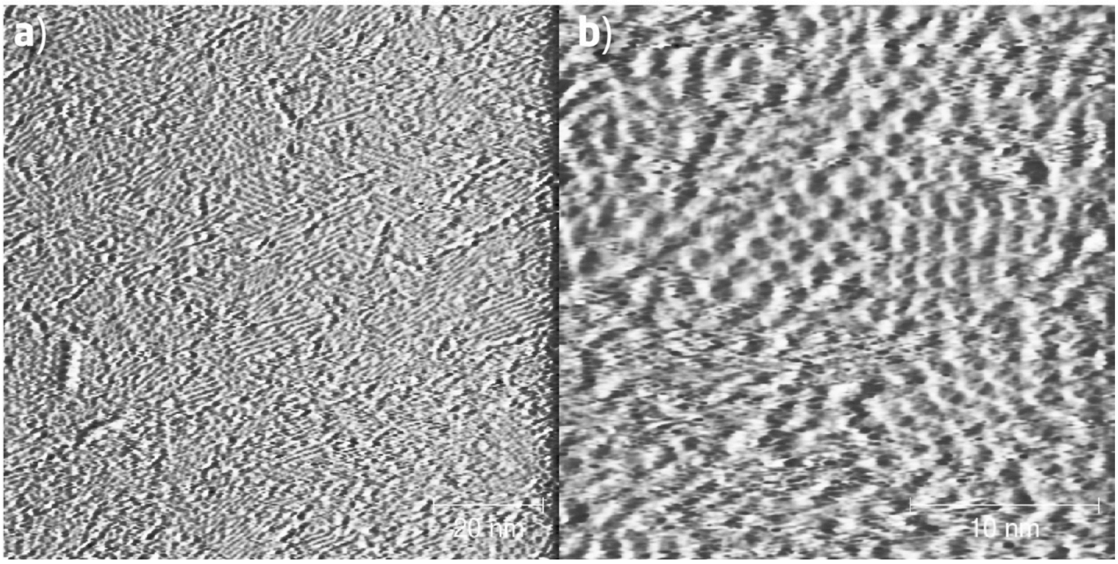

Figure 10: Survey and close up STM images acquired during in the *in-situ* experiment. Note the high concentration of small domains.

Sample	1	2	3	4	5	6	7	8
a (±0.2 nm)	2.9	1.9	1.8	1.9	1.9	1.9	1.8	1.9
b (±0.2 nm)	2.4	1.7	1.7	1.6	1.8	1.8	1.8	1.8
γ (±2°)	85	88	87	84	76	76	78	76
A (±0.5 nm^2)	6.7	3.3	3.1	3.1	3.2	3.2	3.2	3.2

Table 6: Unit cell parameters of the modified assembly of **4** after addition of palladium chloride.

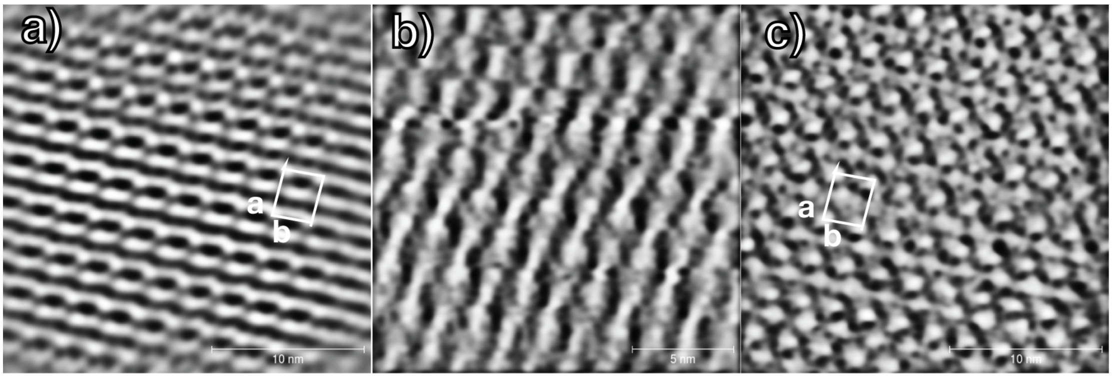

Figure 11: Deposition *ex-situ*. a) STM current and c) height image of a domain of type II, b) height close up image of a domain of type I.

The different behaviors between the two methods of deposition suggest that a role is played by the pyridine complexation. It seems, that with the *in-situ* addition the coordination of the pyridine is favored: with simple kinetic considerations, it is not surprising the possibility to bind in a labile way with the Pd, causing desorption of the structure. After time, and from the *ex-situ* deposition, as expected from chelate[10] and macrocycle effects,[11] the thermodynamic equilibrium is reached: i.e. with the metal coordinated inside the porphyrin core.

2.4: $CoCl_2$

The addition of Cobalt chloride showed the formation of a characteristic packing, with unit cell comparable to the ones previously observed for the porphyrin alone and for the other metals.

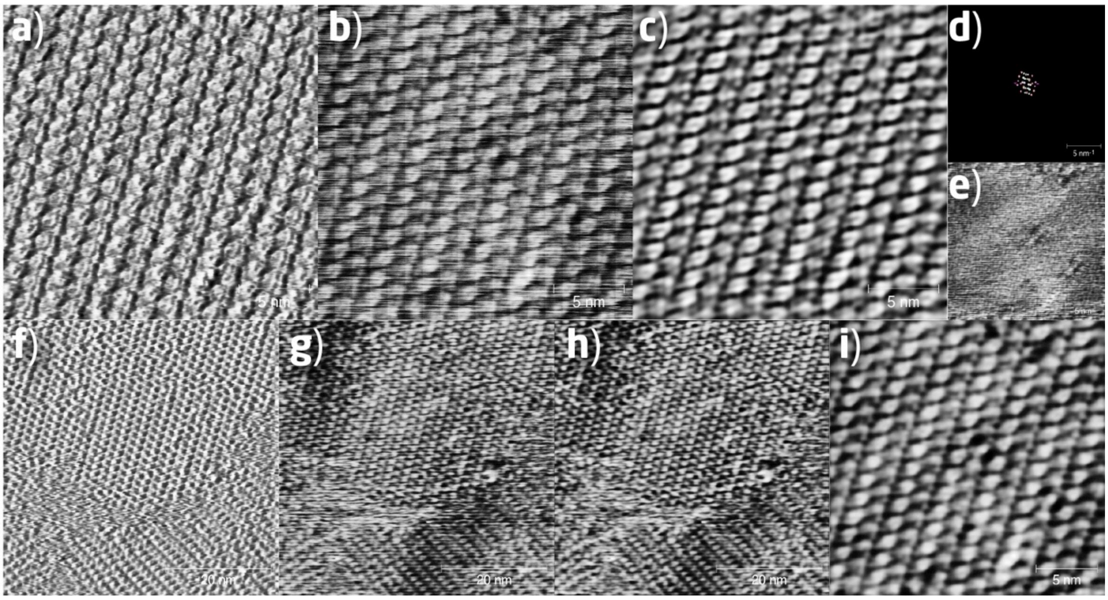

Figure 12: Cobalt chloride modified assembly of **4**. a,b) current and height images, c) FFT filtered height , d)FFT selected peaks and e) image difference. f,g,h) surveys f)current, g,h) raw and filtered height surveys. i) presents the result of the application of a CWT (gaussian 4px) filter on image b).

Sample	**1**	**2**	**3**	**4**	**5**	**6**
a (±0.2 nm)	2.7	2.4	2.1	1.8	2.1	1.7
b (±0.2 nm)	2.2	2.3	1.8	1.8	1.8	1.8
γ (±2°)	89	45	80	75	52	76
A (±0.5 nm^2)	6.1	4.0	3.6	3.1	3.0	3.1

Table 7: Unit cell parameters of the self-assembled monolayer of **4** after addition of $CoCl_2$. The unit cells in samples 1 were calculated considering the differences in contrast, whereas 2-6 considers just for adjacent spots.

The main difference is shown in figure 12: there's the presence of a distinctive contrast motif along the lamellas. Such difference is most likely due to Moiré's patterns, however it's absence in the *ex-situ* experiments is somehow puzzling. One possible explanation is the selective filling of half of the porphyrin cores, which is however entropically unlikely. Since the unit cells are almost identical, such effect has to be investigated further.

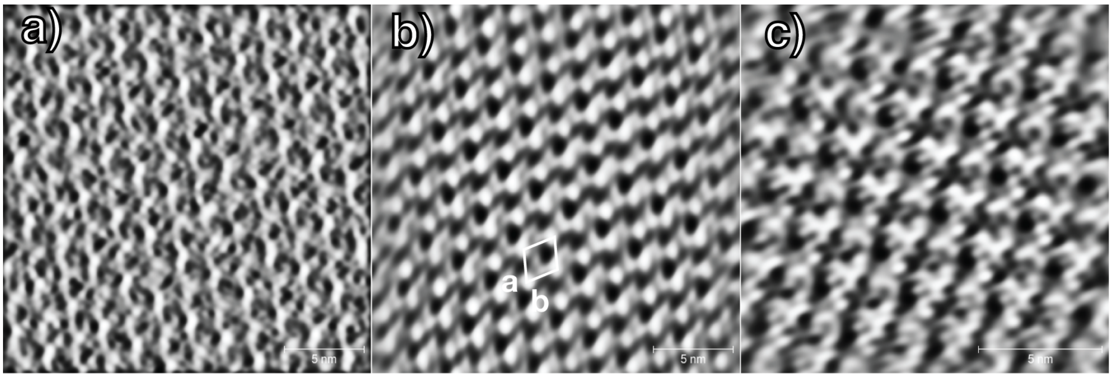

Figure 13: a, b) STM current and heigh images of the motif formed after *ex-situ* deposition. In c) is showed a FFT filtered close up (current).

Conclusions:

We have successfully observed the formation of self-assembled structure of **4** at the nonanoic acid/HOPG interface, and modified such structures with the addition of different metals, both *in* and *ex-situ*. The system has shown to be capable to responds to the addition, either via a change in the packing motif, or with a change in the contrast. A change in the architecture clearly suggest a different polymorph, and a more dramatic interaction between the metal and the tecton. The modification in the contrast and the unit cell parameters (which are left almost identical) on the other side suggest that the metal is complexed inside the porphyrin ring.

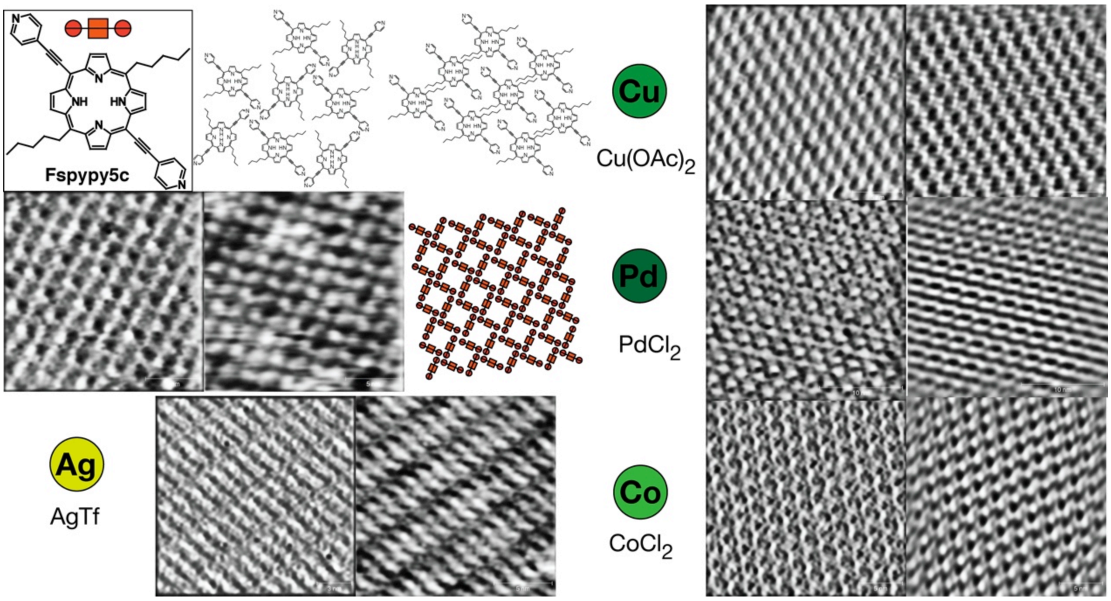

Figure 14: Comparison of the various assemblies observed after deposition of 4 after addition of the metals *ex-situ*.

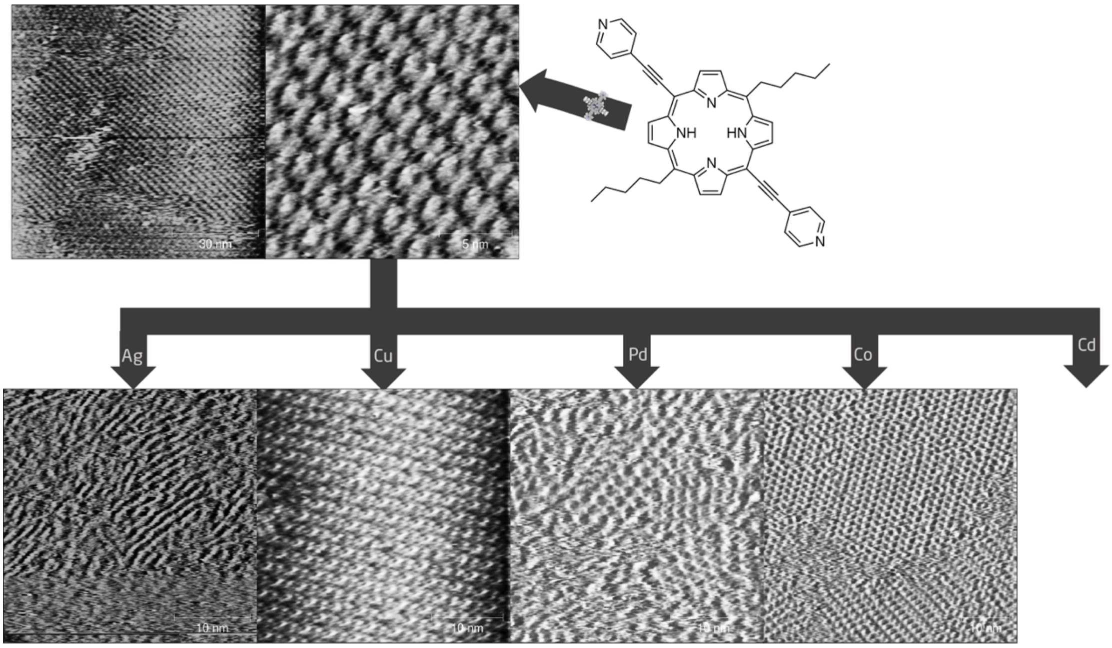

Figure 15: different networks (*in-situ* addition of metal)

The metals Pd, Cu, and Co are reported in literature as being able to "enter" in the porphyrin ring.

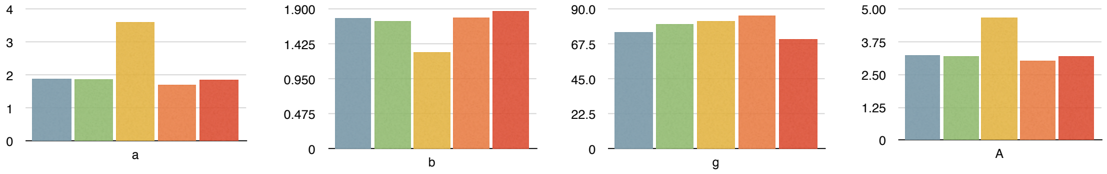

unit cells comparison

	no metal	pd	ag	cu	co
a	1.9 ± 0.1	1.88 ± 0.04	3.602 ± 0.004	1.7 ± 0.1	1.9 ± 0.1
b	1.78 ± 0.03	1.74 ± 0.06	1.312 ± 0.004	1.8 ± 0.2	1.9 ± 0.2
g	75 ± 2	80 ± 4	82.2 ± 0.6	86 ± 2	71 ± 11
A	3.2 ± 0.2	3.20 ± 0.07	4.681 ± 0.008	3.0 ± 0.1	3.2 ± 0.2

Figure 16: Unit cell comparison. – the reported errors are the standard deviations from the average: the standard instrumental error are ±0.2 nm on the a and b determination, ±2 degrees on the angle which sums in ca ±0.5nm^2 on the area.

The differences in the unit cells, suggests accordingly that only the Ag is coordinated by the pyridine, whereas in the other cases the metal get complexed inside the porphyrin ring.

Only two of the tested metals are part of the Irwing-Williams series,[12] i.e. Cobalt and Copper, therefore even though the concentration of defects in those two cases is inversely proportional to the stability of the complex, we could not conclude unequivocally that there's a correlation.

It will be interesting to try to mix different metals, both in bulk and on the surface, in order to I) have eventually a displacement/change in assembly, II) make a double metal pattern: for this, mixing the Ag with one of the other will be the most straightforward experiment. However so far, the test performed with the addition of Pd to a previously Ag modified motif showed that the growth of 3D object is activated, together with instantaneous desorption of the previously assembled architecture.

Addition of a second metal on top of a pre-formed silver SAM has lead to formation of tridimensional structures.

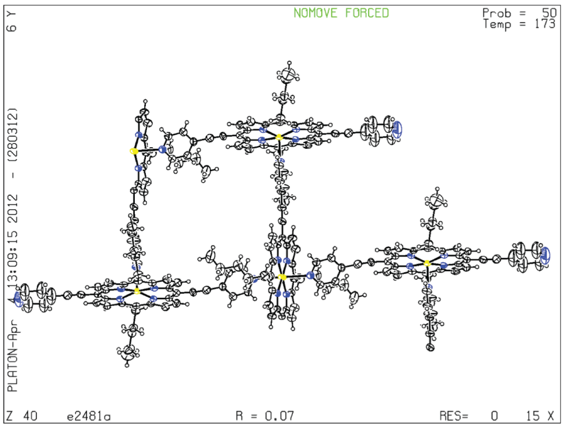

```
Bond precision:   C-C = 0.0064 A          Wavelength=0.71073

Cell:            a=16.9317(4)    b=22.6719(5)      c=16.9189(3)
                 alpha=90        beta=114.776(1)   gamma=90
Temperature:     173 K

                 Calculated                   Reported
Volume           5896.9(2)                    5896.9(2)
Space group      P 21/c                       ?
Hall group       -P 2ybc                      ?
Moiety formula   C132 H114 N18 Zn3            ?
Sum formula      C132 H114 N18 Zn3            C132 H114 N18 Zn3
Mr               2148.59                      2148.52
Dx,g cm-3        1.210                        1.210
Z                2                            2
Mu (mm-1)        0.662                        0.662
F000             2244.0                       2244.0
F000'            2246.31
h,k,lmax         23,31,23                     23,31,23
Nref             16885                        16282
Tmin,Tmax        0.938,0.955                  0.925,0.955
Tmin'            0.924

Correction method= MULTI-SCAN

Data completeness= 0.964          Theta(max)= 29.800

R(reflections)= 0.0661( 8016)     wR2(reflections)= 0.1883( 16282)

S = 1.038                  Npar= 664
```

Figure 17: XRD structure and parameters of the Zn metalated molecule **4**.

The activation of a tri-dimensional growth mode, is not fortuitous considering the connectivity of the building block: in presence of an octahedral complex inside the porphyrin core, it is likely to have the pyridine to coordinate M in the axial position (see xrd in figure 17 for the Zn metallated **4** and as a further example the closely related compound studied by Krupitsky et al.[13]). Such observation however suggest that the silver is replaced by the metal inside the cavity, which is somehow surprising, and must be investigated more thoughtfully: it is compatible with the observed desorption but is unforeseen since the 3D crystallization don't occurs when just one metal is added.

1. M. Jurow, A. E. Schuckman, J. D. Batteas and C. M. Drain, *Coordin Chem Rev*, 2010, **254**, 2297-2310.
2. G. R. Desiraju, *Crystal Engineering. The Design of Organic Solids*, Elsevier, Amsterdam, 1989.
3. J. J. Perry, J. A. Perman and M. J. Zaworotko, *Chem Soc Rev*, 2009, **38**, 1400-1417.
4. a) A. Ciesielski, L. Piot, P. Samorì, A. Jouaiti and M. W. Hosseini, *Adv. Mater.*, 2009, **21**, 1131-1136; b) A. Ciesielski, G. Schaeffer, A. Petitjean, J. M. Lehn and P. Samorì, *Angew. Chem. Int. Ed.*, 2009, **48**, 2039-2043.
5. B. R. Brooks, C. L. B. III, A. D. M. Jr, L. Nilsson, R. J. Petrella, B. Roux, Y. Won, G. Archontis, C. Bartels, S. Boresch, A. Caflisch, L. Caves, Q. Cui, A. R. Dinner, M. Feig, S. Fischer, J. Gao, M. Hodoscek, W. Im, K. Kuczera, T. Lazaridis, J. Ma, V. Ovchinnikov, E. Paci, R. W. Pastor, C. B. Post, J. Z. Pu, M. Schaefer, B. Tidor, R. M. Venable, H. L. Woodcock, X. Wu, W. Yang, D. M. York and M. Karplus, *Journal of Computational Chemistry*, 2009, **30**, 1545-1614.
6. a) T. A. Halgren, *Journal of Computational Chemistry*, 1996, **17**, 490-519; b) T. A. Halgren, *Journal of Computational Chemistry*, 1996, **17**, 520-552; c) T. A. Halgren, *Journal of Computational Chemistry*, 1996, **17**, 553-586; d) T. A. Halgren, *Journal of Computational Chemistry*, 1996, **17**, 616-641; e) T. A. Halgren and R. B. Nachbar, *Journal of Computational Chemistry*, 1996, **17**, 587-615.
7. J. Bjork, F. Hanke, C. A. Palma, P. Samori, M. Cecchini and M. Persson, *J Phys Chem Lett*, 2010, **1**, 3407-3412.
8. H. M. Marques and K. L. Brown, *Coordin Chem Rev*, 2002, **225**, 123-158.
9. a) A. Bultheel, *Bulletin of the Belgian Mathematical Society*, 1995, **2**, 1-46; b) S. G. Chang, B. Yu and M. Vetterli, *Ieee T Image Process*, 2000, **9**, 1522-1531; c) S. G. Chang, B. Yu and M. Vetterli, *Ieee T Image Process*, 2000, **9**, 1532-1546.
10. G. Schwarzenbach, *Helvetica Chimica Acta*, 1952, **35**, 2344-2359.
11. D. K. Cabbiness and D. W. Margerum, *J Am Chem Soc*, 1969, **91**, 6540-6541.
12. H. Irving and R. J. P. Williams, *Journal of the Chemical Society (Resumed)*, 1953, 3192-3210.
13. H. Krupitsky, Z. Stein, I. Goldberg and C. E. Strouse, *Journal of Inclusion Phenomena and Macrocyclic Chemistry*, 1994, **18**, 177-192.

Chapter 4: Induction of 3D growth

One of the greatest challenges in 2D self-assembly at interfaces is the ability to grow spatially controlled supramolecular motifs in the third dimension, exploiting the surface as a template. In this manuscript a concentration-dependent study by scanning tunneling microscopy at the solid–liquid interface, corroborated by Molecular Dynamics (MD) simulations, reveals the controlled generation of mono- or bilayer self-assembled Kagome networks based on a fully planar tetracarboxylic acid derivative. By programming the backbone of the molecular building blocks, we present a strategy to gain spatial control over the adlayer structure by conferring self-templating capacity to the 2D self-assembled network.

Hydrogen bonding is one of the most employed non-covalent interactions in supramolecular chemistry.[1] In particular, the recognition of small organic compounds exposing complementary hydrogen-bonding moieties is the most straightforward pathway for programming the self-assembly of 2D supra- molecular networks.[2] Among non-covalent interactions, H- bonding can feature a wide range of energies, depending on the nature, the number (i.e. multiplicity) and the position of consecutive hydrogen-bond donor and acceptor moieties, which determine the magnitude of both primary and secondary inter- actions. Molecular recognition based on hydrogen bonding between pairs of adjacent carboxylic acids containing strong donor (O–H) and acceptor (C=O) components has recently attracted great attention[3] and is probably the most widely used di-hapto recognition type for programming 2D porous networks formation. Organic 2D porous networks,[4] the analogue of 2D MOFs[5] or inorganic nanomeshes,[6] are ordered structures with cavities formed by organic molecules supported on a solid substrate. To confine the self-assembly process to two dimensions, it is best to use a fairly inert crystalline planar surface (e.g. graphite) so that the substrate itself does not strongly influence the interaction between the molecular building blocks.

Many groups have reported systems relying on the recognition between C_2-symmetric tetracarboxylic building blocks at the solid–liquid interface.[3a, 7] Despite the increasing interest in the field, the knowledge gathered about the extension of the self-assembly process to the third dimension (i.e., the one perpendicular to the basal plane of the substrate) is still relatively poor.[4i, 8] One recent approach[9] involved the use of fullerene C_{60} guest molecules, which were shown to promote ordered growth in the third dimension when trapped in the 2D supramolecular framework formed by tetracarboxylic acid (TCA) derivatives. In that study, the guest was reported to stabilize the interactions between adjacent self-assembled monolayers, thus allowing the formation of ordered supramolecular bilayers. The question naturally arises on whether freestanding 3D monolayers can be assembled *eo ipso* and, along the same line, what would be the key molecular requirements to reach spatial control over the self-assembly in the third dimension.

Engineering methods based on all-atom molecular dynamics have recently been introduced to predict 2D self-assembly of bi- component systems.[10] These methods were shown to be useful in bridging the gap between the chemical nature of the self- assembly modules (i.e. the supramolecular "genotype") and the structural and dynamic properties (i.e. its "phenotype") of the resulting architecture. Their careful use in the context of a feed- back loop with the experiments provides a useful framework to rationalize the chemical design of the self-assembly components.

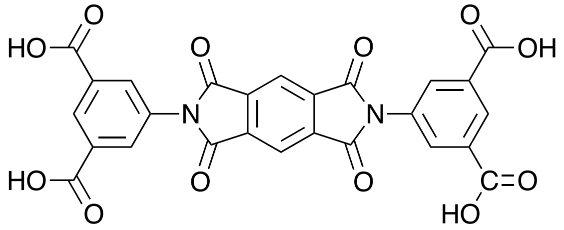

Figure 1: investigated Molecule **1**;

Experimental Results:

STM

We investigate the self-assembly behaviour of a newly synthesized fully planar 5,5o-(1,3,5,7-tetraoxopyrrolo [3,4-f]isoindole-2,6-diyl)diisophthalic acid (TCA) derivative 1 (Figure 1; see the appendix 4 for synthesis and characterisation), capable of undergoing self-association through the formation of four complementary di-hapto H-bonding $R_2^2(8)$ interactions. The molecular recognition of the newly synthesized conformationally rigid TCA derivative is based on eight directional hydrogen bonds between the carboxylic acid groups of four neighboring molecules, which promote assembly into two highly ordered 2D supramolecular porous architectures: the brick-wall array and the 2D Kagomé network.[4h, 7e, 18]

Mother solution of 5,5'-(1,3,5,7-tetraoxopyrrolo[3,4-f]isoindole-2,6-diyl)diisophthalic acid (**1**) was dissolved in DMSO at 95°C and diluted with 1-heptanoic acid to give, 280 μM, 28 μM and 2.8 μM solutions. It is important to note that molecule **1** was visualized at the HOPG–solution interface only upon using 1-heptanoic acid as solvent. Study of this system in different solvents, 1-phenyloctane, 1,2,4-trichlorobenzene and tetradecane, did not produced any ordered monolayers. For this reason, we continued our study using 1-heptanoic as a solvent.

Monolayer pattern formation was achieved by applying onto freshly cleaved HOPG a 4μL of a solution that was heated at 60-70ºC to improve the solubility. Self-assembled monolayers were prepared by applying a 4μL drop of 280 μM, 28 μM and 2.8 μM solutions of **1**, thus containing 6.7×10^{14}, 6.7×10^{13}, 6.7×10^{12} molecules respectively. Noteworthy, the amount of molecules needed to form tightly packed self-assembled monolayer of **1** on 1cm^2 of HOPG surface (no voids present in the structure) is equal to 6.9×10^9 (area of van der Waals projection of molecule **1** on the surface was estimated as 1.44 nm^2). The STM images were recorded only after achieving a negligible thermal drift. By using lower temperature during the heating process, small precipitating agglomerates were observed. On the other hand, in-situ STM experiments at variable temperature cannot be performed using our set-up. Several additional experiments were performed using the solutions with concentrations of 140 μM, 70 μM in order to study the potential growth of adlayer structures of **1** on top of self-assembled 2D Kagomé structures. However, such a phenomenon was never observed.

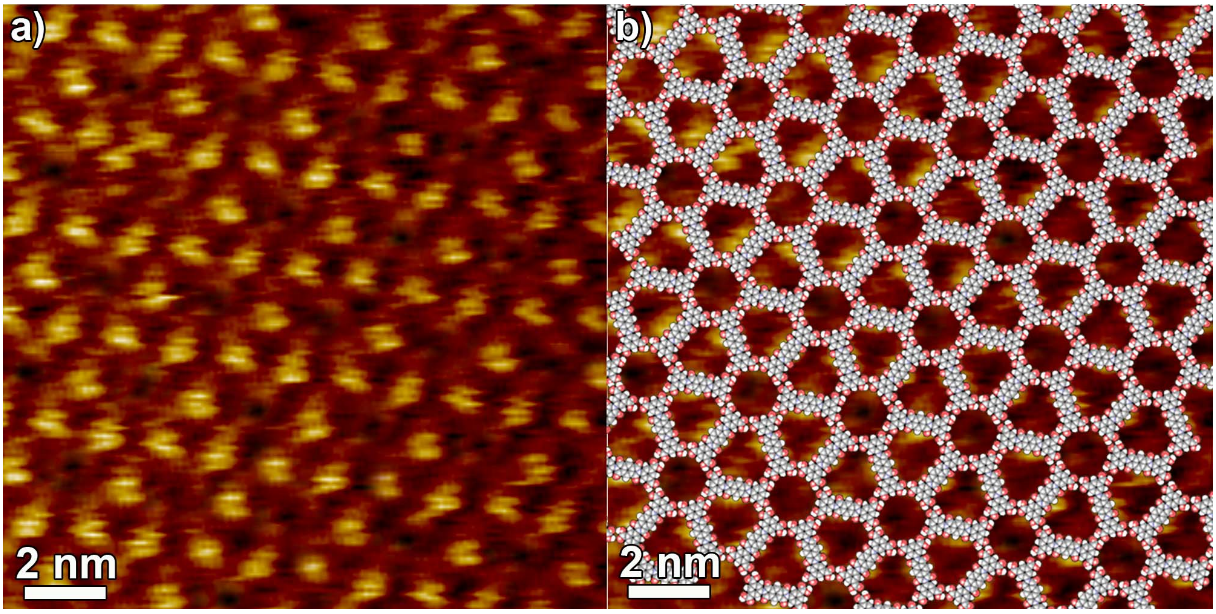

Figure 2: a,b) STM current images of a film of supramolecular H-bonded Kagomé structure at the liquid-graphite interface self-assembled from 28 μM solution of **1** in 1-heptanoic acid forming the 2D nanopattern. Tunneling parameters: Average tunneling current (I_t) = 25pA, tip bias voltage (V_t) = 400 mV.

Figure 2 shows STM current images of the obtained physisorbed monolayer of **1** from 28 μM solution, featuring a polycrystalline Kagomé structure (*K1*), which consists of hundreds of square nanometers large crystalline domains that are stable over several hours (up to 3-4 hours). These domains exhibit a unit cell: $a = (2.7 \pm 0.2)$ nm, $b = (2.8 \pm 0.2)$ nm, $\gamma = (60 \pm 2)°$, leading to an area $A = (6.5 \pm 0.5)$ nm^2, where each unit cell contains three molecules **1**, thus the area occupied by single molecule **1** is equal to $A_{mol} = (2.17 \pm 0.17)$ nm^2.

Figure 3 shows STM current of the obtained physisorbed monolayer of **1** from 2.8 μM solution, featuring a polycrystalline brick-wall architecture, which consists of hundreds of square nanometers large crystalline domains. These domains exhibit a unit cell: $a = (1.9 \pm 0.2)$ nm, $\gamma = (57 \pm 2)°$, leading to an area $A = (3.0 \pm 0.4)$ nm^2, where each unit cell contains one molecule **1**.

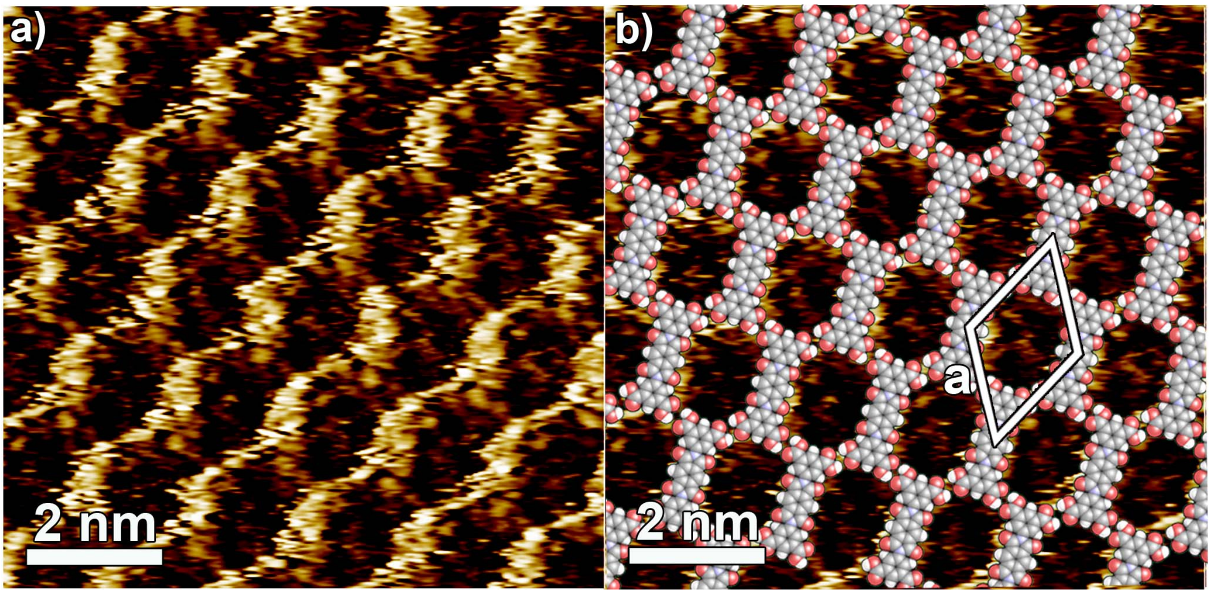

Figure 3**:** a,b) STM current images of a film of supramolecular H-bonded brick-wall structure at the liquid-graphite interface, self-assembled from 2.8 μM solution of **1** in 1-heptanoic acid forming the 2D nanopattern. Tunneling parameters: I_t = 25pA, V_t = 400 mV.

It is important to point out that the lifetime of brick-wall architecture was very short, and it disappeared after few minutes, proving its metastable nature. After ca. 20 min re-adsorption of molecules and appearance of Kagomé pattern was observed. The poor stability of brick-wall architecture was also evidenced by its dynamic behavior on a timescale comparable to that of the tip scanning.

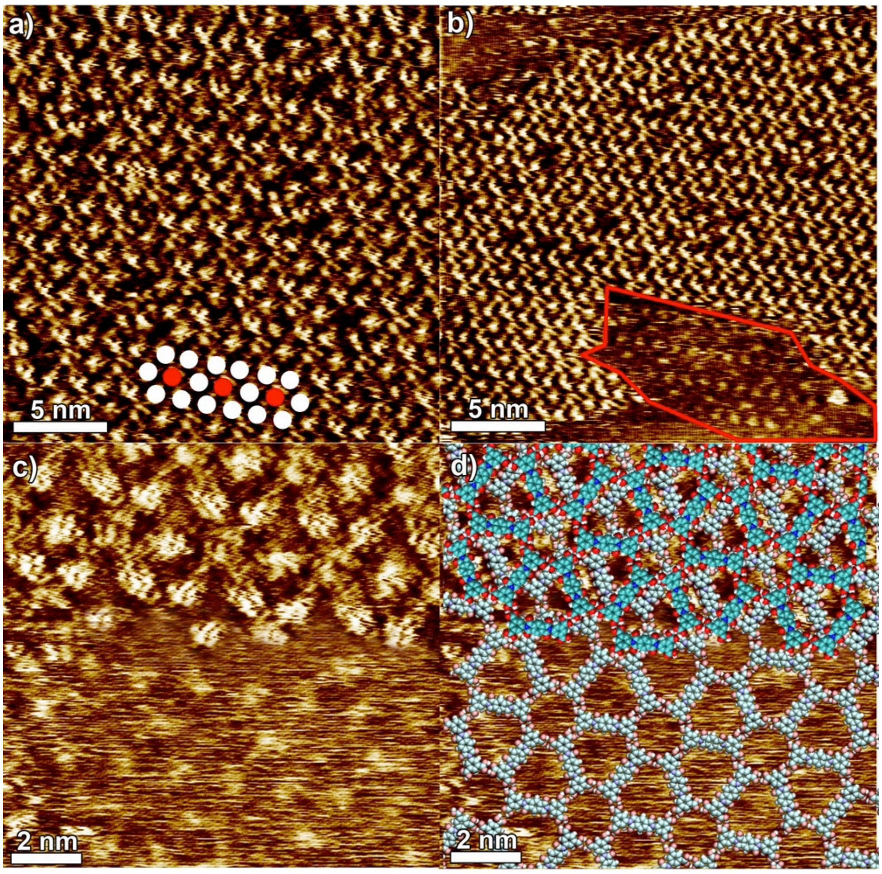

Figure 4: a-c) Series of STM current images of a bilayer supramolecular H-bonded Kagomé structure at the liquid-graphite interface, self-assembled from 2.8 μM solution in 1-heptanoic. Tunneling parameters: Average tunneling current I_t = 25pA, V_t = 100 mV. d) Proposed molecular packing motif of bilayer structure of *K1*.

Figure 4 shows the series of the STM current images of the obtained physisorbed monolayer of **1** after re-adsorption of molecules. Interestingly observed monolayer slightly differs from the one obtained from 28 μM solution of **1** (Fig. 2a). As indicated in Figure 4a appearance of additional bright spots (marked in red) was observed; whereas distribution of spots marked in white perfectly correspond to the *K1* monolayer. Such a phenomenon can be ascribed to the formation of bilayer structures of *K1*, as proven by scanning the area of domain boundaries, where *K1* structures of lower current intensity can be observed (Figure 4b - marked in red). Such a finding can be attributed to the higher stability of Kagomé network over the brick-wall structure.

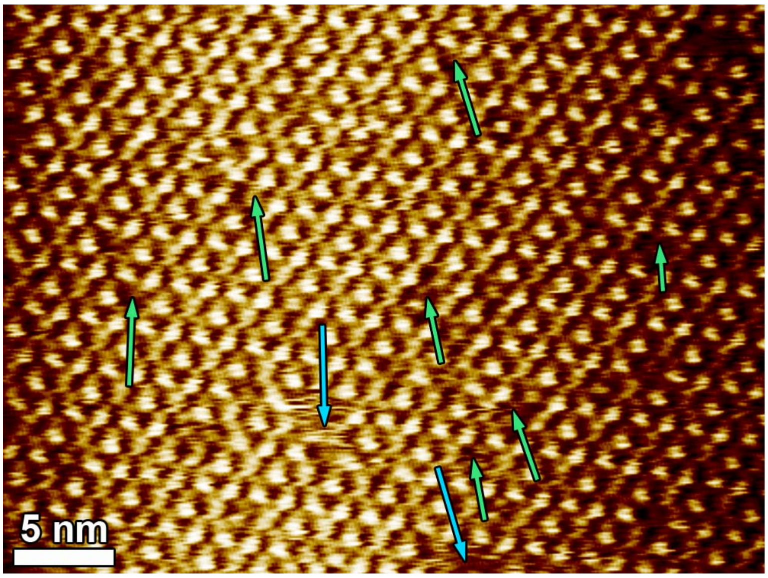

Figure 5: STM height image of a bilayer supramolecular H-bonded Kagomé structure at the liquid-graphite interface, self-assembled from 280 μM solution in 1-heptanoic. Tunneling parameters: I_t = 25pA, V_t = 100 mV.

Films prepared by using highly concentrated solutions, i.e. 280 μM revealed the formation of bilayer structures of ***K1*** (Figure 5). By using such a high concentration we were not able to visualize domain boundaries, which would allow us to observe both monolayer and bilayer structures of ***K1*** as it was possible by investigating films prepared from 2.8 μM solutions. Observed supramolecular architectures are rather uniform, however several defects in the structure can be observed. Two types of defects were found on the large scale STM image: i) lower current intensity can be assigned to the missing molecules in the first layer (marked with green arrows), since current intensity of the molecules form the top layer should be much higher than the molecules from the bottom layer; ii) areas unoccupied by molecules (marked with blue arrow).

Self- assembly of molecules at the solid–liquid interface is a fully reversible process thanks to the presence of supernatant solution; therefore, molecules that once assembled forming stable structures can reassemble with time into energetically more favorable architectures. A careful analysis of the domain boundaries (see Figure 5 for large-scale STM images) revealed a higher tunneling current in the motifs located in the top part of STM image in figure 4a, whereas the structure at the bottom part of the image exhibited a lower tunneling current. The different contrast may be interpreted in terms of the number of molecular layers in the tip-to-substrate junction. As has been reported,[8d] the different contrasts of the molecules observed in STM current images (Fig. 4) can be due to five main effects: (i) artifacts, known as double-tip effects; (ii) defects of the molecular packing on the surface or impurities of the material; (iii) different number of molecules in a stack filling the tunneling gap between the tip and substrate; (iv) different conformations of the molecules; (v) different positions of the molecules in the tip–substrate gap. Double-tip effect (i) can be safely ruled out after analysis of the large-scale images, which show that no double tip effect is present when domain boundaries orthogonal to the scanning direction are mapped (Figure 4). Scenario (ii) may be related to (a) defects in the lattice of HOPG or (b) impurities of the molecular material. While (a) can be ruled out by considering that the defect density on freshly cleaved HOPG surfaces is orders of magnitude smaller, (b) can be neglected because molecule 1 was proven by NMR and mass spectrometry to be analytically pure (see Annex 4). Scenario (iii) can also be eliminated as the array of bright spots observed in Fig. 4a consisting of molecules marked in white and red color is too tight to be accommodated in a single layer; the latter was also shown by simulations. Finally, to gain insight into the role of effects (iv) and (v), we performed molecular dynamics (MD) simulations.

Molecular Dynamics

In order to rationalize the formation of bilayer architectures of **1**, and what is even more important why the adlayer structures shows displacement with respect to the underlying monolayers, several calculations were performed with the program CHARMM[12] using the implementation in the c35b1 update. Parameterization of all investigated molecules was done through the Merck molecular force field MMFF94,[13] automatic module implemented in CHARMM.

Molecular models presented in this section were processed with VMD visualization software.[14]

1 Kagomé on graphene

A 4480 graphene C-atom slab was embedded in a orthorhombic box of lengths equal to 98.38 and 119.14 Å with periodic boundary conditions (PBCs) to simulate an infinite graphene slab for all molecular force-field calculations. A distance cutoff of half-size of the box side was applied to compute the non-bonded interactions. Molecular geometries were optimized by energy minimization in the presence of the graphene slab. In MMFF, all sp2 carbons were assigned the atom type 37 (aromatic), whereas graphene atoms (G) were assigned the atom type 2 (vinylic). The graphene slab was assigned 0 charges, and their coordinates were fixed in space by using CONS FIX. The results obtained by using those parameters, were found to be in good agreement with DFT calculations of the adsorption of neutral (poly)-aromatic and more generally π-conjugated systems on graphene.[15]

CHARMM Keywords:

```
SCALAR CHARGE SET 0 SELECT ATOM G* * * END
…
CONS FIX SELE SEGID G* END
…
CRYSTAL DEFINE ORTHO 98.38 119.14 100 90 90 90
CRYSTAL BUILD CUTOFF 90.0 NOPERATIONS 0
```

As a first step towards the understanding the formation of bilayer structure of ***K1***, we simulated the self-assembly of twelve-molecule-based Kagomé structure of **1** ($K1_{12}$) on graphene slab. Five independent runs were done at 300, 400, 500, 600 and 700K for 100 ns in vacuum with periodic boundary conditions. The SHAKE[16] algorithm was used to reduce the vibration of the H atoms, thus allowing for an integration time step of one femtosecond. Initially pre-assembled $K1_{12}$ structure was placed 8Å above the graphene slab.

CHARMM Keywords:

```
SET NN 1
SET ID 1
SET NMOL 12
LABEL LABELNN
….
COOR TRANS XDIR 15.62 SELECT SEGID MMFF END
CALC ANGLE @NN*60
COOR ROTA ZDIR 1 PHI @ANGLE SELECT SEGID MMFF END
IF @ID .eq. 7 THEN
COOR TRANS XDIR -31.24 SELE SEGID MMFF END
ENDIF
IF @ID .eq. 8 THEN
COOR TRANS XDIR 31.24 SELE SEGID MMFF END
ENDIF
IF @ID .eq. 9 THEN
COOR TRANS YDIR -27.65 SELE SEGID MMFF END
COOR TRANS XDIR 15.62 SELE SEGID MMFF END
ENDIF
```

```
IF @ID .eq. 10 THEN
COOR TRANS XDIR 31.24 SELE SEGID MMFF END
ENDIF
IF @ID .eq. 11 THEN
COOR TRANS XDIR -31.24 SELE SEGID MMFF END
ENDIF
IF @ID .eq. 12 THEN
COOR TRANS YDIR 27.65 SELE SEGID MMFF END
COOR TRANS XDIR -15.62 SELE SEGID MMFF END
ENDIF
INCR ID
INCR NN
IF NN .le. @NMOL GOTO LABELNN
```

Pre-assembled $K1_{12}$ structure have been optimized by applying 200 steps of Steepest Descent minimization (MINI SD), then the system was heated and equilibrated at desired temperature.

```
CHARMM Keywords:
SET TACT 300                                                    !final temperature
SET HSTP 20000                                                  !number of heating steps
DYNAMICS LEAP START -
      TIMESTP 0.002 NSTEP @HSTP -
      FIRSTT 100 FINALT @TACT TEMIC 10 IHTFRQ 1000                         !system is heated
                                                                           by 10K every 1000
                                                                           steps
```

After achieving thermal equilibration, Langevin dynamics have been applied to model the dynamics of molecular systems.

```
CHARMM Keywords:
SET ESTP 10000000                                        !number of dynamic steps
…..
SCALAR FBETA SET 0.05               !sets the friction forces coefficient to 0.05 picosecond-1
```

$K1_{12}$ structures investigated at 300-600K shows no structural evolution, i.e. all H-bonds holding molecules **1** shows high stability during 100 ns of simulation time, only 2D translation and rotation of entire $K1_{12}$ structures was observed. Figure 6 shows initial (Figure 6a) and final (Figure 6b) structures of $K1_{12}$ architecture on graphene substrate investigated at 300K, which well represents the dynamics of Kagomé assemblies investigated in the 300-600K temperature range.

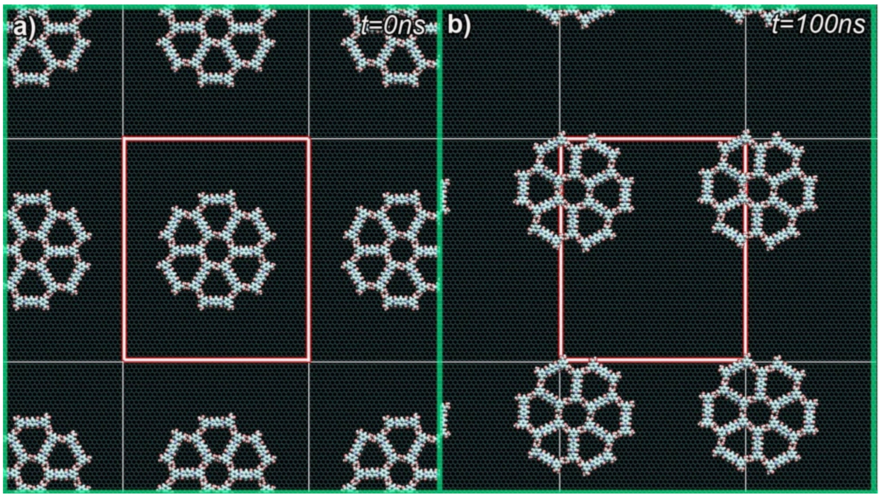

Figure 6: a) View of a manually pre-formed $K1_{12}$ structure on top of graphene slab - initial structure, b) final structure of $K1_{12}$ self-assembled structure investigated at 300K. Rectangular super-cells used for the calculations have been marked in red.

Interestingly, simulations of $K1_{12}$ architecture on graphene at 700K, reveled large deformation of $K1_{12}$ structure until rupture on the nanosecond timescale. Already after 10 ns of simulation, deformation of two H-bonds (indicated with white arrow on Figure 7b) have been observed.

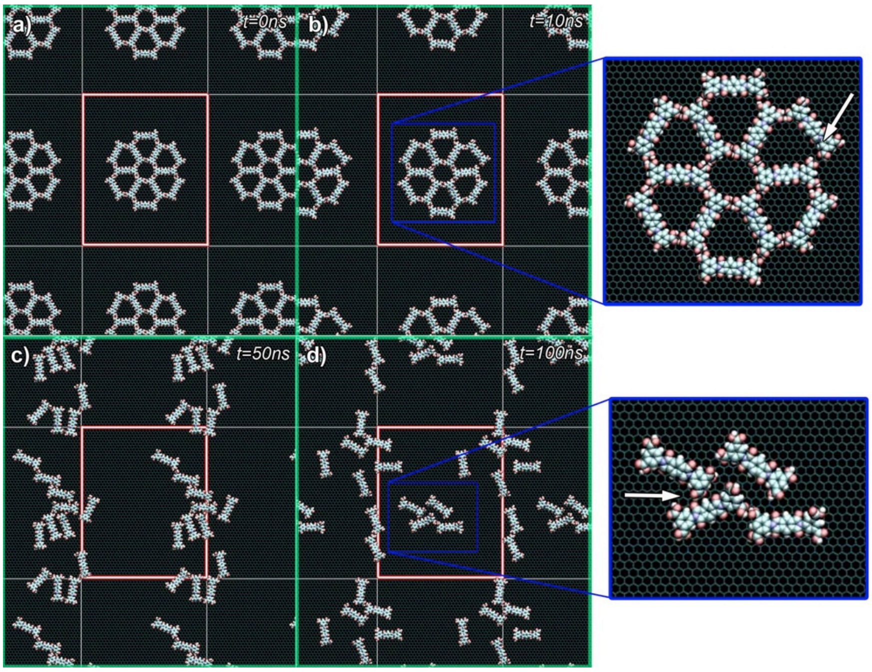

Figure 7: a-d) Representative visualization of $K1_{12}$ self-assembled structure investigated at 700K. Rectangular super-cells used for the calculations have been marked in red.

Complete deformation of $K1_{12}$ architecture and further formation of disordered architecture can be seen in Figure 7c. Such a glass-like architecture consists of brick-wall fragments as well as close-packed structures. Remarkably, self-assembled structures based on COOH···O=Core H-bonds have been detected, as shown in Figure 7d (indicated with white arrows), which indicates that oxygen atoms from the core of **1** can play an important role in the self-assembly processes.

In order to understand better the self-assembly process of **1**, especially the role of oxygen atoms from carbonyl groups in the formation of bilayer architectures, we decided to introduce two additional molecular building blocks (Figure 8), in which the oxygen atoms from the core of the molecule have been replaced with $=CH_2$ groups (**2**) and sulfur atoms (**3**). By replacing oxygen atoms with the methylene groups (**2**) potential energy of molecule has been changed, i.e. partial atomic charges on O atoms (-0.57C) as well as neighboring carbon atoms (0.54C) have been replaced with -0.28C (C atoms in CH_2) and 0.07C (C atoms), whereas by introducing sulfur atoms (**3**), partial charges have been replaced with -0.38C (S atoms) and 0.12C (C atoms). It is important to note, that despite the change of the atomic charges, Pauling radius of carbonyl-oxygen atoms (1.4Å) has been replaced by larger substituents, i.e. 2.0Å in case of methylene group and 1.87Å when sulfur atoms were used. We also decided to compare those three molecules with the TCD derivative, which was reported (STM experiments) to form bilayer structures in the presence of templating C_{60} molecules (**4**).[9]

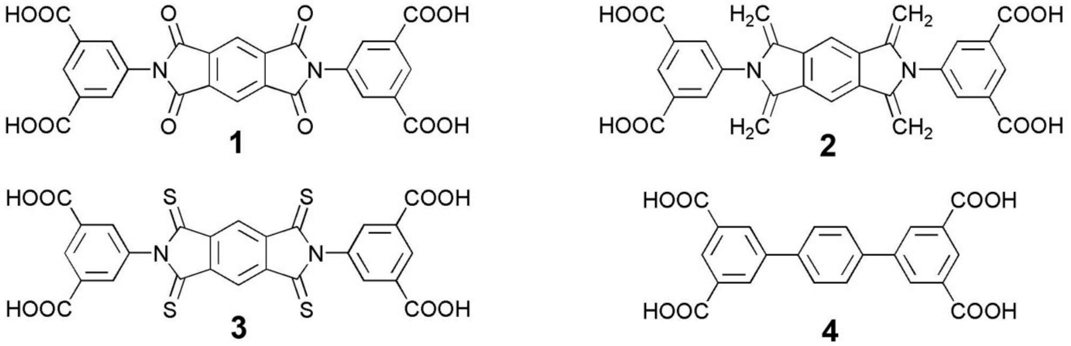

Figure 8: Chemical representation of investigated TCD derivatives **1**-**4**.

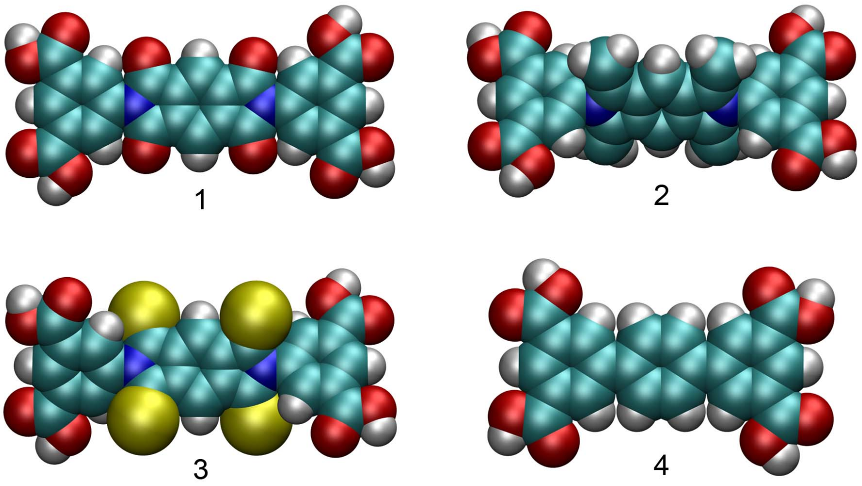

Figure 9**:** Minimized structures of investigated TCD derivatives **1**-**4**.

Self-assembly of K_{12} structures on graphene of three additional molecules, i.e. **2**-**4** have been also simulated, and it was found that the structures based on molecules **2**, **3** and **4** ($K2_{12}$, $K3_{12}$ and $K4_{12}$) are stable over tens of nanoseconds of simulation time as in the case of $K1_{12}$.

2 Kagomé on Monolayer

To achieve a comprehensive understanding of the formation of bilayer structures, we simulated the self-assembly K_{12} structures of **1**, **2**, **3** and **4** on the pre-assemble monolayer architectures and underlying graphene slab. The super-cells of monolayer (Figure 10) were obtained by multiplying the magnitude of the 6-molecule elementary rectangular unit cell vectors (i.e. the smallest rectangular unit cell) by 3 and 2, where the super-cell consists of 36 molecules.

CHARMM Keywords (formation of monolayer - example of **1**):

```
SET NN 1
SET ID 1
SET II 1
SET XX 1
SET YY 1
SET NMOL 36
SET NXCELL 3
SET NYCELL 2
LABEL LABELNN
….
COOR TRANS XDIR 15.62 SELECT SEGID MMFF END
CALC ANGLE @NN*60
COOR ROTA ZDIR 1 PHI @ANGLE SELECT SEGID MMFF END
```

```
IF @ID .eq. 3 THEN
COOR TRANS YDIR -27.69 SELE SEGID MMFF END
COOR TRANS XDIR 46.86 SELE SEGID MMFF END
ENDIF
IF @ID .eq. 2 THEN
COOR TRANS XDIR 31.24 SELE SEGID MMFF END
ENDIF
IF @ID .eq. 4 THEN
COOR TRANS XDIR 31.24 SELE SEGID MMFF END
ENDIF

CALC DX = @XX * 31.93
CALC DY = @YY * 55.3
COOR TRANS XDIR @DX SELE SEGID MMFF END
COOR TRANS YDIR @DY SELE SEGID MMFF END

CALC MM = 6 * @II
IF NN .ge. @MM THEN
  INCR II
  SET ID 0
  IF XX .lt. @NXCELL THEN
    INCR XX
  ELSE
     IF YY .lt. @NYCELL THEN
       INCR YY
       SET XX 1
     ENDIF
  ENDIF
ENDIF
INCR ID
INCR NN
IF NN .le. @NMOL GOTO LABELNN
```

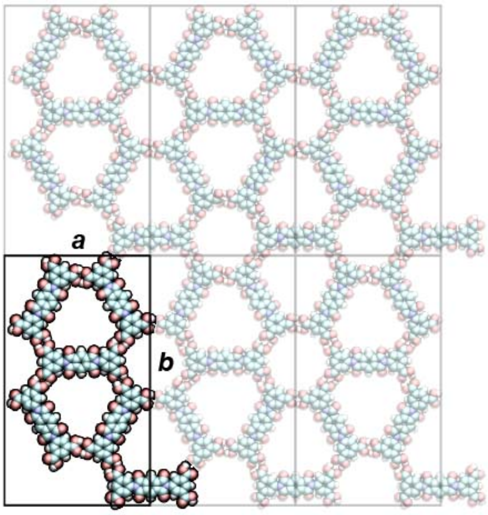

Figure 10**:** a) Rectangular super-cell used for the calculations of bilayer of **1**, based on multiples of elementary rectangular unit cell (marked in black). Unit cell parameters used for molecules **1**-**3**: *a* = 31.19 Å and *b* = 53.11 Å, whereas unit cell parameters for molecule **4**: *a* = 27.95 Å and *b* = 49.70 Å.

Manually pre-formed K_{12} structures have been initially placed 6Å above the monolayer slab (and 12 Å above the graphene slab), and positioned in the fully overlapped fashion in respect with the monolayer (marked in black on Figure 11a), which was embedded in a orthorhombic box of lengths equal to 95.68 and 109.12 Å for the molecules **1**-**3** and equal to 84.76 and 98.24 Å for the molecule **4**, with periodic boundary conditions (PBCs) to simulate an infinite monolayer slab for all calculations. The interaction energy between the K_{12} and K monolayer structures (inter-layer energy) was calculated by subtracting the energy upon displacement of the K_{12} 100Å away from the K monolayer.

Subsequently, 3 sets of 1620 independent energy calculations for **1**-**3** (3 sets of 1344 calculations each for **4**) were performed, where in case of **1**-**3** the surface of 16.2 nm^2 (marked in blue on Figure 11b) have been mapped by analyzing inter-layer energy evolution in 30×54 matrix (28×48 matrix for **4**), where the distance between equally distributed points was equal to 1.03Å. In such a way the fully overlapped K_{12} could be fully translated over the monolayer structure with respect to the initial structure: along X (marked in red on Figure 11a) and Y (marked in blue on Figure 11a); and twice along XY direction (marked in green on Figure 11a).

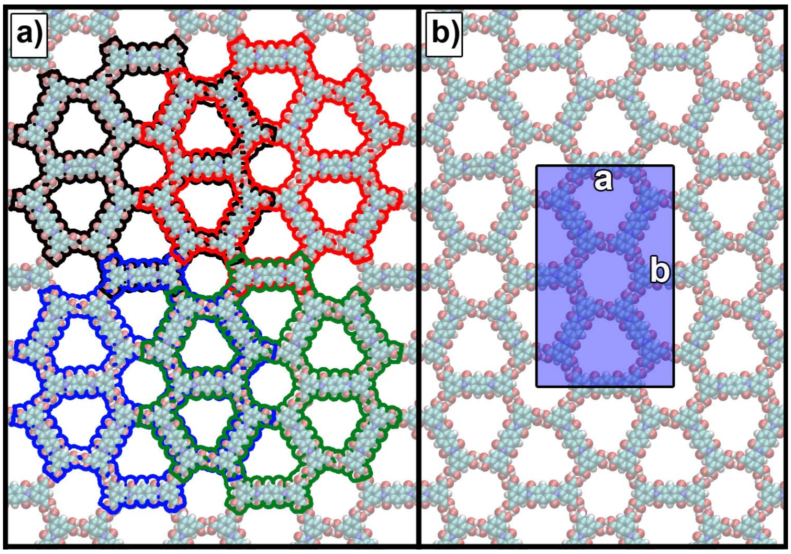

Figure 11: a) Schematic representation of initial fully overlapped (marked in black) and final fully translated structures of $K1_{12}$ (marked in red, blue and green) on K monolayer, graphene slab has been removed for clarity; b) schematic visualization of area sampled by translating $K1_{12}$ assembly, a = 30Å and b = 54Å.

Figure 12 shows the inter-layer energy evolution of K_{12} structures, where interaction energy between K_{12} and K monolayer in the fully overlapped conformation were chosen as a reference points.

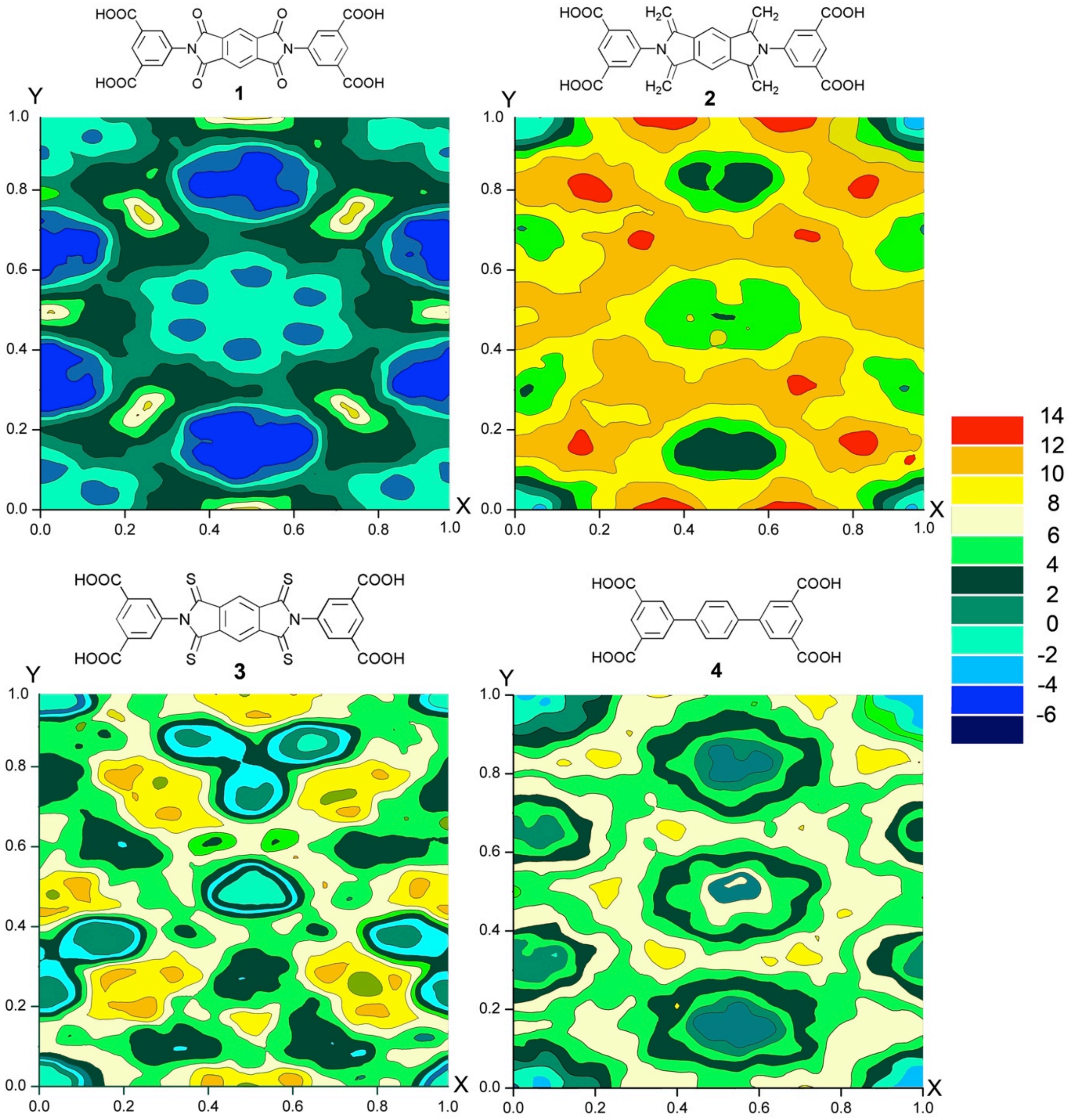

Figure 12**:** Inter-layer energy evolution of single molecule **1** (a), **2** (b), **3** (c) and **4** (d) from ***K*$_{12}$** assemblies with underlying monolayer structures (energies given in kcal mol^{-1}).

2.1 *K1*$_{12}$ on *K1* monolayer

Figure 13a shows representative visualization of energetically favored conformation of *K1*$_{12}$ structure on *K1* monolayer, determined by inter-layer interaction energy evolution (Figure 12a) where *K1*$_{12}$ assembly has been shifted by 15Å in X and 8 Å in Y directions, with respect to the initial fully overlapped structure. Such a phenomenon can be explained by the repulsive interactions between oxygen atoms from carbonyl groups, which results in the shift of *K1*$_{12}$ assembly.

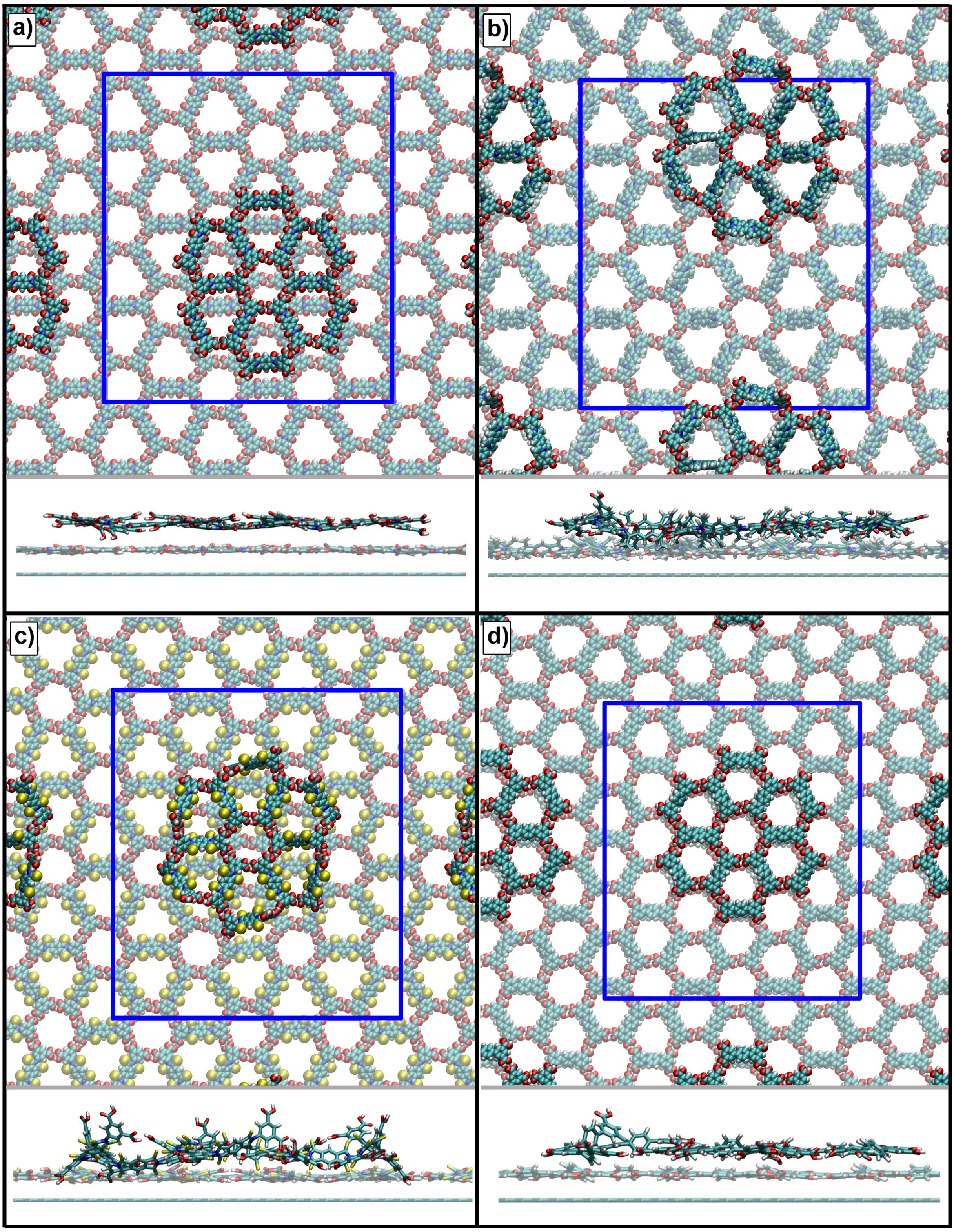

Figure 13**:** Representative visualization of the top and side views of energetically favored self-assembled structures of: $K1_{12}$ (a), $K2_{12}$ (b), $K3_{12}$ (c) and $K4_{12}$ (d) on the corresponding monolayer surfaces.) Rectangular super-cell used for the calculations has been marked in blue.

2.2 *K2*$_{12}$ on *K2* monolayer

Figure 13b shows the visualization of the energetically favored conformation of *K2*$_{12}$ structure on *K2* monolayer (see Figure 12b). Differently than in case of *K1*$_{12}$+*K1*, where *K1*$_{12}$ assembly has been shifted with respect to the initial fully overlapped structure, the highest interaction energy between *K2*$_{12}$ and *K2* monolayer was observed when the two are fully overlapped, which indicates that the presence of oxygen atoms in the core of **1** is causing the shift of the *K1*$_{12}$.

2.3 *K3*$_{12}$ on *K3* monolayer

Figure 13c shows the visualization of the favored conformation of *K3*$_{12}$ structure on *K3* monolayer (see Figure 12c). Similar to the case of *K1*$_{12}$+*K1*, *K3*$_{12}$ has been shifted with respect to the initial fully overlapped structure. Such an observation suggests that whenever negatively charged atoms are introduced to the structure of molecular building block the shifted conformation is favored. Interestingly, differently than in case of *K1*$_{12}$+*K1*, *K3*$_{12}$ structure is not planar. Sulfur atoms which have lowest hydrogen-bonding affinity than oxygen atoms, cannot form H-bonds with hydrogen atoms from isophthalic group of molecule, therefore the molecules **3** are not planar in *K3*$_{12}$ assembly. Remarkably, the molecule **3** can be planarized (not fully) once full monolayer is formed (see side view in Figure 13c).

2.4 *K4*$_{12}$ on *K4* monolayer

Figure Figure 13d shows representative visualization of energetically favored conformation of *K4*$_{12}$ assembly on *K4* monolayer (see Figure 12d). Similar to the case of *K2*$_{12}$+*K2*, complete overlap of *K4*$_{12}$ with underlying *K4* monolayer can be observed, which confirms that by removing partial atomic charges from the molecular building block fully eclipsed conformation is observed.

Figure 14 shows the evolution of dihedral angles of all investigated molecules, in the monolayer and *K*$_{12}$ structures in the simulation time of 1ns.Among all investigated molecules only molecule **1** was found to be fully planar, due to the intramolecular H-bonding between oxygen atoms from carbonyl groups and hydrogen atoms from isophthalic moieties. By introducing methylene groups in the structure, non-planarity of molecule **2** was observed, which can be seen on Figure 14. As mentioned above, sulfur atoms which have lowest hydrogen-bonding affinity than oxygen atoms, cannot form H-bonds with hydrogen atoms from isophthalic group of molecule, therefore the molecules **3** are not planar in both $K3_{12}$ assembly and monolayer structure. Interestingly, non-planarity of 4 is much higher in its $K4_{12}$ assembly than in $K4$ monolayer.

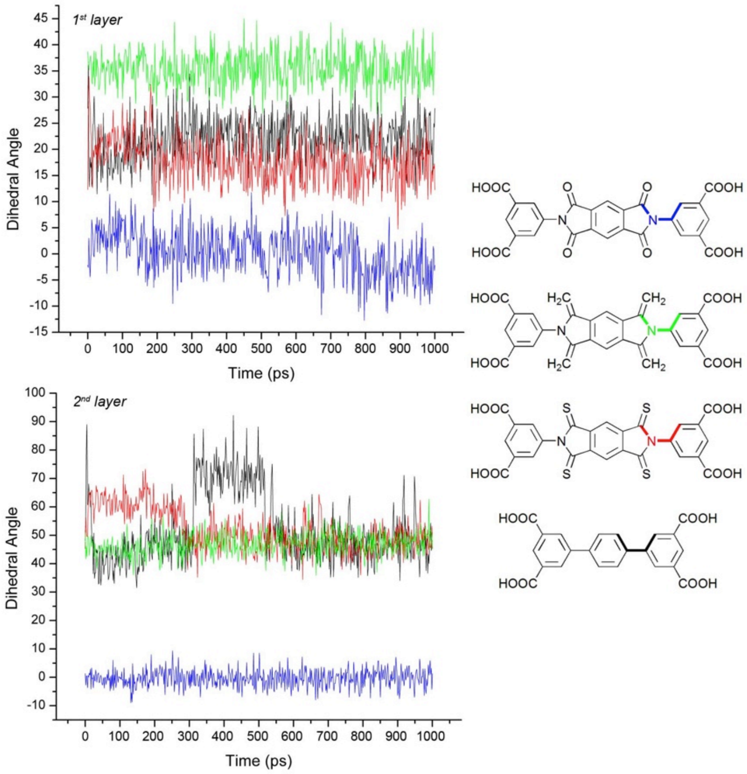

Figure 14: The evolution of dihedral angles of investigated molecules over 1ns of simulation time.

	Dihedral angle	
Molecule	1st layer	2nd layer
1	0.23 ± 4.22	-0.34 ± 2.96
2	35.44 ± 3.32	48.64 ± 3.91
3	17.74 ± 4.27	51.96 ± 7.15
4	21.98 ± 4.09	52.02 ± 12.14

Table 1: Average of dihedral angles of investigated molecules.

Discussion:

To provide a molecular understanding of self-assembly and cast light onto the formation and stability of both monolayer and bilayer motifs, a twelve-molecule Kagomé structure of 1 (**K1**$_{12}$) was modeled in silico on the top of a pre-formed Kagomé **K1** monolayer, the latter being pre-assembled onto a graphene slab.[15] The monolayer was simulated in an orthorhombic box with periodic boundary conditions (PBCs) to mimic an infinite slab. Molecular modeling was done with the program CHARMM[12](c35b1 version) with the Merck molecular force field MMFF94[13] for the parameterization of molecules. The **K1**$_{12}$ structure was initially placed 6 Å above the monolayer **K1** slab (i.e. 12 Å above graphene) in a fully overlapped orientation ("eclipsed" arrangement) and then energy minimized by 200 iterations of Steepest Descent (SD) and 500 iterations of adopted basis Newton– Raphson (ABNR) to ensure convergence of the results. Finally, the interaction energy between **K1**$_{12}$ and the self-assembled monolayer (interlayer energy) was determined by subtracting the energy obtained upon displacement of the former 100 Å away from the latter along the Z-direction, i.e. the one perpendicular to the plane of the substrate. The same procedure was repeated 1620 times by changing the initial coordinates of the **K1**$_{12}$ along the X and Y directions (i.e. parallel to the substrate) with a spatial resolution of 1 Å. The interlayer energy computed at each new position of **K1**$_{12}$ is shown in Fig. 12a projected on the XY plane. The calculations indicate that the deepest interaction energy minimum for molecule 1 corresponds to a shifted supramolecular arrangement (15 Å along X and 8 Å along Y, as well as 1 Å along X and 16 Å along Y), whereas the "eclipsed" arrangement is metastable, although energetically favorable. This is in good accordance with the STM results in Fig. 4. The supramolecular architecture corresponding to the most stable interlayer packing, i.e. featuring the lowest energy, is depicted in Fig. 13a. Although the energetics involved in the stabilization of the shifted bilayer (5.6 kcal mol^{-1}) might appear marginally significant, one should note that the **K1**$_{12}$ supramolecular structure corresponds to the minimal (in size) representation of the adlayer and that, as we shall see, the molecular contributions to the stabilization of the shifted arrangement are small but additive. It follows that the stabilization of the shifted bilayer is expected to grow linearly with the number of molecules involved and to be much more significant for larger assemblies. A one nanosecond molecular dynamics simulation of the bilayer structure starting from the "shifted" arrangement was carried out at 300 K. The analysis of the trajectory shows that molecule 1 retains a planar conformation even in the adlayer, ruling out scenario (iv) as the origin of the different contrast in the STM image in Fig. 4. Interestingly, the planar conformation is a peculiar property that arises from the rigidity of the newly synthesized building block, as well as the intramolecular H- bonding between the oxygen atoms of the core and the hydrogen atoms of the isophthalic moieties.

Following the same procedure, the interlayer properties of three additional TCA derivatives were computed. For this purpose, new building blocks 2 and 3 (Figure 8, 9), chemical derivatives of 1 in which the oxygen atoms of the core have been replaced by -CH_2 groups and sulfur atoms, were designed. Although the molecules 2 and 3 are not easily synthesizable and their stabilities are questionable, their modelling may provide insights onto the chemical nature and the geometrical preference needed to form stable bilayer architecture. Molecule 4 was also chosen as it represents the TCA derivative shown to form bilayer structures only in the presence of templating C_{60} molecules.[9]

By substituting oxygen atoms with methylene groups (in molecule 2), four negatively charged interaction sites of the core are effectively removed; i.e. the partial charge of the substituents changes from 0.57 to 0 elementary charge units (e.u.). Such a chemical modification results in the loss of four intramolecular H-bonding acceptors, which crucially stabilize the fully planar conformation of the TCA derivative. For similar reasons, the substitution of the oxygens of the core with sulfur atoms (molecule 3), which are negatively charged (0.38 e.u.), as well as H-bonding acceptors, leads to molecules featuring a non-planar conformation. This time, the introduction of sterically hyndrant substituents (i.e. the Pauling radius of the group changes from 1.4 to 2.0 Å) is responsible for the change in conformation, i.e. molecular twisting, due to the repulsive interactions between the methylene groups (2)/sulfur atoms (3) and the hydrogen atoms from the phenyl ring of the isophthalic unit. The interlayer energy results obtained for molecule 3 are fully consistent with the analysis of molecule 1 and show that the lowest energy configuration involves the shift of the adlayer structure. By contrast, calculations on compounds 2 and 4 indicate that the “eclipsed” arrangement is the lowest energy architecture. These results suggest that the oxygen atoms substituting the core of molecule 1 play a crucial role in the formation of the bilayer supramolecular structure. Interestingly, MD simulations of bilayers formed by molecules 2–4 starting from the lowest energy interlayer arrangement show a remark- able increase in the instability of the adlayer with time. In fact, unlike compound 1, the average change of dihedral angles of molecules 2–4 in the second layer increases by 10 to 30 degrees, which is expected to effectively hinder the growth in the third dimension. The decomposition of the interlayer energy for the four TCA derivatives shows that the 3D architecture originates from a complex interplay between dispersive (van der Waals) and electrostatic interactions between adjacent layers. In fact, the presence of negatively charged groups in the core of the molecule (derivatives **1** and **3**) destabilizes the “eclipsed” interlayer arrangement for electrostatic repulsions and drives an overall displacement of the adlayer. Conversely, in the absence of partially charged substituents (derivatives 2 and 4), the fully overlapped arrangement, which maximizes the contact area between layers, is preferred.

By stabilizing the fully planar conformation of molecule **1** through the formation of intramolecular H-bonds, the core oxygens of **1** confer self-templating capacity to the self-assembled monolayer and promote the formation of a precise three- dimensional superstructure (interlayer shift) stabilized by inter- layer electrostatic interactions. These findings make it possible to interpret the complex arrangement observed in the STM image in Fig. 4: the Kagomé motif in the first layer is identical to the 2D assembly in the second layer, the latter featuring a lateral shift of 1 Å along X and 16 Å along Y with respect to the “eclipsed” metastable arrangement. Thus the spots marked in red in Fig. 4a can be ascribed to molecules adsorbed in the first layer adjacent to the HOPG substrate, whereas those marked in white are attributed to the second layer.

Conclusions

In summary, we demonstrated the bottom-up fabrication of bilayer supramolecular arrays of polymeric networks composed of 5,5o -(1,3,5,7-tetraoxopyrrolo[3,4-f]isoindole-2,6-diyl)diisoph- thalic acid (1) molecules, capable of self-associating through four strong (O–H/O) hydrogen bonds. STM studies at the solid– liquid interface have revealed the self-assembly into 2D Kagomé supramolecular networks on the HOPG as well as the emergence of a 3D superstructure, i.e. a shifted porous bilayer. The unambiguous assignment of the bilayer structure was possible by combining high resolution STM imaging with all-atom molecular dynamics and force-field calculations. The analysis indicates that the observed bilayer architecture is the result of the self-templating capacity of molecule 1 that is conferred by the presence of four oxygens in the core stabilizing the planar conformation of the TCA derivative in the adlayer.

The present strategy relies on conferring self-templating ability to the 2D self-assembled monolayer. Our analysis shows that the following are all key elements for programming self-assembly into three-dimensional architectures: (i) the presence of “primary” recognition sites on the molecular building blocks, which promote the self-assembly into 2D porous layers, (ii) a fine control of their conformational planarity, which confers the self- templating capacity, and (iii) the introduction of secondary recognition sites, which mediate the interactions between the self- assembled layers. Intriguingly, such a design is reminiscent of the molecular properties of proteins, whose “primary” backbone interactions promote the formation of local structures (α-helices and β-sheets) while “secondary” side-chain interactions fine-tune the overall 3D architecture. This design strategy may open a new avenue to reach structural control on the third dimension.

1. (a) Brunsveld, L.; Folmer, B. J. B.; Meijer, E. W.; Sijbesma, R. P., Supramolecular polymers. *Chem. Rev.* **2001,** *101* (12), 4071-4097; (b) Desiraju, G. R., Hydrogen bridges in crystal engineering: Interactions without borders. *Acc. Chem. Res.* **2002,** *35* (7), 565-573; (c) Greef, T. F. A.; Meijer, E. W., Materials science - Supramolecular polymers. *Nature* **2008,** *453* (7192), 171-173; (d) Lehn, J. M., Supramolecular Chemistry. *Science* **1993,** *260* (5115), 1762-1763; (e) Sherrington, D. C.; Taskinen, K. A., Self-assembly in synthetic macromolecular systems via multiple hydrogen bonding interactions. *Chem. Soc. Rev.* **2001,** *30* (2), 83-93.

2. (a) Ciesielski, A.; Schaeffer, G.; Petitjean, A.; Lehn, J. M.; Samorì, P., STM Insight into Hydrogen-Bonded Bicomponent 1D Supramolecular Polymers with Controlled Geometries at the Liquid-Solid Interface. *Angew. Chem. Int. Ed.* **2009,** *48* (11), 2039-2043; (b) Fan, E.; Vicent, C.; Geib, S. J.; Hamilton, A. D., Molecular Recognition in the Solid-State - Hydrogen-Bonding Control of Molecular Aggregation. *Chem. Mater.* **1994,** *6* (8), 1113-1117; (c) Macdonald, J. C.; Whitesides, G. M., Solid-State Structures of Hydrogen-Bonded Tapes Based on Cyclic Secondary Diamides. *Chem. Rev.* **1994,** *94* (8), 2383-2420; (d) Palma, C.-A.; Bonini, M.; Llanes-Pallas, A.; Breiner, T.; Prato, M.; Bonifazi, D.; Samorì, P., Pre-programmed bicomponent porous networks at the solid-liquid interface: the low concentration regime. *Chem. Commun.* **2008,** (42), 5289-5291; (e) Subramanian, S.; Zaworotko, M. J., Exploitation of the Hydrogen-Bond - Recent Developments in the Context of Crystal Engineering. *Coord. Chem. Rev.* **1994,** *137*, 357-401; (f) Theobald, J. A.; Oxtoby, N. S.; Phillips, M. A.; Champness, N. R.; Beton, P. H., Controlling molecular deposition and layer structure with supramolecular surface assemblies. *Nature* **2003,** *424* (6952), 1029-1031.

3. (a) Blunt, M. O.; Russell, J. C.; Gimenéz-López, M. D.; Garrahan, J. P.; Lin, X.; Schröder, M.; Champness, N. R.; Beton, P. H., Random Tiling and Topological Defects in a Two-Dimensional Molecular Network. *Science* **2008,** *322* (5904), 1077-1081; (b) De Feyter, S.; Gesquiere, A.; Klapper, M.; Müllen, K.; De Schryver, F. C., Toward two-dimensional supramolecular control of hydrogen-bonded arrays: The case of isophthalic acids. *Nano Lett.* **2003,** *3* (11), 1485-1488; (c) Duong, A.; Dubois, M. A.; Wuest, J. D., Two-Dimensional Molecular Organization of Pyridinecarboxylic Acids Adsorbed on Graphite. *Langmuir* **2010,** *26* (23), 18089-18096; (d) Gesquiere, A.; Abdel-Mottaleb, M. M.; De Feyter, S.; De Schryver, F. C.; Sieffert, M.; Müllen, K.; Calderone, A.; Lazzaroni, R.; Bredas, J. L., Dynamics in physisorbed monolayers of 5-alkoxy-isophthalic acid derivatives at the liquid/solid interface investigated by scanning tunneling microscopy. *Chem. Eur. J.* **2000,** *6* (20), 3739-3746; (e) Ivasenko, O.; Perepichka, D. F., Mastering fundamentals of supramolecular design with carboxylic acids. Common lessons from X-ray crystallography and scanning tunneling microscopy. *Chem. Soc. Rev.* **2011,** *40* (1), 191-206.

4. (a) Canas-Ventura, M. E.; Aït-Mansour, K.; Ruffieux, P.; Rieger, R.; Müllen, K.; Brune, H.; Fasel, R., Complex Interplay and Hierarchy of Interactions in Two-Dimensional Supramolecular Assemblies. *Acs Nano* **2011,** *5*, 457-469; (b) Griessl, S. J. H.; Lackinger, M.; Jamitzky, F.; Markert, T.; Hietschold, M.; Heckl, W. A., Incorporation and

manipulation of coronene in an organic template structure. *Langmuir* **2004,** *20* (21), 9403-9407; (c) Llanes-Pallas, A.; Palma, C. A.; Piot, L.; Belbakra, A.; Listorti, A.; Prato, M.; Samorì, P.; Armaroli, N.; Bonifazi, D., Engineering of Supramolecular H-Bonded Nanopolygons via Self-Assembly of Programmed Molecular Modules. *J. Am. Chem. Soc.* **2009,** *131* (2), 509-520; (d) Matena, M.; Llanes-Pallas, A.; Enache, M.; Jung, T.; Wouters, J.; Champagne, B.; Stohr, M.; Bonifazi, D., Conformation-controlled networking of H-bonded assemblies on surfaces. *Chem. Commun.* **2009,** (24), 3525-3527; (e) Nath, K. G.; Ivasenko, O.; Miwa, J. A.; Dang, H.; Wuest, J. D.; Nanci, A.; Perepichka, D. F.; Rosei, F., Rational modulation of the periodicity in linear hydrogen-bonded assemblies of trimesic acid on surfaces. *J. Am. Chem. Soc.* **2006,** *128* (13), 4212-4213; (f) Stepanow, S.; Lingenfelder, M.; Dmitriev, A.; Spillmann, H.; Delvigne, E.; Lin, N.; Deng, X. B.; Cai, C. Z.; Barth, J. V.; Kern, K., Steering molecular organization and host-guest interactions using two-dimensional nanoporous coordination systems. *Nat. Mater.* **2004,** *3* (4), 229-233; (g) Stohr, M.; Wahl, M.; Galka, C. H.; Riehm, T.; Jung, T. A.; Gade, L. H., Controlling molecular assembly in two dimensions: The concentration dependence of thermally induced 2D aggregation of molecules on a metal surface. *Angew. Chem. Int. Ed.* **2005,** *44* (45), 7394-7398; (h) Tahara, K.; Furukawa, S.; Uji-I, H.; Uchino, T.; Ichikawa, T.; Zhang, J.; Mamdouh, W.; Sonoda, M.; De Schryver, F. C.; De Feyter, S.; Tobe, Y., Two-dimensional porous molecular networks of dehydrobenzo[12]annulene derivatives via alkyl chain interdigitation. *J. Am. Chem. Soc.* **2006,** *128* (51), 16613-16625; (i) Ziener, U., Self-assembled nanostructures of oligopyridine molecules. *J. Phys. Chem. B* **2008,** *112* (47), 14698-717.

5. Stepanow, S.; Lin, N.; Payer, D.; Schlickum, U.; Klappenberger, F.; Zoppellaro, G.; Ruben, M.; Brune, H.; Barth, J. V.; Kern, K., Surface-assisted assembly of 2D metal-organic networks that exhibit unusual threefold coordination symmetry. *Angew. Chem. Int. Ed.* **2007,** *46* (5), 710-713.
6. Corso, M.; Auwärter, W.; Muntwiler, M.; Tamai, A.; Greber, T.; Osterwalder, J., Boron nitride nanomesh. *Science* **2004,** *303* (5655), 217-220.
7. (a) Blunt, M.; Lin, X.; Gimenéz-López, M. D.; Schröder, M.; Champness, N. R.; Beton, P. H., Directing two-dimensional molecular crystallization using guest templates. *Chem. Commun.* **2008,** (20), 2304-2306; (b) Garrahan, J. P.; Stannard, A.; Blunt, M. O.; Beton, P. H., Molecular random tilings as glasses. *Proc. Natl. Acad. Sci. U.S.A.* **2009,** *106* (36), 15209-15213; (c) Kampschulte, L.; Werblowsky, T. L.; Kishore, R. S. K.; Schmittel, M.; Heckl, W. M.; Lackinger, M., Thermodynamical equilibrium of binary supramolecular networks at the liquid-solid interface. *J. Am. Chem. Soc.* **2008,** *130* (26), 8502-8507; (d) MacLeod, J. M.; Ivasenko, O.; Perepichka, D. F.; Rosei, F., Stabilization of exotic minority phases in a multicomponent self-assembled molecular network. *Nanotechnology* **2007,** *18* (42), 424031-424040; (e) Zhou, H.; Dang, H.; Yi, J. H.; Nanci, A.; Rochefort, A.; Wuest, J. D., Frustrated 2D molecular crystallization. *J. Am. Chem. Soc.* **2007,** *129* (45), 13774-13775.
8. (a) Li, S. S.; Northrop, B. H.; Yuan, Q. H.; Wan, L. J.; Stang, P. J., Surface confined metallosupramolecular architectures: formation and scanning tunneling microscopy characterization. *Acc. Chem. Res.* **2009,** *42* (2), 249-59; (b) Mohnani, S.; Bonifazi, D., Supramolecular architectures of porphyrins on surfaces: The structural evolution from 1D to 2D to 3D to devices. *Coord. Chem. Rev.* **2010,** *254* (19-20), 2342-2362; (c) Samorì, P.; Fechtenkötter, A.; Jäckel, F.; Böhme, T.; Müllen, K.; Rabe, J. P., Supramolecular staircase via self-assembly of disklike molecules at the solid-liquid interface. *J. Am. Chem. Soc.* **2001,** *123* (46), 11462-11467; (d) Samorì, P.; Severin, N.; Simpson, C. D.; Müllen, K.; Rabe, J. P., Epitaxial composite layers of electron donors and acceptors from very large polycyclic aromatic hydrocarbons. *J. Am. Chem. Soc.* **2002,** *124* (32), 9454-9457.

9. Blunt, M. O.; Russell, J. C.; Gimenéz-López, M. D.; Taleb, N.; Lin, X. L.; Schröder, M.; Champness, N. R.; Beton, P. H., Guest-induced growth of a surface-based supramolecular bilayer. *Nat. Chem.* **2011,** *3* (1), 74-78.

10. Palma, C. A.; Samorì, P.; Cecchini, M., Atomistic Simulations of 2D Bicomponent Self-Assembly: From Molecular Recognition to Self-Healing. *J. Am. Chem. Soc.* **2010,** *132* (50), 17880-17885.

11. Tarini, M.; Cignoni, P.; Montani, C., Ambient occlusion and edge cueing to enhance real time molecular visualization. *IEEE T. Vis. Comput. Gr.* **2006,** *12* (5), 1237-1244.

12. Brooks, B. R.; Bruccoleri, R. E.; Olafson, B. D.; States, D. J.; Swaminathan, S.; Karplus, M., Charmm - a Program for Macromolecular Energy, Minimization, and Dynamics Calculations. *J. Comput. Chem.* **1983,** *4* (2), 187-217.

13. Halgren, T. A., Merck molecular force field .1. Basis, form, scope, parameterization, and performance of MMFF94. *J. Comput. Chem.* **1996,** *17* (5-6), 490-519.

14. Humphrey, W.; Dalke, A.; Schulten, K., VMD: Visual molecular dynamics. *J. Molec. Graphics* **1996,** *14* (1), 33-38.

15. Björk, J.; Hanke, F.; Palma, C. A.; Samorì, P.; Cecchini, M.; Persson, M., Adsorption of Aromatic and Anti-Aromatic Systems on Graphene through pi-pi Stacking. *J. Phys. Chem. Lett.* **2010,** *1* (23), 3407-3412.

16. Ryckaert, J. P.; Ciccotti, G.; Berendsen, H. J. C., Numerical-Integration of Cartesian Equations of Motion of a System with Constraints - Molecular-Dynamics of N-Alkanes. *J. Comput. Phys.* **1977,** *23* (3), 327-341.

17. (a) Ciesielski, A.; Palma, C. A.; Bonini, M.; Samorì, P., Towards Supramolecular Engineering of Functional Nanomaterials: Pre-Programming Multi-Component 2D Self-Assembly at Solid-Liquid Interfaces. *Adv. Mater.* **2010,** *22* (32), 3506-3520; (b) De Feyter, S.; De Schryver, F. C., *Chem. Soc. Rev.* **2003,** *32*, 139-150; (c) Lackinger, M.; Griessl, S.; Heckl, W. A.; Hietschold, M.; Flynn, G. W., Self-assembly of trimesic acid at the liquid-solid interface - a study of solvent-induced polymorphism. *Langmuir* **2005,** *21* (11), 4984-4988; (d) MacLeod, J. M.; Ivasenko, O.; Fu, C. Y.; Taerum, T.; Rosei, F.; Perepichka, D. F., Supramolecular Ordering in Oligothiophene-Fullerene Monolayers. *J. Am. Chem. Soc.* **2009,** *131* (46), 16844-16850; (e) Palma, C.-A.; Björk, J.; Bonini, M.; Dyer, M. S.; Llanes-Pallas, A.; Bonifazi, D.; Persson, M.; Samorì, P., Tailoring Bicomponent Supramolecular Nanoporous Networks: Phase Segregation, Polymorphism, and Glasses at the Solid-Liquid Interface. *J. Am. Chem. Soc.* **2009,** *131* (36), 13062-13071.

18. Schlickum, U.; Decker, R.; Klappenberger, F.; Zoppellaro, G.; Klyatskaya, S.; Auwarter, W.; Neppl, S.; Kern, K.; Brune, H.; Ruben, M.; Barth, J. V., Chiral kagome lattice from simple ditopic molecular bricks. *J Am Chem Soc* **2008,** *130* (35), 11778-11782.

Chapter 5: reactivity on surface: Attempts to build 2D covalent organic frameworks

Some of the most exciting discoveries of the last years are related to different allotropic forms of carbon, ie. Fullerenes, Nanotubes and Graphene,[1] respectively 0, 1, 2 dimensional arrays of sp2 carbons. The relevance of such compounds in the last years trough many branches of science and technology arises from many aspects, but is generally related to the presence of a conjugated π electron cloud which confers different electrical properties to each one. It is necessary to focus with some more details on the properties of graphene as a 2D extended network of sp2 hybridized carbons, which confers it technologically appealing properties such as a remarkable conductivity:

Due to the hexagonal symmetry of the Brillouin zone, the E-k relation is linear for low energies and causes zero effective mass for holes and electrons.[2] Since such a property does not necessarily depend on the carbon atoms,[3] it is difficult to predict changes in properties when modifying the network. In other words, graphene can be viewed as a bi-dimensional analog of polyacetylene, in that its properties can be modulated by the type of "starting monomer" or repeating unit. Indeed, tailoring the hexagonal network is the aim of building 2D COFs, and is an actively pursued research topic in our group. The molecules were synthesized by K. Müllen group in Max Plank Institute for Polymer Research, Mainz.

Reactions on surfaces

The reactivity on surfaces is generally directly linked to the nature of the surface, ranging from nickel and other metals to active carbons and zeolites.[4] The perspective adopted in this work is slightly different, in that we focus on surface-confined reactions. The first objective is not to develop new catalysts but to unveil the mechanisms of formation of 2D supramolecular or polymeric structures. There are numerous examples in the recent literature, aimed towards the polymerization in 2D, clearly winded by the graphene explosion.[5] The questions that such challenge pose are however independent and nowadays way far from any commercial application.

Various approaches exist in the literature that can be grouped in different categories –

Coordination polymers (CP), Metal-Organic Frameworks (MOFs) and Covalent Organic Frameworks (COFs)

The differences between the two frameworks lie in the type of chemical bond involved among the tectons, whereas the difference between CPs and MOFs is a long debated topic.[6] One definition includes the MOFs as a subset of the CP,[7] while *Tranchemontagne et al*, differentiated them by the amount of charge donated by the metal to the ligand.[8]

The generally seeked objective in COFs is to obtain a conjugated macromolecule through formation of C=C bonds using a diverse array of synthetic reactions, .[9] Among many others, current literature reports involve bromination and subsequent nucleophilic substitution?,[10] imine formation, amination, or condensation of boronic acids.[5h, 11]

A key feature of such reactions is *dynamic* and reversible nature, a property allowing for "error-checking", as pointed out by Stoddart in his definition of Dynamic Covalent Chemistry.[12] Such a concept is extremely similar to the one expressed in the Self-assembly section (see chapter 1).

The challenges from both synthetic and theoretical perspectives are substantial, but some successful examples of 2d conjugated polymerization have been recently reported, (figure 1).

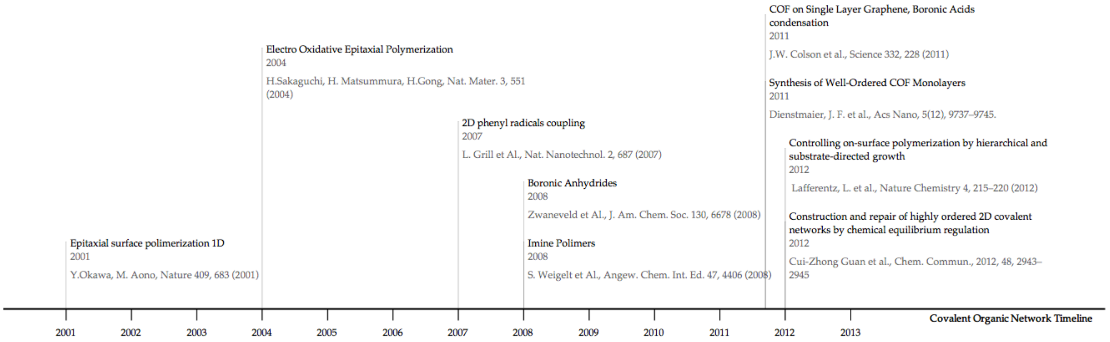

Figure 1: Timeline of some milestone publications in the field.

We chose as suitable reactions the condensation of boronic acids to form boroxines, and their coupling with alcohols. One way to proceed is thermal condensation of boronic acids into boroxines, their cyclic anhydrides (Figure 2).

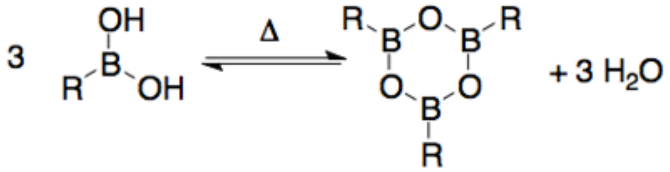

Figure 2: Dehydration reaction of boronic acids Not a chemdraw file, bad quality of picture

Several examples of COFs derived from boronic acid dehydration were reported in the last year.[9a, 13] Nonetheless, the kinetic aspects of polymerization, as well as factors influencing the formation of such complex systems are far from being completely understood.[14] A couple of recent publications showed dramatic improvements of the kinetics of formation of ordered 2D polymers due to the presence of water.[5b,h] Such effects were not taken into consideration in our early work, as it seemed counter-intuitive, based on le Chatelier's principle, to add water to a polycondensation reaction. In this work we tested the conditions reported and tried to modulate the formation of the different 2dCOFs of boronic acids with addition of water in the reaction system. One could also expect to improve the reaction and the connectivity by performing it from a pre-ordered assembly. We reasoned that self assemble the material in a SAM prior to reaction would increase the kinetics of formation and diminish the defects, by reducing the diffusion barrier and pre-arranging the reactive groups.

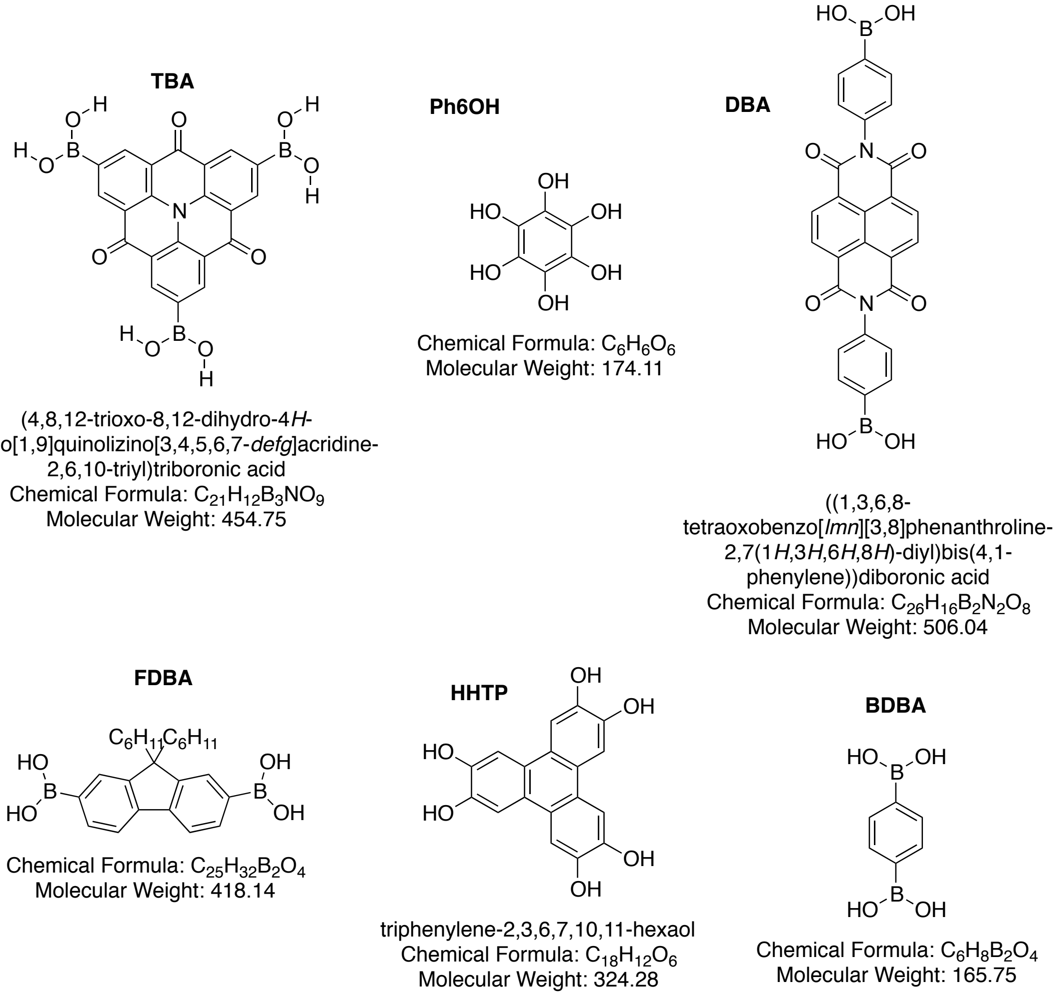

TBA

(4,8,12-trioxo-8,12-dihydro-4*H*-benzo[1,9]quinolizino[3,4,5,6,7-*defg*]acridine-2,6,10-triyl)triboronic acid
Chemical Formula: $C_{21}H_{12}B_3NO_9$
Molecular Weight: 454.75

Ph6OH

Chemical Formula: $C_6H_6O_6$
Molecular Weight: 174.11

DBA

((1,3,6,8-tetraoxobenzo[*lmn*][3,8]phenanthroline-2,7(1*H*,3*H*,6*H*,8*H*)-diyl)bis(4,1-phenylene))diboronic acid
Chemical Formula: $C_{26}H_{16}B_2N_2O_8$
Molecular Weight: 506.04

FDBA

Chemical Formula: $C_{25}H_{32}B_2O_4$
Molecular Weight: 418.14

HHTP

triphenylene-2,3,6,7,10,11-hexaol
Chemical Formula: $C_{18}H_{12}O_6$
Molecular Weight: 324.28

BDBA

Chemical Formula: $C_6H_8B_2O_4$
Molecular Weight: 165.75

Figure 3: Investigated molecules.

The molecules we decided to investigate differ from the previously reported entities at two levels: the presence of heteroatoms and the dimension of the conjugated bridge. One of our objectives was to realize mono-component 2D-COFs from the two boronic acid derivatives **DBA** and **TBA** (figure 4), as well as to produce the mixed COFs via the bi-component reaction with a polyol to form a boronic anhydride. Examples of the target structures are reported in figure 5. The different structures have different pore-sizes, and should be easily distinguishable via STM, once formed.

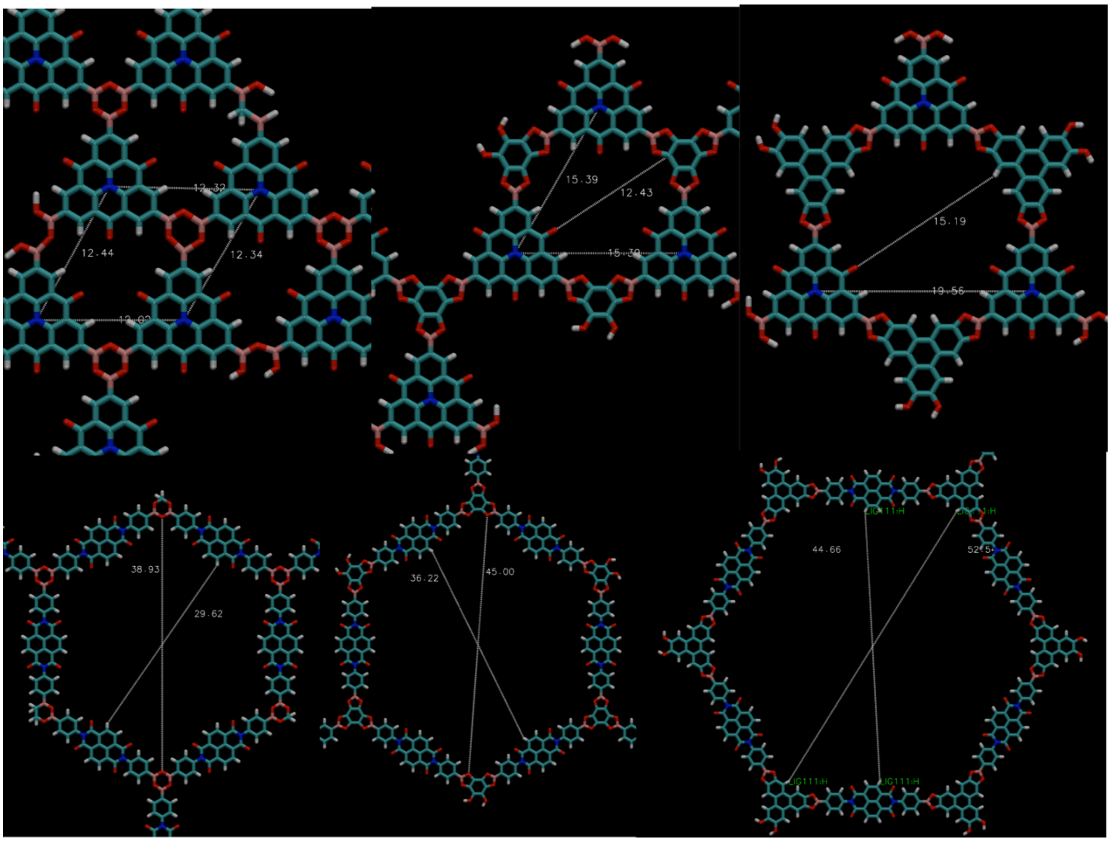

Figure 4 Structures of targeted COFs: clockwise from upper left: pure TBA (pore ø <1nm), TBA+Ph6OH (ø ~ 1.25nm), TBA + HHTP (ø ~ 1.5 nm), DBA + HHTP (ø 4.5nm), DBA + Ph6OH, (ø 3.5nm), pure DBA (ø~ 3nm).

Step 1: Physisorption and first reaction attempts:

The first objective was to form a physisorbed SAM, and then trigger the reaction:

Formation of a SAM on HOPG:

The molecules were dissolved in the solvents reported in table 1 with an approximate concentration of 1 mM, and diluted to the concentrations 100 µM and 10 µM. However, in the case of molecule **DBA**, STM investigation of diluted solutions, i.e. 100 µM and 10 µM did not lead to the formation of ordered monolayers, thus we limited our studies to films obtained from more concentrated solutions (i.e. 1mM).

Solvent	*Concentration*	*Molecule*
NA	**1mM,** 100uM, 10 uM	**TBA, DBA**
PO	1mM, 100uM, 10 uM	**TBA,DBA**
TCB	1mM, 100uM, 10 uM	“”

TD	1mM, 100uM, 10 uM	“”
Mesitylene : dioxane 1:1	1mM, 100uM, 10 uM	“”
HA	1mM, 100uM, 10 uM	“”
OA	1mM, 100uM, 10 uM	“”

Table 1: deposition condition tested.

All molecules were visualized by STM only upon the use 1-nonanoic acid; the use of other solvents, i.e. 1,2,4-trichlorobenzene, 1-phenyloctane, Mesitylene-Dioxane 1:1 mixture, heptanoic acid, octanoic acid, and normal tetradecane, did not lead to the formation of ordered monolayers. A SAM of molecule **TBA** was never observed.

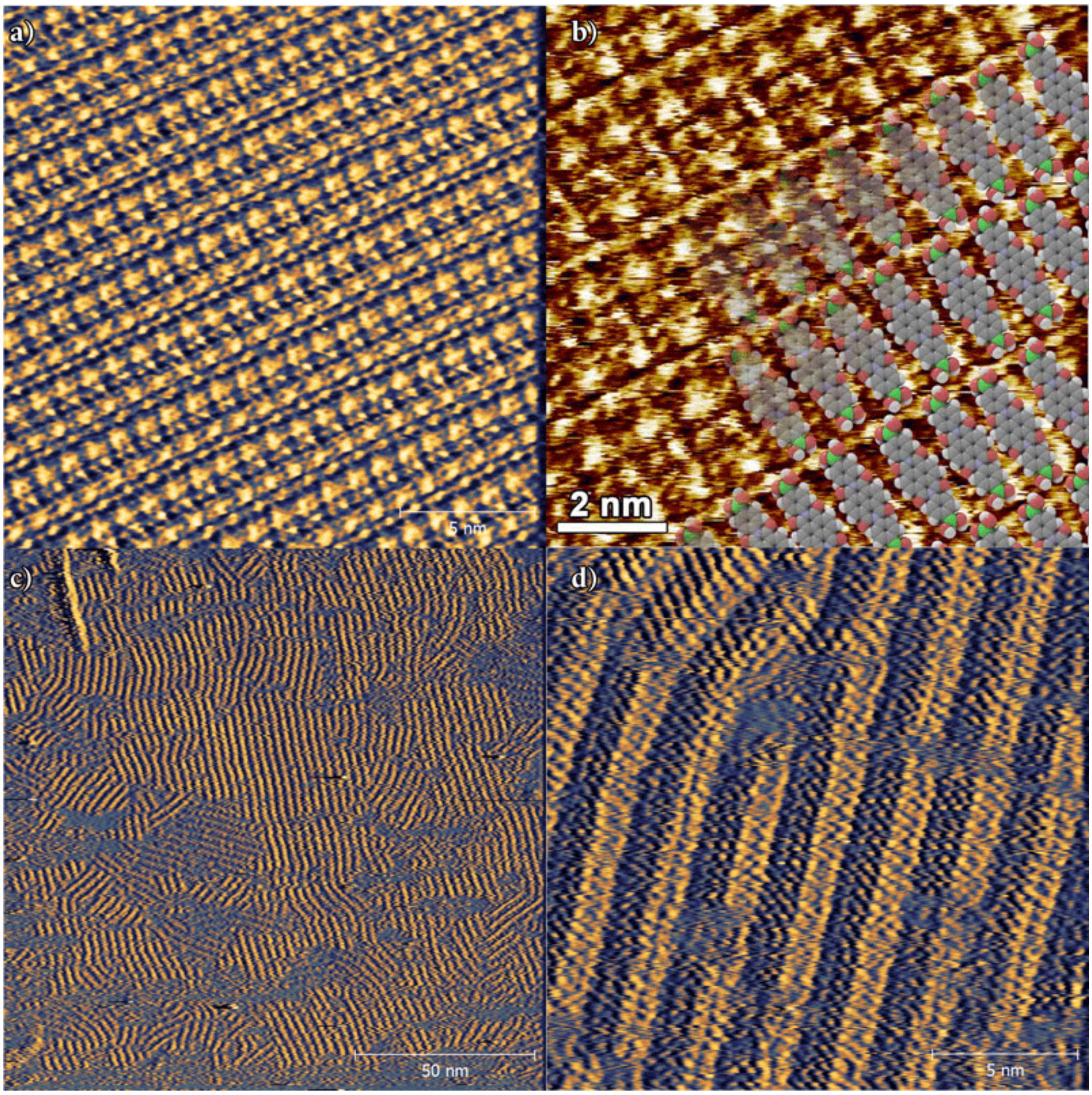

Figure 5: a,b)Scanning Tunneling Microscopy current images portraying the Self Assembled Monolayers of DBA and the proposed packing model at the Nonanoic Acid/HOPG interface; 1.6mM solution, Unit Cell parameters: a: 1.4 ± 0.2 nm, b: 1.0 ± 0.2 nm γ 69 ± 2˚, A:1.3 ± 0.3 nm2; Tunneling Parameters It=10pA, Vt=800mV. c,d) DBA at the Mesitylene-Dioxane/HOPG interface, after deposition from warm solution

(50 ˚C) on pre-heated substrate (90 ˚C); The SAM formed is rich in defects. Probable Co-Adsorption of Solvent Molecules.

The structure is lamellar and the diboronic acid **DBA** showed the formation of a brick wall architecture if dissolved in nonanoic acid, or mesitylene-dioxane(1:1). SAMs of the triboronic acid were not observed under any tested conditions. This might be either related to a nonplanarity of the molecule, or to a too high solubility. The geometrical minimization of the molecule, is under evaluation via DFT calculations, due to ambiguous results obtained with the MM2 optimization.

Solvent	*Conditions*
NA	1mM, bulk, 80˚C
	1mM, RT solution, dropcast on hot substrate (80˚C)
	1mM, 90˚C solution, dropcast on hot substrate (80˚C)
	1mM, RT solution, dropcast on very-hot substrate (>200˚C)
Mesitylene : dioxane 1:1	1mM, bulk, 80˚C
	1mM, RT solution, dropcast on hot substrate (80˚C)
	1mM, 90˚C solution, dropcast on hot substrate (80˚C)
	Solvothermal, 48h 120˚C;
NA + Pyridine	1mM, bulk, 80˚C
	1mM, RT solution, dropcast on hot substrate (80˚C)
	1mM, 90˚C solution, dropcast on hot substrate (80˚C)
MES-DOX 1:1 + Py	1mM, bulk, 80˚C
	1mM, RT solution, dropcast on hot substrate (80˚C)
	1mM, 90˚C solution, dropcast on hot substrate (80˚C)

Table 2: reaction condition tested.

The first attempts to observe a covalent organic framework were conducted as reported in Table 2, by heating the solution or the substrate followed by dropcasting on top of a clean HOPG surface. None of the attempts resulted in the formation of the expected porous structure.

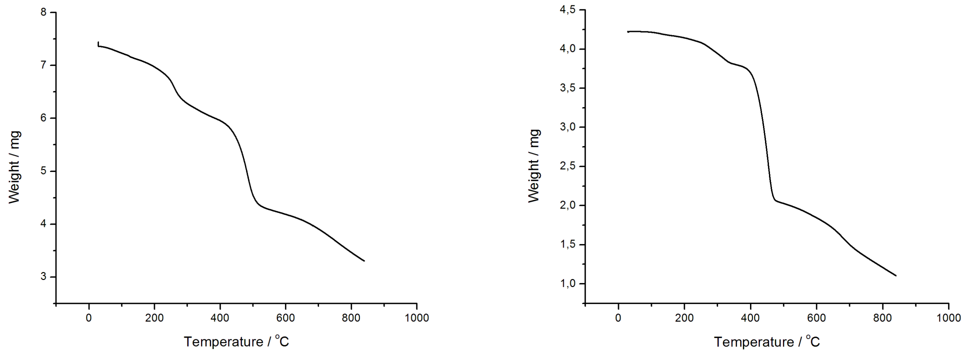

Figure 6: TGA of TBA and DBA respectively.

From the TGAs in fig7 we observed that the first molecular weight loss, probably due to the dehydration, took place at temperature higher than 200°C. We attributed the absence of reaction under the conditions of testing to the lack of catalytic effect of the graphite surface and the absence of pyridine-catalyzed reaction was a surprise. However, the pyridine strongly interacted with the STM measurement, generating heavy capacitive effects and making the imaging impossible if used in concentration higher than 1% (v/v). As a first result we know that higher temperatures are required to achieve the reactions, which therefore have to be probably done in bulk to avoid damaging the instrument. Efforts in the investigation of possible effects of pyridine as a catalyst should be continued, and paired with the testing of multicomponent networks with the formation of a boronic anhydride via the reaction with HHTP.

Water addition

The molecules were dissolved preparing the solutions reported in table 1. According to *Guan et al* [13a] a drop of solution was applied to the basal plane of HOPG, and then the substrate transferred inside a 25 mL pressure tube, containing ca 1.1 g of $CuSO_4$•$5H_2O$ (commercial prolabo crystalline>99%); The pressure tube was then sealed and transferred in an oven and heated according to table 1. After the heating phase, the pressure tube is let to cool down inside the oven until room temperature; the samples were extracted, glued on top of a 15 mm diameter magnetic disk with acrylic "super attak" adhesive, contacted using silver paste (Aldrich Chemicals) to the metal base and investigated by STM. The STM tips were mechanically cut from a Pt/Ir wire (90/10, diameter 0.25 mm, commercially available from Goodfellow.uk).

exp id	solvent	Conc. [µM]	volume [µL]	temp[˚C]	time [h]	notes
1	THF	100	5	150	1	[guan2012]
2	THF	100	100	150	1	
3	THF	100	100	150	1	Open vial
4	NA	1000	5	150	1	sat sol
5	THF	100	100	200	1	
6	THF	100	5	150	1	Htsva
7	NA	1000	5	200	1	
8	NA	1000	5	200	1	Htsva
9	HA	1000	5	150	1	
10	MDOX	1000	5	150	1	Htsva
11	DMSO	10000	5	150	1	

Table 3: experimental condition tested

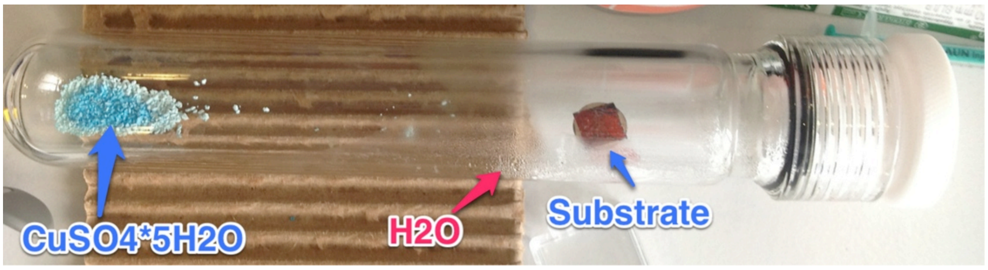

Figure 7 : Image of the pressure tube. There are evidences of the presence of water on the tube walls after being released from the copper sulfate.

None of the tested conditions resulted in observable 2D-cofs on the graphite surface. Most of the samples resulted in formation of a brown powder, which was not enough to allow proper characterization. In all the samples during heating the $CuSO_4$•$5H_2O$ changed colour from deep blue to pale white at the maximal temperature, to recover back the blue color (with a slightly lighter shade) after cooling down. Water droplets were also observed on the tube walls, as well as a pale green compound together with the blue salt (figure 7). Annealing for one hour in a closed vial with water (µL) led to the dissolution of the powder particles . However, only large tridimensional aggregates could be observed with STM.

Samples 6,8,10 presented thin film interference patterns visible under optical microscope, in which small powdery particles were embedded fig.8).

No differences were observed with salt in a closed or open vial conditions.

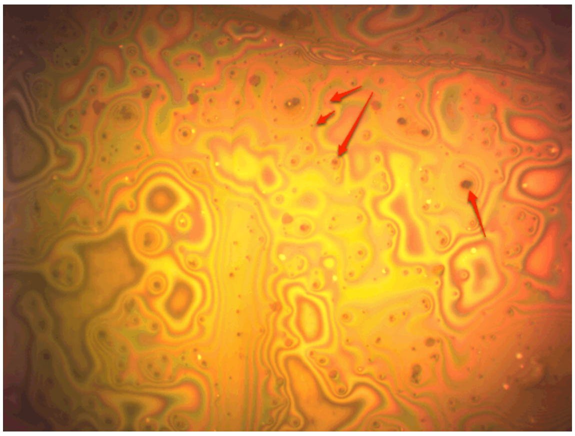

Figure 8: thin film interference showed from sample #8 (nonanoic acid) on top of hopg, optical microscope 40/0.60; Specks of undissolved powders are indicated by red arrows

The presence of powder specks suggested that the monomer was insoluble in the solvents tested This issue of solubility constituted a major hurdle to our studies, combined with a potential chemical degradation of the molecules upon storage

Control of the purity of the monomers

To check the eventual degradation of the monomer, and to see if a thermal or pyridine-catalyzed dehydration occurred, ^{1}HNMRs were conducted on a bruker Avance 400MHz, using a 1mM solution of **DBA** in DMSO-d_6; Thermal sweeps were carried out by heating steps of 10°C and after 5' of equilibration at a given temperature. IR and MS spectra gave inconclusive results and not reported herein.

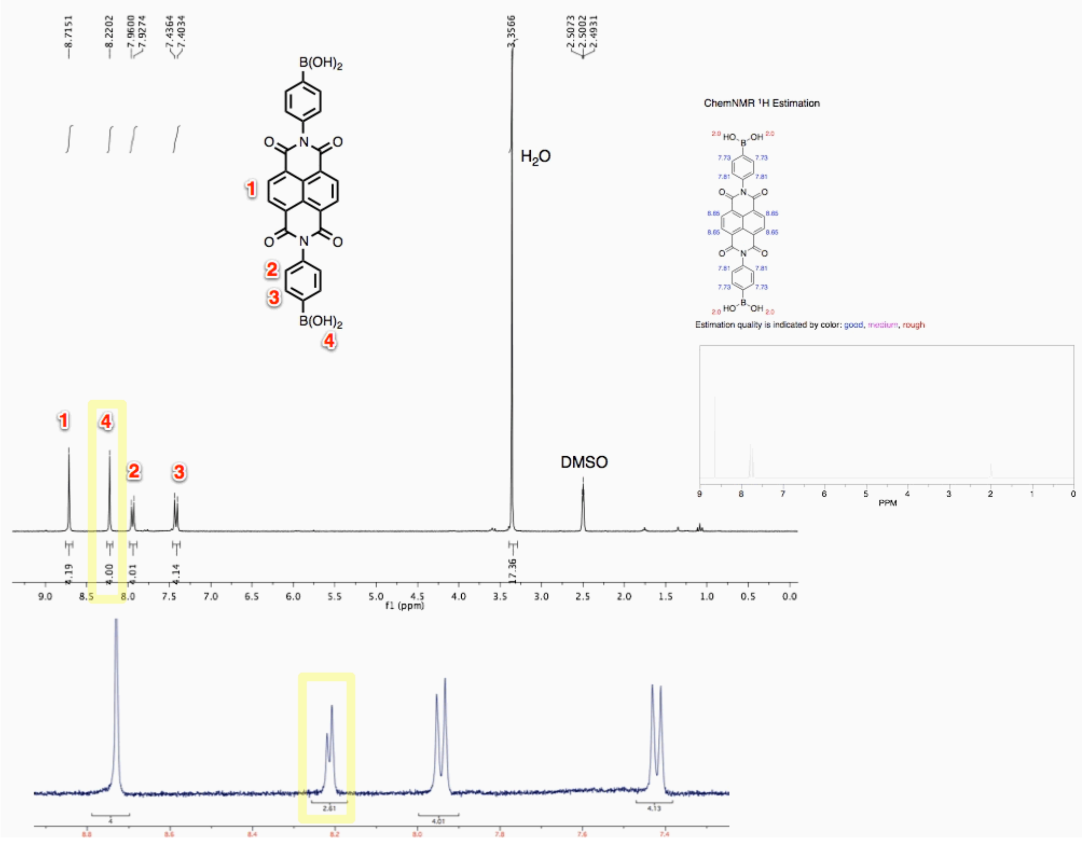

Figure 9: comparison between original(top left), estimated spectrum (top right), and new experimental (bottom) NMRs; Numbers for bottom one? INTEGRATION NUMBERS UNREADABLE

One can observe a close-to-50% decrease in the integral value corresponding to the boronic acid protons over the course of a year (figure 9, yellow rectangle). Combined with the absence of new, uncharacterizable peaks, this observation could be accounted for by an oligomerization of the starting material.

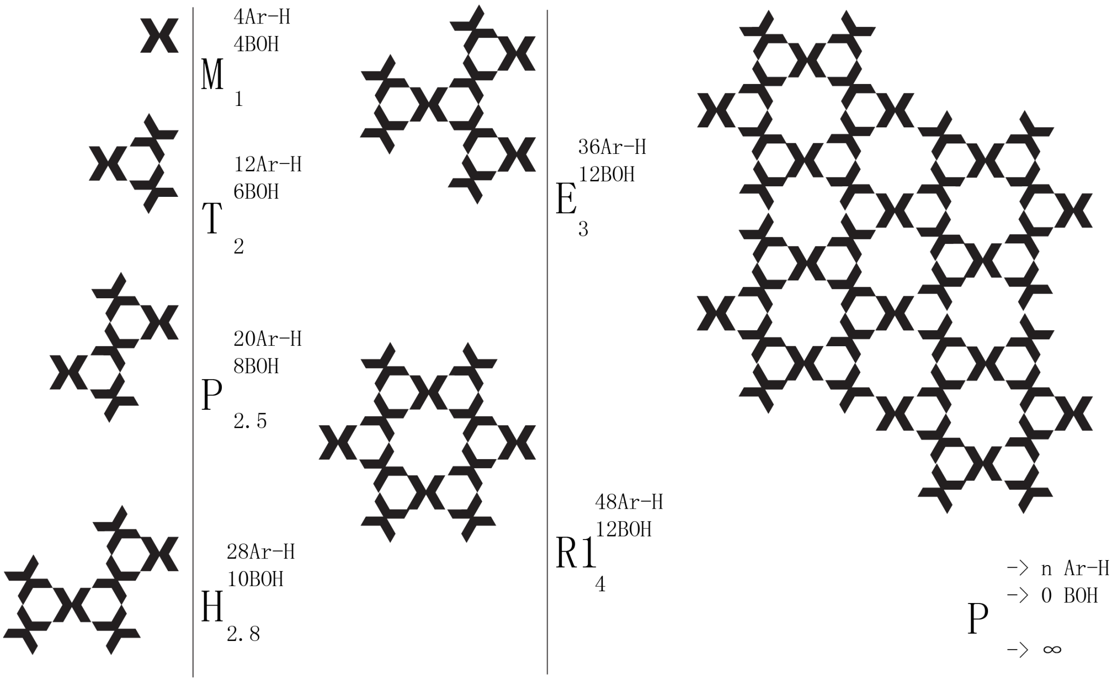

Figure 10: different oligomers, and the relative ratios between aromatic boronic acid protons.

Determination of the presence of specific oligomers and their relative proportions, is under investigation. However, observing the integral value and the change in shape of the peak (figure 9, yellow rectangle) which passes from a singlet to a doublet, it may be in fact be the convolution of two different singlets, one from the trimer and one from the monomer. In such case, an integral of 2.5 is compatible with a ratio 1:1 between monomer and trimer.

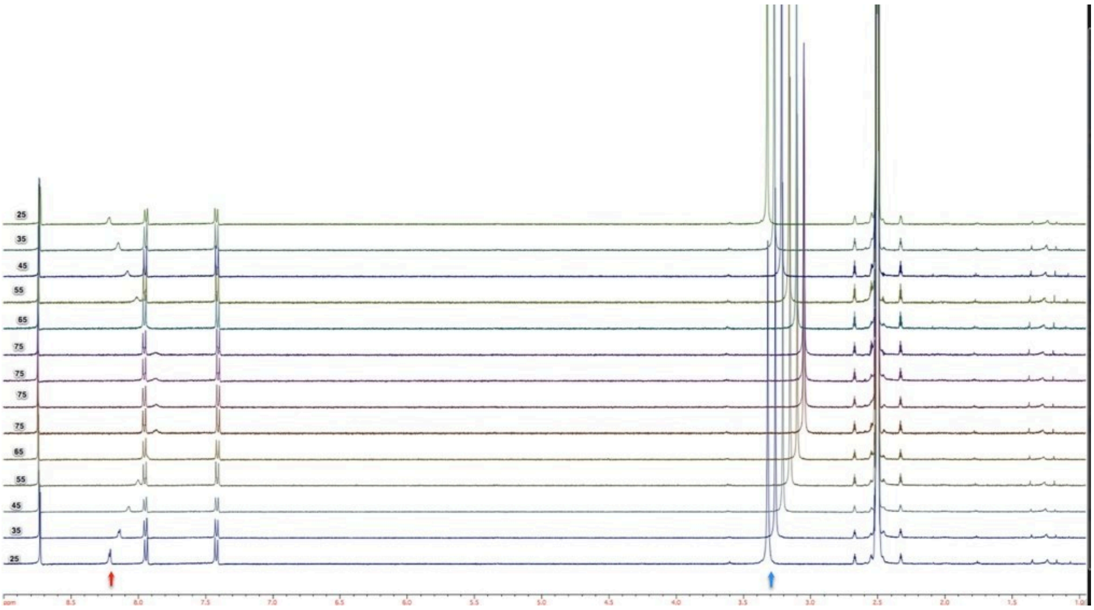

Figure 11: thermal sweeps of the monomer solution. Note the shifts of the boronic acid hydrogen (red arrow) and of the water (blue);

Is also evident from Figure 11 the shift in the field of the peak relative to the boronic acid and of the water. This is compatible with the pH dependence from temperature, which unequivocally identifies the BA proton.;

In Figure 11 is also well visible a broadening of the peak after the thermal treatment.

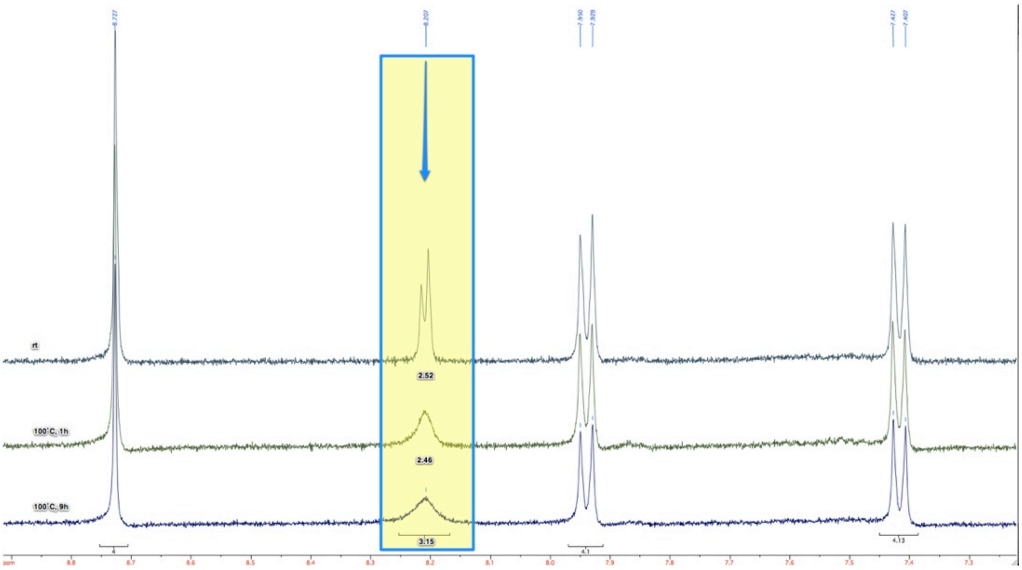

Figure 12: integral evaluation after different heating times (intensities are not in scale);

Such behavior is reported in Figure 12: The dramatic broadening, suggest presence of a distribution of species of BA, whereas the increase in the integral value should indicate the opposite. A possible explanation might be searched in growth mechanisms. If we imagine a critical oligomer dimension at high temperature, the nuclei of a given size might grow, while the oligomer of smaller size will hydrolyze to the monomer.

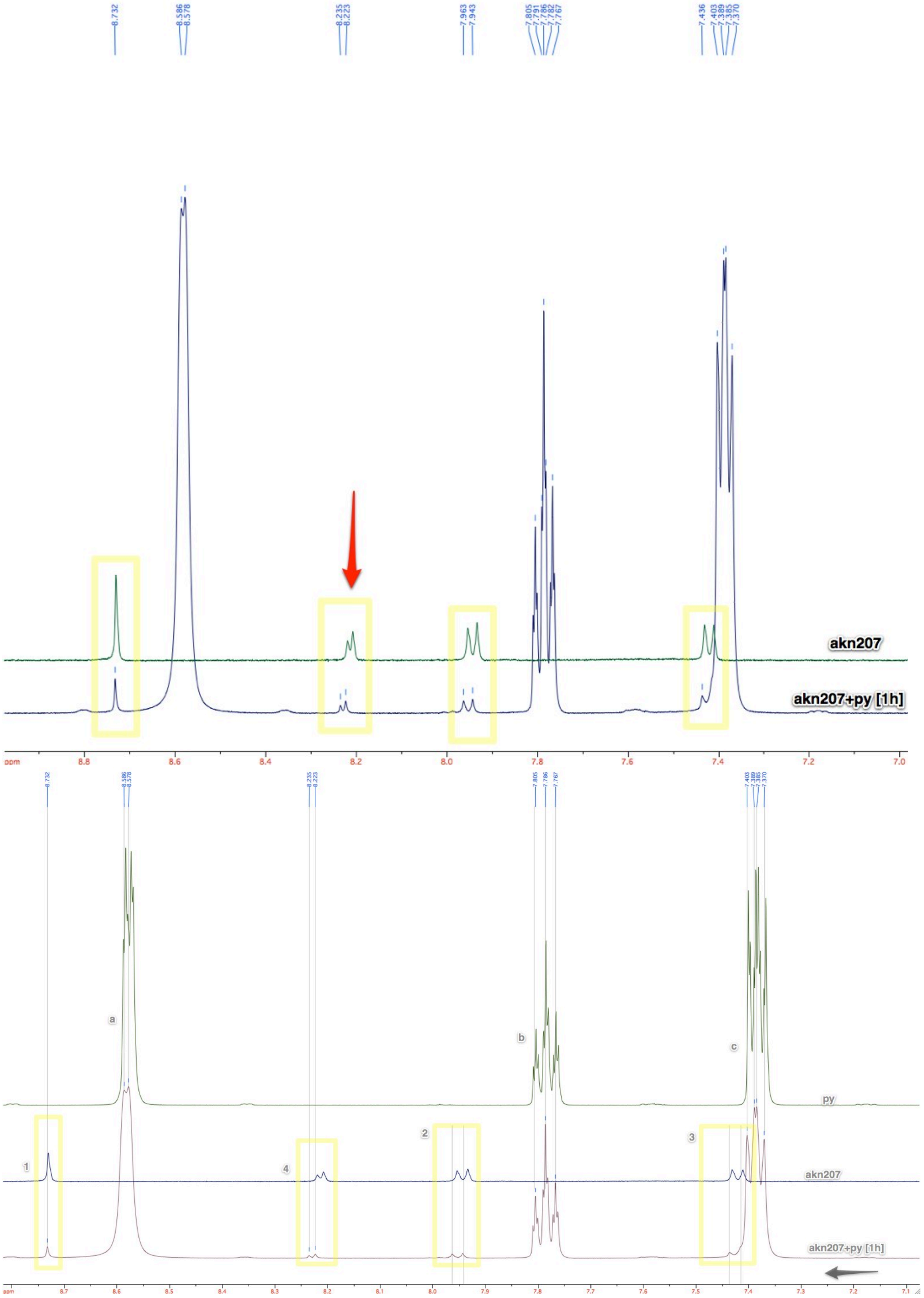

Figure 13: effect of a mixture with a large excess of pyridine, one hour after mixing (intensities are not in scale), and b) same comparison with the pyridine nmr, highliting the shifts.

Figure 13 shows the effect of the mixing with py. The differences in the chemical shifts and in the integral values are probably due to the formation of a complex with the pyridine; the shift is comparable to similar values already reported in literature, for the formation of complexes with an amine[15]. The formation of a complex is not sufficient to demonstrate the formation of boroxine rings. The shift of the pyridine peaks is very small.

In summary, from the performed NMR experiments we can conclude:

1) the monomer is degraded. Probably already contains a mixture of oligomers, most likely a 1:1 ratio of monomer/trimer.
2) There's an effect of the temperature on the shape of the peak, and, in conjugation to the increase in the H_2O integral, suggest the occurrence of the reaction, even at relatively low temperature.
3) In combination with pyridine there's formation of a Boronic-Acid –py or a boroxine-py complex.

Formation of COFs of TBA

The first step was again to obtain a physisorbed SAMs of the boronic acids on highly oriented pyrolitic graphite (HOPG) , and their visualization with scanning tunneling microscopy. Subsequently, after interpretation of the 2D packing, we aimed to induce dehydration of the BA to form a covalent organic framework;

akn205

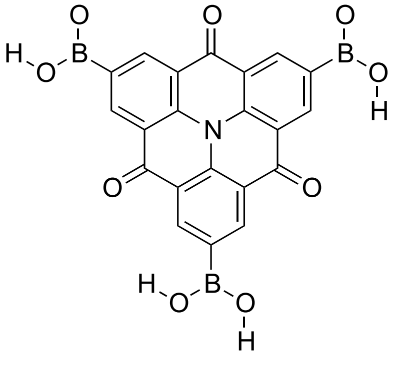

(4,8,12-trioxo-8,12-dihydro-4*H*-
benzo[1,9]quinolizino[3,4,5,6,7-*defg*]acridine-
2,6,10-triyl)triboronic acid
Chemical Formula: $C_{21}H_{12}B_3NO_9$
Molecular Weight: 454.75

The molecules were dissolved in THF until formation of a saturated solution(1.27mg in 2mL THF); a drop of ca 5uL was deposited on hopg. The substrate was then inserted in a pressure tube (140ml) with 1.1 g of $CuSO_4$•$5H_2O$, and heated in oven at 150°C for 1h. The substrate was then extracted rinsed with N_2 and imaged. Due to the presence of aggregates, an annealing procedure was performed, heating the sample inside a tube (30ml) at 110°C in presence of 10μL of water.
After solvent evaporation, an apolar high boiling solvent, ie, heptanoic, octanoic, nonanoic acid, and phenyloctane were added, during the acquisition of the images. Similar procedure was performed with DMSO, and the structure observed in figure 2 comes from a mixture 1:1 with HHTP heated 3h at 100°C.

All the previous attempt never resulted in a formation of an ordered monolayer, whereas using the reported procedure an SAM was observed in three cases:
In NA, PO, and after mixing in dmso with HHTP.

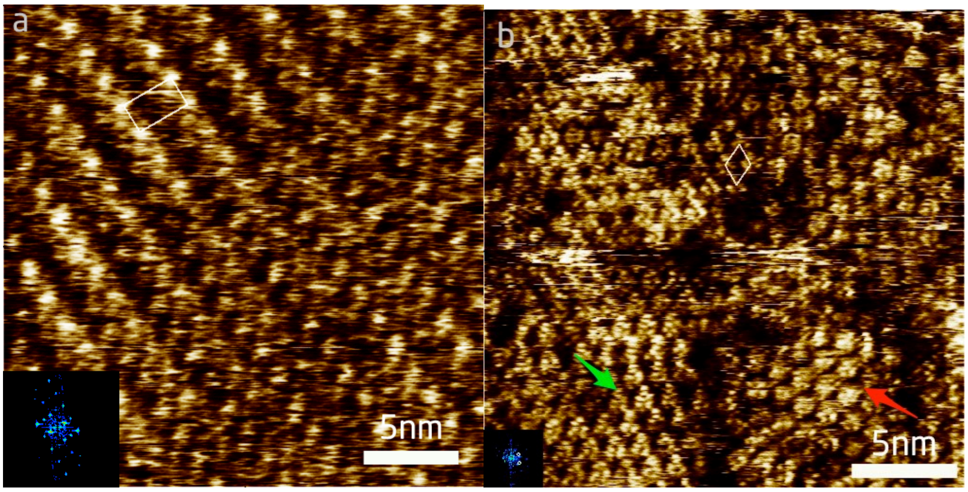

Figure 14: a) height image of the self-assembled hydrogen bonded network of the TBA in nonanoic acid, and the 2dFFT. b) assemblies observed after dropcasting a mixture of TBA and HHTP in dmso and redispersing with nonanoic acid. a) unit cell parameters: a=2.9±0.2nm b=1.7±0.2nm, ϒ=92±2° A=4.8 ± 0.7nm^2. Tunneling parameters, I_t=20pA V_t=250mV. b) unit cell parameters: a=1.2±0.2nm b=1.1±0.2nm, ϒ=63±2° A=1.2 ± 0.3nm^2. Tunneling parameters, I_t=20pA V_t=100mV.

The observed monolayers are very different. The lamellar structure in figure 1a) suggest the formation of an hydrogen bonded network, where the molecules are adopting a syn-anti configuration of the boronic acid moiety. The model, however has still to be perfected. In figure 1b), is apparent the presence of small domains with two diferent hexagonal patterns (red and green arrows), and seems that multiple layers are also present.

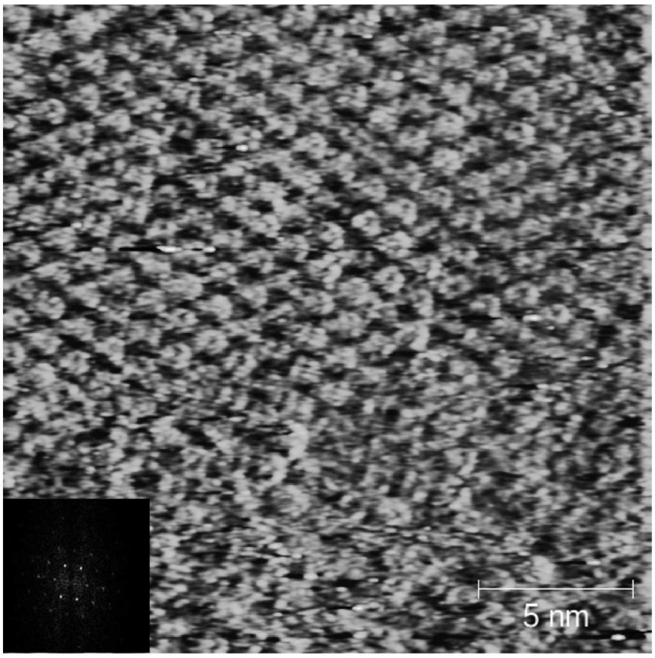

Figure 15: hhtp self assembled on hopg, deposition from nonanoic acid, 166µM solution; unit cell parameters: a=1.0±0.2nm b=1.1±0.2nm, ϒ=120±2° A=0.9 ± 0.3nm^2. Tunneling parameters, I_t=100pA V_t=350mV.

Such pattern, is compatible with the formation of a surface covalent organic framework, and as shown in figure 2 might as well be due to the hydrogen bonded assembly of HHTP. Since the experiment has not been already reproduced, there's no demonstration that the two hexagonal domains might be due to presence of both networks. However, due to the evident differences in contrast and in the aspect of the patterns, the presence within HHTP domains of the 2dCOF of TBA could not be excluded;

Mixed Networks:

Comparison of the reactivity of the monomers towards dehydration or formation of mixed anhydrides.

dehydration
boronic acid

condensation
boronic acid + diol

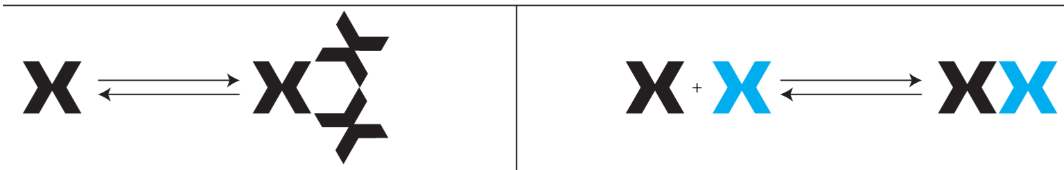

$$\frac{\delta[A]}{\delta t} = k[A]^3$$

$$DP \propto A_0\sqrt{2kt}$$

$$\frac{\delta[A]}{\delta t} = k[A][B] = k[A]^2$$

$$DP \propto A_0 kt$$

Figure 16: comparison of theorical kinetics and degree of polymerization dependence in the two investigated reactions, derived using a simple Flory derivation.

Idea:

Considering scheme 1, is evident that the reaction of condensation via formation of anhydrides might be more rapid and more suitable for the 2D-polymerization.

In this work we verified the different behaviors and the different kinetics of the components in scheme 2.

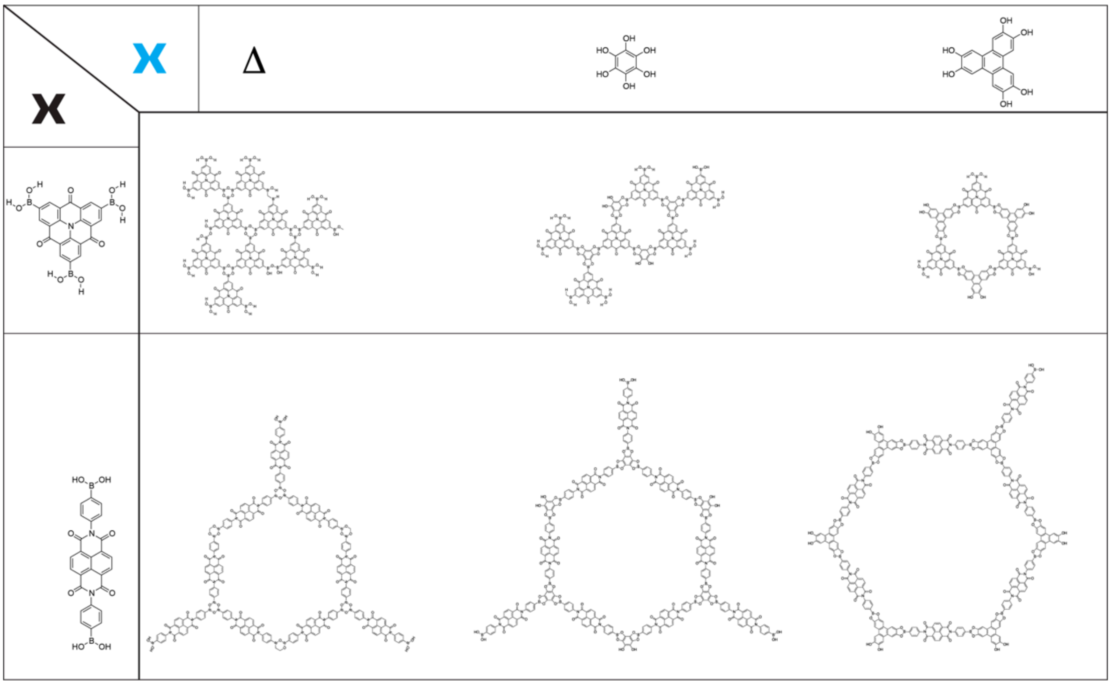

Figure 17: comparison of the expected structures vs the components.

experimental details

NMRs were conducted on a bruker Avance 400MHz, on the solutions reported in table 1 in d-DMSO, at two different concentrations, at room temperature, and after 14h of heating at 100°C.

comp1 A	comp2 B	qty1 [µL]	conc 1 [mM]	tot vol. [µL]	conc1 tube [mM]	qty 2 [µL]	conc 2 [mM]	conc2 tube [mM]	stoicho metric ratio [A/B]
f60h	–	60	1	400	0.15	0	0	0	–
f60h	–	90	2	400	0.45	0	0	0	–
hhtp	–	15	4	400	0.15	0	0	0	–
hhtp	–	30	4	400	0.3	0	0	0	–
TBA	–	15	4	400	0.15	0	0	0	–
TBA	–	30	4	400	0.3	0	0	0	–
DBA	–	90	1	400	0.225	0	0	0	–
DBA	–	180	1	400	0.45	0	0	0	–
f60h	**TBA**	60	1	400	0.15	15	4	0.15	1.00
f60h	**DBA**	60	1	400	0.15	90	1	0.225	0.67
hhtp	**TBA**	15	4	400	0.15	15	4	0.15	1.00
hhtp	**DBA**	10	4	400	0.1	60	1	0.15	0.67
f60h	**TBA**	30	4	400	0.3	60	2	0.3	1.00
f60h	**DBA**	30	2	400	0.15	90	1	0.225	0.67
hhtp	**TBA**	15	4	400	0.15	15	4	0.15	1.00
hhtp	**DBA**	10	4	400	0.1	60	1	0.15	0.67

Table 4 : composition of the various samples.

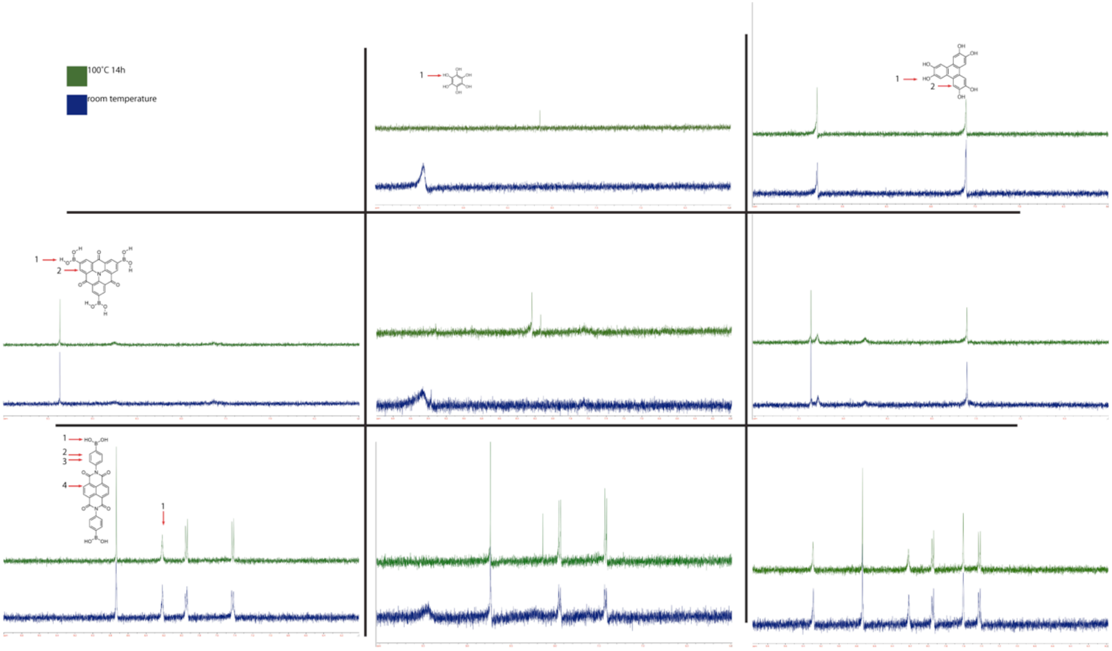

Figure 18: NMR results in the 10/7 ppm range, on the high concentration solutions. The blue line corresponds to the freshly prepared solution, while the green one is after heating 14hours at 100˚C.

Observations:

Work in progress, the experimental results are still under investigation

COFs of smaller molecules - BDBA

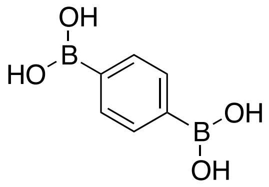

1,4-phenylenediboronic acid
Chemical Formula: $C_6H_8B_2O_4$
Molecular Weight: 165.75

The next step was to reproduce the already reported experiments in order to verify if the reported synthetic procedure is feasible with TBA/DBA.

#	conc [mM]	qty [μL]	solvent	w/	temp	h	res
1	0.1	5	thf	cuso4	150	1	x
2	1	5	thf	cuso4	150	1	x
3	10	5	thf	mgso4	200	1	x
4	sat	5	–	H2o	200	3	pre-poly
5	sat	5	nonac	h2o	120	1	x
6	sat	5	heptac	h2o	120	1	x
7	sat	5	thf	h2o	120	1	x
8	sat	5	thf	h2o	150	1	x
9	sat	5	thf	h2o	130	14	x
10	sat	5	thf	h2o	200	1	x

Table 5: tested samples

- Method 1 - Guam[13a] - samples 1-3,10

ca 1.1 grams of $CuSO_4•5H_2O$, commercial (crystallized >99% PROLABO), or ca 1.3 mg of $MgSO_4•7H_2O$ were weighted and inserted in a 140mL pressure tube (ace). 5μL of a solution of BDBA commercial (sigma-aldrich) (concentration are reported in table1), where dropcasted on top of a freshly cleaved HOPG substrate (already mounted on the support for imaging) and subsequently transferred inside the tube. The tube was closed and inserted in a pre-heated oven at the temperature reported in table 1.

After the heating phase, the pressure tube was open and the substrate imaged with optical microscope and with STM.

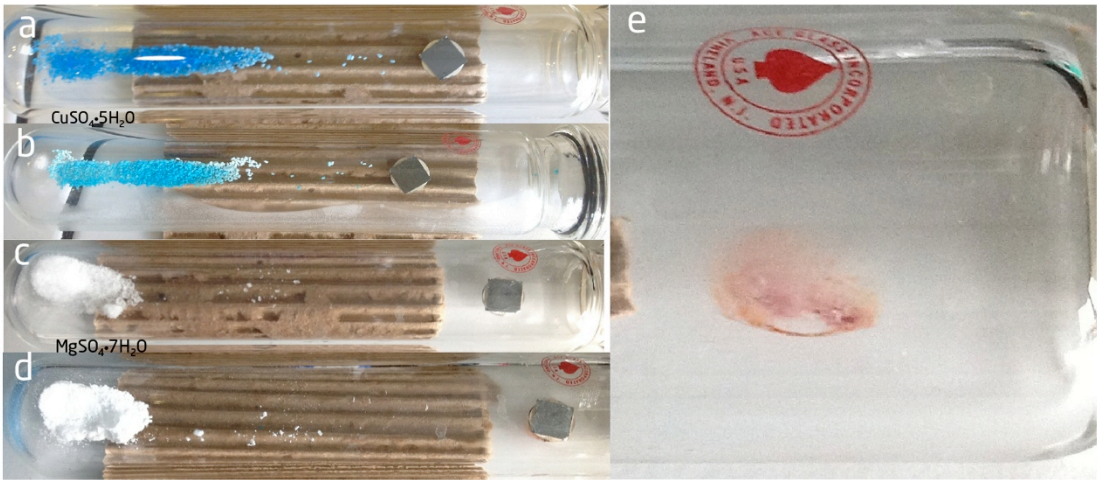

Figure 19: differences pre-and after heating the sample in presence of a water releasing salt. a,c sample 1,3 before heating, b,d,e after heating at 150, 200°C per 1h. e) close up of the system in sample 3 showing the presence of a red liquid inside the pressure tube.

Evident color changes in the salt before and after heating, and evident deposition of H_2O on the tube walls, confirms the dehydration of the salts and the presence of the water in the system during the reaction. There are no evident aggregates on the sample, which surface appears clean and lucid. The small rims formed during evaporation of the thf solution before heating seems to have disappeared. A small qty of a red compound is observed under the substrate when heating at 200°C in presence of $MgSO_4$. STM investigation of the samples 1-3 was negative (nothing on the substrate). In case of sample 10 was not possible scanning due to too high parasitic currents, most likely due to the use of cyanoacrylates for holding the sample.

- Method 2 – Dienstmaier, via pre-polymerization [13b] *- samples 4-6*

A small amount of BDBA commercial (sigma-aldrich) was transferred in a clean 2mL vial, and inserted in a 50mL pressure tube (ace), with ca 1mL of H_2O.

The tube was then introduced in a pre-heated oven at 200°C per 3h.

The resulting product was extracted and dissolved in the solvent reported in table 1.

The same solutions were then used in the second step of the reported procedure, by dropcasting, and then heating facing down at 120°C in presence of 500μL of H_2O.

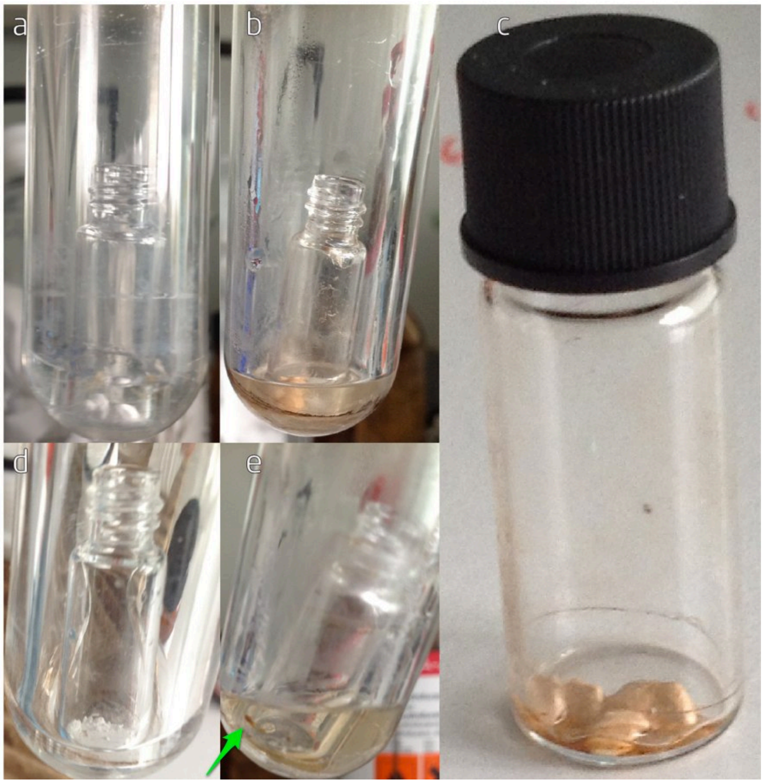

Figure 20: sample 4(a,b,e) and 10(d,e) before and after heating in presence of water. Note in (e) the formation of a small brown aggregate, pointed by the green arrow.

in the first phase, the pre-polymerization there's a change in color of the powders, and of the water present in solution. The product is soluble in nonanoic acid and in heptanoic acid with simple sonication. The observation under stm of the freshly prepared solution presented two different structures: a disordered assemblies of short linear objects and an hexagonal porous phase, with small domains; The annealing procedures (sample 5-6) did not showed any hexagonal phases. With higher annealing temperatures, long striped features extending per hundreds of nanometers were observed. AFM imaging of sample, (performed the day after and after one week), confirmed the presence of a film. Some directional preference is visible in the one day sample, such stripes are not visible one week after.

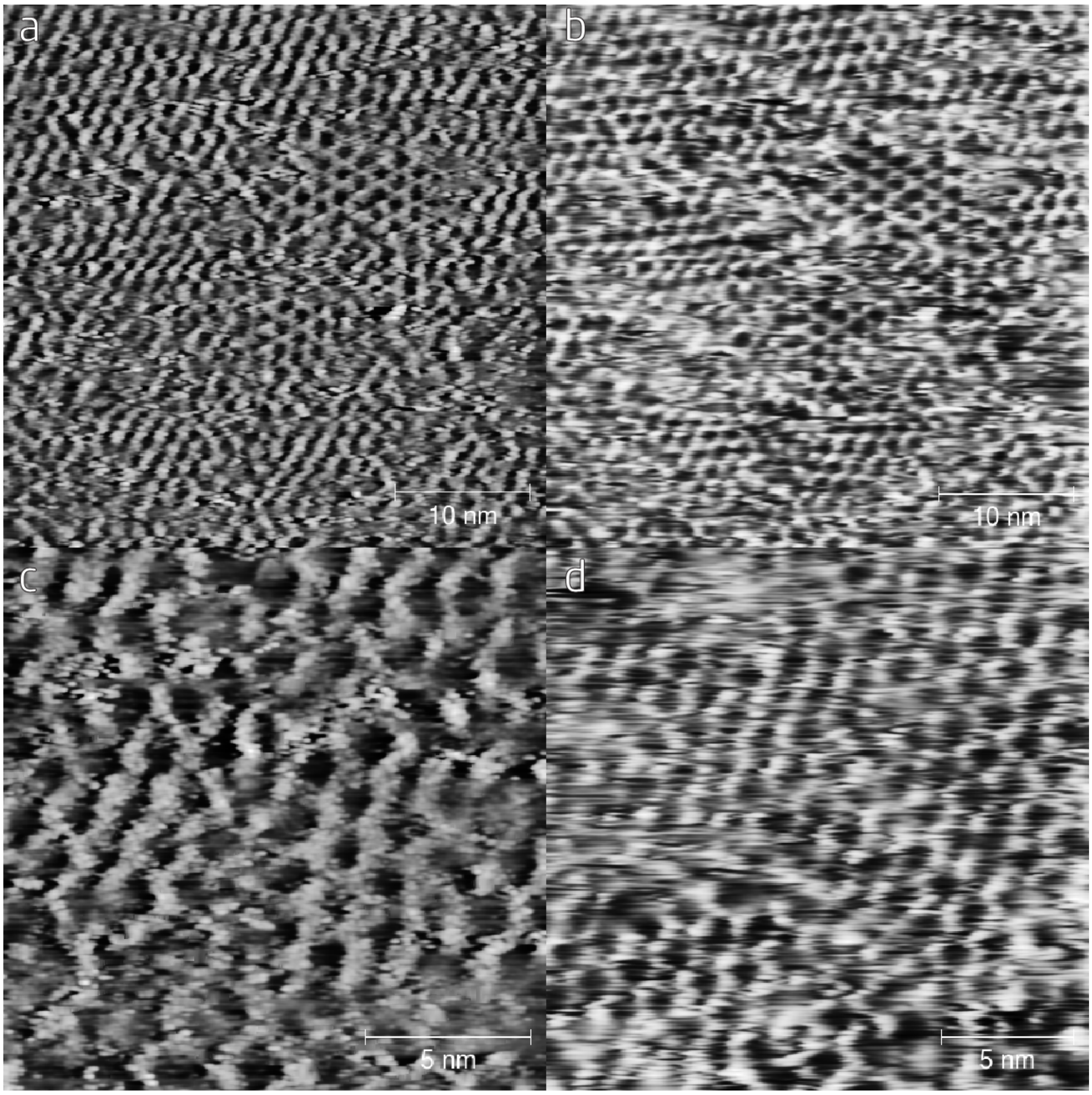

Figure 21 : sample 4, after dispersion in nonanoic acid, (a,c) current images, (b,d) height. unit cell parameters: a=1.7±0.2nm b=1.6±0.2nm, ϒ=55±2° A=2.3 ± 0.4nm². Tunneling parameters, I_t=20pA V_t=100mV.

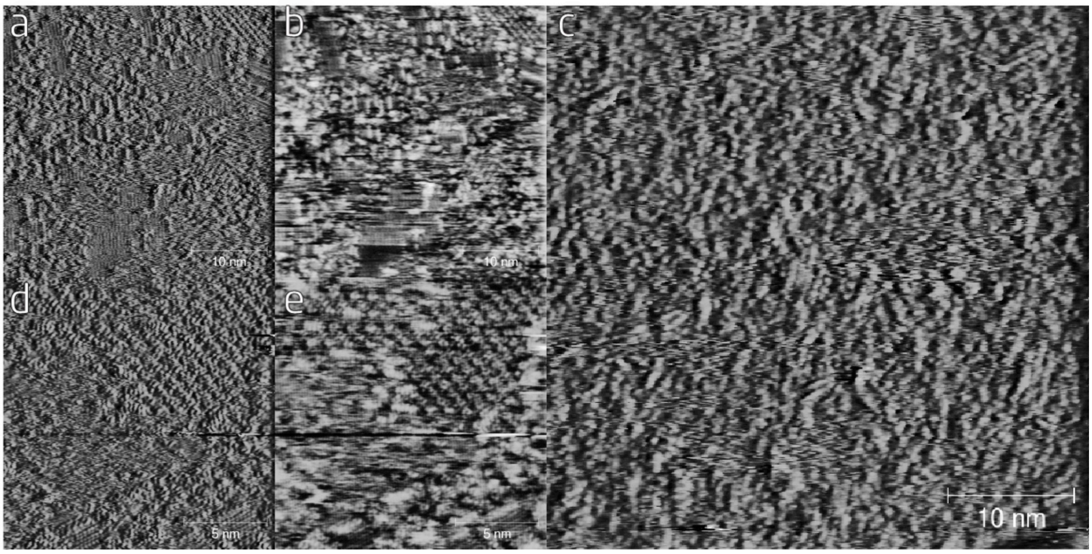

Figure 22: sample 5 after dispersion in heptanoic acid, before (a-d) and after (e) the annealing treatment. (a,c,d) current, (b,e) height. Almost all the ordered features have disappeared in (e).

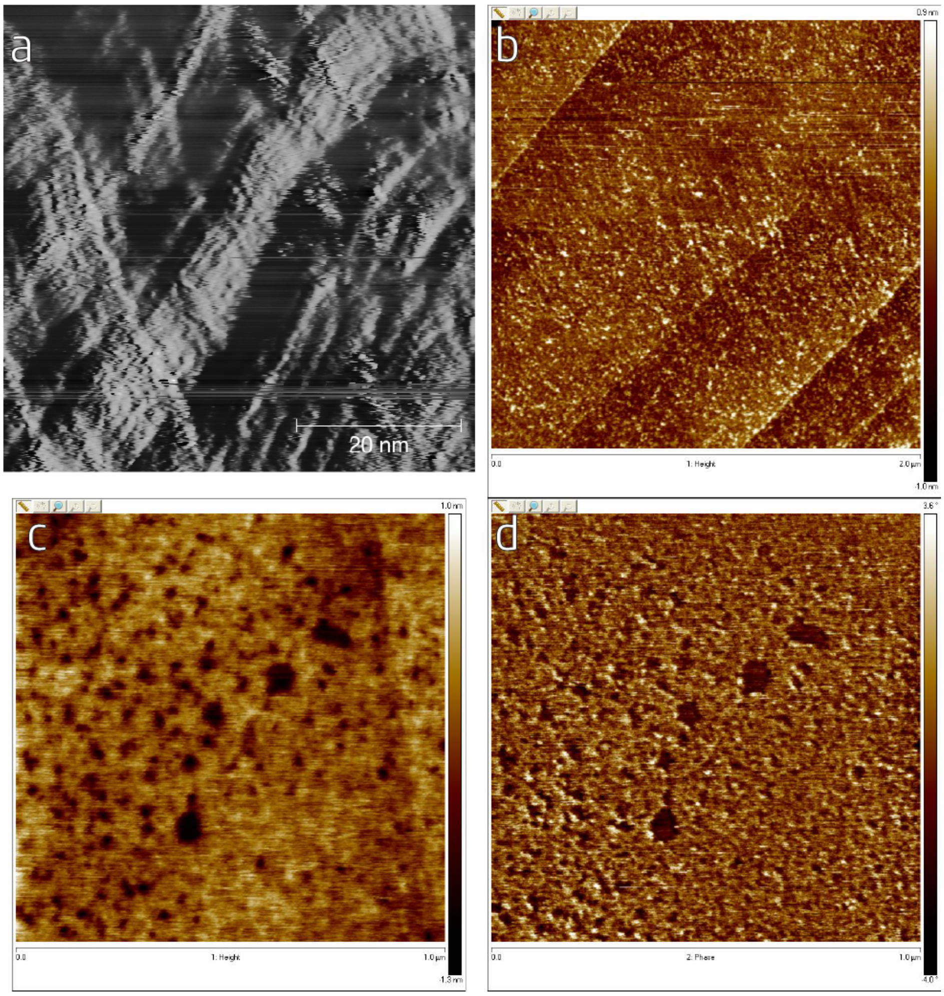

Figure 23: a) high scale stm current image, showing the presence of linear features. b)afm image, 24h later, presenting a directional preference. c,d) height and phase afm images after one week;

- Method 3 – Dienstmaier direct polymerization[13b] *– samples 7-9*

a saturated solution of BDBA was prepared according to table 1, and subsequently dropcasted on top of freshly cleaved HOPG substrate, already connected with the metal base. The substrate was inserted "facing-down" inside a pressure tube (ACE™ 140mL) with 500µL of H_2O and heated in oven at the temperature reported in table 1.

The substrate was held facing down either using a Nd magnet, cyanoacrylate glue or mechanical constriction with two paperclips and a glass slide.

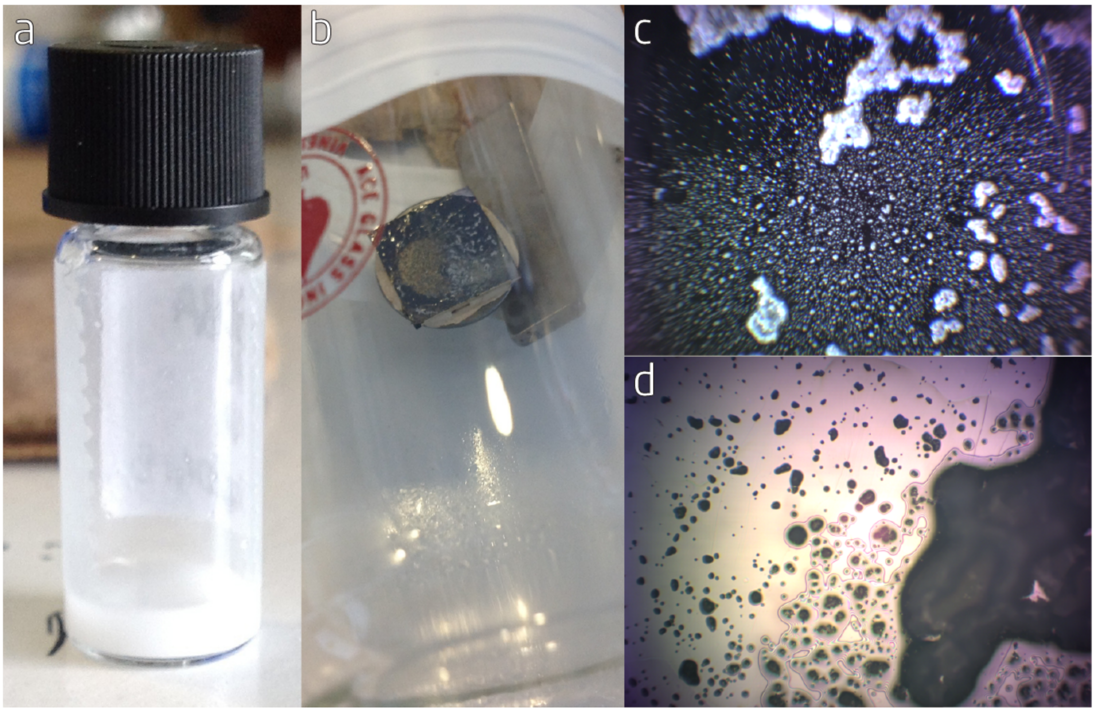

Figure 24: a) dispersion of bdba in nonanoic acid; b) appearance of the film after thermal treatment. c,d) optical microscope pictures of the substrate right after extraction from the pressure tube.

	unit cell				
	observed	*Dienstmaier et al*[13b]	Calculated	*Cote et al*[5b]	HB network calculated
a	1.7 ± 0.2	1.4±0.1	1.525	1.54	2.1
b	1.6 ±0.2	1.4±0.1	1.525	1.54	2.1
ϒ	54 ± 5	60±2	60	60	60

Table 2: Comparison of measured unit cell parameters, with the values reported in literature.

The unit cell parameters measured from the structure are in the experimental error range with the one previously reported, and are distant enough from the calculated 2.05nm of the calculated hydrogen bonded pattern, to safely assume the formation of a 2D COF of BDBA.

In summary it has been possible to reproduce the experimental findings on the bdba but only to a certain extent. Where the two step formation of the COF was successful, up to now no annealing attempt nor direct synthesis produced satisfactory results.
Is it therefore necessary to optimize the procedure. Comparing to the dsc results (see next section) seems that 1h of polymerization is not required, especially at high temperatures. Must be pointed out that there's one difference in the experimental procedure respect to the ones reported: in all the experiments we used a pressure tube rather than a steel autoclave. Therefore, even if unlikely, a possible catalytic effect from the autoclave, or from small traces of transition metals in the steel can not be excluded. Stainless steel contains Fe + C + Cr , plus a plethora of other metals such as Mn, V, Zn, and in literature is reported that it actually catalyzes some oxidation.[16] For this reason couple of attempts were done by inserting some stainless steel (stainless steel wool and screws) in the reaction vessel: even if none of the test produced matching 2D covalent organic frameworks, all of them resulted in 3D aggregates. Such objects should be characterized further before any conclusion withdrawn.

	Guam + stainless steel screws (2 x 30g)	Dienstmaier direct + stainless steel screws (2x30g)	Dienstmaier direct + stainless steel wool
BDBA (sat NA)	no	no	no *
FDBA (sat NA)	no	no	no
DBA (sat ME-DOX)	no	no	no
TBA (sat ME-DOX)	no	no	no

Table 6: test with stainless steel addition inside the reaction vessel. None of the sample has shown the expected structure, but all showed 3dimensional objects. * also showed small domains of hexagonal phase which desorbed in few instants.

Reactivity conditions via DSC

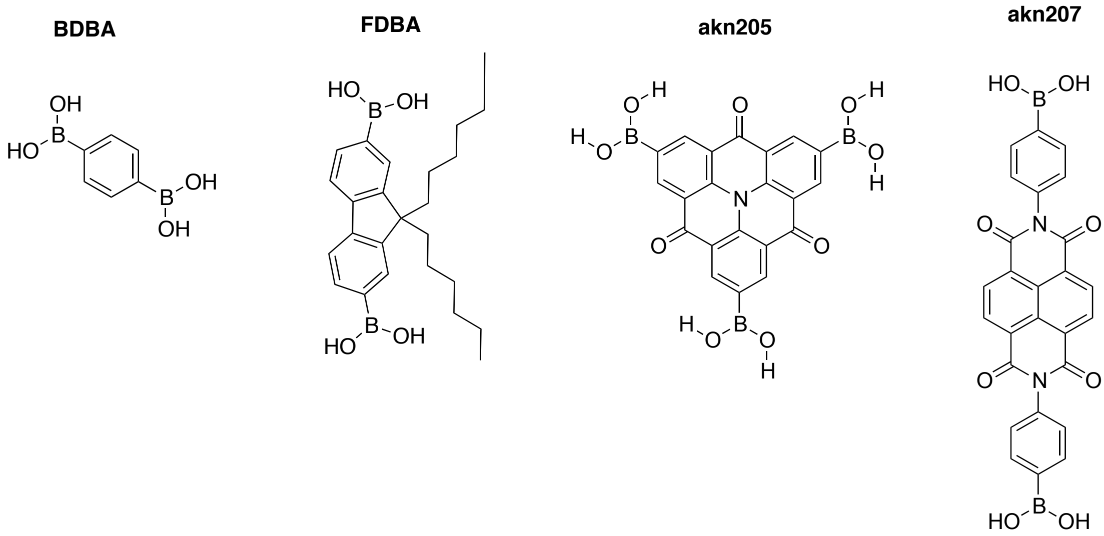

Figure 25: investigated molecules

To have another independent perspective over the temperature behavior of the tested molecules, (figure 25) we decided to use differential scanning calorimetry, even if it is rarely used to perform polymerizations.

Experimental Details:

The molecules were introduced in a pre-weighted crucible, closed and inserted in the Dsc (netzsch Dsc 200f3 Maia) dsc for the experiment.

Heating process:

2' stall, 25-300/400C @ 10k min, 2' stall then, 300/400-25 @ 10k/min, 30''pause, then 25-300 10k/min, then cool down.

Dsc			
Molecule	**Amount [mg]**	**Maximum heating temperature [°C]**	**Crucible weight [mg]**
Bdba	5.2	300	39.5
Fdba	3.4	300	38.9
TBA	3.5	400	39
DBA	3.4	400	39.3

Table 7: details of the samples.

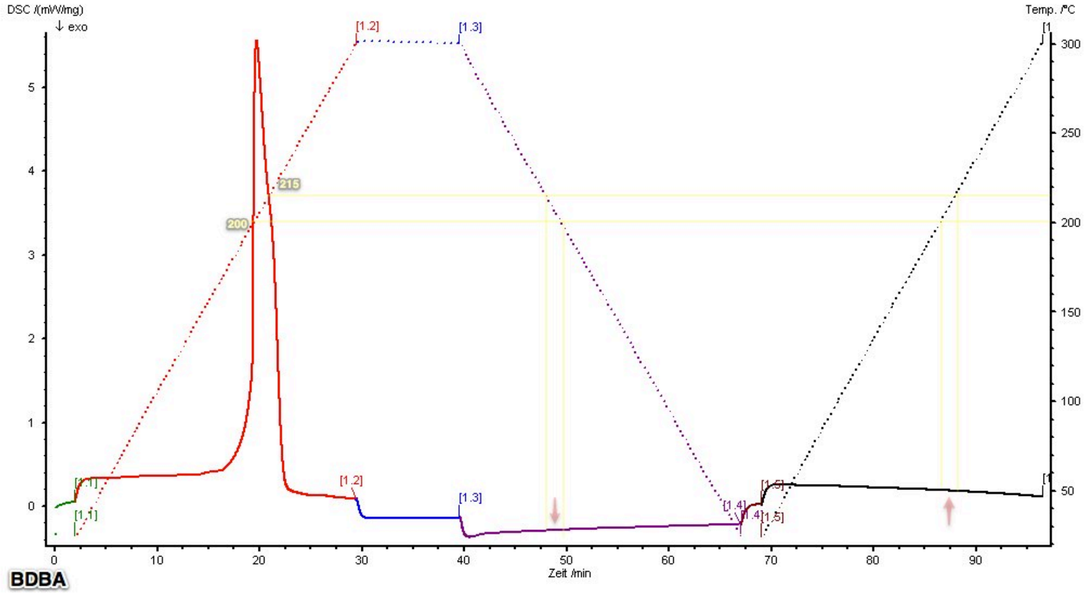

Figure 26: bdba dsc, the transparent-red arrows highlight the range in which, in case of a melting transition, the endothermic peak should be found in the subsequent scans.

Bdba:

The peak highlighted in figure 1, might be due to either polymerization of the monomer or melting of a crystalline phase. Since such feature disappears in the other steps, there's no evidence of any recrystallization, therefore the resulting sample could be or 100% amorphous, or most likely polymerized.

Once dispersed the white solid in 1mL THF, a milk-like dispersion was obtained. Such dispersion formed flacky white crystals after mild heating (50°C), which are readily dispersed after mechanical agitation. After 2 days the suspension become a clear transparent solution.

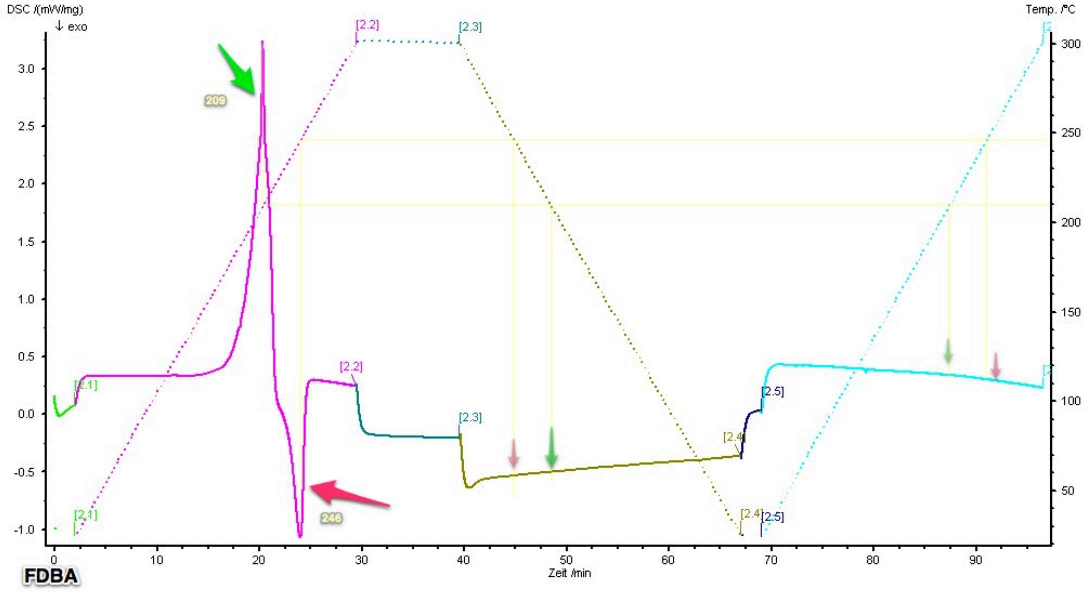

Figure 27: Fdba dsc.

Fdba:

Associated to the endothermic peak there's a deep exothermic at 246°C. Such behavior can be explained with a crystalline fusion, with degradation, or most likely to the formation of the polymer and the subsequent elimination of water from the structure. Again, the absence of any feature in the subsequent ramps, encourage the polymerization.

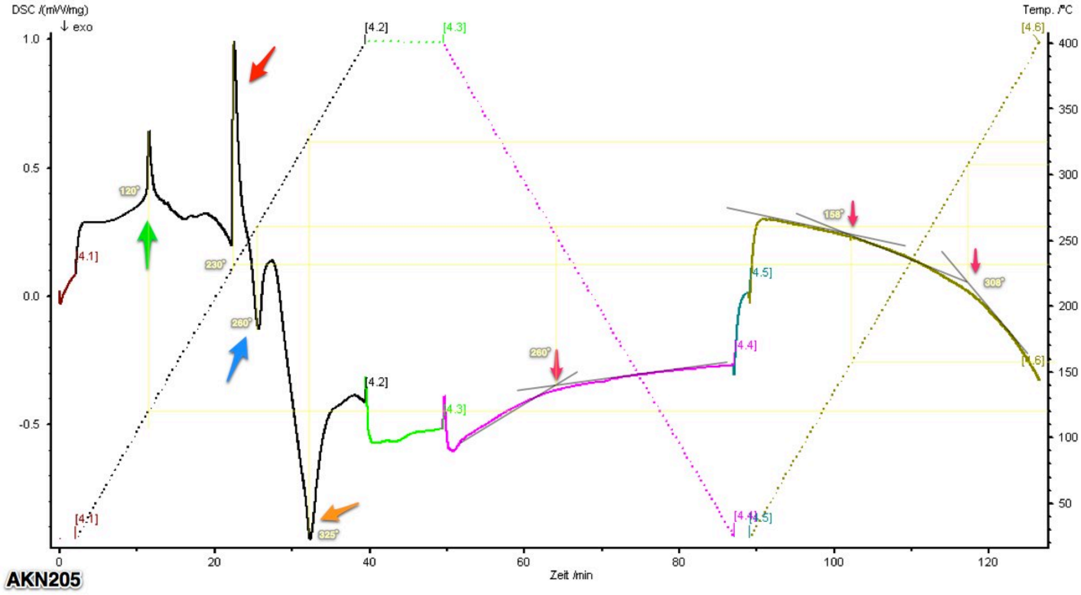

Figure 28: TBA dsc;

TBA:

Besides the consideration already made for BDBA and FDBA, which still stands, in TBA have been observed other features; The first endothermic peak, pointed with a green arrow in figure 3, allege the melting of a crystalline phase. The presence of two second order phase transitions in the second and third heating stages are probably due to glass transitions, therefore encouraging the presence of a polymer. The second exothermic peak (orange arrow) is still under investigation.

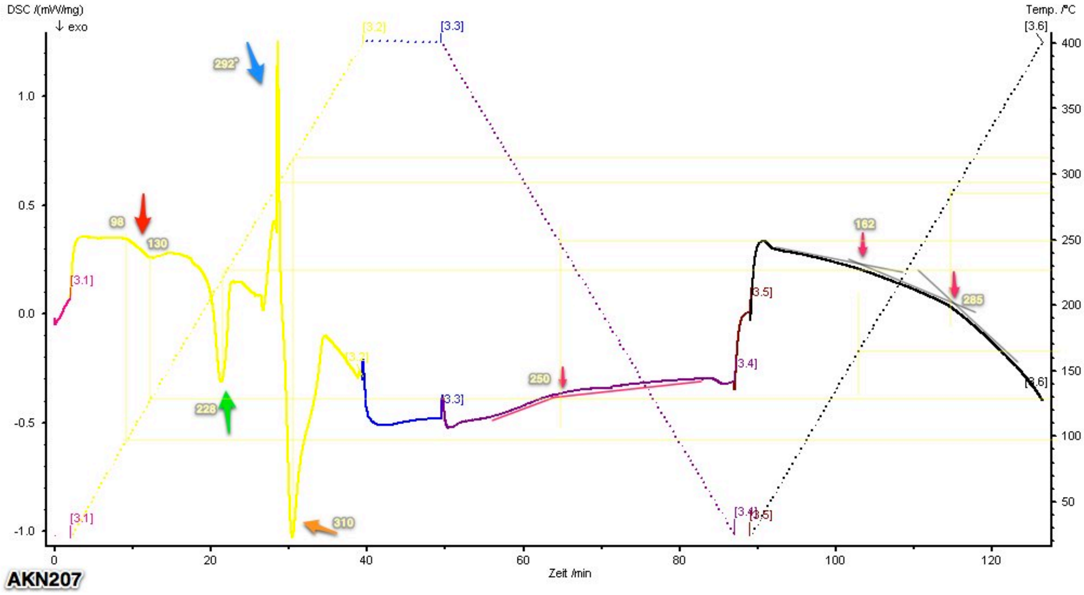

Figure 29: DBA dsc.

DBA:

Again, the same observation of the other samples are still valid, however, there are dramatic difference in the temperature of the major peak, which suggest an higher activation of the polymerization. The first feature is a abrupt change in the thermal capacitance. Subsequently there's an exothermic peak (figure 4, green arrow), which is compatible with the dissociation of trimers;

The presence of two second order phase transitions in the second and third heating stages are probably due to glass transitions, therefore encouraging the presence of a polymer.

Observations: *Observations over the experimental results.*

In all the performed experiments there's at least one peak, which in all the cooling down and second heating is not anymore present. In the cool down and second heating of samples 1 and 2, there are no evident features; there are, in the thermogram of samples 3 and 4 in the cooling phase and second heating, changes of the slope at 250/260°C respectively in the cooling step. In the second heating, TBA has two second order transitions at 158 and 308°C, whereas DBA presents similar features at 162 and 285°C. The main endothermic peak temperature is roughly around 200°C for BDBA and FDBA, 230°C for TBA, and 292 °C for DBA.

At t ~ 20min, in image 4 is present a deep exotermic peak (green arrow).

The investigation highlighted the thermal formation of polymers, and provided the critical temperature for the reaction, in absence of water:

BDBA ~ 200˚C

FDBA ~ 210˚C

TBA~230˚C

DBA~290˚C

The analysis of the experiment is not finished yet, and the enthalpies associated to each transition must be computed.

Is also highly recommended to reproduce the measurements with slower scanning speed in order to verify the presence of low temperature Tg, and to better resolve the peaks.

Conclusions

The implications of the polymerization mechanisms are multiple and deep. The reaction should proceed through equilibrium steps, which implies that the thermodynamic product is obtained. Few important remarks follow directly from this statement:
i) at equilibrium, a certain concentration of active centers must be continuously present, ii) the reaction should proceeds homogeneously without increasing too much the viscosity, iii) only monomers, polymers and oligomers should be present in the system, and they should be interchangeable, and iv) no irreversible side reaction should happen.

Considering the propagation phase of a polymerization, the relationship between enthalpy, temperature and concentration at the equilibrium of the monomer is resumed in
Equation 1.

$$ln[M]_e = \frac{\Delta H^{\circ}}{RT} - \frac{\Delta S^{\circ}}{R}$$

Equation 1

This relationship evidences that for the polymerization to proceed, the right side of the equation must be negative. Therefore if the reaction is both exothermic ($\Delta H_p < 0$) and endoentropic ($\Delta S_p > 0$) it will “always” proceed. More interesting and realistic case is when the reaction is both exothermic and exoentropic ($\Delta H_p < 0$ and $\Delta S_p < 0$) as most of the polymerization, then for a given concentration and solvent there will be a temperature above which the formation of long chains is unfavorable. Such temperature is called ceiling temperature. Similar considerations for endoenthalpic and endoentropic give rise to a floor temperature, below which no polymerization is observed. The last possible case is endoenthalpic and exoentropic, and the polymerization could not occur. Since we are interested in 2D polymerization, into a generally rigid structure, after adsorption on a surface, the loss of degrees of freedom has an entropic contribution which is generally dramatically negative. **It follows that the major concern in the generation of structures is the ceiling temperature.**

It must be noted that in general the reaction removes monomers from the solution to add them on the surface. Or it rearranges the monomer on the surface. This adds two other terms to the old good theory – the diffusion of the monomers and oligomers on the surface, and the gradient of concentration in solution – another important consideration, is that the generation of a double bond will add ca 80kCal/mol, which is in the range, and probably higher of the adsorption energy for small molecules, therefore most likely causing desorption until a critical size is reached.

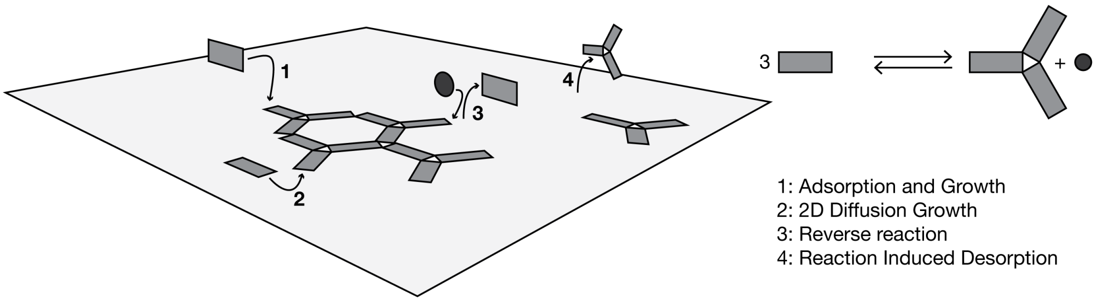

Figure 30: Sketch of what might occur during a surface 2D polymerization.

In summary, we can reassume the aspects which contribute positively or negatively to the 2D polymerization on a surface:

Positive Contributions: remove from solution the products, therefore shifting the reaction equilibria (Le Chatelier); formation of covalent bonds (ΔH<<0).

Negative Contributions: entropy – diffusion – desorption;

For standard polymerization such as polycondensations, the removal of a product is often mandatory to achieve high molecular weights. It has been shown that vice-versa for COFs addition of small amounts of the byproduct helps in reducing the defect concentration in the final structure, and that often the reactions doesn't actually occurs without; observing the scheme in Figure 30 we would expect that the mechanism 1 is the most likely responsible for the growth of the polymer, however 2 might be the prevailing mechanism in high coverage situations and in UHV conditions. We also expect that 3 and 4 are the only mechanisms of *self-healing* of the system. Whereas is still possible for oligomers to react using mechanism 1, it is most unlikely that multiple domains will react after desorption. A ripening mechanism may occur around the thermodynamic equilibrium thanks to 3.

In general we would expect the reaction to proceed according to a step growth process, but since the reported structures have been highly ordered and crystalline is hard to distinguish between the eventual ripening and a chain growth process. The case of chain growth would likely give rise to a fractal growth while clearly a chain growth process would also suggest the presence of a catalyst – which I would search in the stainless steel of the reactor.

1. (a) Geim, A. K.; Novoselov, K. S., The rise of graphene. *Nature Materials* **2007,** *6* (3), 183-191; (b) Novoselov, K. S.; Geim, A. K.; Morozov, S. V.; Jiang, D.; Zhang, Y.; Dubonos, S. V.; Grigorieva, I. V.; Firsov, A. A., Electric field effect in atomically thin carbon films. *Science* **2004,** *306* (5696), 666-669; (c) Law, M.; Goldberger, J.; Yang, P. D., Semiconductor nanowires and nanotubes. *Annual Review of Materials Research* **2004,** *34*, 83-122; (d) Ebbesen, T. W., CARBON NANOTUBES. *Annual Review of Materials Science* **1994,** *24*, 235-264; (e) Iijima, S., HELICAL MICROTUBULES OF GRAPHITIC CARBON. *Nature* **1991,** *354* (6348), 56-58.

2. Wallace, P. R., The Band Theory of Graphite. *Physical Review* **1947,** *71* (9), 622-634.

3. (a) Remskar, M.; Mrzel, A.; Skraba, Z.; Jesih, A.; Ceh, M.; Demsar, J.; Stadelmann, P.; Levy, F.; Mihailovic, D., Self-assembly of subnanometer-diameter single-wall MoS2 nanotubes. *Science* **2001,** *292* (5516), 479-481; (b) Feldman, Y.; Wasserman, E.; Srolovitz, D. J.; Tenne, R., HIGH-RATE, GAS-PHASE GROWTH OF MOS2 NESTED INORGANIC FULLERENES AND NANOTUBES. *Science* **1995,** *267* (5195), 222-225; (c) Joensen, P.; Frindt, R. F.; Morrison, S. R., SINGLE-LAYER MOS2. *Materials Research Bulletin* **1986,** *21* (4), 457-461; (d) Britnell, L.; Gorbachev, R. V.; Jalil, R.; Belle, B. D.; Schedin, F.; Mishchenko, A.; Georgiou, T.; Katsnelson, M. I.; Eaves, L.; Morozov, S. V.; Peres, N. M. R.; Leist, J.; Geim, A. K.; Novoselov, K. S.; Ponomarenko, L. A., Field-Effect Tunneling Transistor Based on Vertical Graphene Heterostructures. *Science* **2012,** *335* (6071), 947-950; (e) Zhu, W. J.; Neumayer, D.; Perebeinos, V.; Avouris, P., Silicon Nitride Gate Dielectrics and Band Gap Engineering in Graphene Layers. *Nano Letters* **2010,** *10* (9), 3572-3576; (f) Guzman-Verri, G. G.; Voon, L., Electronic structure of silicon-based nanostructures. *Physical Review B* **2007,** *76* (7).

4. (a) Ferey, G., Hybrid porous solids: past, present, future. *Chemical Society Reviews* **2008,** *37* (1), 191-214; (b) Diebold, U., The surface science of titanium dioxide. *Surface Science Reports* **2003,** *48* (5-8), 53-229; (c) Stein, A.; Melde, B. J.; Schroden, R. C., Hybrid inorganic-organic mesoporous silicates - Nanoscopic reactors coming of age. *Advanced Materials* **2000,** *12* (19), 1403-1419; (d) Ying, J. Y.; Mehnert, C. P.; Wong, M. S., Synthesis and applications of supramolecular-templated mesoporous materials. *Angewandte Chemie-International Edition* **1999,** *38* (1-2), 56-77; (e) Campbell, C. T., Ultrathin metal films and

particles on oxide surfaces: Structural, electronic and chemisorptive properties. *Surface Science Reports* **1997,** *27* (1-3), 1-111.

5. (a) Jagtap, S. P.; Collard, D. M., 2D Multilayered pi-stacked conjugated polymers based on a U-turn pseudo-geminal 2.2 paracyclophane scaffold. *Polymer Chemistry* **2012,** *3* (2), 463-471; (b) Sakamoto, J.; van Heijst, J.; Lukin, O.; Schlueter, A. D., Two-Dimensional Polymers: Just a Dream of Synthetic Chemists? *Angewandte Chemie-International Edition* **2009,** *48* (6), 1030-1069; (c) Cooper, A. I., Conjugated Microporous Polymers. *Advanced Materials* **2009,** *21* (12), 1291-1295; (d) Zwaneveld, N. A. A.; Pawlak, R.; Abel, M.; Catalin, D.; Gigmes, D.; Bertin, D.; Porte, L., Organized formation of 2D extended covalent organic frameworks at surfaces. *Journal Of The American Chemical Society* **2008,** *130* (21), 6678-+; (e) Weigelt, S.; Busse, C.; Bombis, C.; Knudsen, M. M.; Gothelf, K. V.; Laegsgaard, E.; Besenbacher, F.; Linderoth, T. R., Surface synthesis of 2D branched polymer nanostructures. *Angewandte Chemie-International Edition* **2008,** *47* (23), 4406-4410; (f) Kuhn, P.; Antonietti, M.; Thomas, A., Porous, covalent triazine-based frameworks prepared by ionothermal synthesis. *Angewandte Chemie-International Edition* **2008,** *47* (18), 3450-3453; (g) Han, S. S.; Furukawa, H.; Yaghi, O. M.; Goddard, W. A., III, Covalent organic frameworks as exceptional hydrogen storage materials. *Journal Of The American Chemical Society* **2008,** *130* (35), 11580-+; (h) Cote, A. P.; El-Kaderi, H. M.; Furukawa, H.; Hunt, J. R.; Yaghi, O. M., Reticular synthesis of microporous and mesoporous 2D covalent organic frameworks. *Journal Of The American Chemical Society* **2007,** *129* (43), 12914-+; (i) Goldberg, I., Crystal engineering of porphyrin framework solids. *Chemical Communications* **2005,** (10), 1243-1254; (j) Cote, A. P.; Benin, A. I.; Ockwig, N. W.; O'Keeffe, M.; Matzger, A. J.; Yaghi, O. M., Porous, crystalline, covalent organic frameworks. *Science* **2005,** *310* (5751), 1166-1170; (k) Seward, C.; Jia, W. L.; Wang, R. Y.; Enright, G. D.; Wang, S. N., Luminescent 2D macrocyclic networks based on starburst molecules: {Ag(CF3SO3)(1.5)(tdapb) and {Ag(NO3)(3)(tdapb). *Angewandte Chemie-International Edition* **2004,** *43* (22), 2933-2936; (l) Filler, M. A.; Bent, S. F., The surface as molecular reagent: organic chemistry at the semiconductor interface. *Progress in Surface Science* **2003,** *73* (1-3), 1-56; (m) Susumu, K.; Maruyama, H.; Kobayashi, H.; Tanaka, K., Theoretical approach to the design of supramolecular conjugated porphyrin polymers. *Journal Of Materials Chemistry* **2001,** *11* (9), 2262-2270.

6. Batten, S. R.; Champness, N. R.; Chen, X.-M.; Garcia-Martinez, J.; Kitagawa, S.; Öhrström, L.; O'Keeffe, M.; Suh, M. P.; Reedijk, J., Coordination polymers, metal–organic frameworks and the need for terminology guidelines. *Crystengcomm* **2012,** *14* (9), 3001-3004.

7. O'Keeffe, M., Design of MOFs and intellectual content in reticular chemistry: a personal view. *Chemical Society Reviews* **2009,** *38* (5), 1215-1217.

8. Tranchemontagne, D. J.; Mendoza-Cortés, J. L.; O'Keeffe, M.; Yaghi, O. M., Secondary building units, nets and bonding in the chemistry of metal–organic frameworks. *Chemical Society Reviews* **2009,** *38* (5), 1257-1283.

9. (a) Feng, X.; Dong, Y.; Jiang, D., Star-shaped two-dimensional covalent organic frameworks. *Crystengcomm* **2013**, -; (b) Gourdon, A., On-surface covalent coupling in ultrahigh vacuum. *Angewandte Chemie-International Edition In English* **2008,** *47* (37), 6950-6953.

10. Kempe, K.; Krieg, A.; Becer, C. R.; Schubert, U. S., "Clicking" on/with polymers: a rapidly expanding field for the straightforward preparation of novel macromolecular architectures. *Chemical Society Reviews* **2011**, -.

11. (a) Zhong, D.; Franke, J.-H.; Podiyanachari, S. K.; Bloemker, T.; Zhang, H.; Kehr, G.; Erker, G.; Fuchs, H.; Chi, L., Linear Alkane Polymerization on a Gold Surface. *Science* **2011,** *334* (6053), 213-216; (b) Iruthayaraj, J.; Chernyy, S.; Lillethorup, M.; Ceccato, M.; Ron, T.; Hinge, M.; Kingshott, P.; Besenbacher, F.; Pedersen, S. U.; Daasbjerg, K.,

On Surface-Initiated Atom Transfer Radical Polymerization Using Diazonium Chemistry To Introduce the Initiator Layer. *Langmuir* **2011,** *27* (3), 1070-1078; (c) Sedona, F.; Di Marino, M.; Sambi, M.; Carofiglio, T.; Lubian, E.; Casarin, M.; Tondello, E., Fullerene/Porphyrin Multicomponent Nanostructures on Ag(110): From Supramolecular Self-Assembly to Extended Copolymers. *Acs Nano* **2010,** *4* (9), 5147-5154; (d) Matena, M.; Stoehr, M.; Riehm, T.; Bjoerk, J.; Martens, S.; Dyer, M. S.; Persson, M.; Lobo-Checa, J.; Mueller, K.; Enache, M.; Wadepohl, H.; Zegenhagen, J.; Jung, T. A.; Gade, L. H., Aggregation and Contingent Metal/Surface Reactivity of 1,3,8,10-Tetraazaperopyrene (TAPP) on Cu(111). *Chemistry - A European Journal* **2010,** *16* (7), 2079-2091; (e) Weigelt, S.; Schnadt, J.; Tuxen, A. K.; Masini, F.; Bombis, C.; Busse, C.; Isvoranu, C.; Ataman, E.; Laegsgaard, E.; Besenbacher, F.; Linderoth, T. R., Formation of trioctylamine from octylamine on Au(111). *Journal Of The American Chemical Society* **2008,** *130* (16), 5388-+; (f) Weigelt, S.; Busse, C.; Bombis, C.; Knudsen, M. M.; Gothelf, K. V.; Laegsgaard, E.; Besenbacher, F.; Linderoth, T. R., Surface synthesis of 2D branched polymer nanostructures. *Angewandte Chemie-International Edition In English* **2008,** *47* (23), 4406-4410; (g) Weigelt, S.; Bombis, C.; Busse, C.; Knudsen, M. M.; Gothelf, K. V.; Laegsgaard, E.; Besenbacher, F.; Linderoth, T. R., Molecular self-assembly from building blocks synthesized on a surface in Ultrahigh vacuum: Kinetic control and topo-chemical reactions. *Acs Nano* **2008,** *2* (4), 651-660; (h) Grim, P.; De Feyter, S.; Gesquiere, A.; Vanoppen, P.; Rucker, M.; Valiyaveettil, S.; Moessner, G.; MULLEN, K.; De Schryver, F., Submolecularly resolved polymerization of diacetylene molecules on the graphite surface observed with scanning tunneling microscopy. *Angewandte Chemie-International Edition In English* **1997,** *36* (23), 2601-2603.

12. Rowan, S. J.; Cantrill, S. J.; Cousins, G. R. L.; Sanders, J. K. M.; Stoddart, J. F., Dynamic Covalent Chemistry. *Angewandte Chemie International Edition* **2002,** *41* (6), 898-952.

13. (a) Guan, C.-Z.; Wang, D.; Wan, L.-J., Construction and repair of highly ordered 2D covalent networks by chemical equilibrium regulation. *Chem. Commun. VL - IS -* **2012**, -; (b) Dienstmaier, J. F.; Medina, D. D.; Dogru, M.; Knochel, P.; Bein, T.; Heckl, W. M.; Lackinger, M., Isoreticular Two-Dimensional Covalent Organic Frameworks Synthesized by On-Surface Condensation of Diboronic Acids. *Acs Nano* **2012**, 120716083424002; (c) Varughese, S.; Sinha, S. B.; DESIRAJU, G. R., Phenylboronic acids in crystal engineering: Utility of the energetically unfavorable syn,syn-conformation in co-crystal design. *Science China-Chemistry* **2011,** *54* (12), 1909-1919; (d) Ourdjini, O.; Pawlak, R.; Abel, M.; Clair, S.; Chen, L.; Bergeon, N.; Sassi, M.; Oison, V.; Debierre, J.-M.; Coratger, R.; Porte, L., Substrate-mediated ordering and defect analysis of a surface covalent organic framework. *Physical Review B* **2011,** *84* (12), 125421; (e) Nishiyabu, R.; Kubo, Y.; James, T. D.; Fossey, J. S., Boronic acid building blocks: tools for self assembly. *Chemical Communications* **2011,** *47* (4), 1124-1150; (f) Dienstmaier, J. F.; Gigler, A. M.; Goetz, A. J.; Knochel, P.; Bein, T.; Lyapin, A.; Reichlmaier, S.; Heckl, W. M.; Lackinger, M., Synthesis of Well-Ordered COF Monolayers: Surface Growth of Nanocrystalline Precursors versus Direct On-Surface Polycondensation. *Acs Nano* **2011,** *5* (12), 9737-9745.

14. (a) Sassi, M.; Oison, V.; Debierre, J.-M.; Humbel, S., Modelling the Two-Dimensional Polymerization of 1,4-Benzene Diboronic Acid on a Ag Surface. *Chemphyschem* **2009,** *10* (14), 2480-2485; (b) Spitler, E. L.; Giovino, M. R.; White, S. L.; Dichtel, W. R., A mechanistic study of Lewis acid-catalyzed covalent organic framework formation. *Chemical Science* **2011,** *2* (8), 1588-1593.

15. (a) De, P.; Gondi, S. R.; Roy, D.; Sumerlin, B. S., Boronic Acid-Terminated Polymers: Synthesis by RAFT and Subsequent Supramolecular and Dynamic Covalent Self-Assembly. *Macromolecules* **2009,** *42* (15), 5614-5621; (b) Qin, Y.; Cui, C.; Jäkle, F., Silylated Initiators for the Efficient Preparation of Borane-End-Functionalized Polymers

via ATRP. *Macromolecules* **2007,** *40* (5), 1413-1420; (c) Kua, J.; Gyselbrecht, C. R., Thermodynamics and Kinetics of Methylboroxine ·Amine Adduct Formation: A Computational Study. *Journal Of Physical Chemistry A* **2007,** *111* (22), 4759-4766; (d) Kua, J.; Fletcher, M. N.; Iovine, P. M., Effect of Para-Substituents and Solvent Polarity on the Formation of Triphenylboroxine ·Amine Adducts. *Journal Of Physical Chemistry A* **2006,** *110* (26), 8158-8166; (e) Perttu, E. K.; Arnold, M.; Iovine, P. M., The synthesis and characterization of phenylacetylene tripodal compounds containing boroxine cores. *Tetrahedron Letters* **2005,** *46* (50), 8753-8756.

16. (a) Di Mondo, D.; Ashok, D.; Waldie, F.; Schrier, N.; Morrison, M.; Schlaf, M., Stainless Steel As a Catalyst for the Total Deoxygenation of Glycerol and Levulinic Acid in Aqueous Acidic Medium. *ACS Catalysis* **2011,** *1* (4), 355-364; (b) Loeker, F.; Leitner, W., Steel ‐ Promoted Oxidation of Olefins in Supercritical Carbon Dioxide Using Dioxygen in the Presence of Aldehydes. *Chemistry - A European Journal* **2000,** *6* (11), 2011-2015.

Chapter 6: Conclusions and Outlooks

Through this work of thesis, we have demonstrated how trough interconnecting different techniques both experimental and virtual, is it possible to gather information and finally understand the self-assembly of small molecules. We have applied such concepts in observing how the rotations can affect the self-assembly, then extended in different building blocks, to see then their competition, before introducing the metals complexes. From the acquired knowledge, we demonstrated how is it possible to describe a system capable of self-templating. We also applied such notions in the investigation of the synthesis of covalent organic frameworks based on different building blocks.

Achieving a subtle control over the interplay between various distinct weak interactions between molecular building blocks through a supramolecular design makes it possible the production of self-assembled nanomaterials. This is the chemists "bottom-up" approach to nanoscience and nanotechnology. Such a strategy when applied on programmed tectons provides access towards the fabrication of 1D, 2D and 3D nanoarchitectures with properties at will.

Although the use of weak forces to control self-assembly attracted already a great attention[1], many are the challenges which are still open in the field. In the framework of this thesis we have focused our attention to three main aspects:

- Control over 2D self-assembly, especially addressed to achieving a subtle control over the positioning of functional units and their organization, either with respect the substrate, or with respect to neighboring molecules.
- Expanding the 2D self-assembly to the third dimension, i.e. growing programmed architectures, layer by layer, in a rigidly restrained fashion;
- Reactivity on the surface, which besides the industrial appeal in the development of new more efficient catalyst, may pave the road towards the synthesis of 2D-conjugated thus (semi)conducting polymers as synthetic graphene-like alternatives.

Three complementary topics, constituting the backbone of this thesis work, have been addressed by combining different physico-chemical methods including Scanning Tunneling Microscopy (STM), Molecular modeling relaying on instrumental and software development, respectively. Scanning tunneling Microscopy is a powerful tool to monitor nanoscale phenomena whereas through Simulations one could attain a precise understanding and define design principles.

The first objective of this thesis work was to achieve a control over the forces governing the bi-dimensional self-assembly of different building blocks at surfaces and interfaces. To this end, different systems were considered, ranging from commercially available synthons, to most rare custom made building blocks. STM was employed to explore the self-assembly of the first generation of dendrimers on graphite at the solid-liquid interface[2], providing direct insight into the effect on the supramolecular interactions. Particular attention was also paid to the study of the competition between different adsorbates – an aromatic polyol and a bypiridyn-pirimidin-amine, and to the modification of packing patterns upon addition of different metal salts, *in-situ*, as in the case of a functionalized porphyrinic tecton .

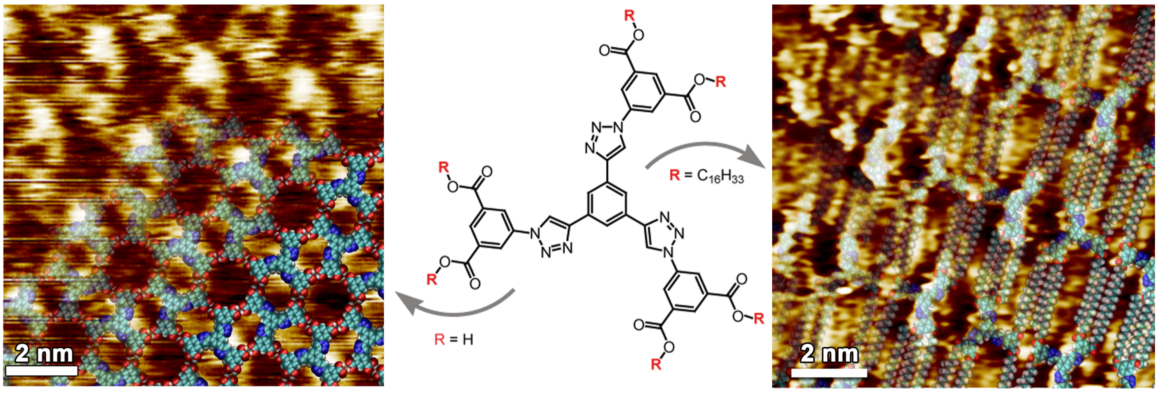

fig:1: Scanning Tunneling Microscopy images recorded at the solid-liquid interface of two first generation of poly(triazole-phenylene) dendrimers, functionalized with different side groups. (reproduced from ref.[2])

Building up on such a knowledge on 2D self-assembly, we have extended to order at the solid-liquid interface to the third dimension. This was accomplished by designing and investigating a hetero-aromatic tetracarboxylic acid building block which was found to form a self-templated bi-layered structure[3]. The unique design principle relies on the presence of four carbonyl moieties inside the conjugated core which we were found playing different roles: (i) they represent “primary” recognition sites on the molecular building blocks, to promote the self-assembly into 2D porous layers, (ii) they offer a fine control of their conformational planarity, which confers the self- templating capacity, and (iii) they introduce secondary recognition sites, which mediate the interactions between the self- assembled layers.

The capacity of forming 2D supramolecular architectures is a prerequisite towards their use for exploring surface reactions, thereby forming frameworks, where the weak forces responsible for the self-assembly are substituted with covalent bonds or strong metallo-ligand links, aiming to obtain infinite two dimensional conjugate network, which will likely cover a key role in the next generation of electronic materials. Many others techniques, i.e. ^{1}H-NMR, Infra-Red and UV-Vis Spectroscopy, Mass Spectrometry and Differential Scanning Calorimetry (DSC) provided important insight into the analysis and interpretation of the experimental results. The synthesis of three different 2D-Metallic Organic Frameworks and five different Covalent Organic Frameworks were investigated.

To facilitate experimental attempts, the predictive and analytical power of molecular mechanics simulation was exploited to gain precise information on the interactions in the bi-layered structures. Moreover, the development of a new software for Monte-Carlo calculations, albeit still to be finalized, will provide understanding of phase boundaries and help programming future architectures.

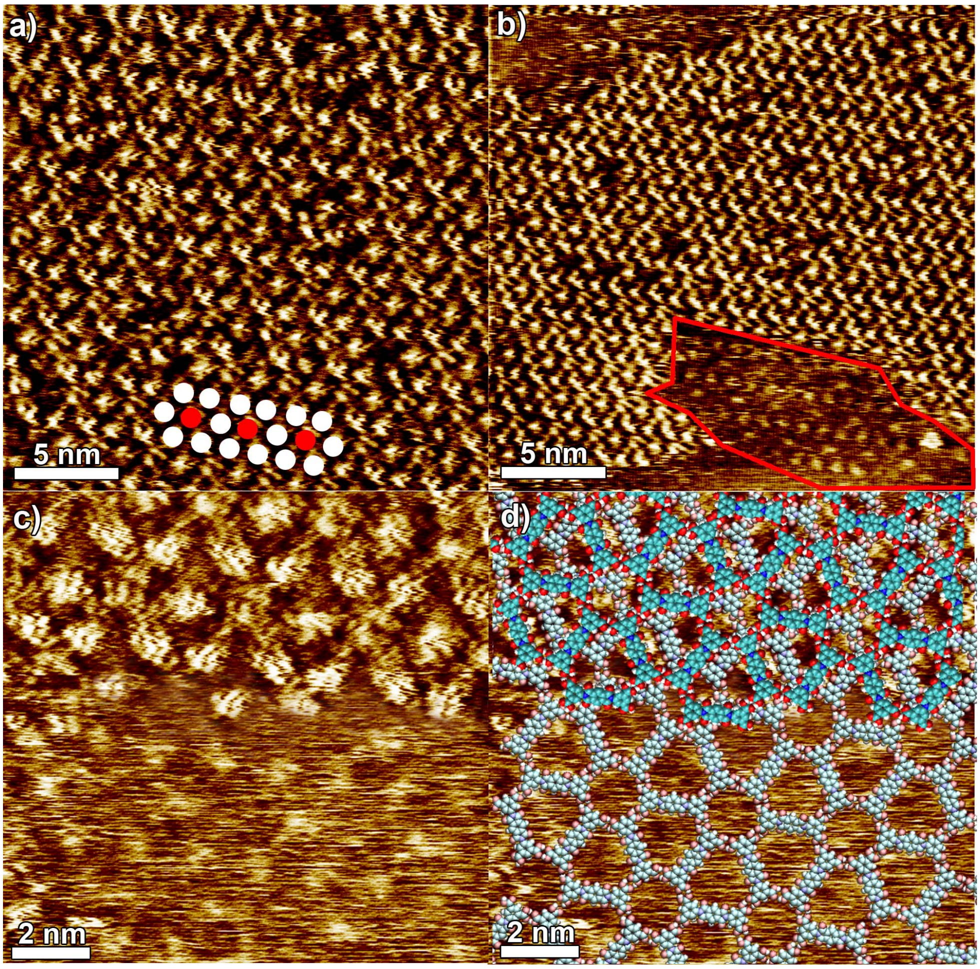

fig 2: Bi-layered self-assembled architecture of 5,5^{1} -(1,3,5,7-tetraoxopyrrolo[3,4-f] isoindole-2,6-diyl)diisophthalic acid reproduced from ref.[3])

Beyond imaging, STM allows to quantitatively explore electronic structures of molecules at the nanoscale via dI/dV imaging. A new setup has been optimized, tested and benchmarked on different molecules, and once completed, applied to provide new insight in the relationship between size and bandgap of nanocrystalline-graphene;

The developed approaches on controlled self-assembly and reactivity can be of importance to the many researchers tackling the challenges raised by controlling the self-assembly, contributing a small step toward the understanding of equilibriums at the nanoscale. Nano-architectures are nowadays subject of research in almost all of the fields of technology: In organic optoelectronics self-assembled monolayers are thoughtfully employed ranging from the production of renewable energy[4], to nano-wires[5] to new multi-responsive devices[6]; in Medicine & Biology , weak forces interactions and the functionalization of nano-objects permeates micro-fluidics[7], tissue regeneration[8], and drug release[8b, 9]. The importance and the research in self-assembled materials definitely spans from Quantum Informatics[10] to new building materials[11].

1. a) D. M. Cyr, B. Venkataraman and G. W. Flynn, *Chemistry of Materials*, 1996, **8**, 1600-1615; b) S. De Feyter and F. C. De Schryver, *Chemical Society Reviews*, 2003, **32**, 139-150; c) S. De Feyter and F. C. De Schryver, *Journal of Physical Chemistry B*, 2005, **109**, 4290-4302; d) A. A. Dhirani, R. W. Zehner, R. P. Hsung, P. GuyotSionnest and L. R. Sita, *Journal of the American Chemical Society*, 1996, **118**, 3319-3320; e) S. Griessl, M. Lackinger, M. Edelwirth, M. Hietschold and W. M. Heckl, *Single Molecules*, 2002, **3**, 25-31; f) F. Rosei, M. Schunack, Y. Naitoh, P. Jiang, A. Gourdon, E. Laegsgaard, I. Stensgaard, C. Joachim and F. Besenbacher, *Progress in Surface Science*, 2003, **71**, 95-146; g) R. K. Smith, P. A. Lewis and P. S. Weiss, *Progress in Surface Science*, 2004, **75**, 1-68.
2. A. Cadeddu, A. Ciesielski, T. El Malah, S. Hecht and P. Samori, *Chemical Communications*, 2011, **47**, 10578-10580.
3. A. Ciesielski, A. Cadeddu, C. A. Palma, A. Gorczynski, V. Patroniak, M. Cecchini and P. Samori, *Nanoscale*, 2011, **3**, 4125-4129.
4. a) B. de Boer, U. Stalmach, P. F. van Hutten, C. Melzer, V. V. Krasnikov and G. Hadziioannou, *Polymer*, 2001, **42**, 9097-9109; b) M. Gratzel, *Journal of Photochemistry and Photobiology a-Chemistry*,

2004, **164**, 3-14; c) J. Peet, A. J. Heeger and G. C. Bazan, *Accounts of Chemical Research*, 2009, **42**, 1700-1708.

5. a) T. Scheibel, R. Parthasarathy, G. Sawicki, X. M. Lin, H. Jaeger and S. L. Lindquist, *Proceedings of the National Academy of Sciences of the United States of America*, 2003, **100**, 4527-4532; b) A. Schenning and E. W. Meijer, *Chemical Communications*, 2005, 3245-3258; c) L. Zang, Y. K. Che and J. S. Moore, *Accounts of Chemical Research*, 2008, **41**, 1596-1608.
6. a) J. M. Mativetsky, G. Pace, M. Elbing, M. A. Rampi, M. Mayor and P. Samori, *Journal of the American Chemical Society*, 2008, **130**, 9192-+; b) Y. L. Guo, G. Yu and Y. Q. Liu, *Advanced Materials*, 2010, **22**, 4427-4447.
7. R. G. Ellis-Behnke, Y. X. Liang, S. W. You, D. K. C. Tay, S. G. Zhang, K. F. So and G. E. Schneider, *Proceedings of the National Academy of Sciences of the United States of America*, 2006, **103**, 5054-5059.
8. a) H. G. Cui, M. J. Webber and S. I. Stupp, *Biopolymers*, 2010, **94**, 1-18; b) M. Goldberg, R. Langer and X. Q. Jia, *Journal of Biomaterials Science-Polymer Edition*, 2007, **18**, 241-268; c) L. A. Smith and P. X. Ma, *Colloids and Surfaces B-Biointerfaces*, 2004, **39**, 125-131.
9. J. P. Lin, J. Q. Zhu, T. Chen, S. L. Lin, C. H. Cai, L. S. Zhang, Y. Zhuang and X. S. Wang, *Biomaterials*, 2009, **30**, 108-117.
10. M. Conrad, *International Journal of Quantum Chemistry*, 1992, **44**, 125-143.
11. D. L. Long, E. Burkholder and L. Cronin, *Chemical Society Reviews*, 2007, **36**, 105-121.

Appendix 1: dI/dV imaging

Observing the models developed to describe the tunneling effect and the current dependence in STM it is possible to devise ways to extract semi-quantitative information from the measurements: the first and most used way consists in reading the variation of the tunneling current with the bias, at a fixed height setpoint. In this way is it possible to extract the characteristic I/V curve. Similar information are gathered with the dI/dV. Both the techniques however are affected by the drift in the scanning process, and are usually meaningful only in UHV and a very low temperature. A possible solution consists in acquiring an image, i.e. doing a Scanning Differential Tunneling Microscopy. The principle has already been shown in low-temperature UHV setups, but in this chapter we show how we were capable to extend the application range of the technique to the solid-liquid interface, and at room temperature. We also show how from such measurements it is possible to study the electronic properties, in particular the size-bandgap dependence in a polydisperse sample of Nano Crystalline Graphene deposed on Au(111). This work has been done inside an extended collaboration: Carlos Andres Palma-Vargas (TUM Munich) and Jose Cojal (Humboltz Berlin) are responsible for the design of the experiments, Andrey Turchanin in Prof. Goelzhauser group (Bielefeld) synthesized the NCG, Marco Virsek and Stefano Prato from APE research in Trieste have modified the instrument.

Part 1: Theory and Proof of Principle:

dI/dV gives quantitative information when performed in ideal conditions which implies low temperatures and vacuum conditions (Grobis, Khoo et al. 2005; Grobis, Wachowiak et al. 2005). However, at ambient and solvent conditions, it does not offer significant advantages, since the drift of the tip and the changing conditions in a solvent would not offer any advantage over STS. An alternative is what we term Scanning Differential Tunneling Microscopy (SDTM), which would allow obtaining full images at specific "positions" (corresponding to the dI/dV amplitude at a specific bias) of the current derivative curve dI/dV. Besides the reproducible information, the interpretation of the derivative of the current is important since it is related to the molecular density of states when the weak coupling regime is considered, i.e. the Tersoff-Hamman approximation and the WKB approximations. Assuming that i) the tip has an uniform DOS, ii) the bias is *low* (~10mV), iii) the temperature is low, and that the major contribution arise from s-wave functions of the tip, Tersoff-Hamann [1] showed that the tunneling can be expressed as:

$$I = \frac{32\pi^3 e^2 \psi^2 R^2 V}{\hbar \kappa^4} e^{2\kappa R} D_t(E_F)\rho(r_0, E_F)$$

therefore the derivative respect to the applied bias results in:

$$\frac{dI}{dV} \propto \rho(r_0, E_F)$$

showing the proportionality between the dI/dV and the density of states. It is then clearly interesting to measure such values to have a direct insight into the electronical properties of the materials. When no strong coupling is considered, by employing this approach it is possible to obtain quantitative information on the molecular orbitals while in the case of strong coupling this approximation doesn't hold.

Nevertheless from a practical point of view the measurement of the derivatives it is not straightforward. The main difficulties from a practical point of view are that is necessary to implement noise reduction, and numerical extrapolation. Furthermore, from a theoretical point of view, it is necessary to demonstrate that the images are proportionally dependent on the density of states, even where the WKB approximation doesn't hold any longer. The approximation holds for low biases (max 20mV) but in general the scanning is performed with bias between -2 and 2 Volts, at room temperature, and in air!!

A possible way to overcome the practical issues is by using a phase sensitive detector (PSD) and by developing a faster electronic circuitry, to reduce the amount of data-fitting required, thus having a cleaner outcome. One solution consists of applying a sinusoidal modulation over the DC bias, with a frequency higher than the response of the piezo, which is subsequently read trough a Phase Sensitive Detector (PSD). Such approach is the one reported by Binnig and Rohrer,[3] and to date has not been extended to the solid-liquid interface.

Two are the major difficulties: i) is to demonstrate that the images observed are still proportionally dependent on the density of states, even outside the applicability of the approximation (where, the scanning conditions have bias in the range between -2 and 2 Volts, and at room temperature, in air) and ii) is to develop an electronic circuit which operates at higher speeds: in UHV the feedback usually works in the kHz range, whereas for the solid liquid interface a response in the range of the hundreds of kHz is needed.

By employing a PSD it will be possible to solve both issues by helping the detection of smaller voltages and closely approximating the analogic dI/dV signal.

The PSD needs to work at the right frequency to obtain a good signal, and at the same time, such frequency should be higher than the feedback response, to avoid the generation of artifacts in the images. Then, clearly, the quality of the signal will be dependent on the integration time, and on the resolution rate of the STM (maximum [pixel]/s). By considering a minimum scan rate of roughly 400 nm/s and a minimum number of 10 periods to obtain a signal, a typical $20nm^2$ picture will be obtained at ~100μs/pixel, the frequency's period will be 10μs, meaning a total PSD frequency in the order of 100kHz.

To couple the STM to the PSD, together with APE research, we made a modification to a commercial setup. The final impedance circuit which allows to decouple the instant current signal from the input signal is presented in Figure 1 while the circuit performing the sum of the AC signal and of the normal tunnelling bias is shown in Figure 2.

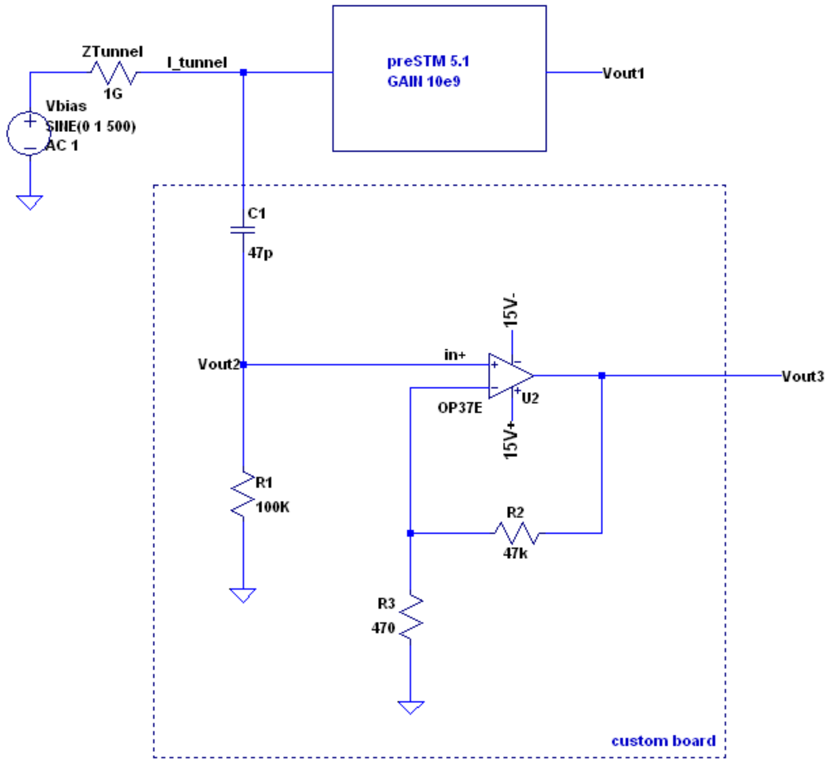

Figure 1 Decoupling circuit between the instant current signal (Vout1) and the input signal of the external lock-in amplifier (Vout3). Courtesy of Stefano Prato, APE Research 2010.

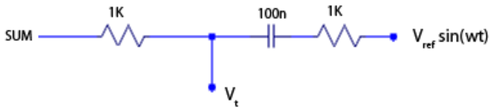

Figure 2: Sum circuit for the applied reference signal and the tunneling voltage V_t, such that the applied $V_{ref\text{-}lockin}$ sin(wt) lock-in reference is decreased in amplitude by 98.4% at 100KHz frequencies.

As proof of concept highly oriented pyrolytic graphite (HOPG) has been studied in 1,2,4-trichlorobenzene solvent (TCB). The dI/dV curves acquired during a period of 1h at a set point I_t = 100pA and V_t=100mV, 30 ms integration step, 20 averages (Figure 3) demonstrate both the sensitivity and reproducibility of the technique. To have a significant statistical value, we performed the data acquisition by doing 10 different experiments and acquiring more than 100 curves. The same measurements, but in air, are shown in Figure 5.

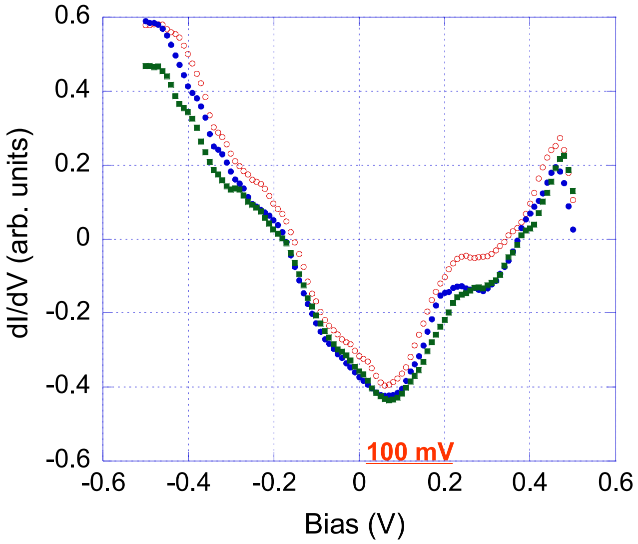

Figure 3: Differential dI / dV spectroscopy of HOPG in TCB. I_t = 100pA V_t = 100mV. Modulation Current V_{ref} = 2mV @ 100KHz integration time-step 30ms.

By comparing hundreds of curves of different systems on HOPG, the presence of reproducible features emerge. The feature at 100mV is likely due to graphite's density of states, being present in 90% of dI/dVs. During the acquisition, the feedback gain is set to the minimum value possible, i.e. very close to zero, to have an almost constant heigh image. Despite such expedient, as shown in Figure 4, the topology channel still presents the typical HOPG features. The dI/dV image, resembles closely the current channel, but only at 100mV bias. This suggests that the minimum of the dI/dV curve corresponds to the HOPG density of states at the equilibrium energy (i.e. at the chemical potential of the system) assuming a 0.8Å distance from the substrate. [4]

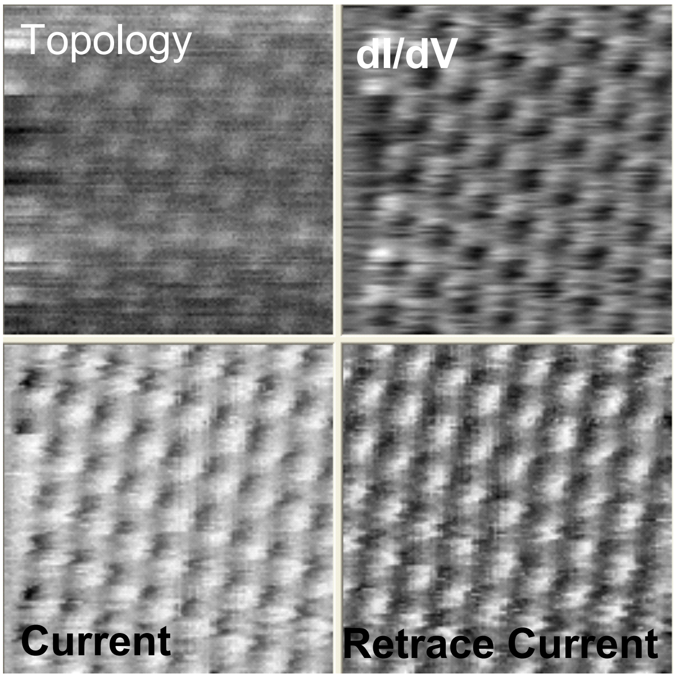

Figure 4**:** Scanning Differential Tunneling Microscopy (SDTM) image of HOPG in TCB solvent. I_t = 100pA V_t = 100mV. Modulation Current V_{ref} = 2mV @ 100KHz with an integration time-step of 1ms.

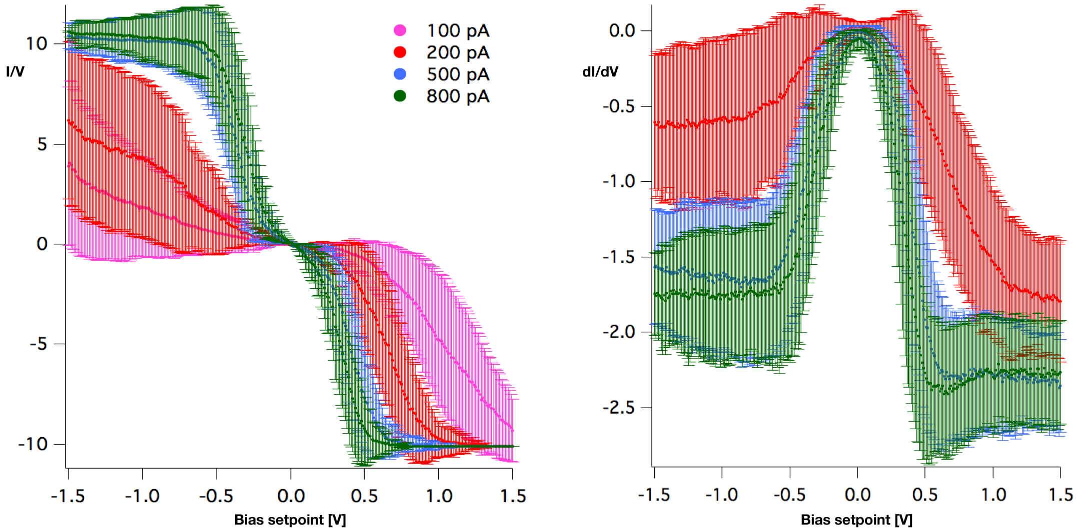

Figure 5: I/V and dI/dV acquired under different bias setpoints at the HOPG/air interface; the shaded areas corresponds to the errors. Calculated from the average over 100 samples.

As an additional proof of principle, we investigated the copper phtalocyanine **1** at the HOPG/TCB interface (figure **6)**.

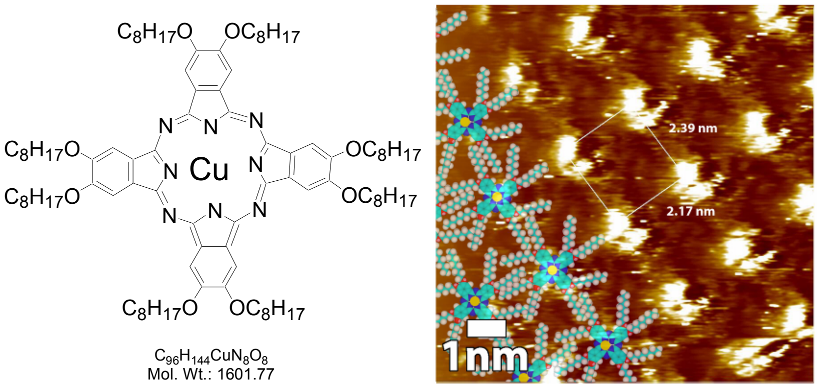

Figure 6**:** STM image of **Molecule 1** in TCB. I_t = 26pA V_t = 472mV

The preliminary dI/dV spectroscopy shows that there is a strong peak at negative biases, -900mV, when acquired over the molecule (Figure 7). At this setpoint (-900mV, I_t=120pA) the topology and current channels shows no signal, whereas in the SDTM a localized contrast arising from the metal center of the molecule is present. The dI/dV is essentially flat in the rest of the range, and the the SDTM channel is constant as expected. The effect is summarized in Figure 7 : changing the sign of the applied bias at half of the acquisition, invert the contrast in the current channel, don't affects the dI/dV image, as expected.

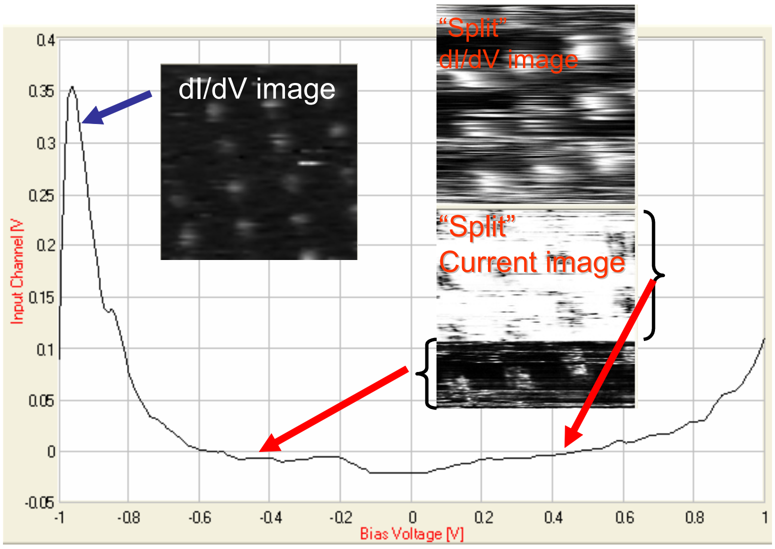

Figure 7: Scanning Differential Tunneling Microscopy (SDTM) images embedded in an dI/dV curve of Molecule 1 in TCB solvent. It = 120pA at Vt -900mV and It = 56pA at Vt = -450mV and 450mV (red arrows). Modulation Current Vref = 4mV @ 100KHz with an integration time-step of 1ms and 12dB filter. Image sizes are 10x10nm2 with a resolution of 256pixels/lines.

Part 2: dI/dV imaging of Polycrystalline Graphene:

Polycrystalline Graphene is a new material (provided by Prof. GoelzHaeuser in Bielefeld) that allows deep understanding of macromolecules made of electronically different molecular-grains. In particular, unraveling the conduction in these materials would allow to understand the first principles of the conduction threshold of crosslinked molecules.

Moreover, these materials are particularly interesting from our stand point since the conductivity for polycrystalline graphene (ca. 0.1mS/sq.) has been demonstrated to follow a semimetal conduction model, and TEM measurements showed that the material consists of covalently bonded 5nmx5nm graphene crystallites.

One of the most interesting scientific questions that such system may help in answering is why the conductivity has a certain threshold value. Discerning whether it is due to the mean free path of the electron, so that the macroscopic conduction can be explained by scattering models, i.e. Bardeen, Landauer or whether the band-gap of the crystallites should be taken into account in a semi-classical approach, such as Marcus theory, or (Franck-Condon) quantum electron blockade. A more immediate objective, is simply to measure the local (nm range) density of states of the polycrystalline material via dI/dV imaging at different biases.

Since pure graphite has a zero bandgap in the density of states dI/dV imaging of graphene/graphite at any bias should result in an homogeneous pixel contrast.

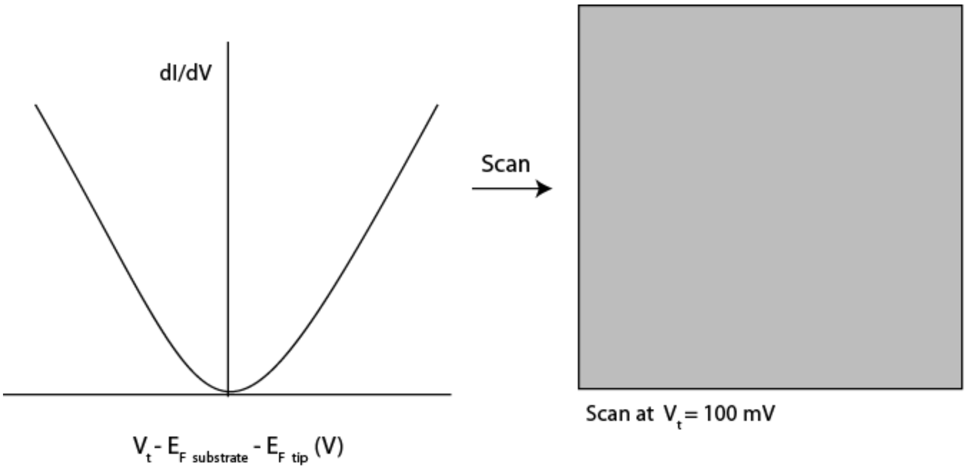

Figure 8: expected behavior of HOPG in a SDTM image. The values of the constrast measured in the SDTM channel should be constant.

Polycrystalline graphene, due to the opening of the bandgap, should show a completely different dI/dV spectroscopy, allowing to recognize areas with small ~100 mV gap between HOMO and LUMO.

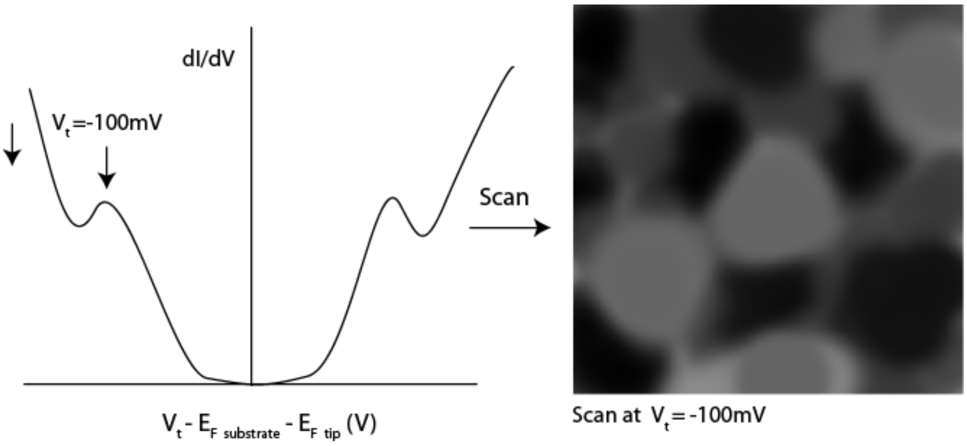

Figure 9: due to the presence of different crystallites with different size, we do expect a different constrast in the SDTM channel, when imaging a sample of NCG.

In conclusion, we expect that in an image acquired at the onset of the DOS (the minimum/maximum of the dI/dV), the maximum contrast will change following the crystallites. By subsequently taking many images from for instance +100 mV to 700mV, the dependence of the contrast from the bias might be extracted. By normalizing the contrast per pixel value in each image and taking a ratio of preference, a color histogram may made be obtained, subsequently fitted by Gaussians or other functions:

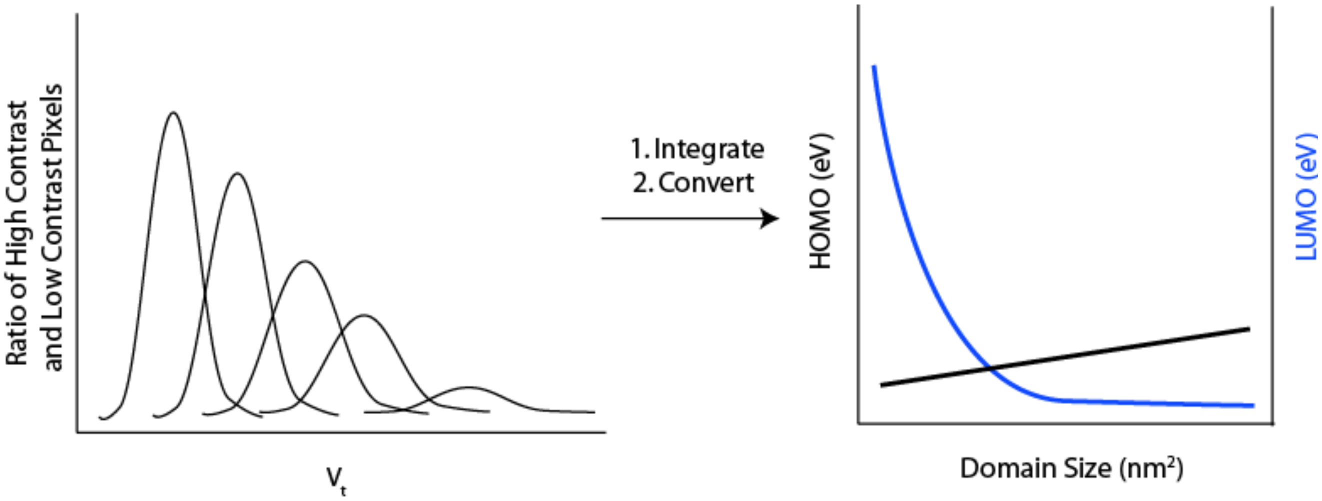

Figure 10: Once the different domains are categorized by their conductivity, it should be possible to extract the function relating the size of the domain with the band-gap.

As seen above, the color histogram may be integrated and transformed into a plot showing the electronic structure of molecular grains, effectively measuring the band-gap of size-dependent crystallites. Notice how at very low and very high biases the image should tend to homogeneous pixel color, since the crystallites should not have a bandgap larger than ~1eV. Furthermore, by comparing the domain size vs. HOMO/LUMO value with a histogram of the grain boundaries the predominant bandgap in the material may be extracted. This may be compared to many bulk charge transfer models and interesting conclusions may be drawn on the physics of conductivity in these material.

Experimental Objectives:

- **STM Imaging of NCG:**
  Direct observation *via* Scanning Tunneling Microscopy has never been reported on such material, thus the observation is the first milestone of the work. *achieved*;
- **dI/dV imaging:**
  Imaging of the LDOS of NCG; *Achieved, despite reproducibility could be largely improved.*
- **Observation of Relationship between bias and normalized dI/dV intensity and Grain Size.**
  The dI/dV should depends on size of the grains and on the applied bias/setpoint. *Work in progress*.

A sinusoidal modulation over the standard DC current was applied and read after passing through the tunneling junction via a PSD mounted in parallel to the standard STM preamplifier. The samples were prepared by evaporating a monolayer of biphenyl thiol on Au Mica to form a SAM, and subsequently annealed at 650°C under UHV following already reported procedure[5]; The resulting NCG samples, were shipped in a closed container to Strasburg. After reception, the samples were gently rinsed with N2, attached on the Mica side to metal disk with small drop of Loctite™ Super Glue3 (cyanoacrilate), and the contacts drew with Ag paste commercially available from Aldrich. Seven contact points between the metal disk and the Au surface were made to make sure even conduction on all the sample. After drawing the contacts the samples were again rinsed with N2 stream, and finally left drying in air for 1h. The samples were stored in air in the instrument sample holder, covered with 1-phenyloctane; no evident degradation was observed after two months.

A STM survey at the interface between the sample and a supernatant 1-phenyloctane solution shows a characteristic distribution of domains (Figure 11).

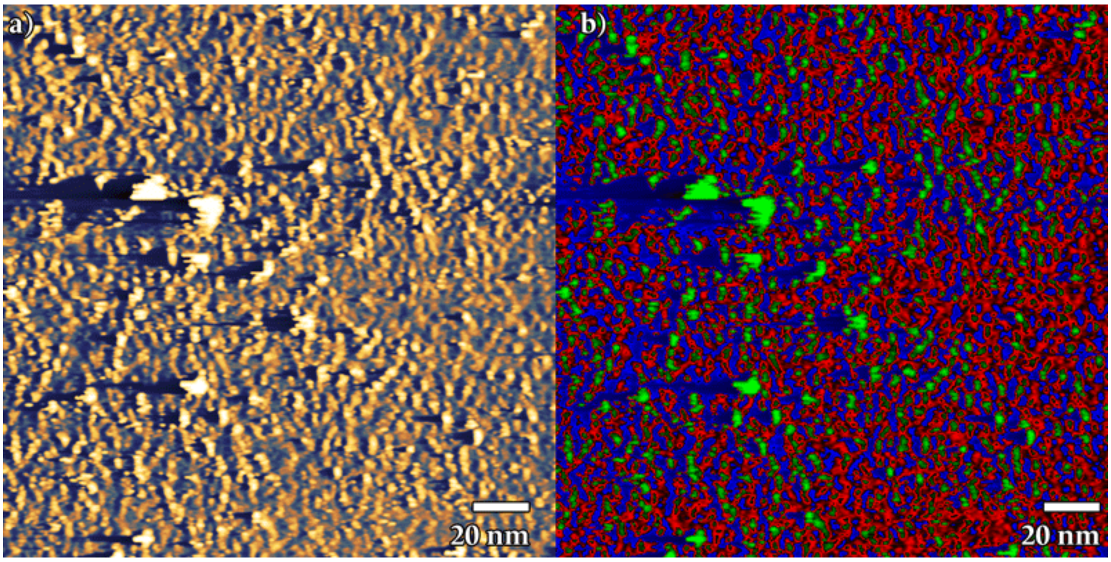

Figure 11: Survey of the sample, a) current image, b) current image recolored to highlight grain distribution of the sample.

The grains have an average surface of 154nm, and their size is distributed accordingly to a lognormal distribution. This behavior is probably related to the pyrolytic synthesis employed: as *Hu et al* observed for nanocomposites, "*With the energy difference (*ΔJ*) between nanocrystalline/nanocrystalline boundary energy and nanocrystalline/amorphous interfacial energy increasing to* ~ $7k_B$T*, the microstructure in the system (...) has smaller grain size, longer grain boundaries, and approximately lognormal grain size distribution.*". The details of the grain distribution are reported in Figure 12.

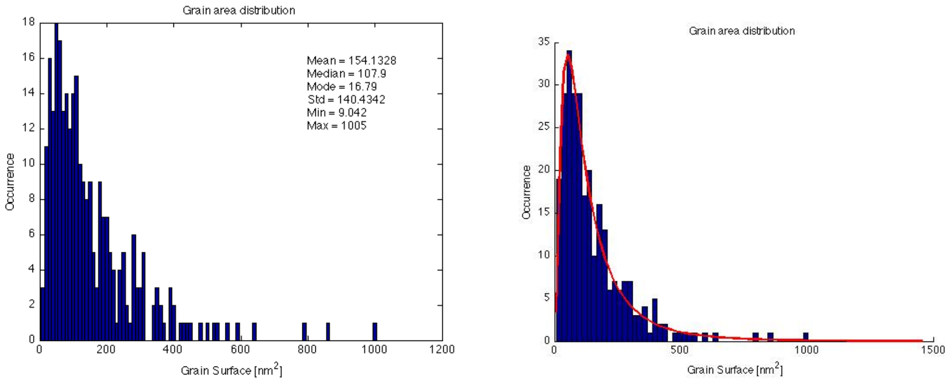

Figure 12: grain statistics (over ca 300grains on 10 images in different spots); lognormal distribution fitting superposed to the grain size distribution.

The STM height images of the samples, observer with higher magnification as shown in Figure 13, shows that the domains are in general flat, confirming the expectations.

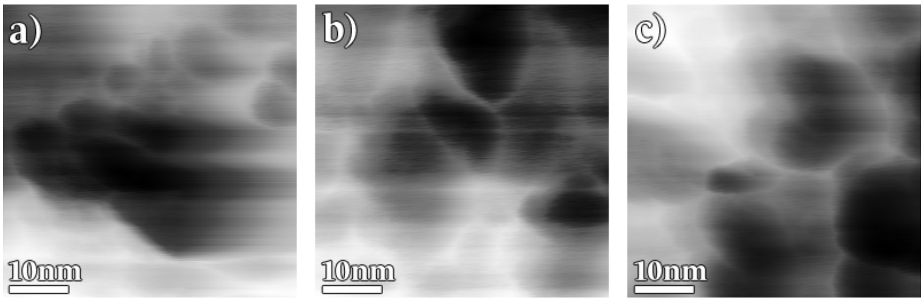

Figure 13: typical height images showing the NCG; 100x100nm, 50mV modulation, 100kHz, 12db, 3ms integration time, 200 nm/s. a) I_t = 250pA, V_t = 220mV, b) I_t = 250pA, V_t = 200mV, c) I_t = 250pA, V_t = 140mV.

The acquisition of dI/dV images, was performed using the modified Ape™ STM, previously introduced. The scanning conditions as well as PSD parameters are reported in each caption. To preserve the sample-tip separation, the following protocol was used: before starting the acquisition, a grain of a fixed size (150nm^2) was individuated and a fixed setpoint imposed (200pA, 200mV). Only on top of such point, the feedback loop was reduced to the minimum possible value, (usually $0.5 \leq I_g \leq 5$) and the dI/dV acquisition started.

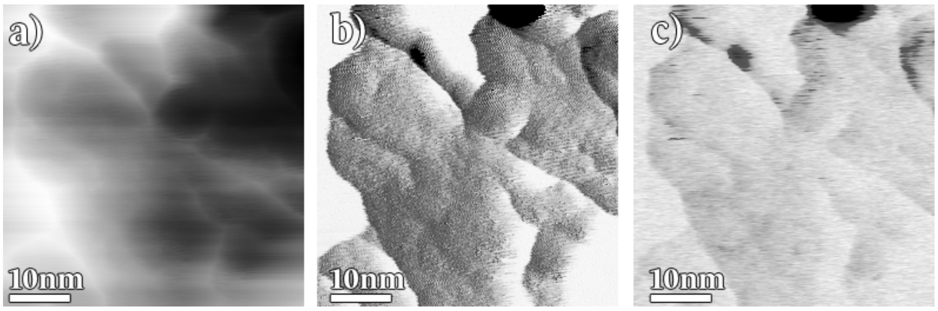

Figure 14: typical acquired raw image, showing a) height, b) current, c) dI/dV channels. To brighter color corresponds higher conductivity.

In Figure 14, an exemplificative image is reported to highlight the distinction between the three channels. For each experiment, 10 images per bias set point were acquired. The images were subsequently exported using the Open Source software Gwyddion[6] , in order to convert from the proprietary ApeResearch ".dat" format into the open format ".png" , to allows further treatment. Before the exportation, the images were corrected using a mean plane subtraction, a line-by-line correction by matching height median, an horizontal scars corrections, and finally the values have been offset to have zero as the minimum value, using the software predefined functions.

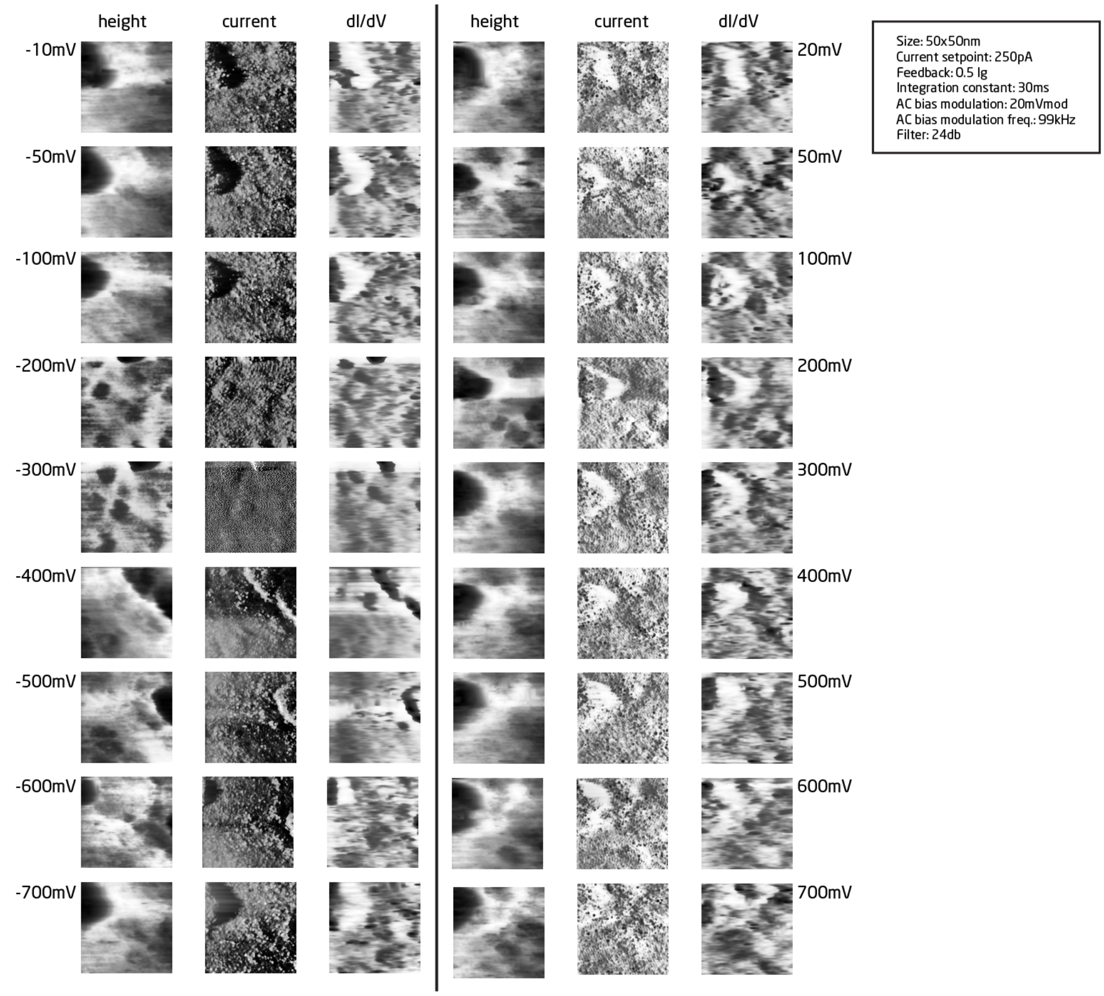

Size: 50x50nm
Current setpoint: 250pA
Feedback: 0.5 Ig
Integration constant: 30ms
AC bias modulation: 20mVmod
AC bias modulation freq.: 99kHz
Filter: 24db

Figure 15: effect of bias change at a fixed current setpoint.

A series of images is presented in Figure 15. It can be noticed how there's a variation in contrast in the dI/dV channel, especially in the low bias regime.

To extract quantitative and statistically meaningful informations about the conductivity of the different grains, some considerations are necessary:

i) During the file conversion, is necessary to minimize the loss of information due to digitalization: in this case, there are two steps: the acquisition, and the conversion between formats. The first digitalization is automatically performed by the STM controller, whereas the conversion was done by exporting a 16bit gray-scale image.

ii) Thousands of images and domains have to be analyzed in order to gather significant statistics: the analysis of the full images, require deep knowledge of image processing, and provides average results. For a more meaningful analysis of the single domains, is necessary to develop a software which will i)identify the grains, and ii) correct the drift, and iii) extract the dI/dV curves from the series.

The development of such software is still ongoing, and some details are reported in appendix 2. The analysis of the full images however was performed.

The thousands of images acquired, were analyzed using Wolfram Matlab™, with a 4 level threshold model. The grayscale value of each pixel has been converted in the range between 0 (black) and 1 (white). Then four threshold levels were defined (i.e. 0.25, 0.45, 0.65, 0.85) and the evolution of the number of pixels falling in each range with the bias is shown in Figure 16. Such plot shows how the amount of "contributing" domains increases with increasing bias.

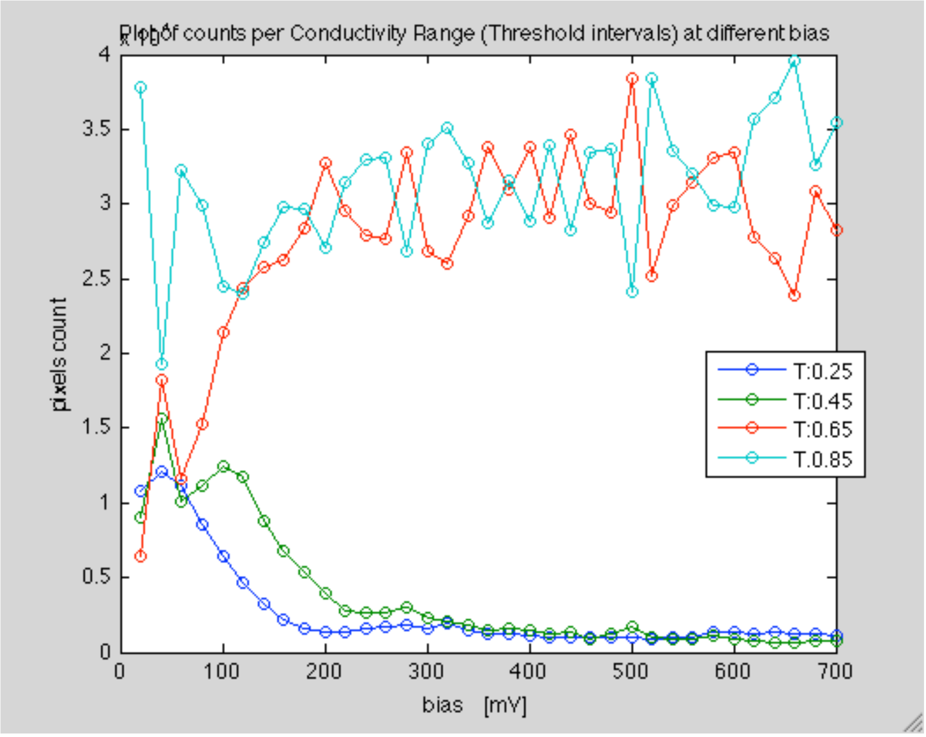

Figure 16: Plot of the number of pixel in a certain conductivity range, calculated by extracting the number of pixel in a certain threshold range: to each pixel in each image has been assigned a value between 0(black) and 1 (white).

There are in literature numerous algorithms for the auto-detection of domains, which in general belongs to two categories, edge detection (sobel, canny, etc.), or grain detection (such as watershed). As can be seen in Figure 17, their application is not suitable for our system, since the low resolution and the limited color gradient between the pixels. One other attempted way to auto-detect the domains was to apply a transformation to L*a*b space and clustering with euclidean norm. The result of such process are shown in Figure 18, and as can be seen with more promising outcomes.

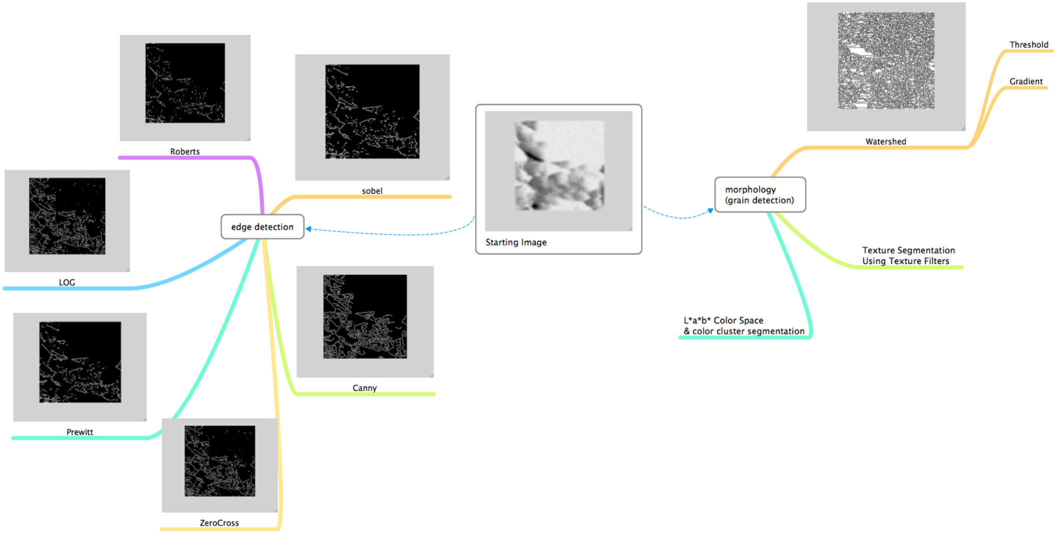

Figure 17: comparison of the most common grain detection algorithms.

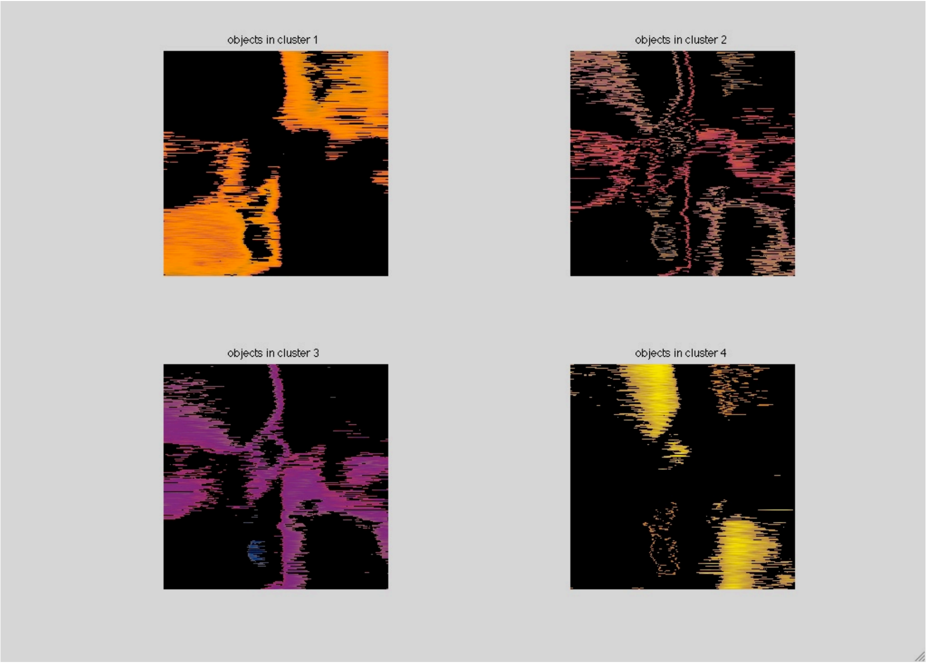

Figure 18: An example of the areas detected by using a mapping on a L*a*b* color space and K-means clustering.

Conclusions

Imaging of the NCG at the Au(111)-PO interface has been achieved, and grain statistics shows an average grain area of roughly 150 nm^2. No definitive observation of a dependence of contrast from the bias could be reported. Other methods of normalization are under investigation, since they might highlight features currently underweighted. As an example, the renormalization of all the images in the same color-range further corrected by the set point has been performed but so far did not produce any new conclusion and is currently under investigation.

Another point to stress, is that it has been shown that nanographenes have a diode like behavior[7], and the obtained result might not be surprising for positive sample bias: the bigger the nano-graphene the smaller the gap, and the more likely is a resonance through the homo/lumo levels. Which it is in order responsible for the non linear diode-like behavior. This means, that on one side, eg. negative, (assuming only one between homo and lumo is in resonance conditions) the contrast has to change linearly, while the resonant capable has to vary exponentially. The expected behavior is that each domain will, according to his size, vary is contrast as a function of the bias at a different rate. Even if all the datas have been acquired, the extrapolation of the results has been more complex than what expected, therefore the investigation is still ongoing.

1. (a) Grobis, M.; Khoo, K. H.; Yamachika, R.; Lu, X. H.; Nagaoka, K.; Louie, S. G.; Crommie, M. F.; Kato, H.; Shinohara, H., Spatially dependent inelastic tunneling in a single metallofullerene. *Physical Review Letters* **2005,** *94* (13), -; (b) Grobis, M.; Wachowiak, A.; Yamachika, R.; Crommie, M. F., Tuning negative differential resistance in a molecular film. *Applied Physics Letters* **2005,** *86* (20), -.

2. Tersoff, J.; Hamann, D. R., Theory of the Scanning Tunneling Microscope. *Phys Rev B* **1985,** *31* (2), 805-813.

3. (a) Binnig, G.; Rohrer, H.; Salvan, F.; Gerber, C.; Baro, A., Revisiting the 7x7 Reconstruction of Si(111). *Surf Sci* **1985,** *157* (2-3), L373-L378; (b) Binnig, G.; Frank, K. H.; Fuchs, H.; Garcia, N.; Reihl, B.; Rohrer, H.; Salvan, F.; Williams, A. R., Tunneling Spectroscopy and Inverse Photoemission - Image and Field States. *Phys Rev Lett* **1985,** *55* (9), 991-994.

4. Cisternas, E.; Stavale, F.; Flores, M.; Achete, C. A.; Vargas, P., First-principles calculation and scanning tunneling microscopy study of highly oriented pyrolytic graphite (0001). *Physical Review B* **2009,** *79* (20), -.

5. Turchanin, A.; Weber, D.; Buenfeld, M.; Kisielowski, C.; Fistul, M. V.; Efetov, K. B.; Weimann, T.; Stosch, R.; Mayer, J.; Golzhauser, A., Conversion of Self-Assembled Monolayers into Nanocrystalline Graphene: Structure and Electric Transport. *Acs Nano* **2011,** *5* (5), 3896-3904.

6. Nečas, D.; Klapetek, P., Gwyddion: an open-source software for SPM data analysis. *Central European Journal of Physics* **2012,** *10* (1), 181-188.

7. Böhme, T.; Simpson, C. D.; Müllen, K.; Rabe, J. P., Current–Voltage Characteristics of a Homologous Series of Polycyclic Aromatic Hydrocarbons. *Chemistry – A European Journal* **2007,** *13* (26), 7349-7357.

Appendix 3: Software

Part of this thesis work has been aimed to the development of different software tools to speed up the processing involved in many routine techniques. Some operations are dramatically time consuming, such as the manual processing of different images or the preparation of structures for MD simulations. Such operations can usually require up to a week of repetitive work, by manually editing file by file or by opening an STM image, applying the filters, and exporting the results. Such operations have been optimized and automated for being performed in a couple of minutes.

Furthermore an important software principle was implemented, i.e. Object Oriented Programming (OOP). The largest advantage consist in organizing the software to be composed of modules (Objects, or more in particular Classes) in order to, eventually expand and modify just part of the code. It has also the advantage of helping the collaboration between multiple programmers. We applied such approach in the development of a MonteCarlo suite, which is flexible enough to span between simulation in vacuum, on lattices, and implements genetic search of the configurations.

Coding generalities:

In the following section a very basic and brief description of key concepts is presented, for who has never had the opportunity or the time to write a program.

Languages, and pseudo languages:

In order to provide instruction to a computer is necessary to transform the desired operation in a sequence of bits (the *machine-code*), which will be finally processed by the device. Luckily, such step has been hidden from the final user trough the abstraction of coding languages, and two tools: the *interpreter* and the *compiler*. As in normal human languages, there are some grammar rules necessary for producing meaningful sentences, therefore a coding language is required to discuss with the *interpreter* that will translate with the aid of the *compiler*, the program in machine-code.

The series of instructions that makes a program, is often a written text, called *source-code*, or simply *source*.

In general computer algorithms and codes are **sequential**: they consist in a list of *instructions*, which are blindly performed by the Computer, one by one, in series. The art of coding resides in generating a meaningful (for the computer, and for the humans) set of instructions, to perform the desired task.

As previously said different languages present different grammar rules, and different syntaxes, but nowadays the efficiency in the process of *abstraction*, and the introduction of *high-level* languages allows for almost perfectly human-readable programs.

Even when few differences are present from the "normal" languages, they may seems surprising: By far, the most famous one is the assignation operator "=".

It really differs from the mathematical identity, as it means to assign to the operand on the left, the value on the right.

The assign operation often resembles a mathematical blasphemy:

```
a=a+3
```

and will give the goose bumps to many, but when *coded* simply means to assign to the *variable* a, the value that already contains, incremented by 3.

The "Esperanto" of the computer coding is called pseudo-language. Is a fake language, which serves only for explanatory reasons.

Logic and conditions:

Logic in informatics is roughly equivalent to evaluating the effects of binary operations, and to build a table of truth. Usually to the logic value "True" is assigned the value 1, and to the value "FALSE" is assigned the value 0. Which means, that the *bits* also represents logical values. It behave in fact as an electrical switch: on and off. It automatically derives, that transistors naturally performs the logic operation AND (if considered digitally). If source and gate are biased, then there's measurable current in the drain. If only one of the two "inputs" is active, then there will not be current measured in the drain "output", therefore it will be considered a 0. From this small assumption derives most of the technological revolution that occurred in the 70's .

Conditions are fundamental when programming. By far the most important one is the "if" construct. Beautiful in its simplicity, is best described with a pseudocode example.

```
Do something…
IF condition is True: do something more
And finally do something-else
```

With a more realistic example,

```
A=3
B=A *3
C=6
If B>A then C=10
D=A/C
```

Which will execute always returning D=0.3;

Loops:

Next important concept is the one of *loops*, which consent "flow control" while *processing* (or *parsing*) the code.

The major two are the **for** loops, and the **while** loops. Again, their incarnation in languages closely reminds English, therefore the explanation is almost elementary.

For, means to repeat the same operation (or *block*) a certain number of times, or even better, *for a certain sequence of steps*. **While**, on the other side, usually means to repeat the same block as long as a certain condition is valid.

Examples:

```
Do something
For i =[1:10]:{
 Repeat this
}
do something else
```

```
Do something
While i<10:{
Repeat adding 1 to i
}
do something else
```

Functions:

A function is a smaller program inside the program. Sometimes, it is useful to reuse a certain block of code in different parts of a *source*; in this case it may be better to generate a *function* and then reference to it with the desired parameters, rather than writing again all the operations. If used properly, functions greatly improve the efficiency and readability of a software. Let's consider as an over simplistic example the product between two integers. A product, is a sequence of addictions. Therefore we can either repeat a series of addiction, every time we have to multiply something, or define a function which do it, improving the "readability". Again, we can write that 3x3= 3+3+3, that 5x4=5+5+5+5, or define once for all the function multiplication between A and B as product(A,B)=A+A+A+A…+.A (b times), and then simply use it whenever is needed referencing to it as "product(x,y)" where x and y are called *parameters*.

Objects:

So far, with functions and loops is possible to reproduce almost all the software around. However, since a couple of years, a new abstract entity has entered the coding community: the objects. Reminiscent of the platonic "world of ideas", objects are collections of functions (which are called *methods)* and values: e.g: different pens (fountain, ballpoint, blue, etc.) are different *instances* of the same object, called pen. All share the same method "write", and possess an "ink level". Such abstraction, comes really useful when the projects are developed by large teams, or to avoid editing all the sources for a minor change. It is usually more efficient to separate the program in many objects, which are then employed by the *main* function (if your chair or pen is broken, is easier to replace it rather than changing all the office).

CDX2MRK – from chemdraw sketches to MD simulations:

The standard procedure used to prepare a structure to be investigated using molecular dynamics, has been quite farraginous and complicate, requiring the interaction between different software, often running under different Operative Systems (OS), and hours of manual operations. A general flowchart picturing the procedure is reported in Figure 1. The biggest user-time losses are:

1)The manual generation of the desired supra-molecular architecture: it usually comports to edit the simulation input file, to generate a dummy output that must then be visualized and compared to the target structure, in a trial and error way, until a sufficient agreement is reached.

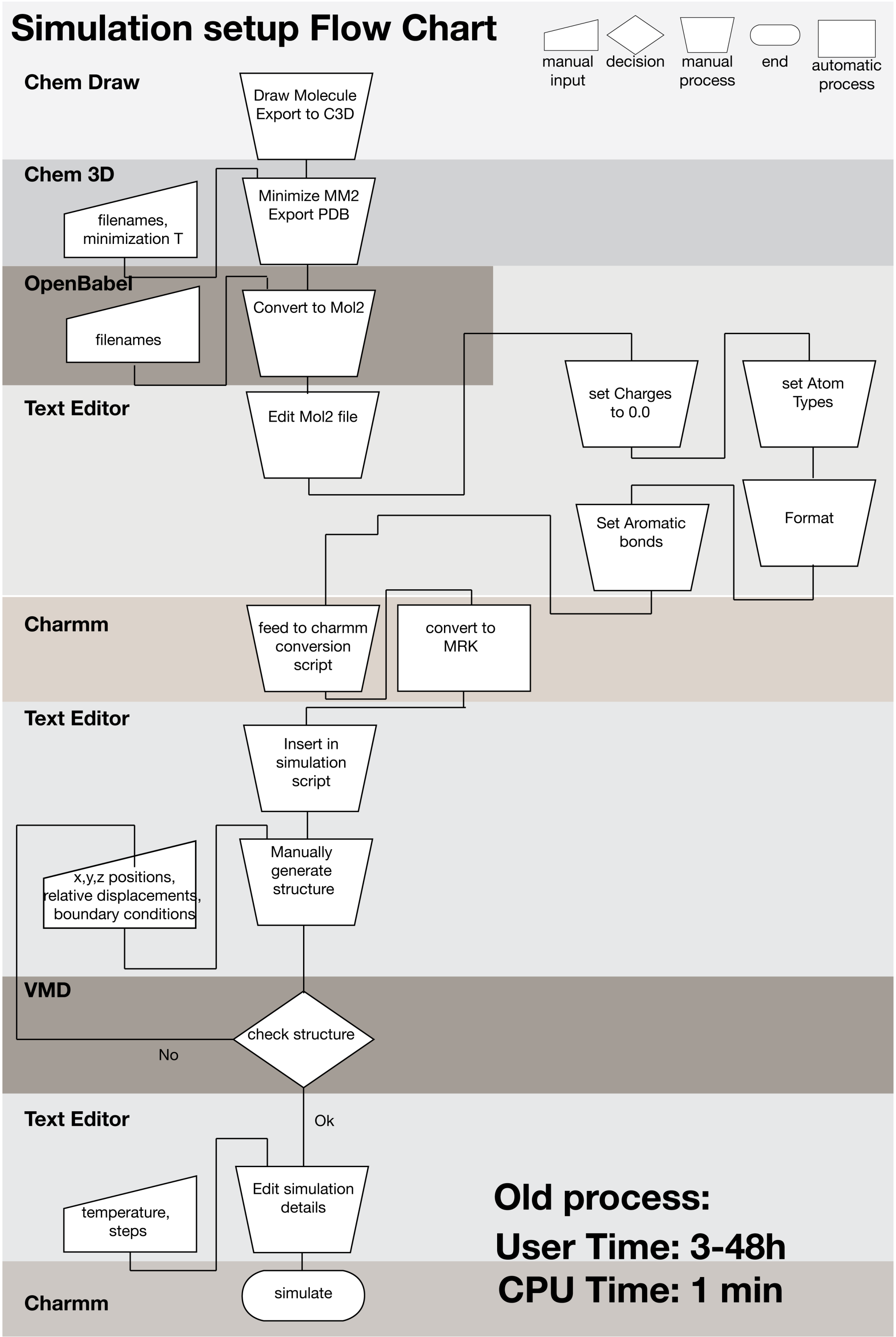

Figure 1: Flow chart of the standard procedure.

2) The manual formatting and editing of the file containing the molecular coordinates and atoms, before converting it applying MMFF94[1] force field: There's a mismatch between the fixed fields read by CHARMM[2] and the one of the Tripos mol2 standard.[3] Such highly repetitive and simple, albeit time consuming, tasks were not yet automated. However, the major difficulty to set-up a fully automatic procedure has been the conversion from a bi-dimensional Cambridge Soft Chemdraw file (extension CDX[4]) to a tri-dimensional Mol2:

The conversion for a single molecule is trivial using the Cambridge Soft C3D software (which is only available in MS Windows)or using Wavefunction Spartan10. But for multiple molecules, e.g. an hydrogen bonded dimer, this approach fails: the information of the relative coordinates is lost during the export. Another possible path, consist the direct conversion from the 2D CDX to the 3D mol2 using the open Source software OpenBabel.[5] The generation using babel however affected the bond lengths, resulting in completely wrong atomic distances;

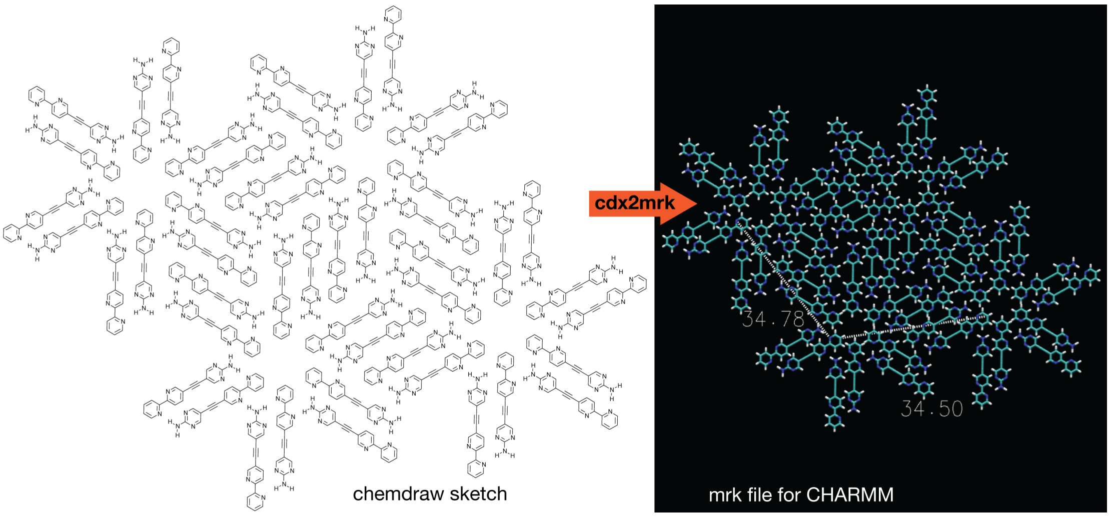

Figure 2: initial and final structure after the application of the cdx2mrk conversion.

In front of such issue, we coded a fully automated procedure, which permits to use complicate patterns generated in ChemDraw and transforms them to the Mrk ready for the simulation – an example is shown in Figure 2:

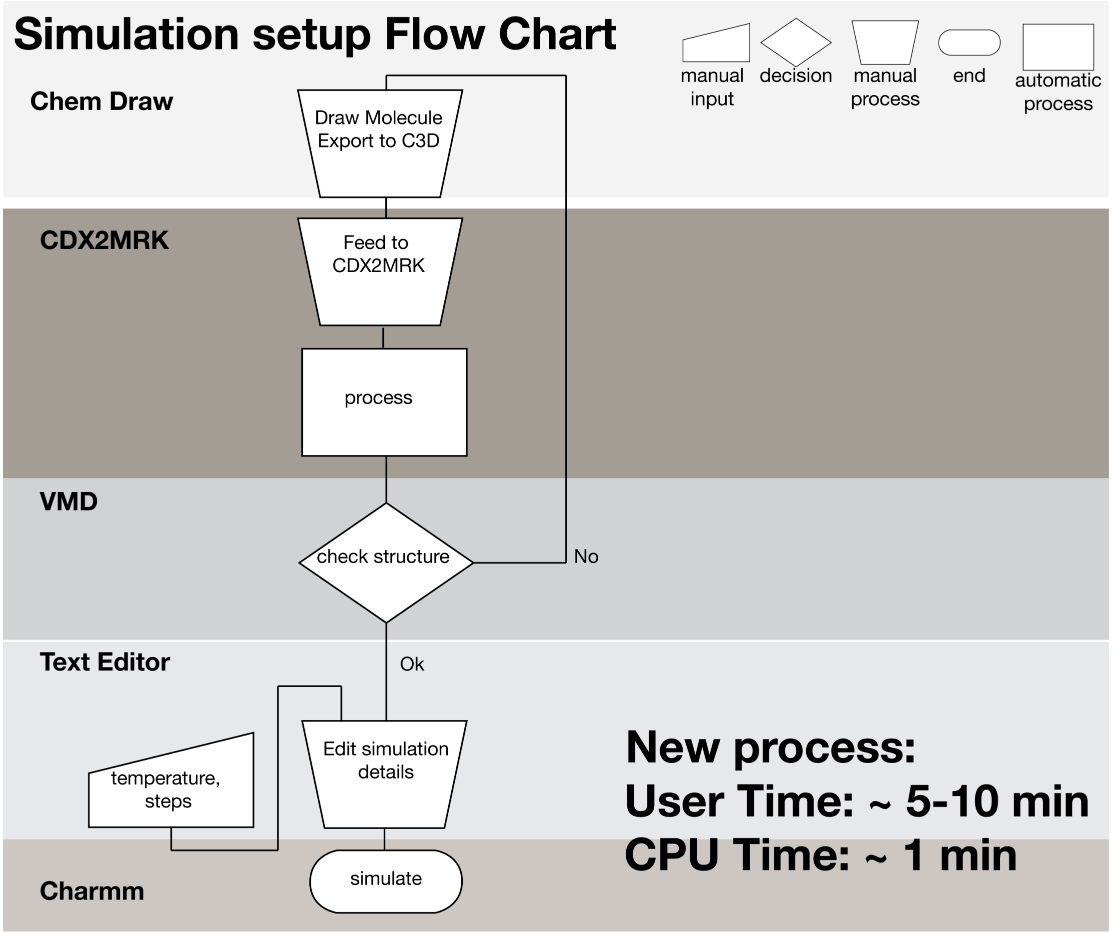

Figure 3: optimized process

generating a similar structure would have probably been one to two days of trial and error tests. The final flow chart of the process, is pictured in Figure 3: it shows how all the intermediate steps are handled by the automatic procedure cdx2mrk.

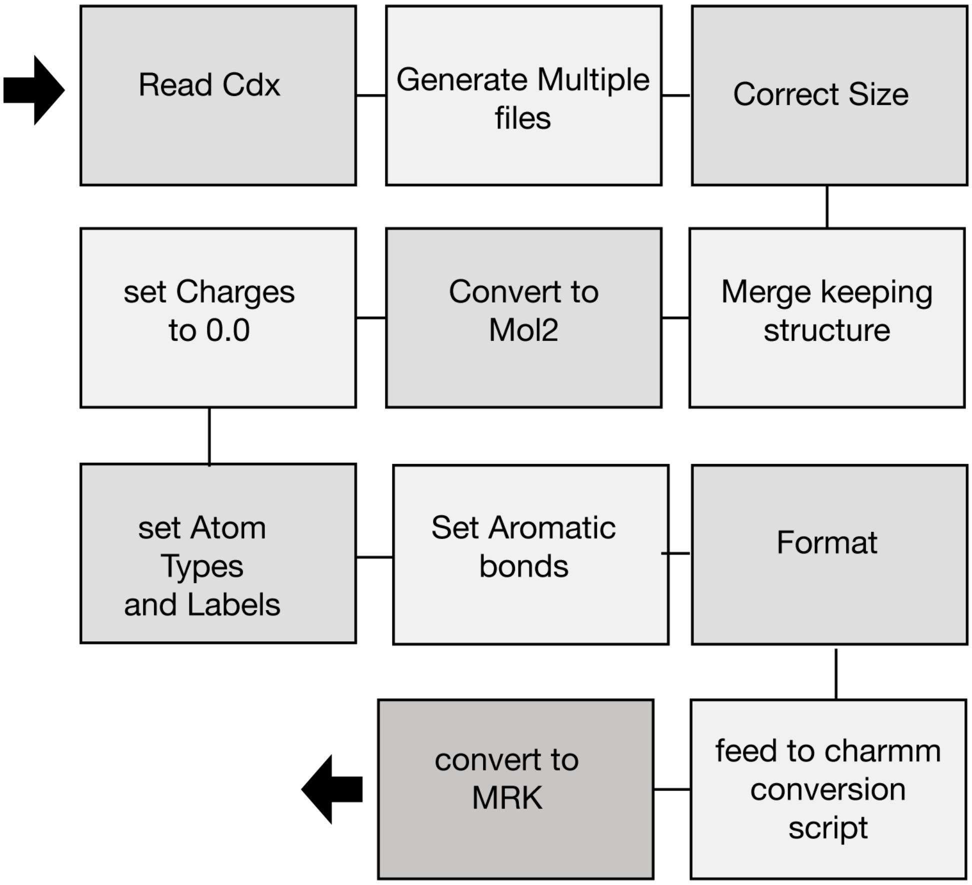

Figure 4: Internal procedure of Cdx2Mrk

The core of the cdx2mrk software is showed in Figure 4. It has clearly the same procedure of the part it replaces, but in an automated way. The more important steps will be discussed in the following sections.

Step 1: OpenBabel conversion, corrections and merging

The more convenient option to automate the conversion from ChemDraw CDX format, is using the open source software Openbabel,[5] which has a command line interface (CLI) and fully support scripting. The conversion however is affected by a scale error, as shown in Figure 5. After multiple trial and errors, we noted that the bond lengths of the generated structure are generally proportional to the Style of the document of the CDX file.

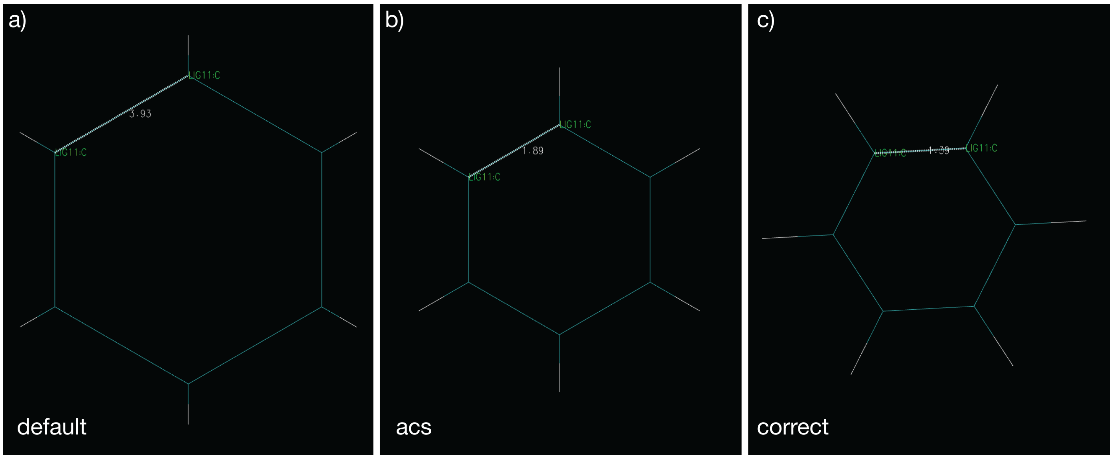

Figure 5: benzene representation after direct conversion (a, b) and the correct dimensions, starting from a) cdx default style, b) ACS style. The length of the C—H bond is in all the occurrence 1.09 Å.

To avoid the scaling error, OpenBabel has a –gen3d flag which add explicit hydrogens and minimize the structure using MMFF. Such approach generally fails (entering in infinite loops) in presence of polyaromatics or complex supramolecular structures. However, observing the generated files, is it evident how the error between the non "–gen3d" structure and the desired one is just a scale factor (without considering the hydrogen). The addition of the explicit hydrogen must be done after the correction of the bond lenghts. Luckily, the Babel OpenSource Community provides a Python[6] application programming interface (API) allowing to code a short conversion script, *via* the specific functions of file handling of the software. The relevant part of the code is reported in Snippet 1.

```
import sys, pybel, openbabel
inp=str(sys.argv[-1])
factor=1.39/1.89 # this value is a constant for each chemdraw style -
check if not using ACS style;
molecules=list(pybel.readfile("cdx", inp))for mol in molelecules:for
each in mol.atoms:

   x=each.coords[0]*factor
   y=each.coords[1]*factor
   z=each.coords[2]*factor
   each.OBAtom.SetVector(x,y,z)
 mol.addh()
outf=inp[:-3]+"mol2"
output = pybel.Outputfile("mol2", outf,"overwrite=True")for mol in
molecules:
    output.write(mol)
output.close()
```
Snippet 1: python conversion script to perform the scaling

This function subsequently generate a single file with the supramolecular structure in format Mol2.

Formatting and editing of mol2 files.

Charmm, and more in particular, the algorithm that parses the MMFF94 atom types definitions require a precise format for the input mol2 files, which is generally not compatible with the one exported by most software (Figure 6). For this reason one had to edit manually the file properties:

A typical example of the file format before formatting is reported in Figure 6.

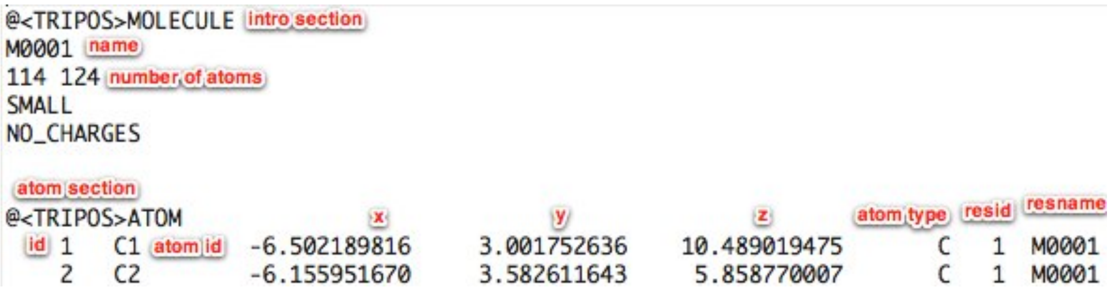

```
@<TRIPOS>MOLECULE
M0001
114 124
SMALL
NO_CHARGES

@<TRIPOS>ATOM
      1  C1   -6.502189816   3.001752636   10.489019475   C   1  M0001
      2  C2   -6.155951670   3.582611643    5.858770007   C   1  M0001
```

Figure 6: extract of a file with highlighted the respective datas. Is not formatted correctly.

The two functions that take care of the formattation are

```
def string_formatter_atom(lines):
    if lines.startswith("@"):return"@<TRIPOS>ATOM"
    line=lines.split()
    atom_id=line[0].rjust(6)
    tmp=line[1]+line[0]
    atom_name="   "+ tmp.ljust(8)#col10-19
    x=line[2].rjust(10)     #col 20-27
    y=line[3].rjust(10)     #col 28-37
    z=line[4].rjust(10)     #col 38-47
    atom_type="  "+ line[5].ljust(8)#col 48#
    subst_id = line[6].ljust(4)     #col 56
    tmp="LIG"
    subst_name =tmp.ljust(10)# line[7].ljust(10)
    charge=" 0.0000"#line[8].rjust(7)
    #atom_id

    return atom_id + atom_name +x +y +z +atom_type+subst_id+
subst_name +charge

def string_formatter_bond(lines):
    if lines.startswith("@"):return"@<TRIPOS>BOND"

    line=lines.split()
    bond_id=line[0].rjust(6)
    A=line[1].rjust(5)
    B=line[2].rjust(5)
    order="  "+line[3].ljust(1)

    return bond_id+A+B+order
```

Snippet 2: Formatting functions.

mol2 2 mrk

The last step is converting to Mrk format – this is done feeding the single file containing all the molecules trough a predefined Charmm script – to avoid entering the file names of the input and the output files manually the following vulgar hack has been implemented coding a bash script.

```
#! /bin/bashfile=$1
cp $file filenaem.mol2
~/.mrkconverter/megamol2.py mol2 filenaem.mol2
cp filenaem_mmff.mol2 filenaem.mol2
#charmm < ~/dokz/tools/2mrkconverter/mtf.MMFF.inp#charmm <
~/dokz/mine/2mrk_converter/mtf.MMFF.inp
charmm < ~/.mrkconverter/mtf.MMFF.inp
~/.mrkconverter/megamol2.py mrk filenaem.mrk
cp filenaem_processed.mrk filenaem.mrk
mv filenaem.pdb ${file%.mol2}.pdb
mv filenaem.mrk ${file%.mol2}.mrk
rm filenaem.mol2 filenaem.tmp filenaem_mmff.mol2
filenaem_processed.mrk
echo" here are your brand new pdb and mrk files. "
```

Snippet 3: script handling the formattation and the conversion.

as can be seen in Snippet 3 the script make a duplicate of the file always with the operative name “filenaem”, then invokes two other programs – the python script megamol2 wich operates the formattation and subsequently charmm with the edited input files. Then It removes the temporary files and returns a pdb another mol2 and the mrk files to import in the charm simulation.

Limitations:

The conversion in mrk, and more precisely the attribution of MMFF atomtypes is limited to 1000 atoms, therefore for bigger structures it is necessary to import multiple substructures already converted.

MCSuite – Monte Carlo tools and libraries

Monte Carlo Simulations are well known and widely employed in many fields of the nanotechnology and physical-chemistry, since they are fast, flexible and can provide insight in systems consisting of a large (if compared to Ab-initio, dft, or MD) number of simulated moieties. The objective of this work was to generate a library of functions and classes capable to handle different simulations, of molecules in vacuum and on a fixed lattice surface. The secondary objective was to allow for expansion for the software, in order to speed up any subsequent modification.

A general sketch of the general composition of the suite are reported in Figure 7;
The solution to the software expansion, relies on the Object Oriented Programming paradigm, therefore each of those components has his specific characteristics, and is "self-sufficient", i.e. possesses certain methods and data which don't depends on the specific instance; -To clarify the concept with a naïve example: a chair is somewhere people can sit. Then there are billions of different chair (instances). But their method "supportSomeoneSitting" takes the same kind of input whomever will be sitting on whatever instance. The consequence of OOP is that the same code is generally able of processing different molecules, on different lattices as hexagonal, triangular, square or without, and carry on the same class of experiment.
It follows a brief description of each class and the implementation of the most important functions, together with few experimental results.

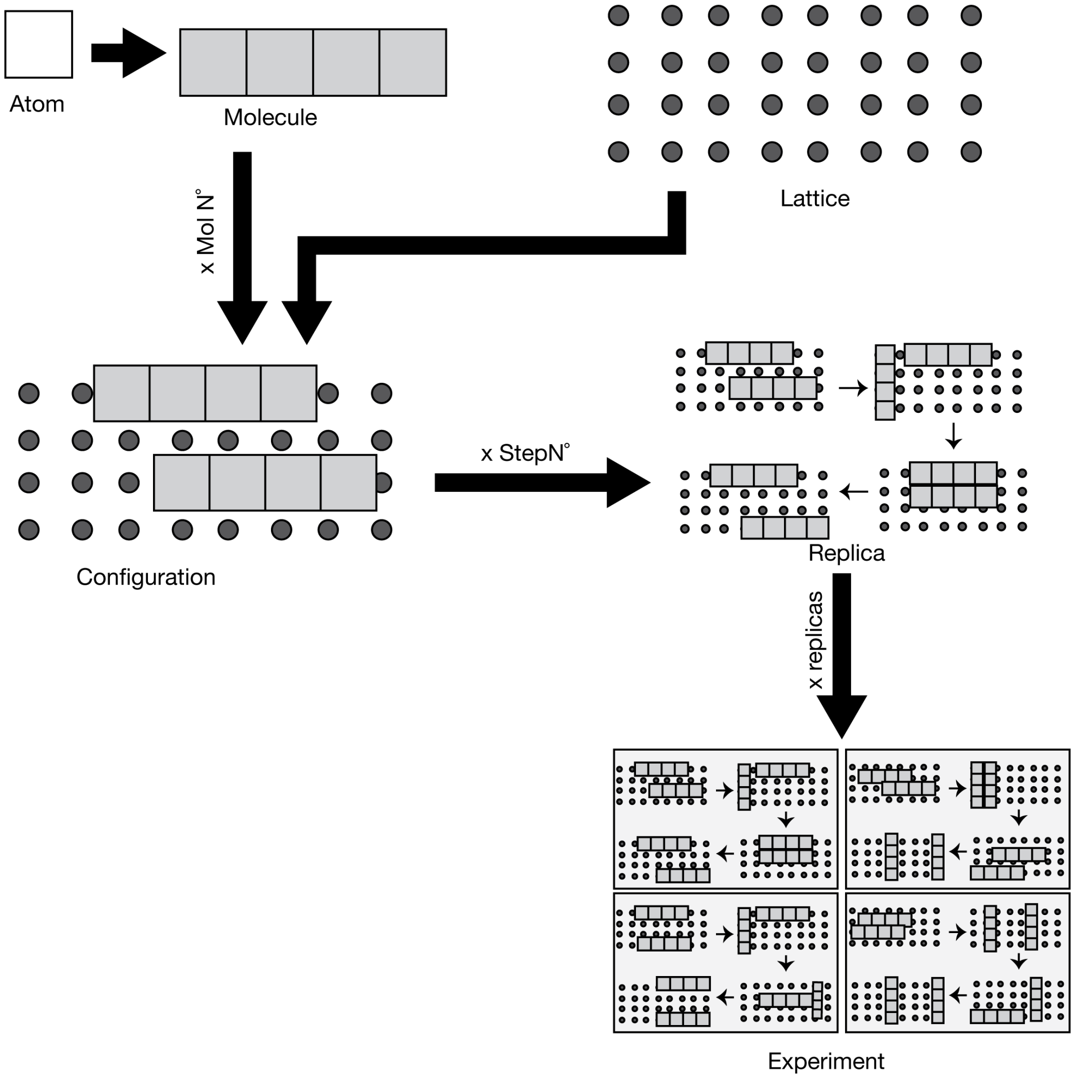

Figure 7: general scheme of the simulation logic, and of the corresponding class hierarchy: ie: each molecule is a container of a certain number of objects "atom"; a configuration is generated by a collection of molecules, eventually fixed on a lattice. Each configuration is part of a replica, which is itself part of an experiment.

Atom Class

The basic building block, is in effect quite simple – it is just a data container with few methods – it is capable to return a vector (position) where is usually stored the position relative to the molecule center of mass. In case of experiment where more atomic properties are interesting, other fields are implementable, such as "kind" or "charge";

```
atom.py
-----------------------------------------------------------
__metaclass__=typeclass Atom:
   """store details of atoms"""
```

```
   def__init__(self, pos=[0,0]):
     from numpy import array
         #operative params
            self.pos = pos
            self.bonded =False

   def setLabel(self, label):
    self.label=label
    return self.label
   def setPos(self, pos):
       self.pos = pos
   def getPos(self):
       return self.pos
   def setAbsPos(self, pos):
       self.absPos = pos
   def getAbsPos(self):
       return self.absPos
```

Snippet 4: Atom Class.

Molecule Class:

Again the molecule object is quite simple, it presents however few more characteristics – it has to include a series of methods to handle the atoms, the positioning and the rotations in space and on a lattice. The details of the rotations on the lattice are discussed in the lattice section; In the Snippet 5 are reproduced the identity functions of the molecules (set and get AtomPos), which are responsible for setting and returning the absolute position of the molecule and of all his atoms; It is also reported the implementation of a diatomic molecule.

```
Diatomic molecule.py
---------------------------------------------------------
__metaclass__=typeclass Molecule:
   """store details of molecules"""
   def__init__(self):#, box_size=[10,10]):
     #from numpy import array
         #operative params
         self.en=0
     self.label=1
     self.atoms=[]
     self.rotate()
     self.addAtom([0,0])
     self.addAtom([1,0])

   def addAtom(self, atompos, label=1):
    from atom import Atom
    a=Atom(atompos)#InternalCoordinates
    a.setLabel(label)#a.setAbsPos()
    self.atoms.append(a)


  def setAtomsAbsPos(self):
    from atom import Atom
    from numpy import array,dot
    Y=self.dir
    X=self.axis_rot(self.dir)
```

```
 for i inrange(len(self.atoms)):
     x=dot(self.atoms[i].absPos,Y)+array(self.pos[1])
     y=dot(self.atoms[i].absPos,X)+array(self.pos[0])
     self.atoms[i].absPos=([x,y])


def getAtomsAbsPos(self,box='nonspecified'):
 self.updateAtomsAbsPos()
 from numpy import array
 M=[]
 if box =='nonspecified':
    for each in self.atoms:
     M.append(array(each.absPos))
 else:
    limits=box
    for each in self.atoms:
     pos=each.absPos
     x=pos[0]%limits[0]
     y=pos[1]%limits[1]
     M.append(array([x,y]))
 return M
```

Snippet 5: implementation, and atoms handling functions.

In general, it is possible to define a new molecule, by simply adding atoms via the addAtom method of the molecule class. Or creating a new class, inheriting from the molecule class, specifying in the constructor (__init__) the desired atomic structure. The move() method, has a switch case function where it allows for the presence of boundary conditions;

Lattice

The lattice class contains the general properties of the lattice, as shape, boundary conditions, and the functions relative to molecule positioned on top: neighbours determination etc.

It must be highlighted the implementation of the triangular lattice: it may be done using a standard square matrix, but allowing for two extra interactions, along the directions +1+1 and -1-1. This, as shown in Figure 8, is topologically equivalent (the transform is skew 30°).

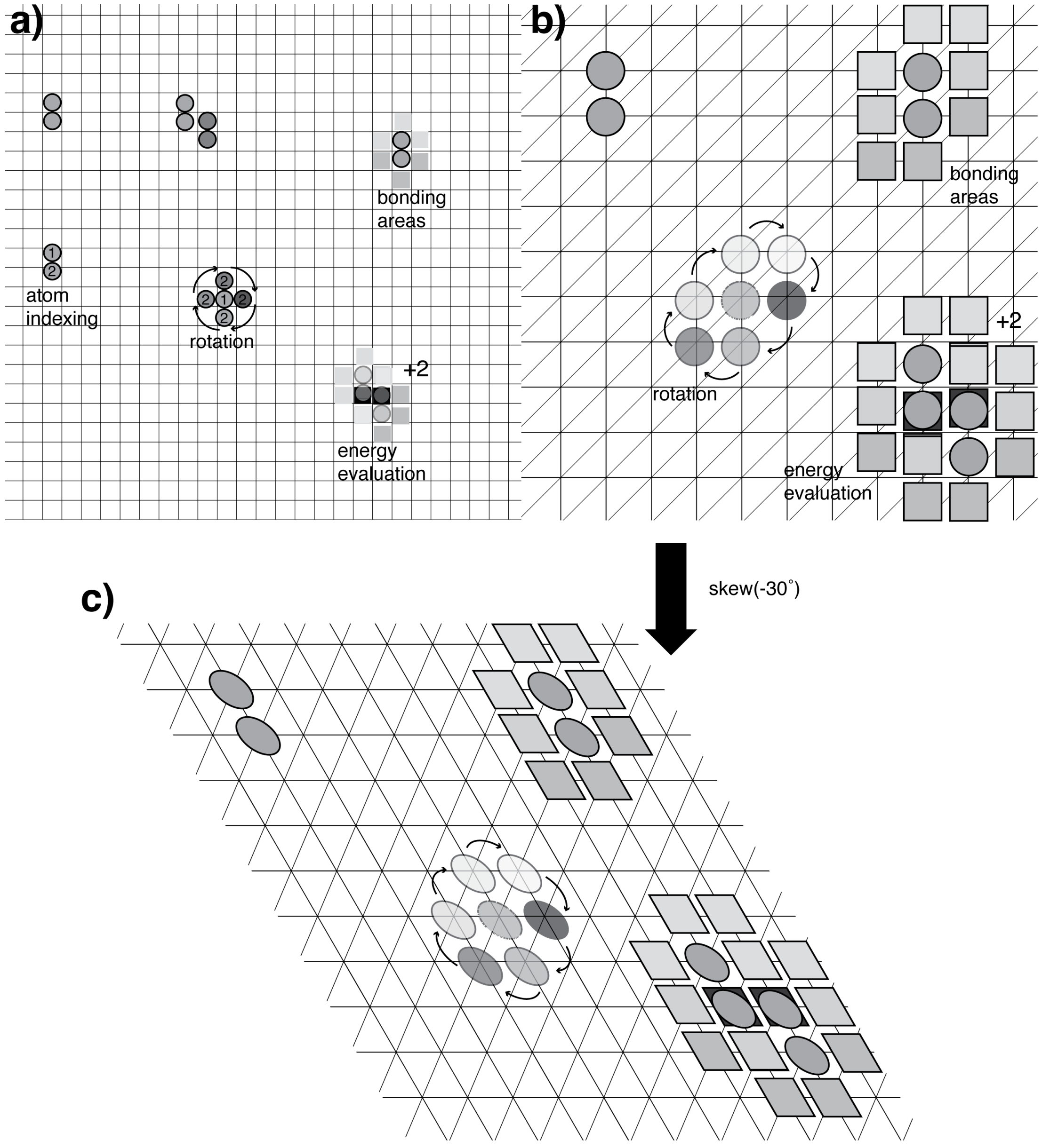

Figure 8: The different lattices are implemented by morphing a square matrix: in case of a triangular lattice is topologically equivalent to use a square one and allow an extra interaction in the directions +1+1 and -1-1;

Configuration:

It contains finally the lattice, its molecules, and performs the computations of the energy. The most important features are the energy evaluation and the metropolis[7] algorithm.

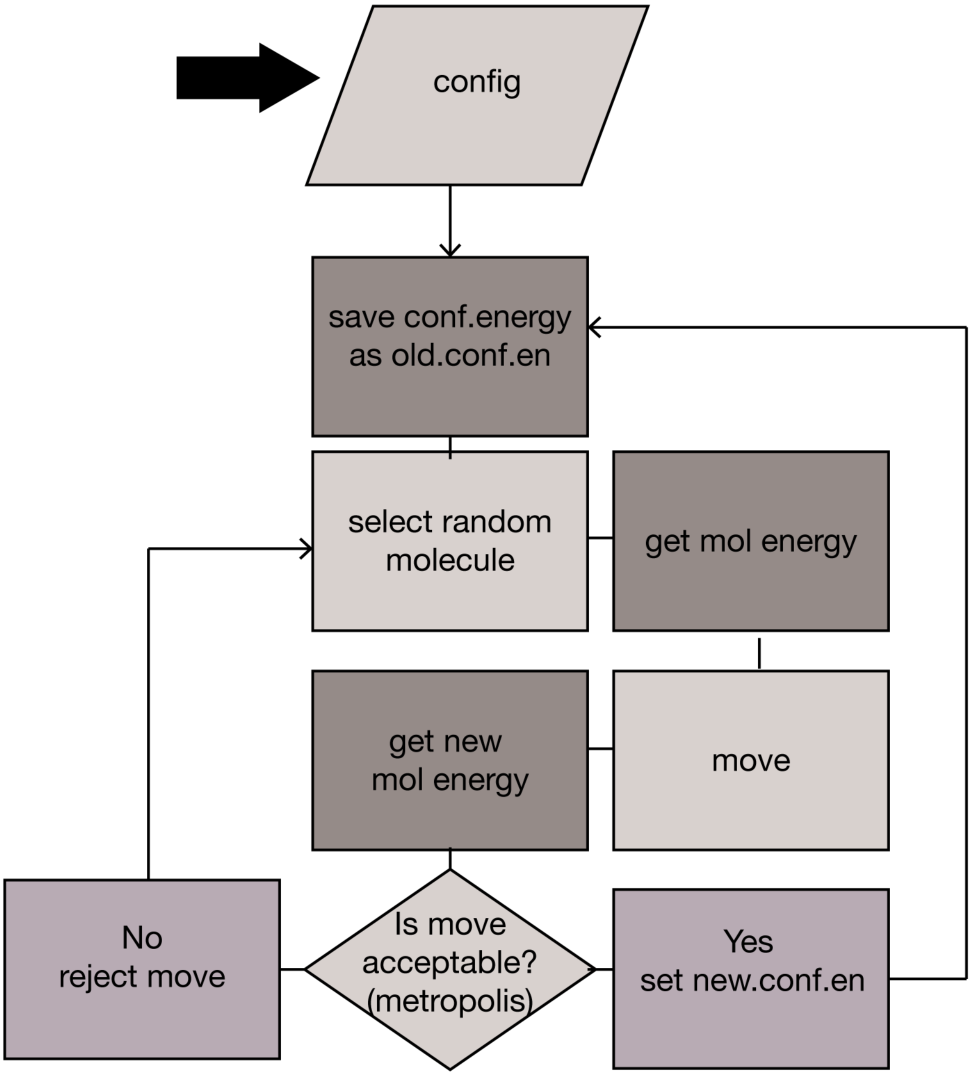

Figure 9: main loop of the simulation.

The main loop of the simulation, is pictured in Figure 9, is a classical Monte Carlo metropolis scheme. It consist in a random selection of a molecule, and then a move (which, depending on the specific experiment may be more or less complicate) obeying the Markov chains, which is accepted according to Metropolis evaluation.

Replica, Experiment:

In general are two classes, which handles a series of configurations, useful for more complicate experiments, e.g. the variation of the energy of the interaction or the temperature of the system (Figure 10 c) or the number of molecules. In Figure 10a, is portrayed an example of how the simulation converges as a function of the temperature.

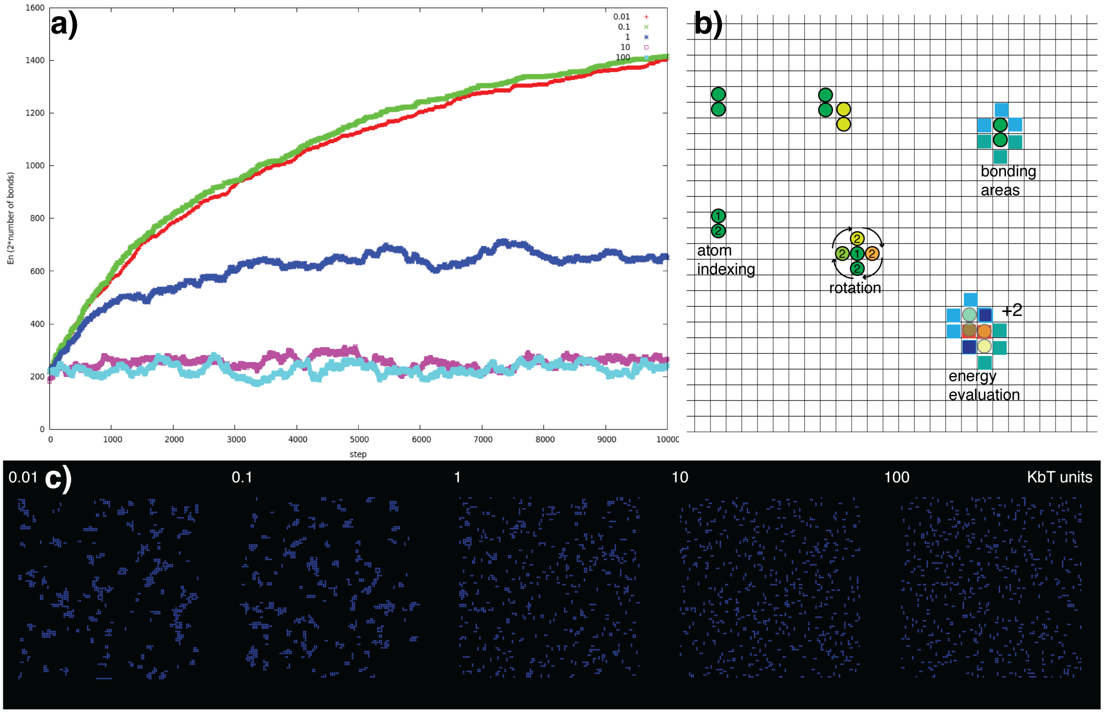

Figure 10: a) evolution of the energy (absolute value) vs steps for a biatomic molecule – the interactions and the details of the motions are reported in b), and the resulting structures are in c); note how the clusters present in c-0.01KbT are dissolving with the raising of the temperature.

Gwyddion – Batch file export, normalization and misc.

Processing multiple image files, applying the same corrections to acquire enough points for statistics can be very time consuming. Furthermore the Ape Research SDTM, uses a proprietary file format that other applications (e.g. Matlab) cannot read. To stress the importance of automating the procedure, the following example can be done:

In the data acquisition phase, we decided to investigate 20 spots, and acquire images at 10 mV intervals in the range between -900 and +900 mV; the typical acquisition time is ca. 90 second per image: this adds up to:

```
20*length([-900:10:900])= 3620 images (* 90s /3600 sec/hour)= 90.5
hours
```

for the acquisition only. This process requires user control, and automation on this phase is not needed. However, the further processing of the acquired data is definitely prone to automation: In each acquired file, 3 channels have to be exported, and on each channel, the standard image corrections have to be applied. This means, that each data file must be manually loaded, (after the AutoSaving function to avoid the loss the filename - 5 clicks, and implying to not having to search the file, t ≥ 20seconds) then filtered manually and saved again in a raster format (7 clicks, ~ 20sec if the gamma correction is not required) per each channel. This add up to

`(5*3620 + 3*7*3620) = 94120cliks (20+(20*3))*3620= 289600s`
more than 80 hours!

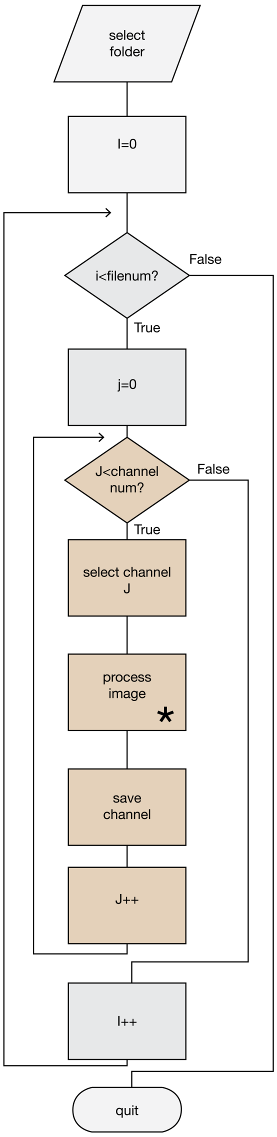

Figure 11

The automatic procedure is based on an open source SPM software named Gwyddion[8], which has the remarkable property of possessing python APIs.

```
from gwy import*from gwyutils import*
def batchDo(filelist):
```

```
    for each in filelist:
        imgWork(each)
    returnTruedef imgWork(container):
    A=gwy_app_file_load(container)
    datafields=get_data_fields(A)
    count=0
    datafield_names= A.keys_by_name()
    for each in datafields:
        a=0.0
        b=0.5
        c=1.0
        count=count+1
        each.fit_plane(a,b,c)#
        p=each.fit_polynom(1,1)
        each.subtract_polynom(1,1,p)
        save_dfield_to_png(A,datafield_names[count], container
+str(count)+".png", RUN_NONINTERACTIVE)
    returnTrue
import os
os.chdir('/home/cadeddu/dokz/didv/')
folder=os.getcwd()
datfiles=filter(lambda x: x.endswith('.dat'), os.listdir(folder))
filelist=datfiles
batchDo(filelist)#gwy.app.quit()
```
Snippet 6: batch exporting script

The optimized script is presented in Snippet 6;

Matlab – dI/dV profiles extractor

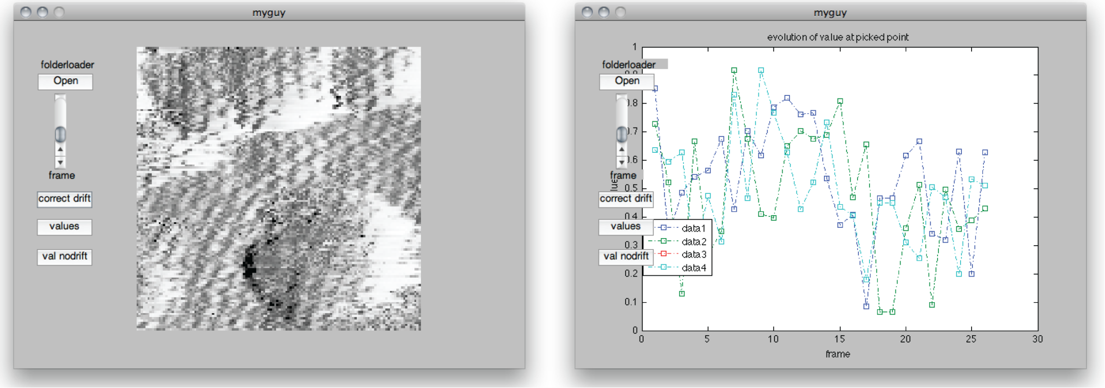

Figure 12: Graphical user interface of the profile extractor

In order to acquire the dI/dV curves out of multiple image files on the same point, a Graphical User Interface has been coded using matlab. The objective is to select points on one image and extract the values of the selected pixel from all the acquired frames. The software also has two other functions, a drift correction and a drift-corrected profile extraction. Such functions are still in development. The implementation simply consist in loading all the frames (Snippet 7),

```
[filename,path]= uigetfile('*.png','Choose stack:');%load the stack,
if it exists
if(filename)%[stk,stacklength]=imread([path filename]);
cd(path);
filelist=dir('*.png');
filenames = {filelist.name}';
filenum=length(filenames)
stack=cell(1,filenum);
for(j=1:filenum)
        I=imread(filenames{j});
        filenames{j};
        I=im2double(I);
        stack{j}=I;
    end
```

Snippet 7: image loading;

then allowing the user to select one or more point

```
imshow(stk{handles.i});
[y,x,p]= impixel;
```

which subsequently are extracted from all images into a list, and plotted in the main window.

```
for j = 1:length(x) kymo = [];
      for i = 1:length(stk) im = im2double(stk{i});
      c = im(x(j),y(j));
      kymo = [kymo c]; % concatenation
      end kymo = kymo'; spots=[spots kymo];
end
plot(spots, '-.s'); title('evolution of value at picked point');
xlabel('frame'); ylabel('Value');
legend(x', 'Location','NorthEastOutside');
```

Snippet 8

References

1. (a) Halgren, T. A., Merck molecular force field .1. Basis, form, scope, parameterization, and performance of MMFF94. *Journal of Computational Chemistry* **1996,** *17* (5-6), 490-519; (b) Halgren, T. A., Merck molecular force field .2. MMFF94 van der Waals and electrostatic parameters for intermolecular interactions. *Journal of Computational Chemistry* **1996,** *17* (5-6), 520-552; (c) Halgren, T. A., Merck molecular force field .3. Molecular geometries and vibrational frequencies for MMFF94. *Journal of Computational Chemistry* **1996,** *17* (5-6), 553-586; (d) Halgren, T. A., Merck molecular force field .5. Extension of MMFF94 using experimental data, additional computational data, and empirical rules. *Journal of Computational Chemistry* **1996,** *17* (5-6), 616-641; (e) Halgren, T. A.; Nachbar, R. B., Merck molecular force field .4. Conformational energies and geometries for MMFF94. *Journal of Computational Chemistry* **1996,** *17* (5-6), 587-615.

2. The details are reported in the Charmm MMFF documentation page, an online version is reperible at http://www.charmm.org/documentation/c36b1/mmff.html

3. the details of the Tripos Mol2 formats can be downloaded from http://tripos.com/index.php?family=modules,SimplePage,Mol2_File_Format2009
4. details on the file format can be found at http://www.cambridgesoft.com/services/documentation/sdk/chemdraw/cdx/IntroCDX.htm
5. O'Boyle, N.; Banck, M.; James, C.; Morley, C.; Vandermeersch, T.; Hutchison, G., Open Babel: An open chemical toolbox. *Journal of Cheminformatics* **2011,** *3* (1), 33.
6. More details about Python language can be found here: http://docs.python.org/reference/
7. Metropolis, N.; Rosenbluth, A. W.; Rosenbluth, M. N.; Teller, A. H.; Teller, E., Equation of State Calculations by Fast Computing Machines. *The Journal of Chemical Physics* **1953,** *21* (6), 1087-1092.
8. Necas, D.; Klapetek, P., Gwyddion: an open-source software for SPM data analysis. *Cent Eur J Phys* **2012,** *10* (1), 181-188.

Annex 1: Rotatable arms in simple tripods: conformers, dipole and self-assembly – Supporting information

- STM
- General procedure
- More Images
- Image Processing
- Moiré determination
- Generation of conformer library
- Equilibrium Distribution
- Frequency of rotation
- MD
- Packing connectivity
- Dipolar moment
- Adsorption Energy
- Rotational barrier on graphene
- Relative stability of the assemblies
- DFT
- Charges and electrostatic potentials
- Dipolar moments
- Rotational barriers
- Simulated IR
- IR
- Experimental solutions
- Powder

STM:

The STM study of the self-assembly in two dimensions was performed using a Veeco scanning tunneling microscope (multimode Nanoscope III, Veeco) at the interface between highly oriented pyrolitic graphite (HOPG) and a supernatant solution. Solutions of investigated molecules were applied to the basal plane of the surface. For STM measurements the substrates were glued on a magnetic disk and an electric contact is made with silver paint (Aldrich Chemicals). The STM tips were mechanically cut from a Pt/Ir wire (90/10, diameter 0.25 mm, commercially available from Goodfellow.uk). The raw STM data were processed through the application of background flattening (2nd degree least square polynomial fitting on both X and Y directions) and the drift was corrected using the underlying graphite lattice as a reference. Further filtering is discussed in the next section. The lattice was visualized by lowering the bias voltage to 20 mV and raising the current to 65 pA.

The use of other solvents such as nonanoic acid, 1,2,4-trichlorobenzene or tetradecane did not lead to ordered 2D assemblies.

Moreover, discerning if the assembly is moderately aperiodic or not was not possible due to the remarkable difference of resolution of the STM at the solid liquid interface compared to UHV-STM.

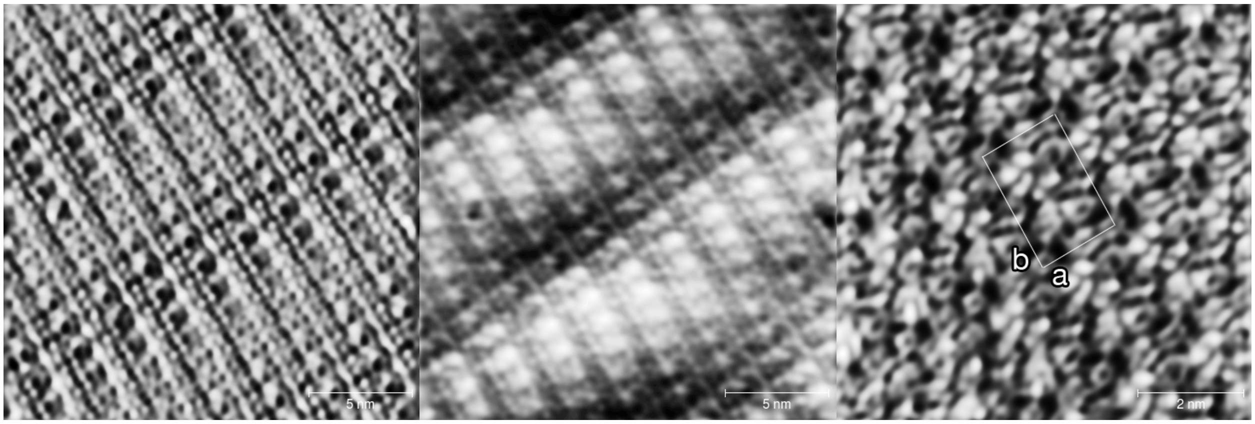

Figure S 1: Current and height STM images of M. Tunneling parameters: It=25pA, Ut=200mV. Unit cell parameters: 1.3 ± 0.2 nm, 3.1 ± 0.2 nm, 91°±2°; 4.0 ±0.7 nm2 [CWT gaussian 6px filter.]

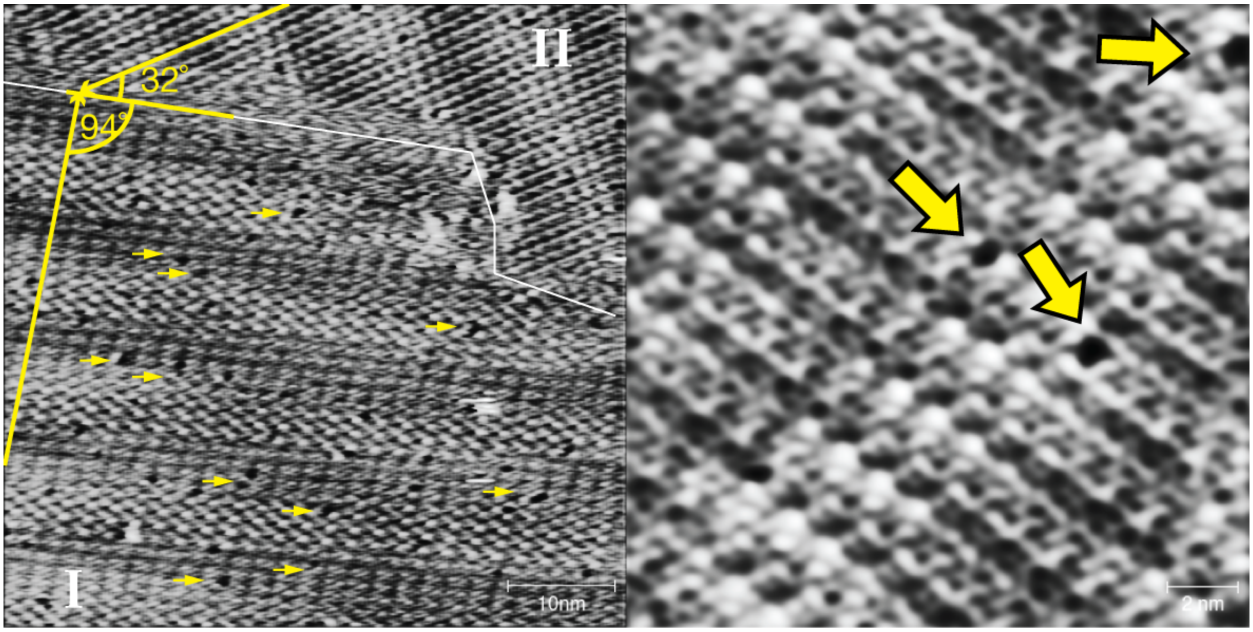

Figure S 2**:** height STM images of **M**. a) large scale showing the defect observed: yellow arrows are a guide to the eye to highlight the vacancies in the pattern. The white line indicate the grain boundary, whereas the yellow lines indicate the lamella axis (and the respective angles with the boundary); b)close up showing the vacations with increased detail. Tunneling parameters: I_t=25pA, U_t=200mV. [CWT gaussian 6px filter.]

Image processing:

In order to denoise the images and to enhance the features a Gaussian Continuous Wavelet Transform[1] with a width of 6px has been applied using the predefined Gwyddion[2] (2.28) 2D Integral transform routines. The result is shown in Figure S 3 together with the raw datas.

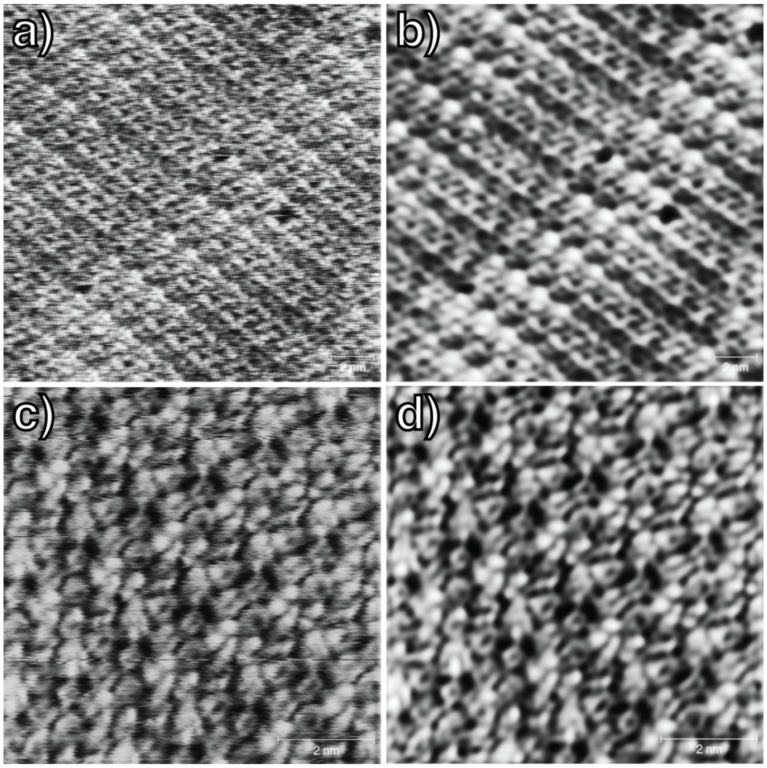

Figure S 3**:** raw height images, before and after the application of CWT gaussian 6px filter

Moiré determination

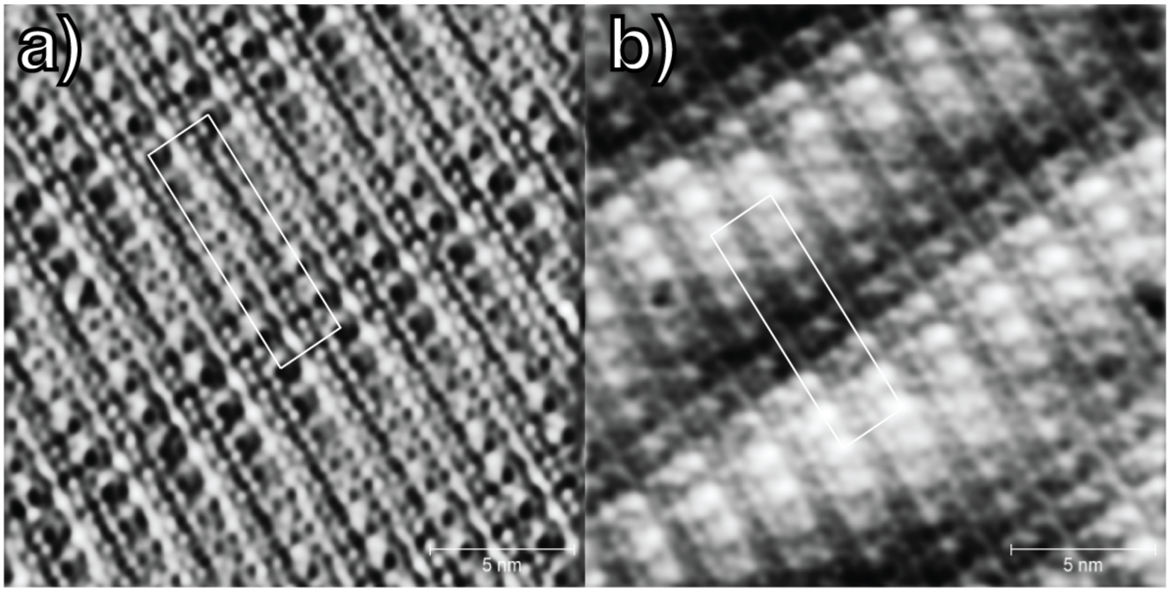

Figure S 4: Current and Height images with superposed the supercell used for Moiré evaluation.

The motif exhibits a Moiré pattern, therefore epitaxial registration according to Hooks et al.[3] has been computed. The measured azimuthal rotation of the overlayer is 88 ± 2°, as measured from the principal lattice vectors, and the registration between the two lattices occurs at a length scale of approximately 4.5 nm along b and ca. 2nm along the a axis; the calculated matrix elements (p=3.0, q=20.0, r=-8.95, s=2.10) are within the experimental agreement with a point-on-line Coincidence-IA.

Generation of conformers library

To calculate the entropic contribution and the degeneracy of the system, under the assumption of a weak energy barrier and of 4 different rotation states per ring (up, down, right, left – referred to the position of the nitrogen respect to the core), the library of conformers in Figure S 5 has been generated

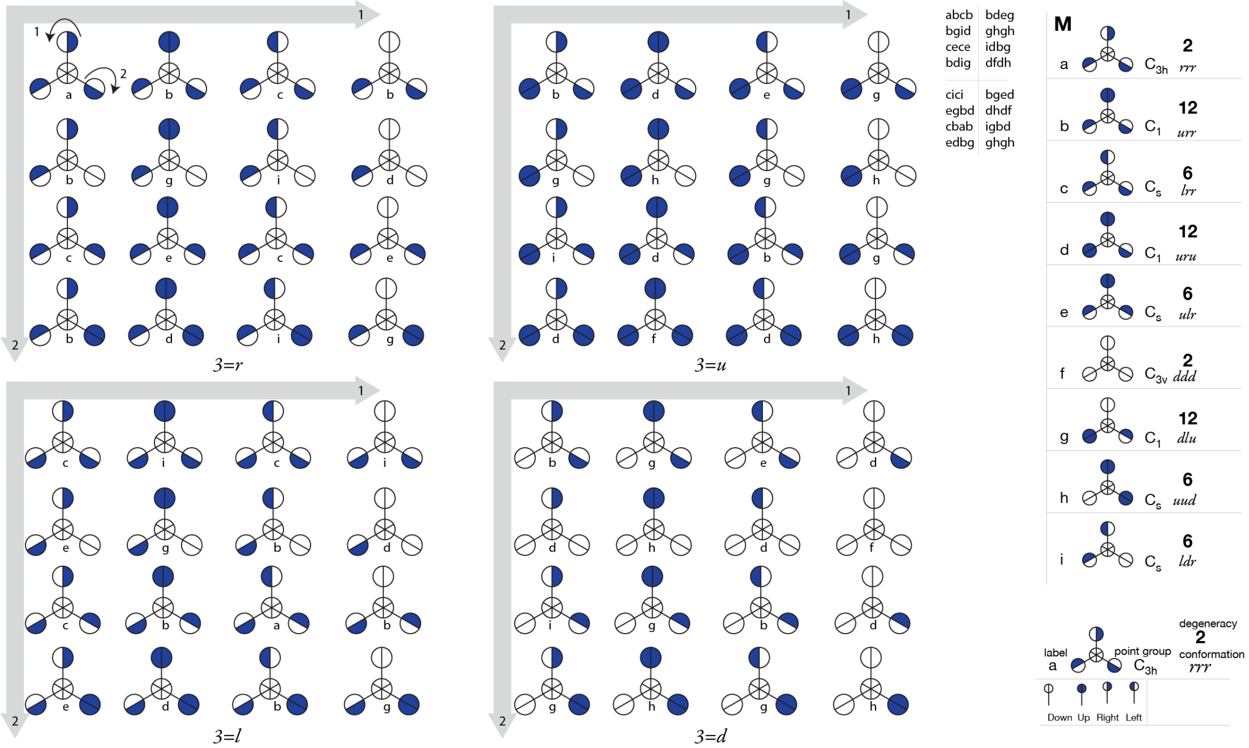

Figure S 5**:** all the conformers generated after independent 90° rotation of a pyridine ring, on the right are summarized the irreducible representations the respective symmetry and their degeneracy.

Distribution in vacuum and on surface:

To calculate the probability of obtaining the conformer C3h on the graphite surface the following consideration has been done: assuming that on the surface the only two possible states are c3h and cs, the final probability will be the sum of the products of the probability of being in the ith conformer state (P_i)times the probability of this latter to end in c3h once adsorbed (P_i^{c3h})

$$P(C3h)_{hopg} = \sum_{i=1}^{n} P_i \cdot P_i^{c3h}$$

the evaluation of P_i^{c3h} is rapidly done assuming that I) the possibility for a ring perpendicular to the core to assume the right or left conformation once adsorbed is 1:1, and II) the rings which are already in a r or l conformation don't change during the adsorption;

The calculated values are:

a	b	c	d	e	f	g	h	i
1.0	0.5	0.0	0.25	0.0	0.33	0.25	0.33	0.0

The probability P_i of starting from a certain conformation might be calculated using the Boltzmann distribution, and the relative energies calculated in vacuum per each conformer.

$$P_i = g_i \frac{e^{-\beta\epsilon_i}}{\sum_i g_i e^{-\beta\epsilon_i}}$$

the resulting values are:

	a	b	c	d	e	f	g	h	i
g_i	2	12	6	12	6	2	12	6	6
Ei	4.47	6.67	4.97	11.46	11.01	14.89	11.33	0.0	7.99

The probabilities of occupying the ith state (Pi) at temperature T are then:

	RT	80°C
a	0.0387	0.0444
b	0.0957	0.1260
c	0.0950	0.1124
d	0.0139	0.0247

7

e	0.0083	0.0144
f	0.0006	0.0013
g	0.0146	0.0258
h	0.7052	0.6109
i	0.0281	0.0402

those values are also plotted in Figure S 6

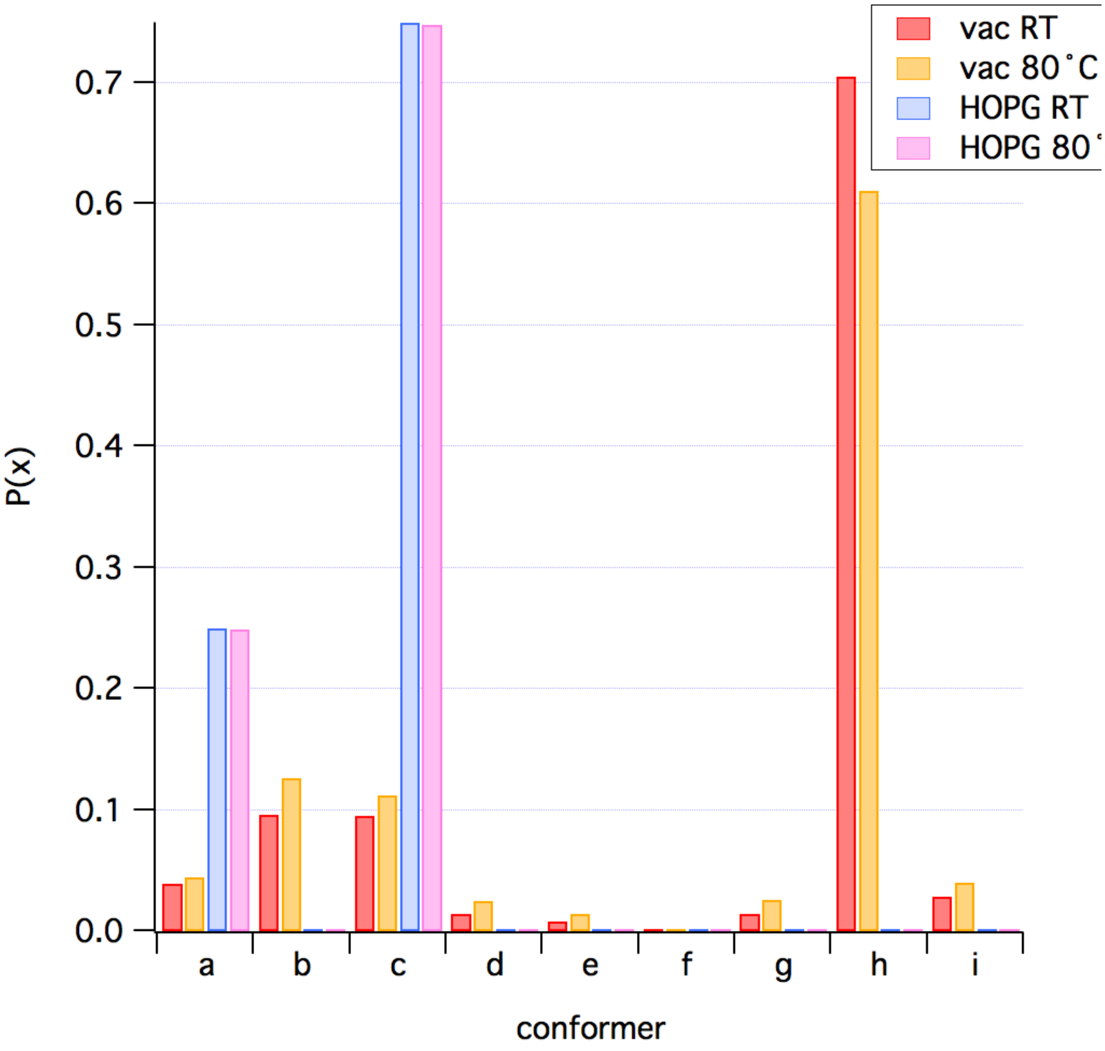

Figure S 6**:** Probability of each configuration in vacuum and on the graphene slab, computed using bolzmann distribution.

Substituting those values in the previous formula gave the probability $P(c3h)_{hopg}$ = 0.3266 and 0.3221 respectively at room temperature and at 80˚C.

The values of the distribution calculated from the adsorption energies on graphite, are rather different:

	RT	80°C
a	0.2498	0.2493
b	0.0002	0.0009
c	0.7494	0.7478
d	0.0000	0.0000
e	0.0003	0.0010
f	0.0000	0.0000
g	0.0000	0.0000
h	0.0000	0.0000
i	0.0003	0.0010

Frequency of rotation in solution and on HOPG surface:

In the case of one single molecule either in vacuum or physisorbed on the graphite surface, it is possible to have an estimate of the frequency of rotation using the eyring[4] equation:

$$k = \frac{K_B T}{h} e^{-\left(\frac{\Delta G}{RT}\right)}$$

We evaluated the results according to J. M. Goodman[5] For the calculated energy barriers we have:

	Calculated energy barrier kJ/mol	Frequency at RT	Frequency at 80°C
vacuum	1.8548	1.36674441E12	2.38826313E12
HOPG	178	0.39024962E-18	2.05720407E-4

MD

To monitor different properties of the molecule M, we used CHARMM[6] and parametrized all molecules with MMFF94,[7] which has already been proven successfully capable of providing insight on self assembly.[8]

Packing connectivity

to analyze possible geometries of the assembly 1ns of simulation has been run with 36 randomly disposed molecules in a slab of graphene under periodic boundary conditions. The boundaries are highlighted with a blue frame in Figure S 7. The medium-low coverage has been selected in order to analyze the possible different interaction between molecules. The molecules were first heated to room temperature using a

```
DYNAMICS LEAP START -
      TIMESTP 0.002 NSTEP 10000-
      FIRSTT 100 FINALT 300 TEMINC 20 IHTFRQ 1000 -
      IASORS 1 IASVEL 1 -
      ICHECW 0 TWINDL -10.0 TWINDH 10.0 -
      INBFRQ -2 IHBFRQ 0 IEQFRQ 0 -
      IUNREA -1 IUNWRI 15 IUNCRD 20 KUNIT -1 -
      ISVFRQ 10000 NSAVC 100 NPRINT 1000 -
      IMGFRQ -1 ECHECK 1000
```

And then passed to a function processing the langevin dynamics, which allows the molecules to physisorb on the surface, and diffuse according to the friction factor (fbeta).

```
SCALAR FBETA SET 0.05
DYNAMICS LEAP LANGEVIN RESTART TIMESTP 0.002 NSTEP @ESTP -
         ILBFRQ @ESTP RBUF 0.0 TBATH @TACT -
      IPRFRQ @ESTP IHTFRQ 0 IEQFRQ 0 NTRFRQ 0 -
      IUNREA 16 IUNWRI 15 IUNCRD 20 KUNIT -1 -
      ISVFRQ 10000 NSAVC 1000 NPRINT 1000 -
```

```
        INBFRQ -1 IHBFRQ 0 IMGFRQ -1
```

to simplify the simulation the graphene slab was constrained:

```
CONS FIX SELE SEGID G* END
```

The periodic boundary conditions were included as:

```
CRYSTAL DEFINE ORTHO 98.38 119.14 100 90 90 90
CRYSTAL BUILD CUTOFF 90.0 NOPERATIONS 0
IMAGE BYRES XCEN 0.0 YCEN 0.0 ZCEN 0.0 SELE SEGID B* END
```

the non bonded interaction were evaluated using the following instruction:

```
NBONDS ELEC ATOM CDIE SHIFT VDW VATOM VSHIFT -
      CUTNB 16.0 CTONNB 14.0 CTOFNB 12.0
```

The resulting connections are in general weak hydrogen bonds, with a length spanning between 2.4 and 3.2 angstroms; the connectivity shows as hydrogen-bond acceptor the pyridine nitrogen, and as donors the unsubstituted positions of the core and the meta position of the pyridine rings.

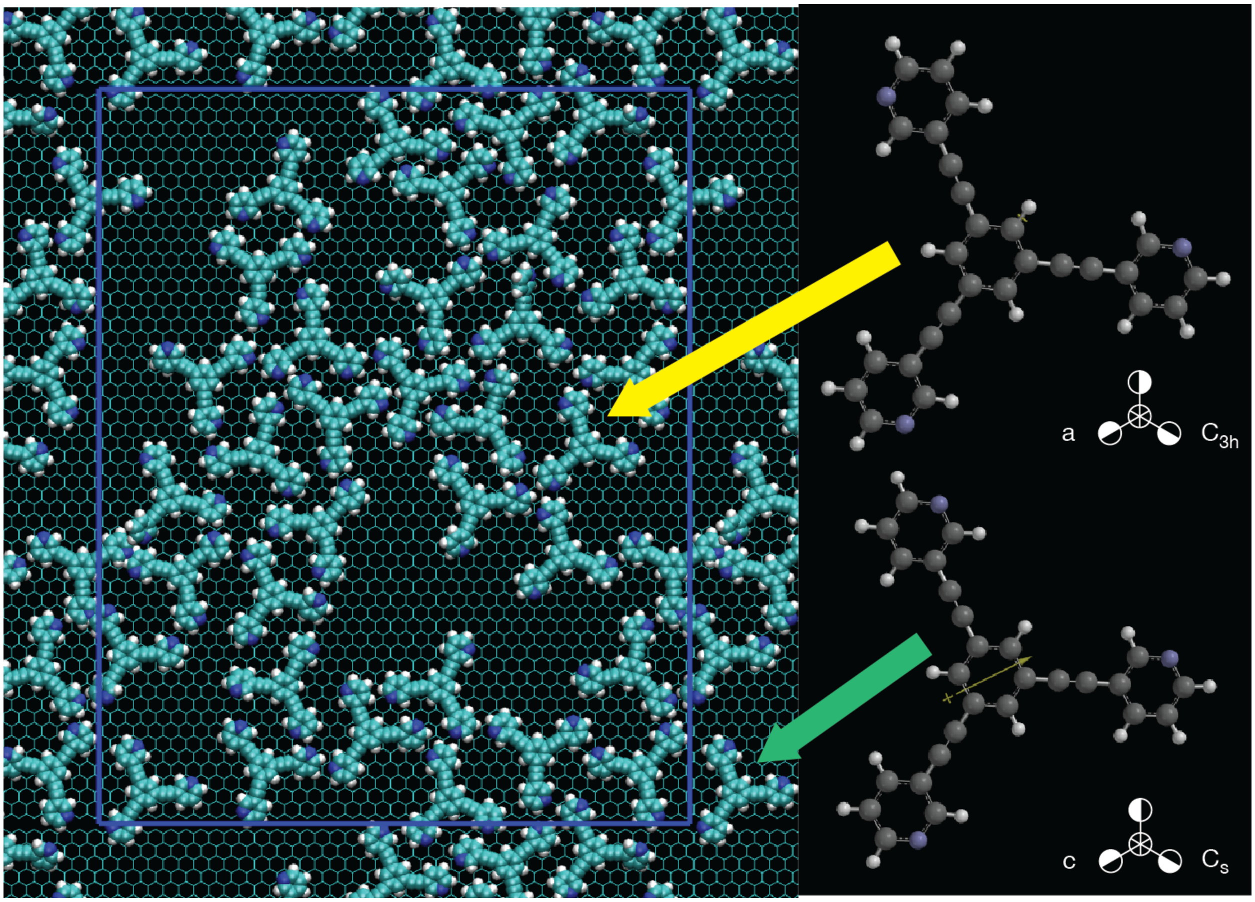

Figure S 7: simulation trajectory snapshot imaged with VMD[9] to highlight the tipical possible connectivity between molecules. Different hydrogen bond interactions, and two different conformers are present.

The simulation also evidence the presence of two different conformers on the substrate (appearance during the heating stage, thus before adsorption!), with different symmetry: The ratio between the two conformers is a/c ~ 0.25 with a P(a) 20%;

Dipolar moment evolution

An important difference in the symmetry of the molecule such as the rotation of a pyridine ring, has a remarkable effect on the dipolar moment, which then becomes and handy observable to monitoring the amount and the occurrence of ring rotation.

a single molecule has been investigated both in vacuum and once physisorbed on a graphene sheet, starting from 2 different flat conformations, one with symmetry Cs (M-Cs) and the other C3h (M-C3h). their dipolar moment has been monitored for 10 ns. – during the first ps the temperature has been rised from 100K to 300 K, and kept constant for the rest of the simulation.

```
SHAKE BONH PARAMETERS

DYNAMICS LEAP START -

        TIMESTP 0.001 NSTEP 10000000 -

        FIRSTT 100 FINALT 300 TEMINC 20 IHTFRQ 1000 -

        IASORS 1 IASVEL 1 -

        ICHECW 0 TWINDL -10.0 TWINDH 10.0 -

        INBFRQ -1 IHBFRQ 0 IEQFRQ 0 -

        IUNREA -1 IUNWRI 15 IUNCRD 20 KUNIT -1 -

        ISVFRQ @HSTP NSAVC 100 NPRINT 10000 -

        IMGFRQ -1 ECHECK 1000
```

The same measurement has been repeated with DFT calculated charges, in vac and on hopg, manually setting the charge values using the command:

```
SCALAR CHARGE SET value SELECT ATOM segment residue atom id END
```

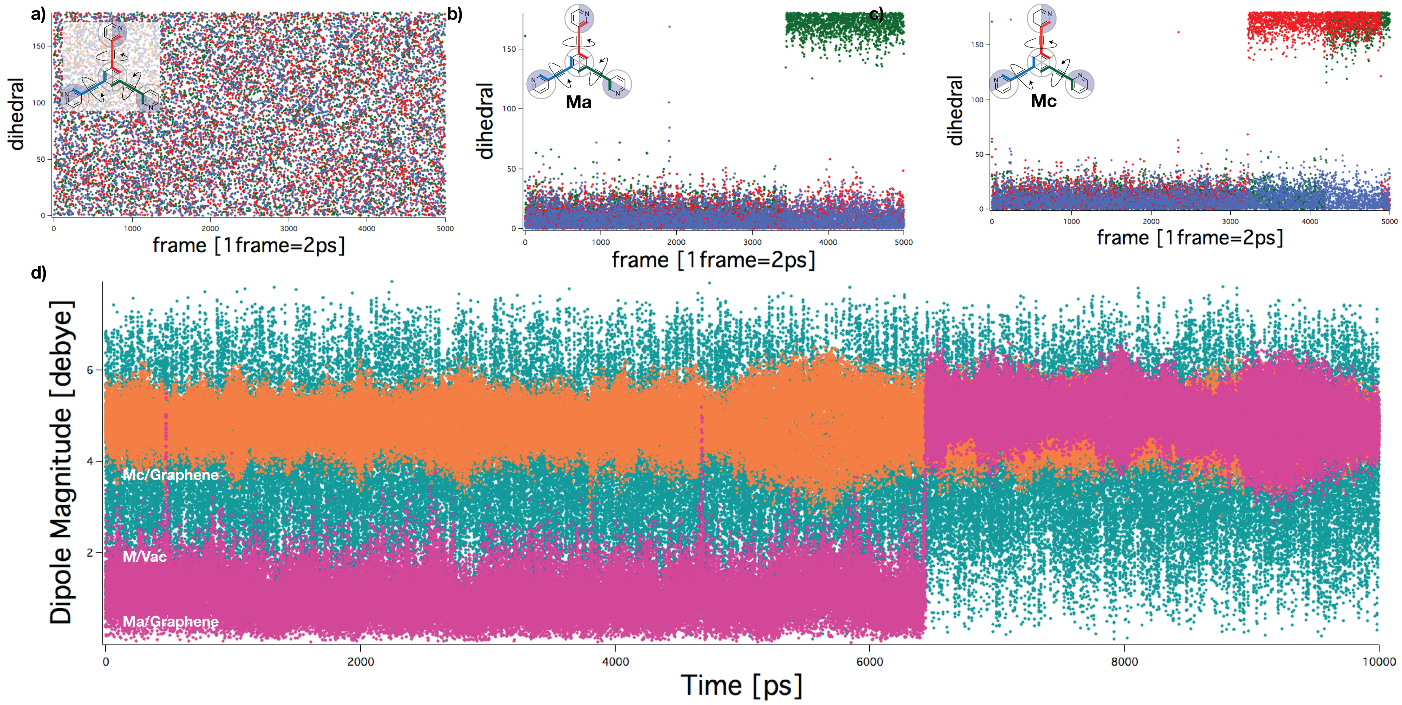

Figure S 8**:** typical plot of the evolution of the dihedrals a-c) and of the dipole moment d) on a graphene slab of the two conformers. The dihedral correspond to the highlighted bonds in the insets. In d) the net dipole moment of Mc (orange) and Ma (purple) is compared with the values of Ma in vacuum (cyan) (NBO charges);

In Figure S 8 is summarized the time evolution of all the dihedrals and the dipolar moment for the configurations. It can be noticed that the rotation is almost free in vacuum, and that once adsorbed on the surface the **Ma** conformer is stable for ca 6 ns – after, a rotation of a ring occurs, which statistically hinders the system to going back to the C3h conformation – the simulation also shows that the cs conformer **Mc** on the hopg surface possess a net dipole moment which is uniform along the simulated time frame.

Adsorption energy

For each of the conformers, the adsorption energy has been computed using CHARMM and MMFF94. The dihedral angles of each molecule were constrained, and the structure minimized on the graphene surface. After the minimization, the structure was moved along the z-axis up to a distance of 20nm, at 2 angstrom steps.

```
SET ZINDEX 0
```

```
SET MAXSTEPS 100
```

```
SET DELTAZ 0.20
LABEL LOOPBEGIN
            COOR TRANS ZDIR @DELTAZ SELECT SEGID B* END
            CONS HARM SELE SEGID B* END
            INCR ZINDEX
            ENER
IF ZINDEX .LT. @MAXSTEPS GOTO LOOPBEGIN
```

The energy of adsorption of each configuration was then calculated as the difference between the initial minimum state and the final one. A typical profile si reported in Figure S 9

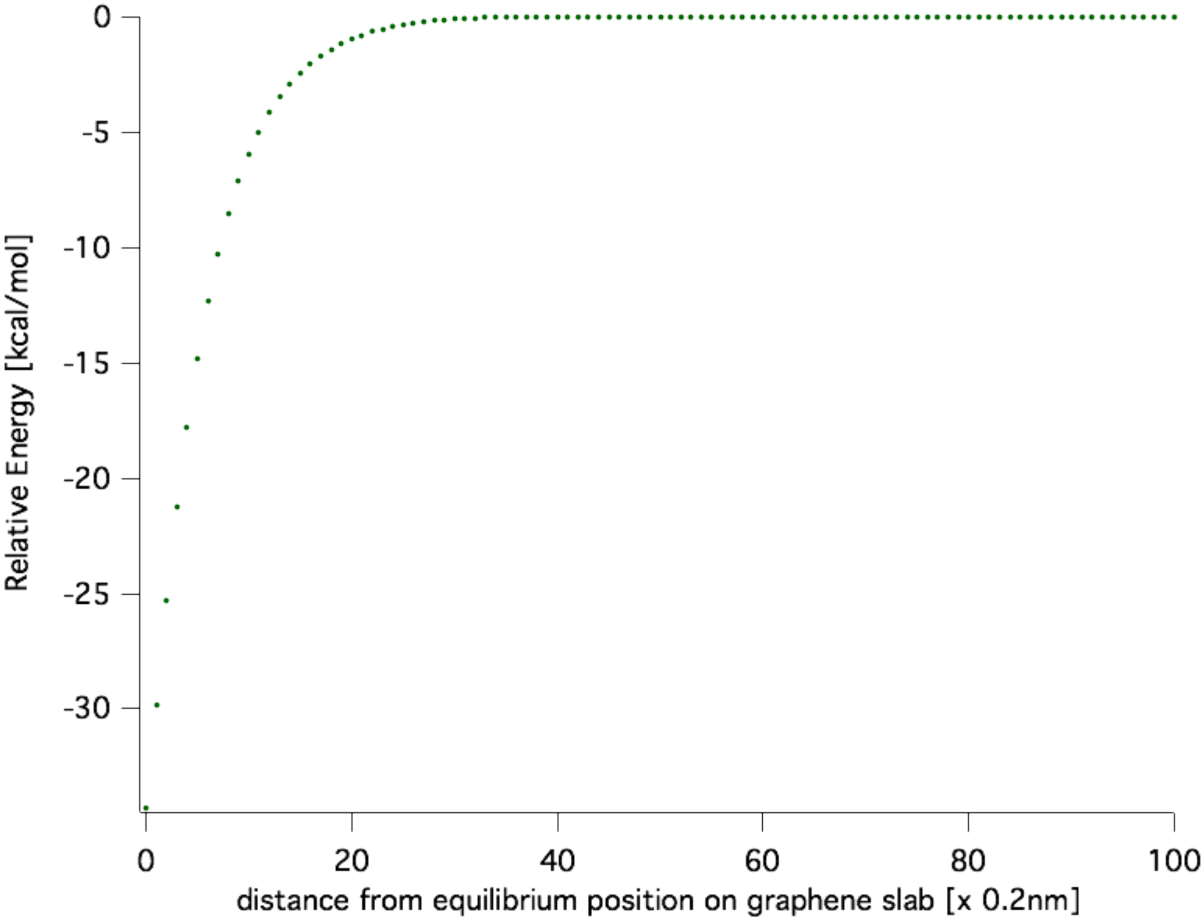

Figure S 9**:** tipical profile observed during the calculation (Ma conformer).

Each member of the library has ben computed two times, approaching from both z directions.

The results are summarized in Figure S 10, together with the DFT (b3lyp-631g) calculated dipolar moment;

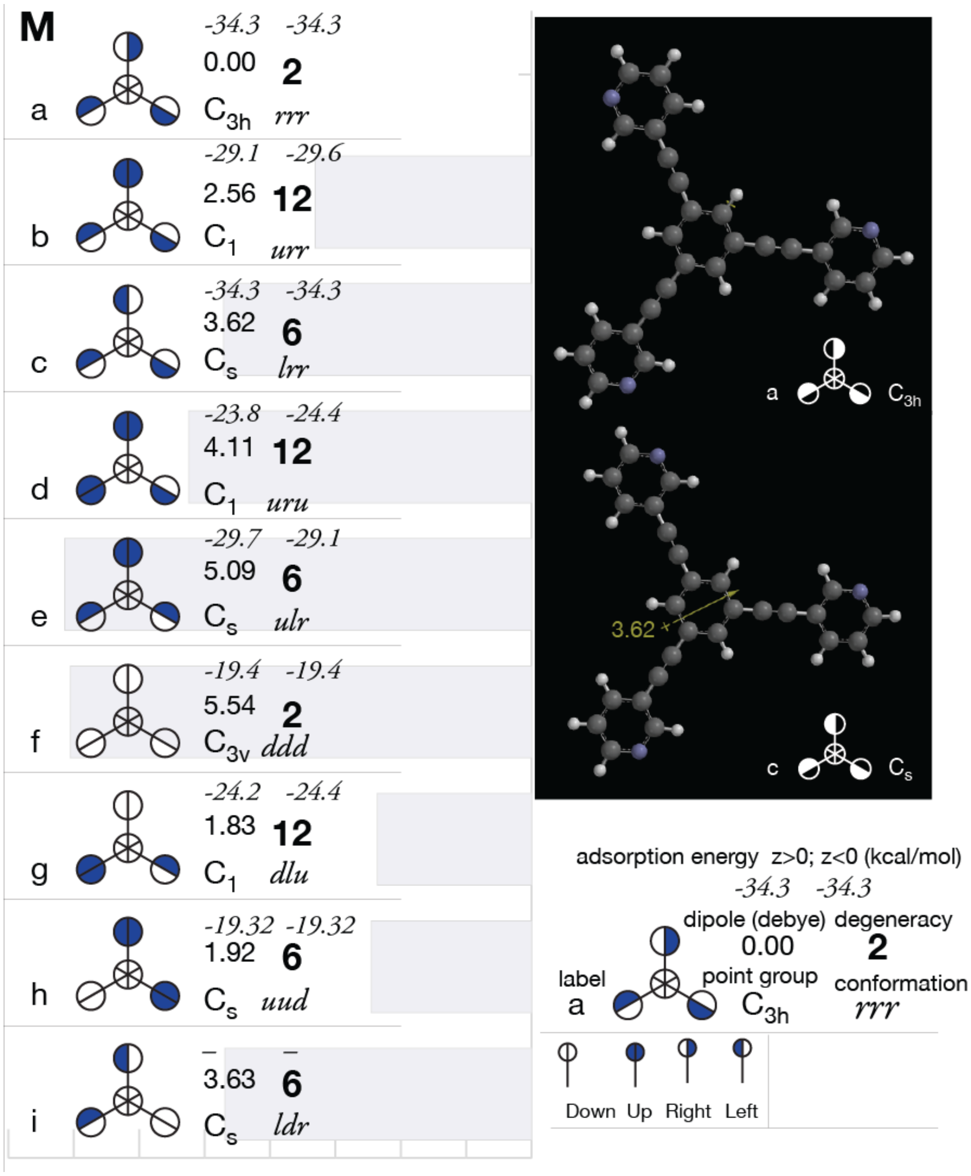

Figure S 10: Adsorption energy (MMFF), dipole (DFT), degeneration and point group per each irreducible representation.

Dipole moment measured with MMFF

0.000379	a
3.49474	b
4.94243	c

5.47493	d
4.89732	e
7.3458	f
2.59295	g
2.45677	h
4.90707	i

Rotational barrier on HOPG:

The same consideration were done using molecular dynamics (charmm MMFF 94) with the rotation of a single ring on a molecule in vacuum and physisorbed on the surface. The same calculation has been repeated for different values of the charges, in order to minimize the eventual error of MMFF – however the differences on the resulting energy barriers on the physisorbed object are minimal. The results in vacuum converge to the one of the DFT for ..

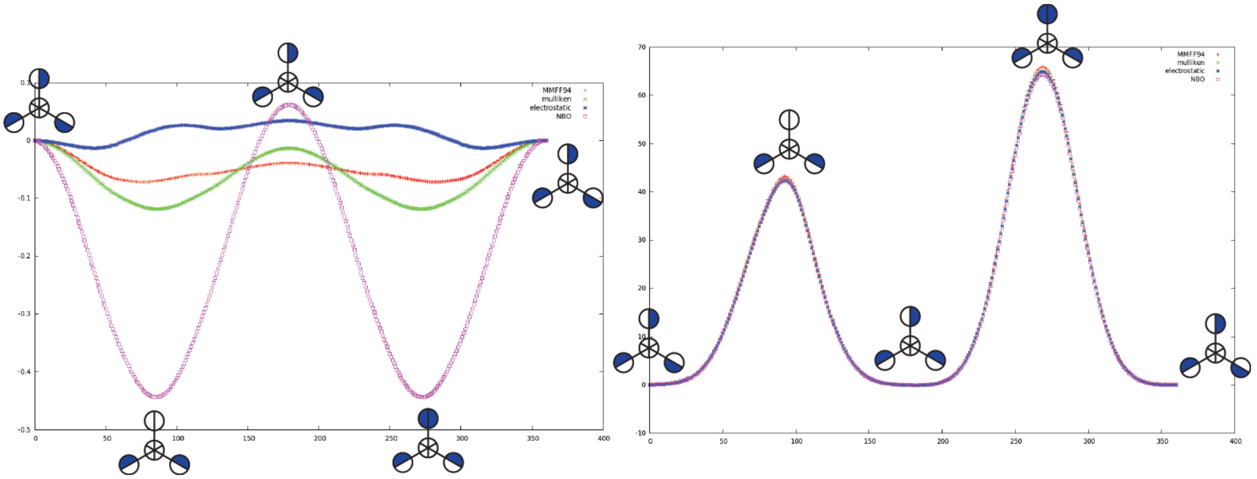

Figure S 11: rotational barrier evaluated with different ad-hoc charges

loop used during the energy evaluation

```
set stepindex 0
```

```
set maxsteps 360

set deltaz 1.0

coor axis select BYNU 13 end select BYNU 26 end

label loopone

                    coor rota axis phi @deltaz select .byres. resid 3 end

                    cons harm sele segid b* end

                    incr stepindex

                    ener

if stepindex .lt. @maxsteps goto loopone
```

Relative stability of the assemblies:

The different arrangements of the two conformers were tested by preforming a small assembly with 2 different packing motifs: in Figure S 12 are reported the four results, together with the energy of the assembly, relative to the Ma parallel motif.

The structures were manually assembled and then minimized with a steepest descent (10000steps) before, and 20000 steps after being placed on top of a graphene slab. Subsequently each of the molecules of the periphery was displaced of 20nm away from his original position, along the correspondent graphene axis, and the structure minimized. The energy reported in Figure S 12 for each structure was then evaluated as the energy of the final – the initial conformation. In Figure S 14 are reported the relative energies after each step.

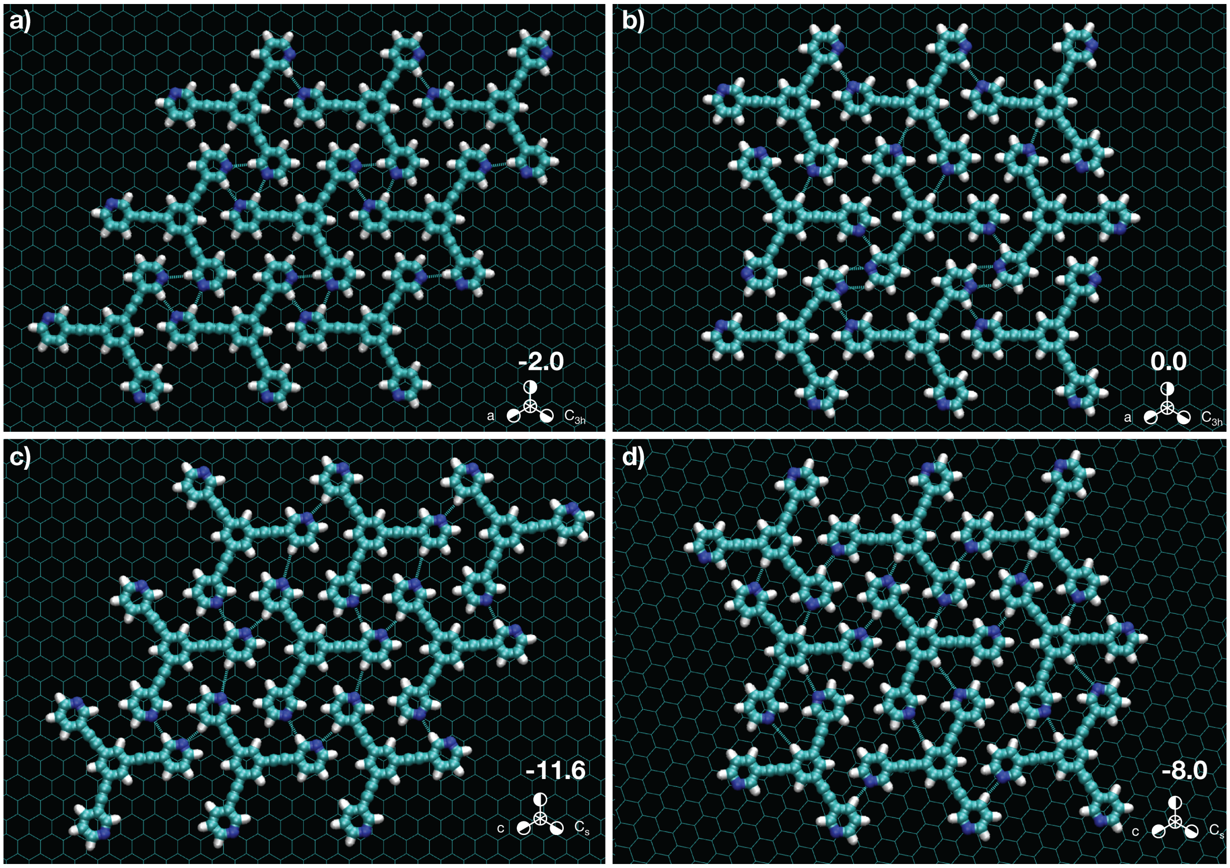

Figure S 12**:** comparison of the different architectures, a,b) **Ma** parallel and antiparallel respectively c,d) **Mc** parallel and antiparallel arrangements. In the corner are reported the energies relative to **Ma** antiparallel.

Note how:

Ma is dramatically less stable than **Mc** – the hydrogen bond network that are formed are less stable due to the formation of strained hydrogen bonded rings. The Ma antiparallel (fig. S12b) requires the formation of $[R_2^2(6)]$ dimers. For **Ma** parallel is topologically impossible to form hydrogen bonds between the pyridine nitrogen and the core hydrogen. There are only $[R_3^3(9)]$ HB motifs (Figure S 12a).

The parallel conformations, are ca 2 kcal/mol more stable than the respective antiparallel arrangements.

Mc parallel result in being the thermodynamic minimum, but due to the finite size of the cluster the presence of a net dipole moment is probably underestimated.

We therefore recognize **Mc** antiparallel as the most likely assembly on the HOPG surface. More in detail we can observe the presence of C(14) $[R_2^2(16)]$ $[R_2^2(16)]$ hydrogen bond motifs. In Figure S 13 b) the hydrogen bond pattern can be observed with more detail. In red is reported one of the $[R_2^2(16)]$ motifs, involving the N29---H8-C4 of two adjacent molecules. In green, it can be individuated another identical $[R_2^2(16)]$ motif based on two N41---H7-C3 hydrogen bonds, and the C(14) chain based on N19---H43-C49. It is interesting to observe that those two latter motifs insist on the same pyridine ring, inducing ca. 1Å of shrinking in the distance.

The **Mc** parallel conformation, has 3 different hydrogen bond motifs one dimeric, graph D, between N29---H22-C18 and one chain C(10) (can be seen following the cyan and purple lines) composed by the alternation of N41---H21-C17 and N49---H43-C19 :

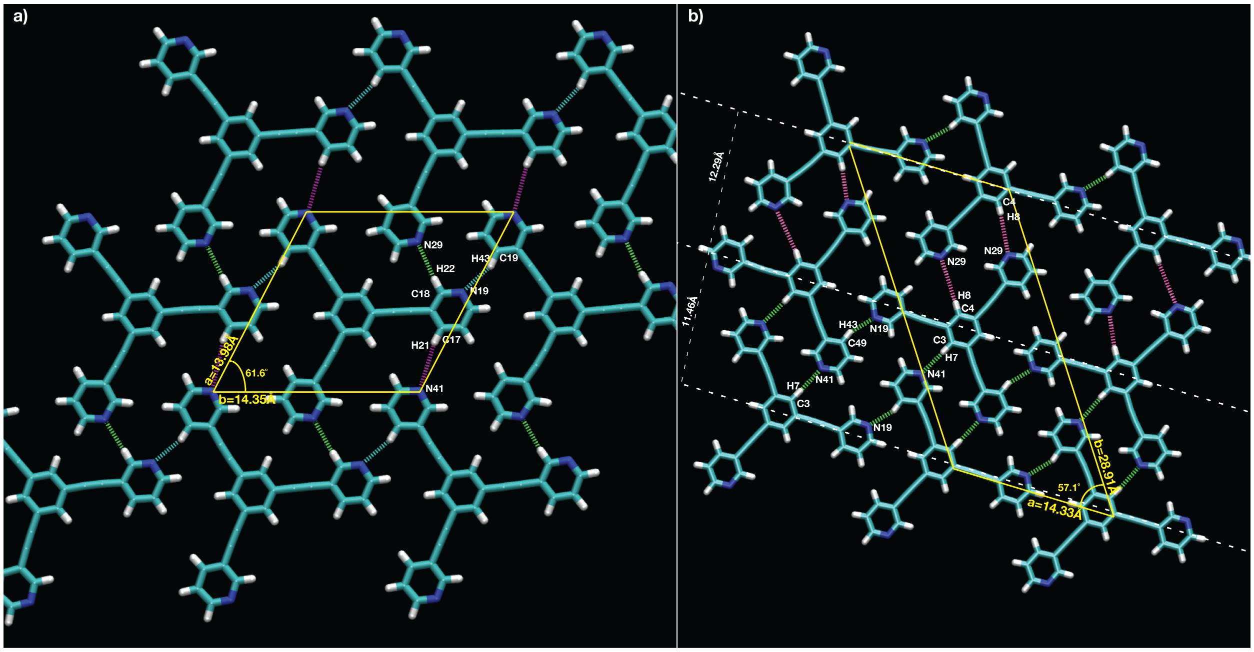

Figure S 13: hydrogen bond motif and calculated unit cell of Mc parallel a), and antiparallel b).

the main deviation appears to be the work necessary to build the polymorph, suggesting that after the first adsorption of a Mc conformer, the dipolar interactions select the antiparallel packing as a metastable minimum.

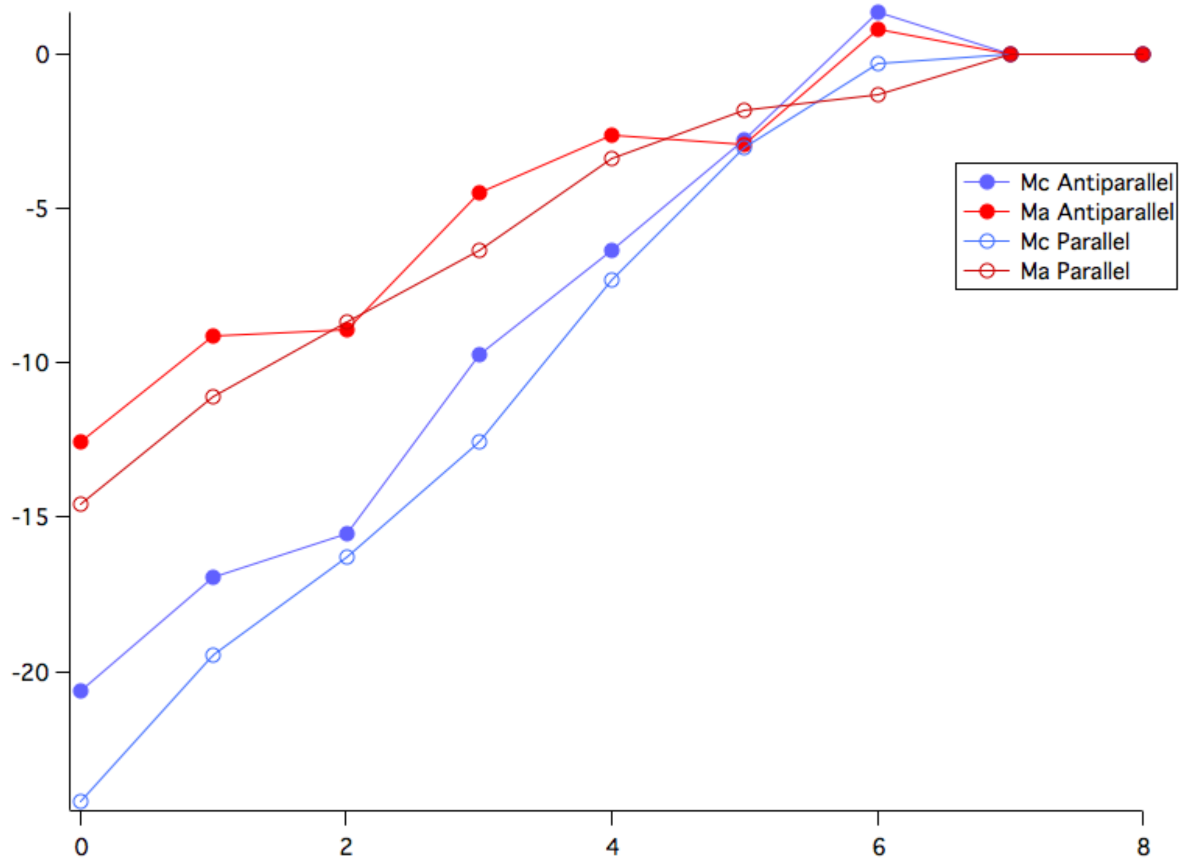

Figure S 14: energy of each conformation, after the “removal” of one of the peripheral molecules.

To evaluate the effect of the dipolar interaction we designed the following experiment: three antiparallel Mc assemblies of 9, 25, 49 molecules were physisorbed on a graphene slab. After minimization (20000steps of SD) the center molecule was translated along z for 10nm. The results are reported in Figure S 15.

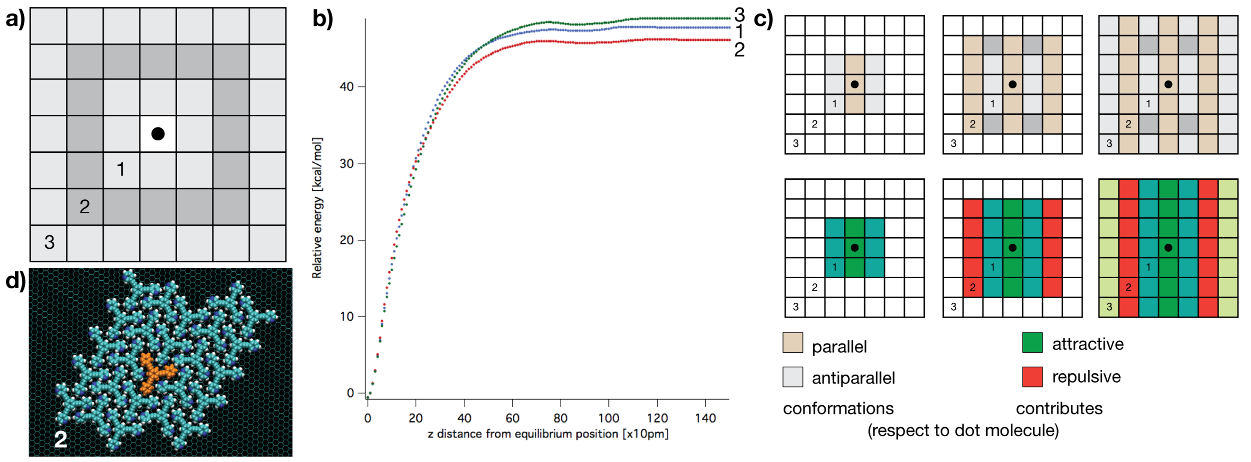

Figure S 15: The work necessary to remove a molecule from the packing is dependent on the number of neighbors layers. The center molecule, (dot in a and c, and orange in d)) has been lifted 10nm from the surface, in b) is reported the behavior for the first 1.5 nm, and in c) the contributions to the force acting on the molecule (red and greens) and the conformation (parallel or antiparallel).

Assuming the initial configuration as the zero energy state, is evident how it is more energetically expensive to remove a molecule from a small assembly than from larger structures. Which demonstrate how the structure is stabilized by long range interactions. The work to remove one molecule is clearly dependent on the other layers: if we consider the case 2, the presence of two parallel layers (therefore repulsive contribution) the work necessary to remove the molecule is smaller than the case with one layer. And so on for extended structures.

Critical domain size:

1 – Existence of a finite limit

the hamiltonian of our system has a contribution

$$H = H_{HB} + H_D = h(n) + d(n) = \sum_{i=1}^{n} E_{HB_i} + \sum_{i=1}^{n}\sum_{j=1}^{n} E_{D_{i,j}}$$

$$\forall i, j \in \mathbb{N} : i \neq j$$

which has been assumed separable in two contribution, $H_[10]$ accounting for all the hydrogen bonds and H_{D} as the sum of all dipolar interactions. It is evident that both are functions of n, and specifically the sum of the series; To demonstrate that the dipolar interaction prevails for large assemblies, means showing that the limit of the ratio between the two functions goes to zero. i.e.

$$\lim_{n\to\infty} \frac{h(n)}{d(n)} = \lim_{n\to\infty} \frac{E_{HB}}{E_D} = 0$$

which is evident as the order of the two functions is

$$O(h) = n$$

$$O(d) = (n^2 - n)/2$$

to calculate the critical n, it must demonstrated that the repulsive component of two adjacent rows will prevail over the parallel attractive interaction along the same row. In a similar fashion:

$$\lim_{n\to\infty} \frac{h(n) + d_{att}(n)}{d_{rep}(n)} = 0$$

$$\lim_{n\to\infty} \frac{d_{att}(n)}{d_{rep}(n)} = 0$$

if we assume the dipolar moment allineated in a square lattice, along the y axis (columns), we have that along each row

$d_{rep} = \sum_{i,j} Dij$ where Di, j belongs to the column $a, a+1, a+2, ...ax+1 :$ $a \in \mathbb{N}$

whereas the attractive interaction only operates along the columns. Therefore, in case of lateral growth (i.e. along x):

$$O(d_{att_x}) = C$$

and

$$O(d_{rep_x}) = n^2$$

in case of pure vertical growth, i.e. only along y

$$O(d_{att_y}) = n$$

and the repulsion will be along all the elements except the one of the ith column, therefore in a NxM (rows x columns) array

$$O(d_{rep_y}) = (n)(n-1) - n = n^2 - 2n$$

which is dominant we can generalize that for any mechanism of growth with more than 2 columns the repulsion will have "more" terms. therefore demonstrating the assumption that $\lim_{n\to\infty} \frac{d_{att}(n)}{d_{rep}(n)} = 0$ it follows that

$$\lim_{n\to\infty} \frac{d_{att}(n) + h(n)}{d_{rep}(n)} = 0$$

observing that the order of the repulsive term is at least $n^2 - 2n$, which proofs the limit is zero per the de L'hopital rule.

2 – critical size evaluation

DFT

All the calculations were performed with wavefunction Spartan '10[11] _ENREF_2using different methods:

calculations were done using Semiempirical PM3[12], restricted Hartree-Fock and DFT B3LYP[13]; further details are reported in the following sections.

Charges and electrostatic potentials

The general structure of Hydrogen bond is –A---H-D- where a hydrogen bond donor (D) forms a polar σ bond with hydrogen, and the hydrogen carries a partial positive charge. The group D-H has an attractive interaction with at least one acceptor atom (or group) A, thanks to the accumulation of the electron density on the acceptor.[14] Therefore hydrogen bonds, have a very strong electrostatic component; hence one of the most handful techniques to preview the pattern of connections between molecules is to observe the electrostatic potential and the charge distribution of all the atoms of the molecule, and then pair the best acceptor with the best donor. The simulation shows that:

The more positively charged hydrogen are pointed by the arrows in Figure S 16 – the carbons bearing those hydrogen will act as the HB donor; and the most negative atoms are the three pyridine nitrogens, which will consequently act as HB acceptors. The two possible position for binding will have consequences on the polymorphism of the system.

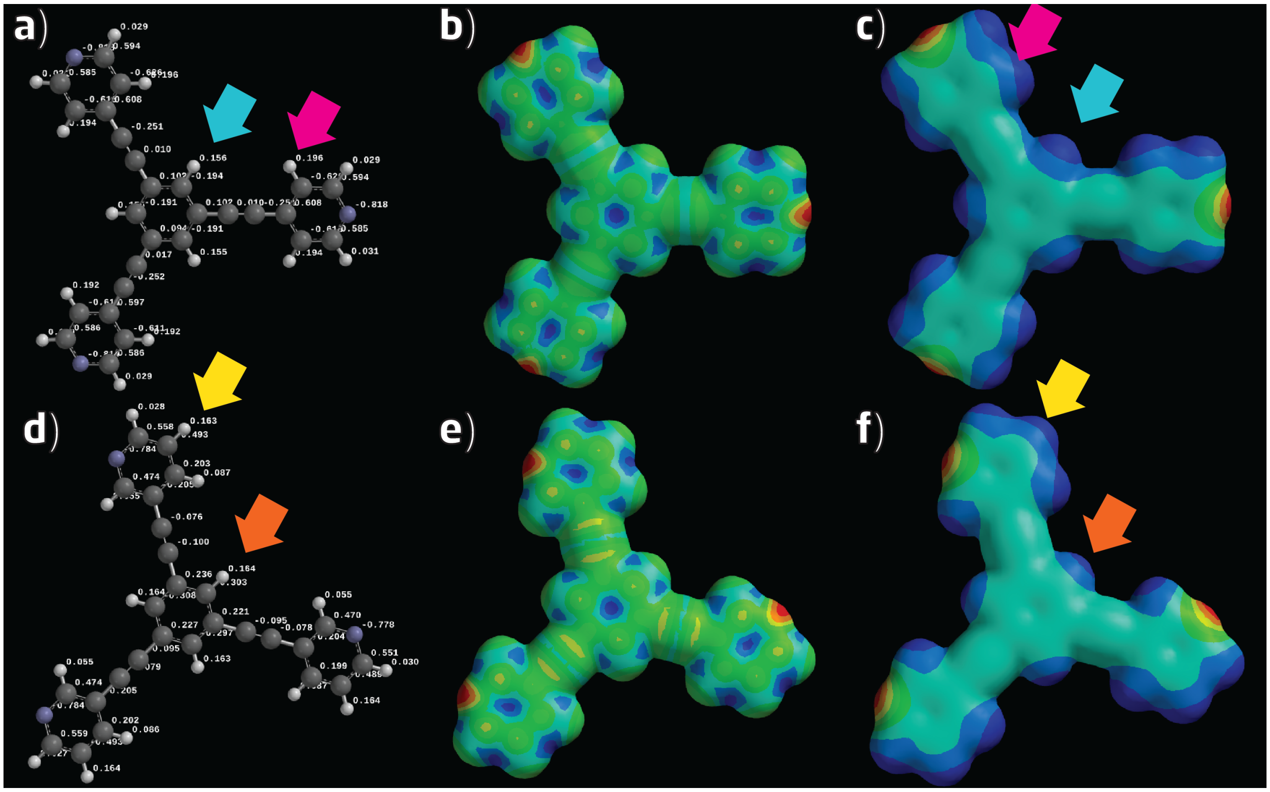

Figure S 16: DFT b3lyp method and a 631g* basis set calculated charge distribution (Mulliken showed) charge density and electrostatic map of **P** (a-c) and **M** (d-f).

Energies and Dipole moments

The relative energies in vacuum and the dipole moment of all the conformers of the library have been computed with DFT b3lyp method and a 631g** basis set - The values shows that the most stable conformer is the DUU conformation, i.e. all the pyridine rings are rotated 90° with respect to the phenyl core, and two of the nitrogens are "pointing up", and the other one is pointing down. (this state is also 6 degenerate); - the next two states are the c3h (RRR or LLL) and the cs ([LLR or RRL] and all the permutations) – the difference is

Method: RB3LYP

Basis set: 6-31G**

Number of shells: 165

Number of basis functions: 525

Multiplicity: 1

Dipole (debye)	conformation	label	Rel en :	Point group

			kJ/mol - kCal/mol	
2.56	RRU	b	6.67 – 1.59	C1
1.83	LUD	g	11.33 – 2.71	C1
4.11	LUU	d	11.46 – 2.74	C1
0.00	RRR	a	4.47 – 1.07	c3h
5.54	UUU	f	14.89 – 3.56	c3v
3.64	RLU	i	7.99 – 1.91	cs
3.62	LLR	c	4.97 – 1.19	cs
5.09	RDL	e	11.01 – 2.63	cs
1.92	DUU	h	0.0 – 0.0	cs

Rotational barriers

To estimate the value of the rotational barrier in vacuum, we used the restricted Becke three-parameter hybrid exchange functional combined with the Lee–Yang–Parr correlation functional (B3LYP) with 6-31G+(d,p) basis set,[13a, 13b] and performed a separate calculation on a library o conformers, generated by rotating the dihedral highlighted in red in Figure S 17 at 10° steps; All the other angles and dihedrals in the molecule were constrained.

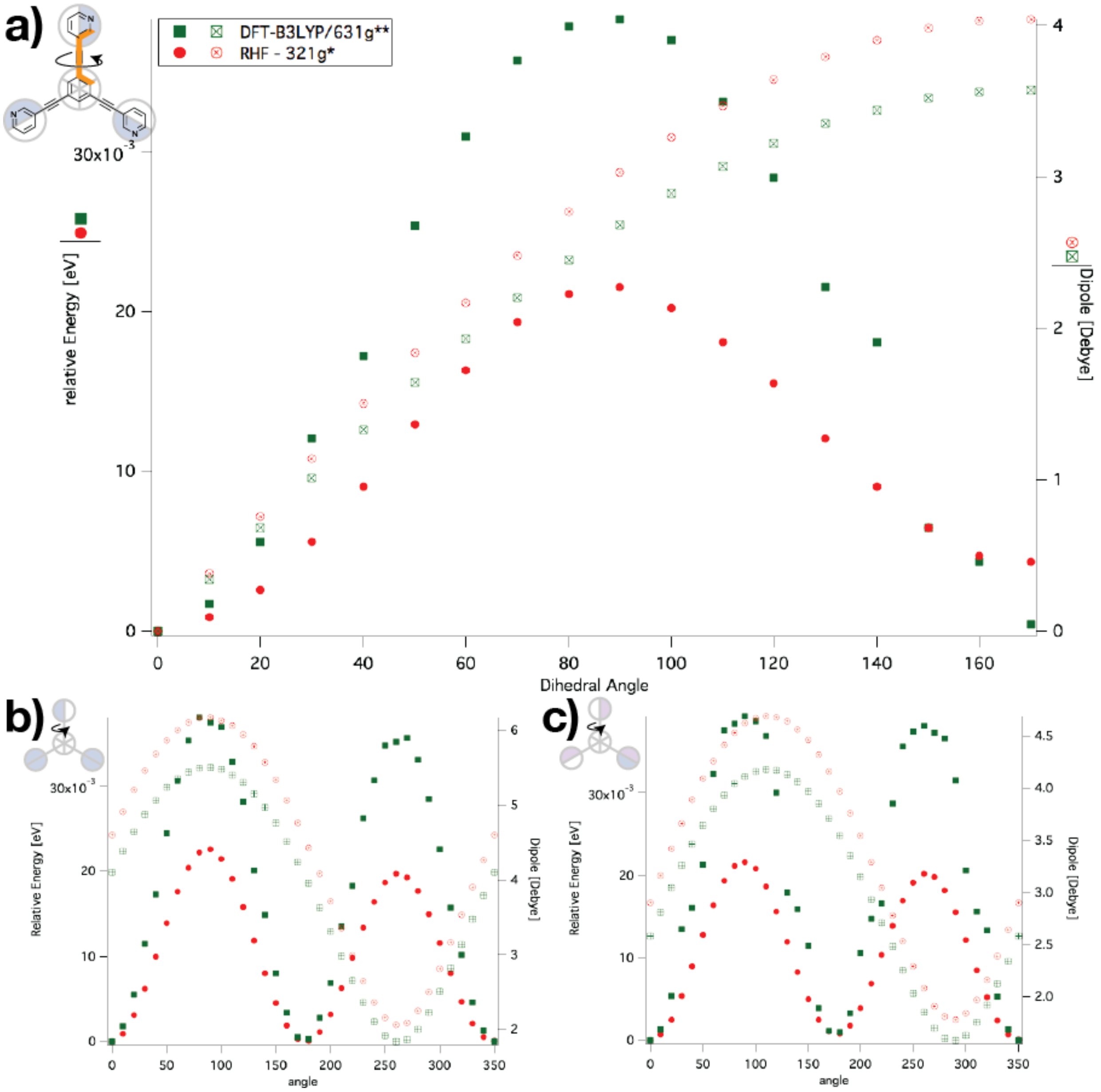

Figure S 17: rotational barriers evaluated from a) RRR (**Ma)**, b) LUU (**Md**), c) RUR (**Mb**) configurations.

Job type: Geometry optimization. Method: RHF	Job type: Geometry optimization. Method: RB3LYP Basis set: 6-31G**

Basis set: 3-21G(*) Number of shells: 120 Number of basis functions: 300 Multiplicity: 1	Number of shells: 165 Number of basis functions: 525 Multiplicity: 1

Simulated IR

In order to demonstrate the how the differences in the point group and consequently in the IR/raman active modes, both were calculated for all the library of conformers using the DFT b3lyp method and a 631g* basis set.

The strongest difference between those two conformers, is in the symmetry, and consequently in the dipole moment. To further demonstrate the stability and the existence of a Cs conformer we resourced to FT-IR spectroscopy – in principle, having the two conformers different point group, they must have definitely different active modes: If we compare the calculated dft (B3lyp 631g) IR for the two conformers the differences between the two curves are striking.

Ma

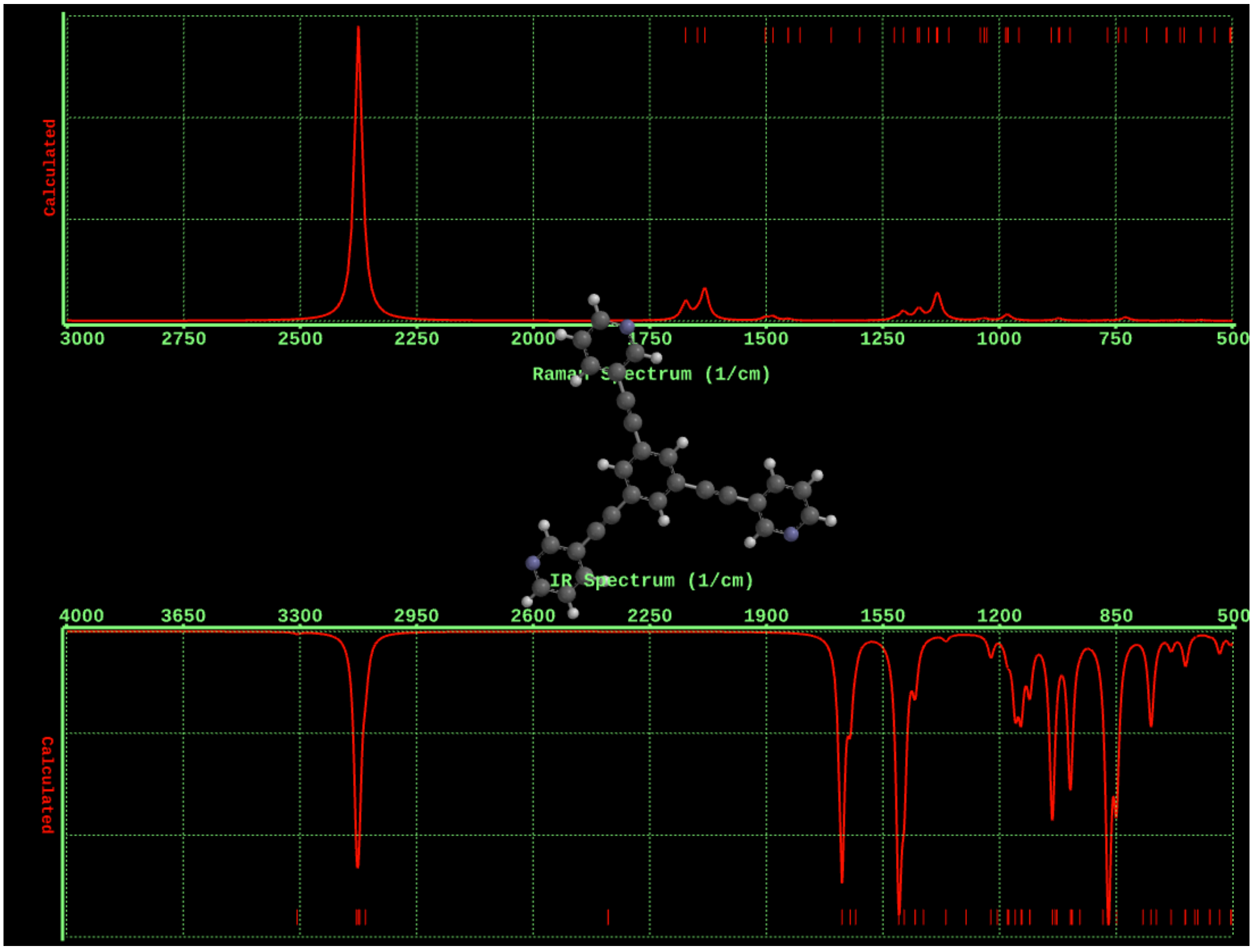

Figure S 18

Mc

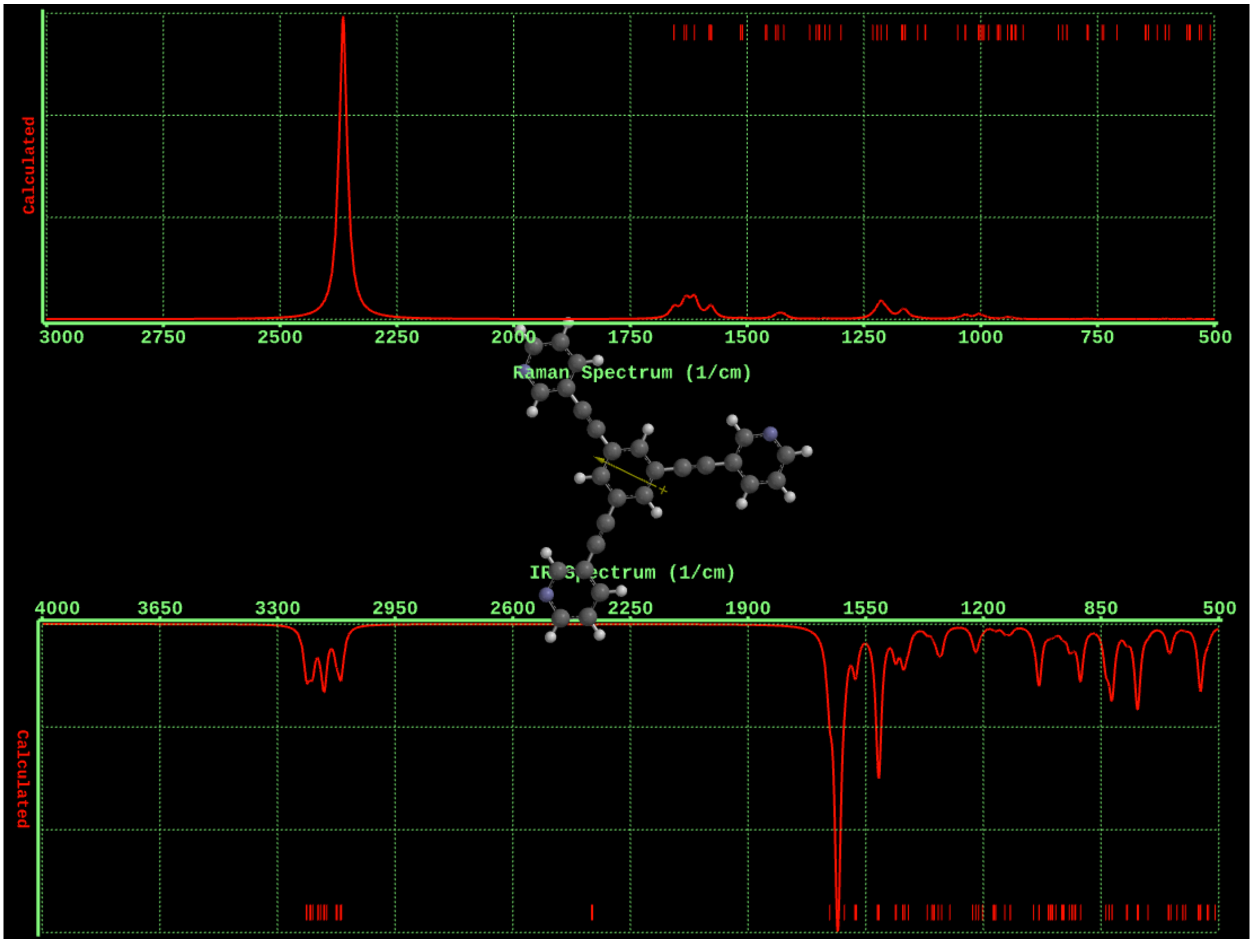

Figure S 19

IR

In order to compare experimental data with the theoretical calculations, we performed a series of FT-IR measurement: It is not possible (with our setup) to collect the spectra on the physisorbed monolayer, however we collected from the 1mM solution in 1-phenyloctane used for the STM experiments, and in solid on the powder of the compound, with a thermo scientific Nicolet 6700; diamond window Atr

Spectra range from 750.19 to 3999.7 cm-1, resolution: 1.9285 cm-1

Experimental solutions

z

Powder

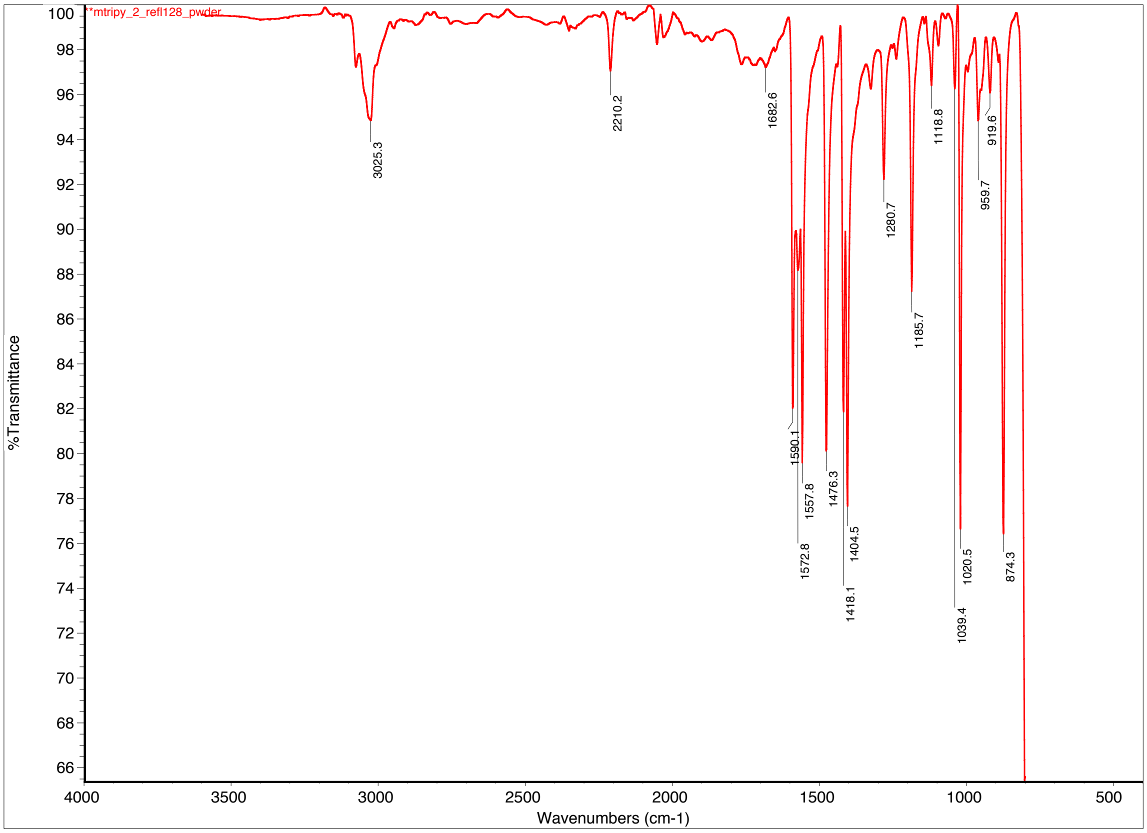

Figure S 20

Synthesis and Characterization

References:

1. a) A. Bultheel, Bulletin of the Belgian Mathematical Society, 1995, **2**, 1-46; b) S. G. Chang, B. Yu and M. Vetterli, Ieee T Image Process, 2000, **9**, 1522-1531; c) S. G. Chang, B. Yu and M. Vetterli, Ieee T Image Process, 2000, **9**, 1532-1546; d) S. G. Chang, B. Yu and M. Vetterli, Ieee T Image Process, 2000, **9**, 1631-1635.

2. D. Necas and P. Klapetek, Cent Eur J Phys, 2012, **10**, 181-188.

3. D. E. Hooks, T. Fritz and M. D. Ward, Advanced Materials, 2001, **13**, 227-+.

4. M. G. Evans and M. Polanyi, Transactions of the Faraday Society, 1935, **31**, 875-894.

5. J. M. Goodman, P. D. Kirby and L. O. Haustedt, Tetrahedron Lett, 2000, **41**, 9879-9882.

6. B. R. Brooks, C. L. B. III, A. D. M. Jr, L. Nilsson, R. J. Petrella, B. Roux, Y. Won, G. Archontis, C. Bartels, S. Boresch, A. Caflisch, L. Caves, Q. Cui, A. R. Dinner, M. Feig, S. Fischer, J. Gao, M. Hodoscek, W. Im, K. Kuczera, T. Lazaridis, J. Ma, V. Ovchinnikov, E. Paci, R. W. Pastor, C. B. Post, J. Z. Pu, M. Schaefer, B. Tidor, R. M. Venable, H. L. Woodcock, X. Wu, W. Yang, D. M. York and M. Karplus, Journal of Computational Chemistry, 2009, **30**, 1545-1614.

7. T. A. Halgren, Journal of Computational Chemistry, 1996, **17**, 490-519.

8. a) A. Ciesielski, A. Cadeddu, C. A. Palma, A. Gorczynski, V. Patroniak, M. Cecchini and P. Samori, Nanoscale, 2011, **3**, 4125-4129; b) C. A. Palma, P. Samori and M. Cecchini, Journal of the American Chemical Society, 2010, **132**, 17880-17885.

9. W. Humphrey, A. Dalke and K. Schulten, J Mol Graph Model, 1996, **14**, 33-38.

10. T. A. Halgren and R. B. Nachbar, Journal of Computational Chemistry, 1996, **17**, 587-615.

11. D. Young, Computational Chemistry: A Practical Guide for Applying Techniques to Real World Problems, Wiley-Interscience, 2001.

12. a) J. J. P. Stewart, Journal of Computational Chemistry, 1989, **10**, 209-220; b) J. J. P. Stewart, Journal of Computational Chemistry, 1989, **10**, 221-264; c) J. J. P. Stewart, Journal of Computational Chemistry, 1991, **12**, 320-341; d) J. J. P. Stewart, J Mol Model, 2004, **10**, 155-164.

13. a) A. D. Becke, Phys Rev A, 1988, **38**, 3098-3100; b) C. Lee, W. Yang and R. G. Parr, Physical Review B, 1988, **37**, 785-789; c) P. J. Stephens, F. J. Devlin, C. F. Chabalowski and M. J. Frisch, J Phys Chem-Us, 1994, **98**, 11623-11627.

14. a) G. R. Desiraju, Acc. Chem. Res., 2002, **35**, 565-573; b) G. R. Desiraju, Crystal design, John Wiley & Sons Inc., 2003.

Annex 2: synthesis of TBTAs

Chemicals. Solvents and starting materials were used as received. Tetrahydrofuran (THF) and triethylamine (TEA) were distilled under an inert gas (Ar) atmosphere from sodium/benzophenone and CaH_2, respectively, prior to use and were prepared using previously published procedures. $Pd(PPh_3)_4$ was freshly prepared.[1] All reactions requiring inert gas were performed under an Ar-atmosphere. The Cu-catalyzed 1,3-dipolar cycloaddition reactions were performed in the dark under an Ar-atmosphere, using $CuSO_4 \cdot 5H_2O$ as copper source, solid sodium ascorbate as the in-situ reducing agent, and tris[(1-benzyl-1*H*-1,2,3-triazol-4-yl)methyl]amine (TBTA)[2] as the supporting ligand. An aqueous ethylenediamine-tetraacetic acid disodium salt solution (EDTA) (16 g/L Na_2-EDTA), adjusted to pH ~ 8-9, was used to remove Cu-ions in aqueous extraction steps. Column chromatography was carried out with 130 – 400 mesh silica gel using the eluents specified (PE = petroleum ether, EA = ethyl acetate).

Spectroscopy. NMR spectra were recorded on a 300 MHz (75.6 MHz for ^{13}C) Bruker DPX 300 spectrometer or a 600 MHz Bruker Avance II spectrometer at 23 °C using residual protonated solvent signals as internal standard (^1H: $\delta(CHCl_3) = 7.28$ ppm, $\delta(D_2O) = 4.79$ ppm and ^{13}C: $\delta(CHCl_3) = 77.16$ ppm). Assignments are based on chemical shifts (Ar is used as abbreviation for assigning aromatic phenyl as well as triazole moieties). Mass spectrometry was performed on Thermo LTQ FT instrument (ESI, ESI-HRMS; additives of mixtures of MeOH/H_2O 75/25 + 0.5 % formic acid) and MSI Concept 1H (EI, 70 eV ionization) as well as on a QSTARXL Applied Biosystems ESI Q-TOF with a ISV of 950 V. UPLC measurements were performed with Waters Alliance systems consisting of a Waters Separations Module 2695, a Waters Diode Array detector 996 and a Waters Mass Detector ZQ 2000. (mixtures and gradient mixtures of acetoneitrile/water, flow = 0.6 ml/min) equipped with a 100 x 2.1 mm AQUITY HSST3 column (1.8 µm phenyl-hexyl material). Conditions

---

[1] D. R. Coulson, *Inorg. Syn.* **1971**, *13*, 121.

[2] T. R. Chan, R. Hilgraf, K. B. Sharpless, V. V. Fokin, *Org. Lett.* **2004**, *6*, 2853-2855.

are specified when describing the corresponding substances. Peak areas have been calculated from detection by UV between 200-400 nm (MaxPlot).

Synthesis

*5-Azidoisophthalic acid **6**.*[3]

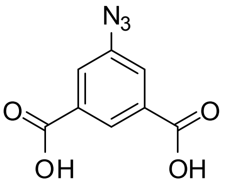

Compound **1** was prepared as described by *Yielding.*[3]

Bis(n-hexadecyl) 5-azidoisophthalate **7.**

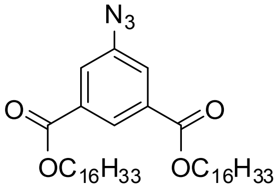

5-Azidoisophthalic acid **6** (1.0 g, 5.52 mmol, 1 equiv.), 1-hexadecanol (2.66 g, 10.98 mmol, 1.99 equiv.), and DMAP (1.34 g, 11.04 mmol, 2 equiv.) were dissolved in 40 mL of CH_2Cl_2, cooled to 0 °C and EDC (4.23 g, 22.08 mmol, 4 equiv.) was added. The solution was allowed to warm up to rt and stirred for 24 h. Purification using column chromatography (PE/CH_2Cl_2 4/6) gave 2.8 g of the desired product as a colourless solid (76%). **TLC** (PE/CH_2Cl_2 4/6) $R_f = 0.71$. **^{1}H-NMR** (300 MHz, $CDCl_3$): **^{1}H-NMR** (300 MHz, $CDCl_3$): δ (ppm) = 8.45(s, H, Ar*H*), 7.88 (s, 2H, Ar*H*), 4.39 (t, ^3J= 6.76 Hz, 4H, CO_2CH_2), 1.82-1.77 (m, 4H, CH_2), 1.45-1.27 (m, 52H, CH_2), 0.92 (t, ^3J = 6.55 Hz, 6H, CH_3). **^{13}C-NMR** (75 MHz, $CDCl_3$): δ (ppm) = 165.03 (-CO_2-), 141.10 (C_{Ar}), 132.65 (C_{Ar}), 126.83 (C_{Ar}), 123.88 (C_{Ar}), 65.87 (OCH_2), 31.93 (CH_2), 29.70 (CH_2), 29.59 (CH_2), 29.53 (CH_2), 29.37 (CH_2), 29.27 (CH_2), 28.64 (CH_2), 25.98 (CH_2), 22.70 (CH_2), 14.12 (CH_3).

Bis(3,6,9-trioxadecyl) 5-azidoisophthalate **8.**

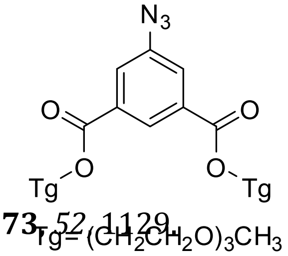

5-azidoisophthalic acid **6** (1.00 g, 5.52 mmol, 1 equiv.), triglyme (1.72 g, 10.98 mmol, 1.99 equiv.), and DMAP (1.34 g, 11.04 mmol,

---

[3] W. E. White, Jr., K. L. Yielding, *Biochem. Biophys. Res. Comm.* **1973**, *52*, 1129.

2 equiv.) were dissolved in 40 mL CH_2Cl_2, cooled to 0°C and EDC (4.23 g, 22.08 mmol, 4 equiv.) was added. The solution was allowed to warm up to rt and stirred for 2 d. Purification using column chromatography (CH_2Cl_2/Acetone 9/1) gave 3.03 g of yellow oil (65%). TLC (CH_2Cl_2/Acetone 9/1) $R_f = 0.41$.**^{1}H-NMR** (300 MHz, $CDCl_3$): δ (ppm) = 8.44 (t, ^3J = 2.9 Hz 1H, Ar*H*), 7.86 (d, ^2J = 1.45 Hz 2H, Ar*H*), 4.51 – 4.48 (m, 4H, CO_2CH), 3.85 – 3.82 (m, 4H, CH_2), 3.71 – 3.61 (m, 12H, CH_2), 3.53 – 3.50 (m, 4H, CH_2), 3.34 (s, 6H, OCH_3).**^{13}C-NMR** (75 MHz, $CDCl_3$): δ (ppm) = 164.86 (-CO_2-), 141.12 (C_{Ar}), 132.24 (C_{Ar}), 127.08 (C_{Ar}), 124.15 (C_{Ar}), 71.81 (CH_2), 70.64 (CH_2), 70.59 (CH_2), 70.54 (CH_2), 68.99 (CH_2), 64.69 (CH_2), 58.98 (OCH_3). **UPLC** R_t = 2.12 min, 99.8 % peak area. **HRMS** (ESI) *m/z* = 522.5010 (calcd 522.5012 for [M + Na$^+$]).

1,3,5-Triethynylbenzene **9.**[4]

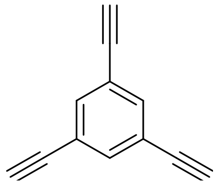

Compound **9** was prepared as described by *Kijima.*[4]

Hexakis(n-hexahexadecyl) dendrimer **2.**

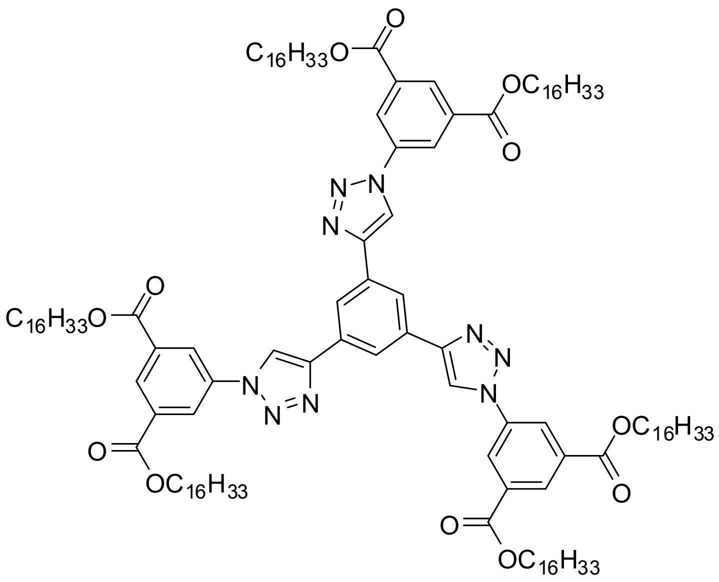

A three necked flask was charged with 1,3,5-triethynylbenzene **9** (541 mg, 3.6 mmol, 1 equiv.) and bis (*n*-hexadecyl) 5-azidoisophthalate **7** (7.79 g, 11.8 mmol, 3.3 equiv.), sodium ascorbate (214 mg, 1.08 mmol, 0.3 equiv.), TBTA (287 mg, 0.54 mmol, 0.15 equiv.) and a solvent mixture of H_2O/^{tert}BuOH/CH_2Cl_2 (1/2/8). The flask was evacuated and flushed with

---

[4] N. Kobayashi, M. Kijima, *J.Mater. Chem.* **2007**, *17*, 4289.

argon repeatedly (3 cycles). $CuSO_4 \cdot 5H_2O$ was added (135 mg, 0.54 mmol, 0.15 equiv.) and the mixture was stirred for 2 d at rt in the dark. After the acetylene starting material was consumed indicated by TLC monitoring (PE/EA 9/1) the mixture was diluted with CH_2Cl_2 and transferred into a separation funnel. The organic phase was washed with aqueous Na_2-EDTA solution (1 x), the aqueous phase was extracted with CH_2Cl_2 (3 x), and afterwards the combined organic phases were washed again with aqueous Na_2-EDTA solution (2 x) and once with aqueous sat. NaCl solution. After drying over $MgSO_4$, filtration, and removal of the solvent *in vacuo* the title compound was obtained by column chromatography (PE/EA 9/1) as colorless solid (6.5 g, 85%). **TLC** (PE/EA 9/1) $R_f = 0.6$.**^{1}H-NMR** (300 MHz, $CDCl_3$): δ (ppm) = 8.77 (m, 3H, Ar*H*), 8.70 (ss, 6H, Ar*H*), 8.62 (s, 3H, Ar*H*), 8.54 (s, 3H, Ar*H*), 4.44 (t, ^3J = 6.82 Hz, 12H, CO_2CH_2), 1.91-1.81 (m, 12H, CH_2), 1.48-1.25 (m, 156H, CH_3), 0.88 (t, ^3J = 6.91Hz, 18H, CH_3).**^{13}C-NMR** (75 MHz, $CDCl_3$): δ (ppm) = 164.56 (-CO_2-), 147.89 (C_{Ar}), 137.21 (C_{Ar}), 132.94 (C_{Ar}), 131.38 (C_{Ar}), 130.47 (C_{Ar}), 124.83 (C_{Ar}), 122.99 (C_{Ar}), 118.33 (C_{Ar}), 66.22 (OCH_2), 31.92 (CH_2), 29.64 (CH_2), 29.58 (CH_2), 29.37 (CH_2), 29.32 (CH_2), 28.69 (CH_2), 25.98 (CH_2), 22.69 (CH_2), 14.14 (CH_3). **MS** (EI, T = 37°C - 50 °C)**:** *m/z* = 2119.55 (calcd 2119.16 for $[M + H^+]$).

Hexakis(triglyme) dendrimer **10.**

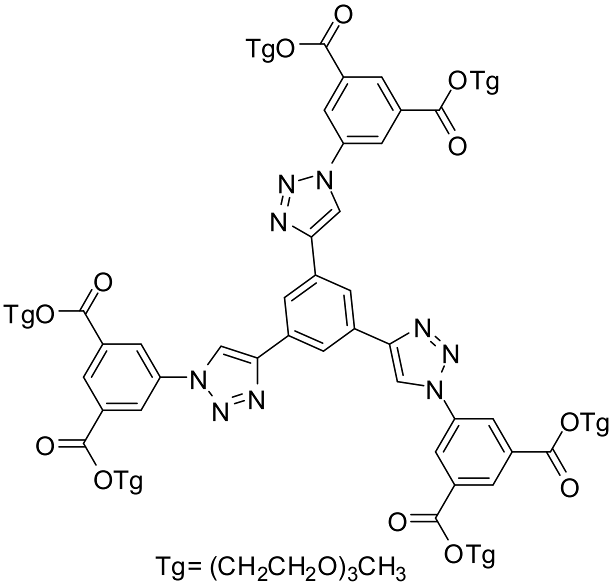

A three necked flask was charged with 1,3,5-triethynylbenzene (811 mg, 5.40 mmol, 1 equiv.) and bis(3,6,9-trioxadecyl) 5-azido-isophthalate **8** (8.90 g, 17.82 mmol, 3.3 equiv.), sodium ascorbate (321 mg, 1.62 mmol, 0.3 equiv.), TBTA (430 mg, 0.81 mmol, 0.15 equiv.) and a solvent mixture of $H_2O/^{tert}BuOH/CH_2Cl_2$ (1/2/8). The flask was evacuated and flushed with argon repeatedly (3 cycles). An aqueous stock solution of $CuSO_4$ was added (0.81 mmol, 0.81 equiv.; stock solution: 10 mg $CuSO_4$ per 0.3 mL of water) and the mixture was stirred for 3 d at rt in the dark. After the acetylene starting material was consumed indicated by TLC monitoring (CH_2Cl_2/Acetone 5/5) the mixture was diluted with CH_2Cl_2 and transferred into a separation funnel. The organic phase was washed with aqueous Na_2-EDTA solution (1 x), the aqueous phase was extracted with CH_2Cl_2 (3 x), and afterwards the combined organic phases were washed again with aqueous Na_2-EDTA solution (2 x) and once with aqueous sat. NaCl solution. After drying over $MgSO_4$, filtration, and removal of the solvent *in vacuo* the title compound was obtained by column chromatography (CH_2Cl_2/Acetone 5/5) as yellow oil (679 mg, 75.3%). **TLC** (CH_2Cl_2/Acetone 5/5) $R_f = 0.25$.**^{1}H-NMR** (300 MHz, $CDCl_3$): δ (ppm) = 8.80 (s, 3H, Ar*H),* 8.73-8.71 (m, 9H, Ar*H),* 8.52 (s, 3H, Ar*H),* 4.58-4.55 (m, 12H, CO_2CH_2*),* 3.93-3.90 (m, 12H, C*H₂),* 3.78-3.49 (m, 48H, CH_2), 3.30 (s, 18H, OCH_3*).***^{13}C-NMR** (75 MHz, $CDCl_3$): δ (ppm) = 164.34 (-CO_2-), 147.60 (C_{Ar}), 137.18 (C_{Ar}), 132.20 (C_{Ar}), 131.20 (C_{Ar}), 130.01 (C_{Ar}), 124.51 (C_{Ar}), 122.41 (C_{Ar}), 118.92 (C_{Ar}), 71.77 (CH_2), 70.64 (CH_2), 70.56 (CH_2), 70.45(CH_2), 68.89 (CH_2), 64.89 (CH_2), 58.77 (OCH_3). **UPLC** $R_t = 5.30$, 98.81% peak area**. HRMS** (ESI) *m/z* = 1648.7115 (calcd 1648.7057 for [M + H^+])

Hexakis(acid) dendrimer **1.**

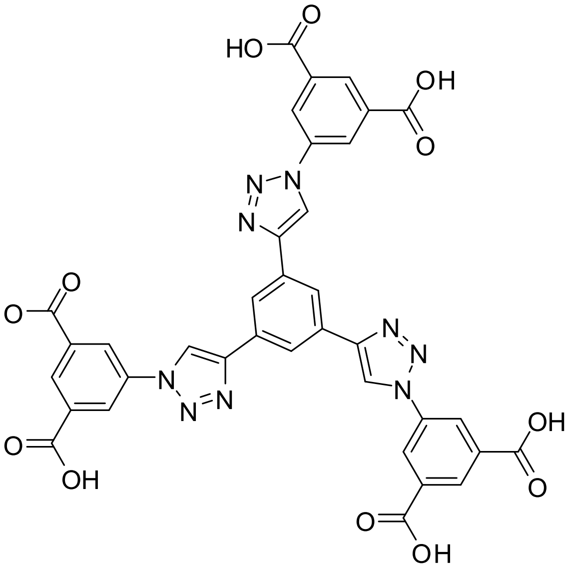

A one necked flask was charged with hexakis(triglyme) dendrimer **10** (0.84 g, 0.51 mmol, 1 equiv.), 40 mL of a mixture of H_2O/EtOH 1/2 and 0.315 mg of KOH (5.61 mmol, 11 equiv.). The reaction mixture was stirred for 4 h at 78 °C and after consumption of starting material **6** indicated by TLC monitoring. EtOH was evaporated and the aqueous layer was acidified with 1N HCl to pH 2, filtration, washed with water and removal of the solvent *in vacuo* the title compound was obtained as colorless solid (354 mg, 90%) which was used for characterization without further purification. **^{1}H-NMR** (300 MHz, D_2O): δ (ppm) = 9.81 (s, 3H, Ar*H*)*,* 8.74 - 8.73 (ss, 6H, Ar*H*)*,* 8.67 (s, 3H, Ar*H*)*,* 8.56 (s, 3H, Ar*H*)*.***^{13}C-NMR** (75 MHz, D_2O): δ (ppm) = 166.11 (-CO_2-), 149.38 (C_{Ar}), 138.95 (C_{Ar}), 133.97 (C_{Ar}), 132.98 (C_{Ar}), 131.78 (C_{Ar}), 126.28 (C_{Ar}), 124.19 (C_{Ar}), 120.69 (C_{Ar}).

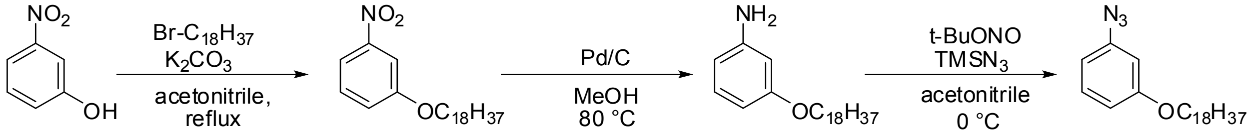

Figure S1. Synthesis scheme of 1-azido-3-(n-octadecyloxy) benzene **13**.

1-Nitro-3-(n-octadecyloxy) benzene **11.**

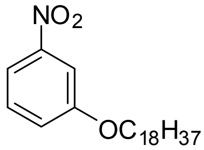

In a 3-necked flask equipped with a condenser 4.17 g (30.0 mmol, 1 equiv.) of 3-nitrophenol, 10.31 g (30.0 mmol, 1 equiv.) of 1-bromooctadecane, 10.36 g (75 mmol, 2.5 equiv.) of potassium carbonate, 0.39 g (1.5 mmol, 0.05 equiv.) of 18-crown-6 and 0.55 g (1.5 mmol, 0.05 equiv.) of tetrabutylammonium iodide (TBAI) were suspended in 600 mL of acetonitrile and the mixture was degassed at rt by evacuating under stirring and flushing with argon (4 cycles). The suspension was stirred at 80 °C over night and after TLC monitoring the yellow solution was transferred into a separation funnel and diluted with EtOAc. The organic phase was washed with sat. aq. $NaHCO_3$ solution (3 x), water (3 x) and brine (1 x). After drying over $MgSO_4$ and filtration the solvent was removed *in vacuo*. Purification by column chromatography (PE/EA 25/1) gave 11.3 g (96.2%) of the title compound as pale yellow solid. **TLC** (PE/EA 25/1) $R_f = 0.60$. **^{1}H-NMR** (300 MHz, $CDCl_3$): δ (ppm) = 7.83-7.80 (m, 1H, Ar*H*), 7.73 (t, ^3J = 8.22 Hz, 1H, Ar*H*), 7.42 (t, ^3J = 6.52 Hz, 1H, Ar*H*), 7.24-7.20 (m, 1H, Ar*H*), 4.04 (t, ^3J = 6.42 Hz, 2H, OCH_2), 1.85-1.78(m, 2H, OCH_2CH_2), 1.50-1.27 (m, 30H, CH_2), 0.89 (t, ^3J = 6.44 Hz, 3H, CH_2CH_3). **^{13}C-NMR** (75 MHz, $CDCl_3$): δ (ppm) = 159.69 (OC_{Ar}), 149.19 (O_2NC_{Ar}), 129.82 (HC_{Ar}), 121.67 (HC_{Ar}), 115.49 (HC_{Ar}), 108.64 (HC_{Ar}), 68.73 (OCH_2), 31.93 (CH_2), 29.71 (CH_2), 29.67 (CH_2), 29.59 (CH_2), 29.55 (CH_2), 29.37 (CH_2), 29.34 (CH_2), 29.01 (CH_2), 25.95 (CH_2), 22.70 (CH_2), 14.13 (CH_3). **MS** (ESI) *m/z* = 391.36 (calcd 391.31 for $[M^+]$). **HPLC** (Luna Phenyl-Hexyl 3 um 2 x 150, acetonitrile/water 8/2, det. UV 220–380 nm, ret. time 26.85 min.): 97.6 area %.

3-(n-Octadecyloxy) aniline **12.**

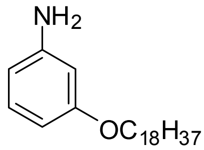

In a one necked flask 6.0 g (15.32 mmol) of 1-nitro-3-(n-octadecyloxy) benzene **11** were dissolved in 50 mL of MeOH, 600 mg Pd on charcoal (10 wt%) were added, the stirred mixture was degassed at rt *in vacuo* and flushed with H_2 (3 cycles). After stirring for 24 h at 60 °C in H_2 atmosphere (2 bar) the mixture was filtered through a celite pad and the solvent removed *in vacuo*. Purification by column chromatography (PE/EA 25/1) gave 5.2 g (93.8%) of a colourless solid. TLC (PE/EA 25/1) $R_f = 0.42$. ^{1}H-NMR (300 MHz, CDCl3): δ (ppm) = 7.04 (t, $^3J = 7.97$ Hz, 1H, Ar*H*), 6.34-6.25 (m, 3H, Ar*H*) 3.91 (t, $^3J = 6.58$ Hz, 2H, OC*H₂*), 2.93 (br s, 2H, Ar-N*H₂*), 1.78-1.73 (m, 2H, $OCH_2C\mathit{H_2}$), 1.49-1.27 (m, 30H, C*H₂*), 0.89 (t, $^3J = 6.51$ Hz, 3H, $CH_2C\mathit{H_3}$). ^{13}C-NMR (75 MHz, CDCl3): δ (ppm) = 160.29 (OC_{Ar}), 147.61 (H_2NC_{Ar}), 130.01 (HC_{Ar}), 107.78 (HC_{Ar}), 104.67 (HC_{Ar}), 101.72 (HC_{Ar}), 67.78 (O*C*H₂), 31.93 (*C*H₂), 29.71 (*C*H₂), 29.62 (*C*H₂), 29.43 (*C*H₂), 29.38 (*C*H₂), 29.32 (*C*H₂), 26.08 (*C*H₂), 24.20 (*C*H₂), 22.70 (*C*H₂), 19.76 (*C*H₂), 14.13 (*C*H₃). MS (ESI) m/z = 362.40 (calcd 362.34 for $[M + H^+]$). HPLC (Luna Phenyl-Hexyl 3 um 2 x 150, acetonitrile/water 8/2, det. UV 220 nm - 380 nm, ret. time 16.62 min.): 98.1 area %.

<u>*1-Azido-3-(n-octadecyloxy) benzene* **13.**</u>

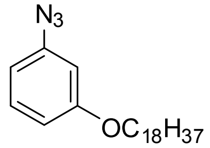

In a round-bottomed flask 1.08 g (3 mmol, 1 equiv.) of 3-(*n*-octadecyloxy) aniline **12** was dissolved in 6 mL of acetonitrile and cooled to 0 °C in an ice bath. To this stirred mixture were added 0.46 g (4.5 mmol, 1.5 equiv.) of *t*-BuONO followed by 0.41 g (3.6 mmol, 1.2 equiv.) $TMSN_3$ dropwise. The resulting solution was stirred at rt for 1 h. The reaction mixture was concentrated under *vacuo* and the crude product was purified by column chromatography (PE) to give 0.74 g (64.2%) of a brown solid. **TLC** (PE) $R_f = 0.50$. **^{1}H-NMR** (300 MHz, $CDCl_3$): δ (ppm) = 7.25-7.23 (m, 1H, Ar*H*), 6.71-6.62 (m, 2H, Ar*H*), 6.56 (t, $^3J = 2.22$ Hz 1H, Ar*H*), 3.95 (t, $^3J = 6.54$ Hz, 2H, OCH_2), 1.84-1.74 (m, 2H, OCH_2CH_2), 1.48-1.27 (m, 30H, CH_2), 0.90 (t, $^3J = 6.26$ Hz, 3H, CH_2CH_3). **^{13}C-NMR** (75 MHz, $CDCl_3$): δ (ppm) = 160.37 (OC_{Ar}), 141.17 (N_3C_{Ar}), 130.37 (HC_{Ar}), 111.17 (HC_{Ar}), 111.08 (HC_{Ar}), 105.44 (HC_{Ar}), 68.14 (OCH_2), 31.95 (CH_2), 29.73 (CH_2), 29.69 (CH_2), 29.62 (CH_2), 29.59 (CH_2), 29.40 (CH_2), 29.19 (CH_2), 26.03 (CH_2), 22.72 (CH_2), 14.15 (CH_2CH_3). **MS** (ESI) *m/z* = 410.37 (calcd 410.31 for [M + Na^+]). **HPLC** (Luna Phenyl-Hexyl 3 um 2 x 150, acetonitrile/water 8/2, det. UV 220 nm - 380 nm, ret. time 22.53 min.): 97.1 area %.

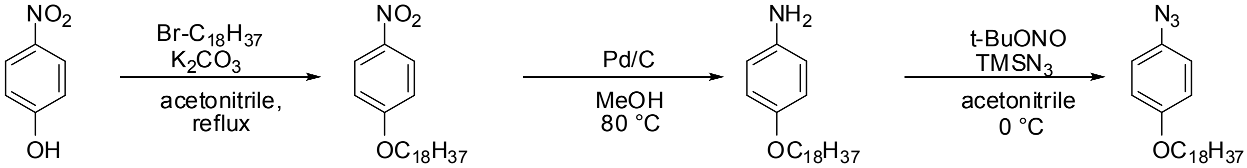

Figure S2. Synthesis scheme of 1-azido-4-(octadecyloxy) benzene **16.**

<u>*1-Nitro-4-(n-octadecyloxy) benzene **14**.*</u>

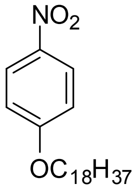

In a 3-necked flask equipped with a condenser 4.17 g (30.0 mmol, 1 equiv.) of 4-nitrophenol, 10.31 g (30.0 mmol, 1 equiv.) of 1-bromooctadecane, 10.36 g (75 mmol, 2.5 equiv.) of potassium carbonate, 0.39 g (1.5 mmol, 0.05 equiv.) of 18-crown-6 and 0.55 g (1.5 mmol, 0.05 equiv.) of tetrabutylammonium iodide (TBAI) were suspended in 600 mL of acetonitrile and the mixture was degassed at rt by evacuating under stirring and flushing with argon (4 cycles). The suspension was stirred at 80 °C over night and after TLC monitoring the yellow solution was transferred into a separation funnel and diluted with EA. The organic phase was washed with sat. aq. $NaHCO_3$ solution (3 x), water (3 x) and brine (1 x). After drying over $MgSO_4$ and filtration the solvent was removed *in vacuo*. Purification by column chromatography (PE/EA 25/1) gave 11.51 g (98%) of the title compound as pale yellow solid. **TLC** (PE/EA 25/1) $R_f = 0.53$. **^{1}H-NMR** (300 MHz, $CDCl_3$): δ (ppm) = 8.23-8.18 (m, $^3J = 2.18$, 2H, Ar*H*), 6.98-6.92 (m, 2H, Ar*H*), 4.08 (t, $^3J = 6.53$ Hz, 2H, OCH_2), 1.86-1.79 (m, 2H, OCH_2CH_2), 1.50-1.27 (m, 30H, CH_2), 0.89 (t, $^3J = 6.41$ Hz, 3H, CH_2CH_3). **^{13}C-NMR** (75 MHz, $CDCl_3$): δ (ppm) = 164.26 (OC_{Ar}), 141.28 (O_2NC_{Ar}), 125.89 (HC_{Ar}), 114.38 (HC_{Ar}), 68.89 (OCH_2), 31.93 (CH_2), 29.71 (CH_2), 29.68 (CH_2), 29.58 (CH_2), 29.54 (CH_2), 29.37 (CH_2), 29.32 (CH_2), 28.97 (CH_2), 25.91 (CH_2), 22.70 (CH_2), 14.12 (CH_3). **MS** (ESI) *m/z* = 391.28 (calcd 391.31 for [M^+]). **HPLC** (Luna Phenyl-Hexyl 3 um 2 x 150, acetonitrile/water 8/2, det. UV 220 nm - 380 nm, ret. time 26.71 min.): 98 area %.

4-(n-Octadecyloxy) aniline **15.**

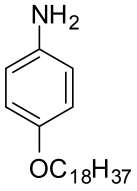

In a one necked flask 6.0 g (15.32 mmol) of 1-nitro-4-(n-octadecyloxy) benzene **14** were dissolved in 50 mL of MeOH, 600 mg Pd on charcoal (10 wt%) were added, the stirred mixture was degassed at rt *in vacuo* and flushed with H_2 (3 cycles). After stirring for 24 h at 60 °C in H_2 atmosphere (2 bar) the mixture was filtered through a celite pad and the solvent removed *in vacuo*. Purification by column chromatography (PE/EA 25/1) gave 5.4 g (97%) of a colourless solid. TLC (PE/EA 25/1) $R_f = 0.45$. ^{1}H-NMR (300 MHz, CDCl3): δ (ppm) = 6.78-6.74 (m, 2H, Ar*H*), 6.68-6.64 (m, 2H, Ar*H*), 3.89 (t, $^3J = 6.61$ Hz, 2H, OCH_2), 2.94 (br s, 2H, Ar-NH_2), 1.80-1.71 (m, 2H, OCH_2CH_2), 1.47-1.28 (m, 30H, CH_2), 0.90 (t, $^3J = 6.44$ Hz, 3H, CH_2CH_3). ^{13}C-NMR (75 MHz, CDCl3): δ (ppm) = 152.36 (OC_{Ar}), 139.74 (H_2NC_{Ar}), 116.44 (HC_{Ar}), 115.65 (HC_{Ar}), 68.70 (OCH_2), 31.94 (CH_2), 29.72 (CH_2), 29.63 (CH_2), 29.45 (CH_2), 29.39 (CH_2), 26.08 (CH_2), 22.71 (CH_2), 14.14 (CH_3). MS (ESI) m/z = 362.44 (calcd 362.34 for [M^+]). HPLC (Luna Phenyl-Hexyl 3 um 2 x 150, acetonitrile/water 8/2, det. UV 220 nm - 380 nm, ret. time 11.82 min.): 98.8 area %.

1-Azido-4-(n-octadecyloxy) benzene **16.**

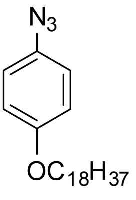

In a round-bottomed flask 1.08 g (3 mmol, 1 equiv.) of 4-(*n*-octadecyloxy) aniline **15** was dissolved in 6 mL of acetonitrile and cooled to 0 °C in an ice bath. To this stirred mixture were added 0.46 g (4.5 mmol, 1.5 equiv.) of t-BuONO followed by 0.41 g (3.6 mmol, 1.2 equiv.) $TMSN_3$ dropwise. The resulting solution was stirred at rt for 1 h. The reaction mixture was concentrated under *vacuo* and the crude product was purified by column chromatography (PE) to give 0.81 g (70%) of a brown solid. **TLC** (PE) $R_f = 0.41$. **^{1}H-NMR** (300 MHz, $CDCl_3$): δ (ppm) = 6.98-6.88 (m, 4H, Ar*H*), 3.94 (t, $^3J = 6.57$ Hz, 2H, OCH_2), 1.84-1.74 (m, 2H, OCH_2CH_2), 1.49-1.28 (m, 30H, CH_2), 0.93 (t, $^3J = 6.41$ Hz, 3H, CH_2CH_3). **^{13}C-NMR** (75 MHz, $CDCl_3$): δ (ppm) = 156.56 (OC_{Ar}), 132.06 (N_3C_{Ar}), 119.93 (HC_{Ar}), 115.70 (HC_{Ar}), 68.40 (OCH_2), 31.95 (CH_2), 29.69 (CH_2), 29.62 (CH_2), 29.59 (CH_2), 29.40 (CH_2), 29.26 (CH_2), 26.03 (CH_2), 22.72 (CH_2), 14.14 (CH_2CH_3). **HPLC** (Luna Phenyl-Hexyl 3 um 2 x 150, acetonitrile/water 8/2, det. UV 220 nm - 380 nm, ret. time 21.59 min.): 97.9 area %.

Synthesis of the tris(octadecyloxy) dendrimers **3-5**

Tris(ortho-octadecyloxy) dendrimer **3.**

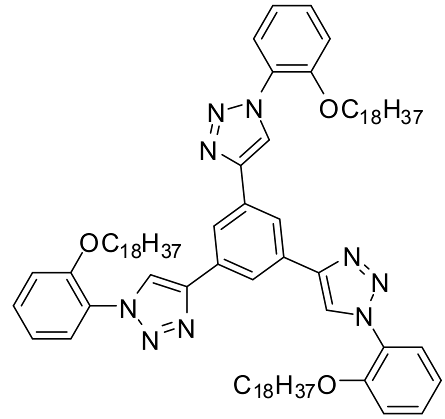

A three necked flask was charged with 1,3,5-triethynylbenzene **9** (300 mg, 2 mmol, 1 equiv.) and 1-azido-2-(*n*-octadecyloxy) benzene[5] (2.55 g, 6.6 mmol, 3.3 equiv.), sodium ascorbate (119 mg, 0.60 mmol, 0.3 equiv.), TBTA (159 mg, 0.30 mmol, 0.15 equiv.) and a solvent mixture of $H_2O/^{tert}BuOH/CH_2Cl_2$ (1/2/8). The flask was evacuated and flushed with argon repeatedly (3 cycles). $CuSO_4{\cdot}5H_2O$ was added (75 mg, 0.30 mmol, 0.15 equiv.) and the mixture was stirred for 2 d at rt in the dark. After the acetylene starting material was consumed indicated by TLC monitoring (PE/EA 9/1) the mixture was diluted with CH_2Cl_2 and transferred into a separation funnel. The organic phase was washed with aqueous Na_2-EDTA solution (1 x), the aqueous phase was extracted with CH_2Cl_2 (3 x), and afterwards the combined organic phases were washed again with aqueous Na_2-EDTA solution (2 x) and once with aqueous sat. NaCl solution. After drying over

---

[5] L. Piot, R. M. Meudtner, T. El Malah, S. Hecht, P. Samorì, *Chem. Eur. J.* **2009**, *15*, 4788.

$MgSO_4$, filtration, and removal of the solvent *in vacuo* the title compound was obtained by column chromatography (PE/EA 9/1) as colorless solid (2.49 g, 95%). **TLC** (PE/EA 9/1) $R_f = 0.58$.^{1}**H-NMR** (300 MHz, $CDCl_3$): δ (ppm) = 8.61 (s, 3H, Ar*H*), 8.53 (s, 3H, Ar*H*), 7.90-7.86 (dd, 3H, Ar*H*), 7.48-7.42 (m, 3H, Ar*H*), 7.17-7.12 (m, 6H, Ar*H*), 4.14 (t, $^3J = 5.95$ Hz, 6H, OCH_2), 1.88-1.79 (m, 6H, CH_2), 1.47-1.16 (m, 90H, CH_2), 0.89 (t, $^3J = 6.01$ Hz, 9H, CH_3). ^{13}**C-NMR** (75 MHz, $CDCl_3$): δ (ppm) = 150.67 (C_{Ar}), 146.64 (C_{Ar}), 132.04 (C_{Ar}), 130.07 (C_{Ar}), 126.55 (C_{Ar}), 125.43 (C_{Ar}), 122.44 (C_{Ar}), 121.05 (C_{Ar}), 113.39 (C_{Ar}), 69.31 (OCH_2), 31.94 (CH_2), 29.72 (CH_2), 29.69 (CH_2), 29.60 (CH_2), 29.56 (CH_2), 29.39 (CH_2), 29.30 (CH_2), 29.00 (CH_2), 26.04 (CH_2), 22.70 (CH_2), 14.14 (CH_3). **MS** (EI, T = 37°C - 50 °C)**:** *m/z* = 1314.20 (calcd 1313.99 for $[M + H^+]$).

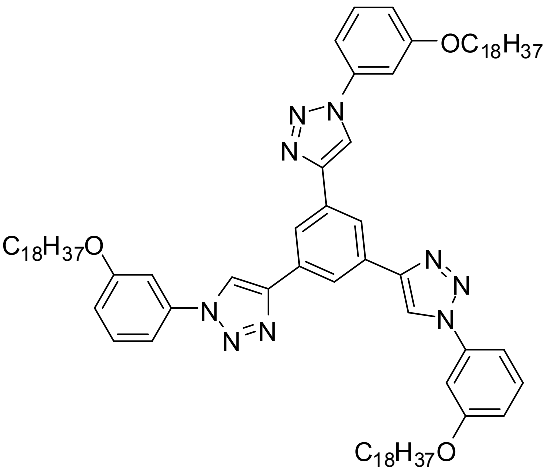

Tris(meta-octadecyloxy) dendrimer **4.**

A three necked flask was charged with 1,3,5-triethynylbenzene **9** (74 mg, 0.49 mmol, 1 equiv.) and 1-azido-3-(*n*-octadecyloxy) benzene **13** (626 mg, 1.61 mmol , 3.3 equiv.), sodium ascorbate (29 mg, 0.15 mmol, 0.3 equiv.), TBTA (39 mg, 0.07 mmol, 0.15 equiv.) and a solvent mixture of $H_2O/^{tert}BuOH/CH_2Cl_2$ (1/2/8). The flask was evacuated and flushed with argon repeatedly (3 cycles). $CuSO_4 \cdot 5H_2O$ was added (18 mg, 0.07 mmol, 0.15 equiv.) and the mixture was stirred for 2 d at rt in the dark. After the acetylene starting material was consumed indicated by TLC monitoring (PE/EA 9/1) the mixture was diluted with CH_2Cl_2 and transferred into a separation funnel. The organic phase was washed with aqueous Na_2-EDTA solution (1 x), the aqueous phase was extracted with CH_2Cl_2 (3 x), and afterwards the combined organic phases were washed again with aqueous Na_2-EDTA solution (2 x) and once with aqueous sat. NaCl solution. After drying over $MgSO_4$, filtration, and removal of the solvent *in vacuo* the title compound was obtained by column chromatography (PE/EA 9/1) as colorless solid (591 mg, 95%). **TLC** (PE/EA 9/1) $R_f = 0.55$. ^{1}**H-NMR** (300 MHz, $CDCl_3$): δ (ppm) = 8.26 (s, 6H, Ar*H*), 7.36-7.25 (m, 9H, Ar*H*), 6.90-6.87 (m, 3H, Ar*H*), 3.98 (t, $^3J = 5.93$ Hz, 6H, OCH_2), 1.86-1.76 (m, 6H, CH_2), 1.49-1.27

(m, 90H, CH_2), 0.88 (t, ^{3}J = 6.69 Hz, 9H, CH_3). **^{13}C-NMR** (75 MHz, CDCl$_3$): δ (ppm) = 160.07 (C_{Ar}), 147.25 (C_{Ar}), 137.73 (C_{Ar}), 131.31 (C_{Ar}), 130.33 (C_{Ar}), 122.28 (C_{Ar}), 118.12 (C_{Ar}), 115.13 (C_{Ar}), 111.74 (C_{Ar}), 106.00 (C_{Ar}), 68.41 (OCH$_2$), 31.95 (CH$_2$), 29.75 (CH$_2$), 29.70 (CH$_2$), 29.51 (CH$_2$), 29.40 (CH$_2$), 29.25 (CH$_2$), 26.08 (CH$_2$), 22.71 (CH$_2$), 14.13 (CH$_3$). **MS** (EI, T = 37°C - 50 °C)**:** *m/z* = 1314.18 (calcd 1313.99 for [M + H$^+$]).

Tris(para-octadecyloxy) dendrimer **5.**

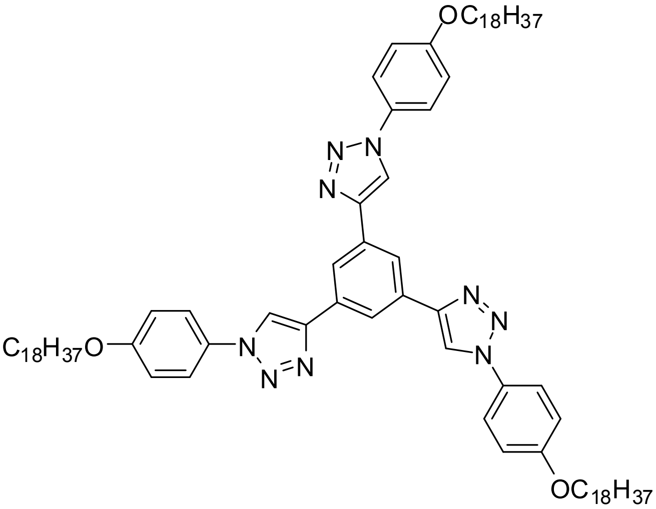

A three necked flask was charged with 1,3,5-triethynylbenzene **9** (150 mg, 1 mmol, 1 equiv.) and 1-azido-4-(*n*-octadecyloxy) benzene **16** (1.28 g, 3.3 mmol , 3.3 equiv.), sodium ascorbate (59 mg, 0.3 mmol, 0.3 equiv.), TBTA (80 mg, 0.15 mmol, 0.15 equiv.) and a solvent mixture of H_2O/^{tert}BuOH/CH_2Cl_2 (1/2/8). The flask was evacuated and flushed with argon repeatedly (3 cycles). $CuSO_4 \cdot 5H_2O$ was added (37 mg, 0.15 mmol, 0.15 equiv.) and the mixture was stirred for 2 d at rt in the dark. After the acetylene starting material was consumed indicated by TLC monitoring (PE/EA 9/1) the mixture was diluted with CH_2Cl_2 and transferred into a separation funnel. The organic phase was washed with aqueous Na_2-EDTA solution (1 x), the aqueous phase was extracted with CH_2Cl_2 (3 x), and afterwards the combined organic phases were washed again with aqueous Na_2-EDTA solution (2 x) and once with aqueous sat. NaCl solution. After drying over $MgSO_4$, filtration, and removal of the solvent *in vacuo* the title compound was obtained by column chromatography (PE/EA 9/1) as colorless solid (1.26 g, 96%). **TLC** (PE/EA 9/1) $R_f = 0.56$. **^{1}H-NMR** (300 MHz, $CDCl_3$): δ (ppm) = 8.34 (s, 3H, Ar*H*), 8.25 (s, 3H, Ar*H*), 7.66 (d, $^2J = 8.97$ Hz, 6H, Ar*H*), 6.99 (d, $^2J = 9.06$ Hz, 6H, Ar*H*), 3.96 (t, $^3J = 6.59$ Hz, 6H, OCH_2), 1.82-1.75 (m, 6H, CH_2), 1.48-1.28 (m, 90H, CH_2), 0.89 (t, $^3J = 6.70$ Hz, 9H, CH_3). **^{13}C-NMR** (75 MHz, $CDCl_3$): δ (ppm) = 159.33 (C_{Ar}), 147.28 (C_{Ar}), 131.55 (C_{Ar}), 130.12 (C_{Ar}), 122.29 (C_{Ar}), 121.76 (C_{Ar}), 118.35 (C_{Ar}), 115.17 (C_{Ar}), 68.42 (OCH_2), 31.95 (CH_2), 29.74 (CH_2), 29.69 (CH_2), 29.65 (CH_2), 29.49 (CH_2), 29.39 (CH_2), 29.24 (CH_2), 26.06 (CH_2), 22.71 (CH_2), 14.14 (CH_3). **MS** (EI, T = 37°C - 50 °C)**:** *m/z* = 1314.19 (calcd 1313.99 for $[M + H^+]$).

5. Copies of Spectral Data (^{1}H-NMR, ^{13}C-NMR) of Dendrimers

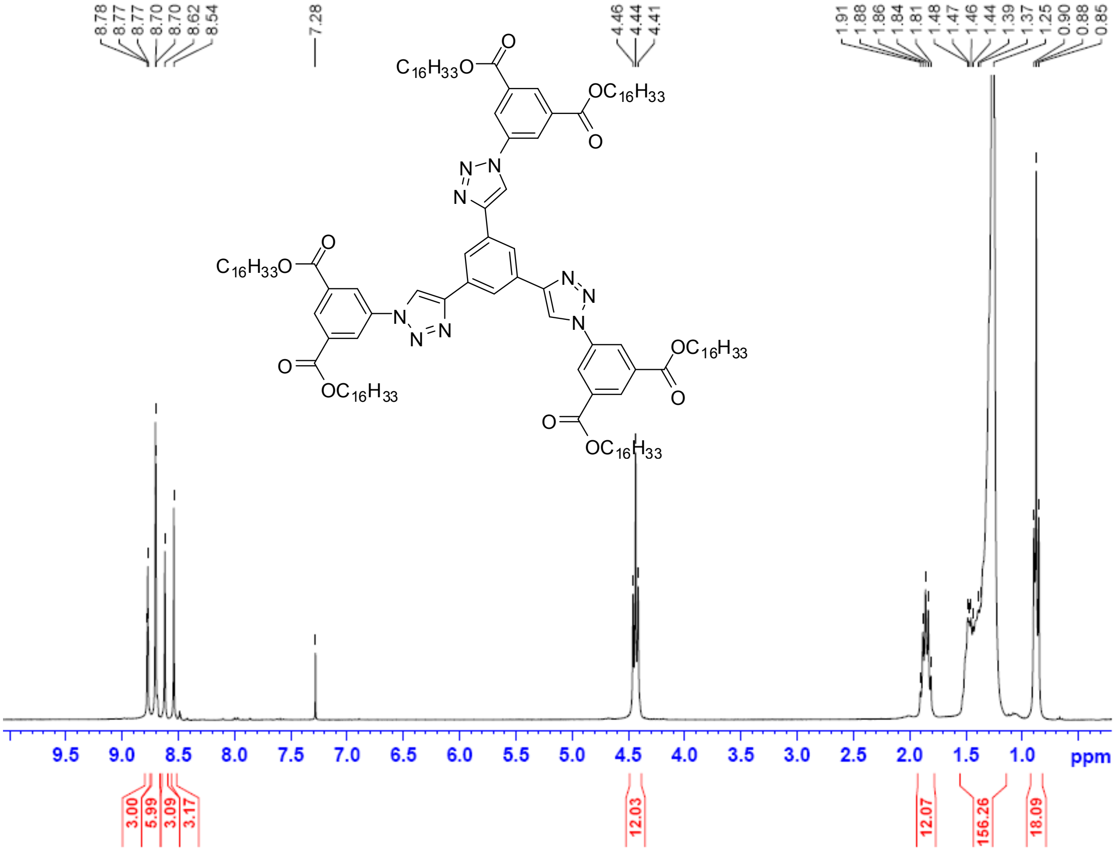

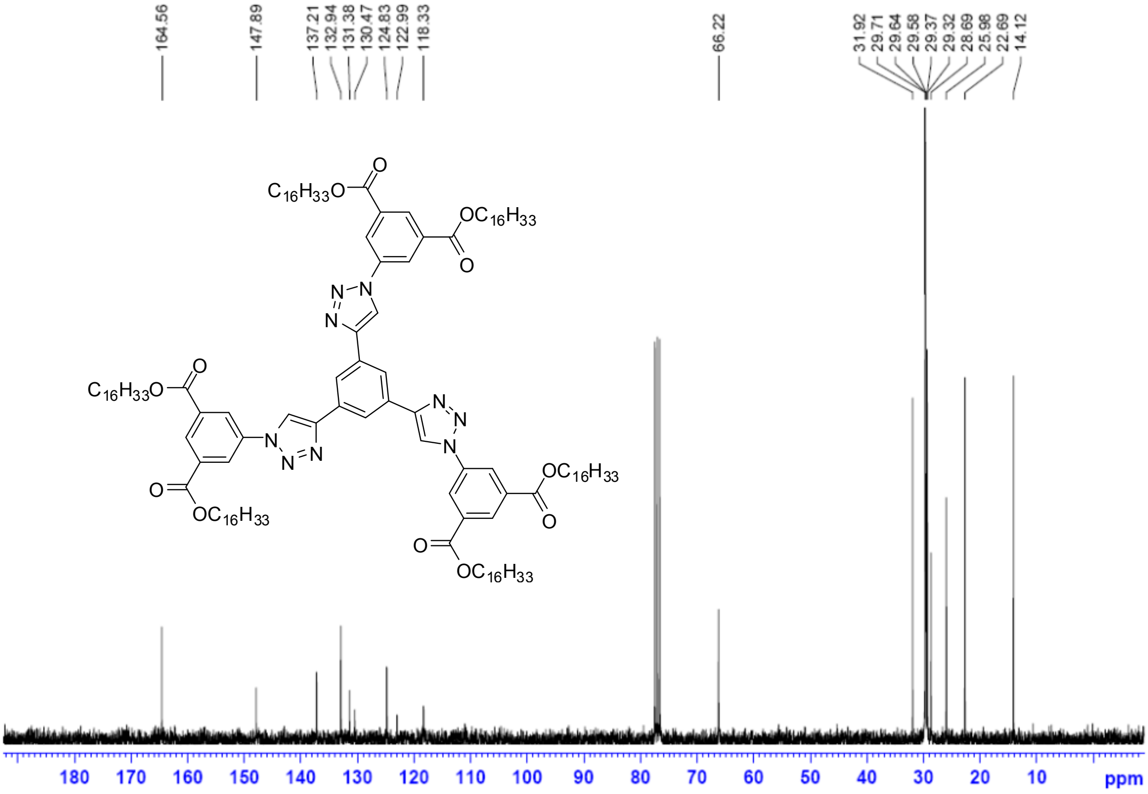

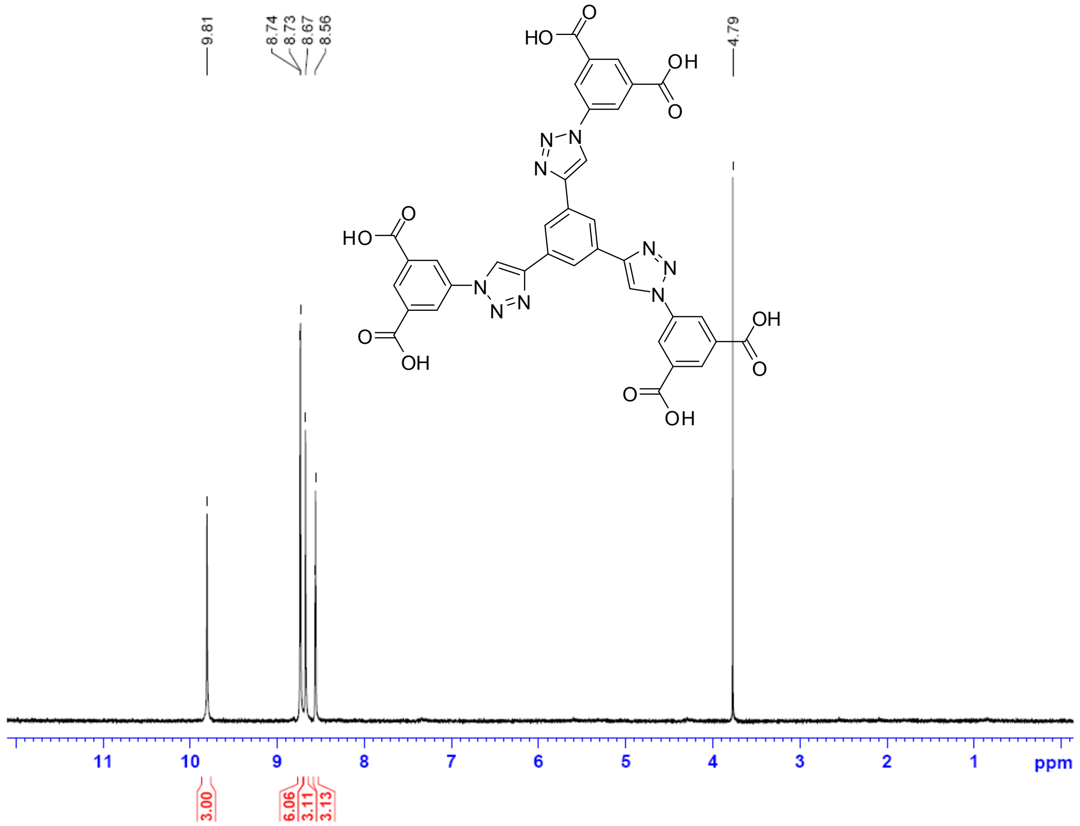
9.81
8.74
8.73
8.67
8.56
4.79
HO
O
OH
N
11
10
9
8
7
6
5
4
3
2
1
ppm
3.00
6.06
3.11
3.13

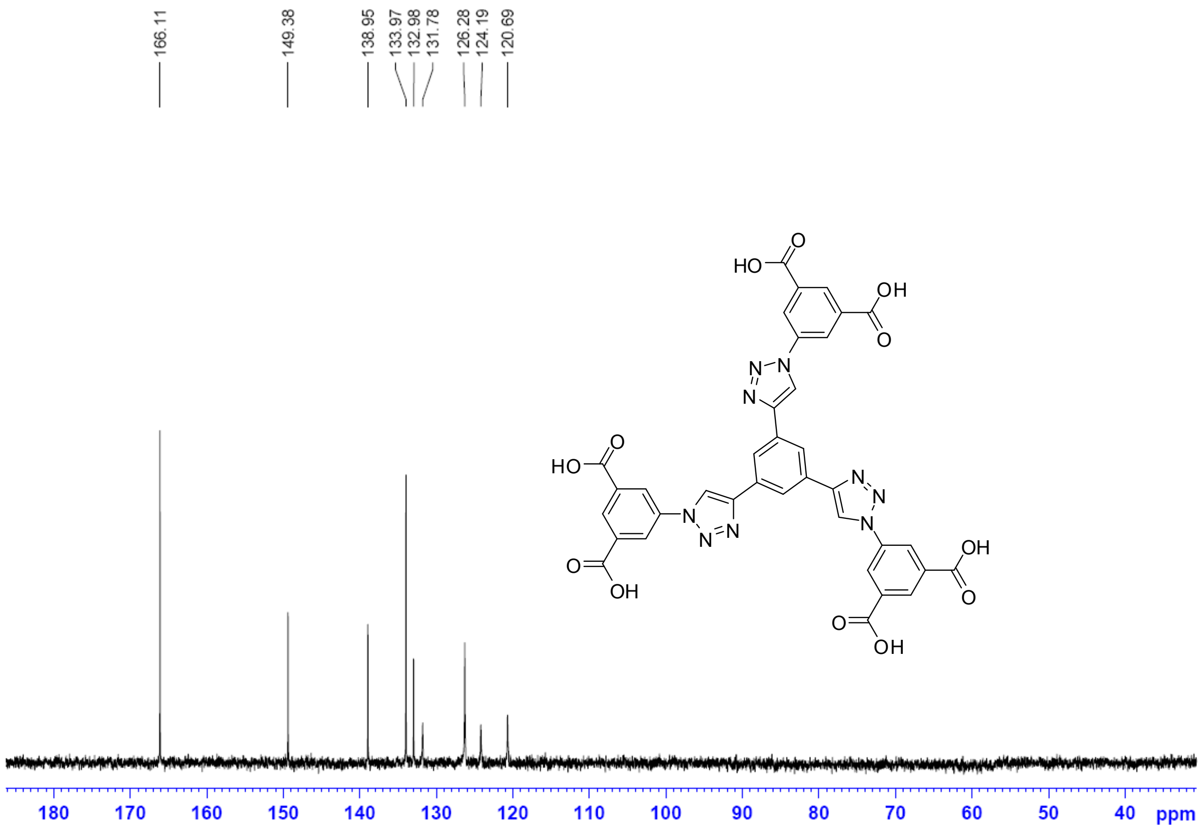
166.11
149.38
138.95
133.97
132.98
131.78
126.28
124.19
120.69
HO
O
OH
N
180
170
160
150
140
130
120
110
100
90
80
70
60
50
40
ppm

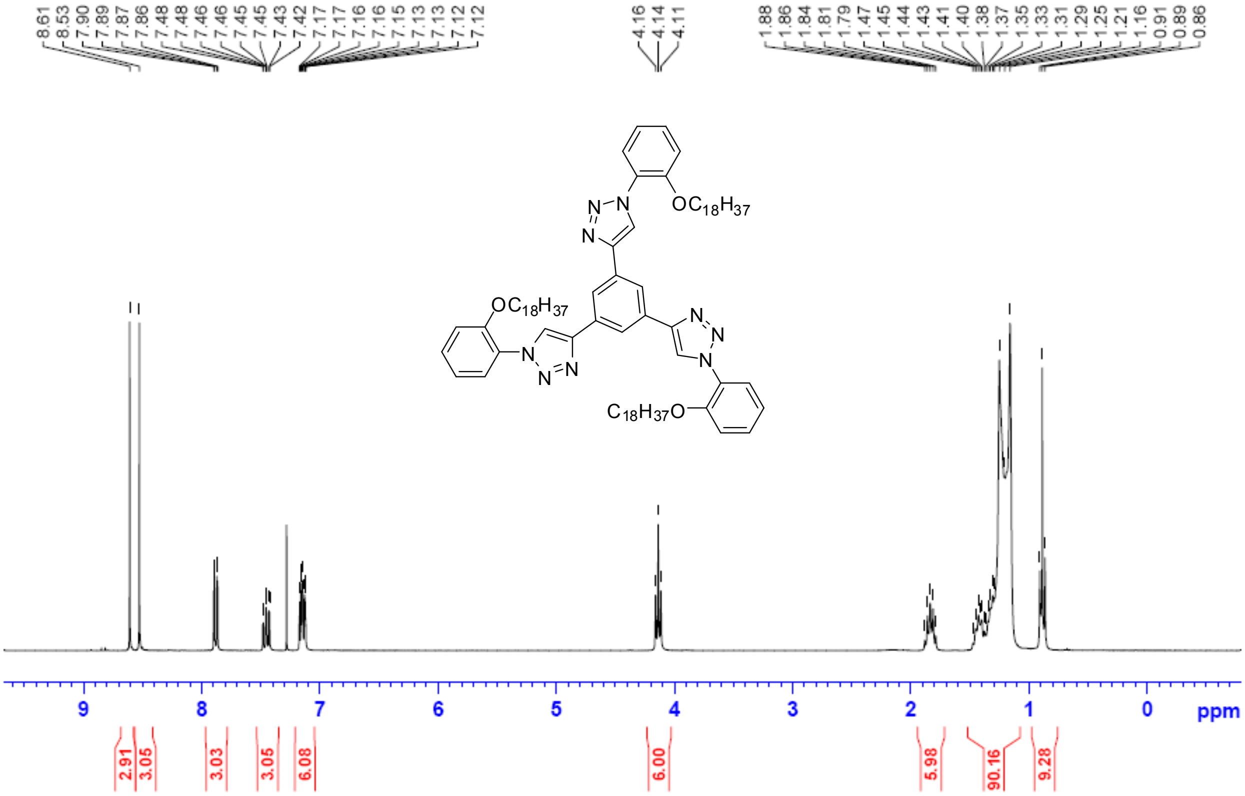
8.61
8.53
7.90
7.89
7.87
7.86
7.48
7.48
7.46
7.45
7.45
7.43
7.42
7.17
7.17
7.16
7.15
7.13
7.13
7.12
7.12
4.16
4.14
4.11
1.88
1.86
1.84
1.81
1.79
1.47
1.45
1.44
1.43
1.41
1.40
1.38
1.37
1.35
1.33
1.31
1.29
1.25
1.21
1.16
0.91
0.89
0.86
N
N
N
OC18H37
OC18H37
N
N
N
N
N
N
C18H37O
9
8
7
6
5
4
3
2
1
0
ppm
2.91
3.05
3.03
3.05
6.08
6.00
5.98
90.16
9.28

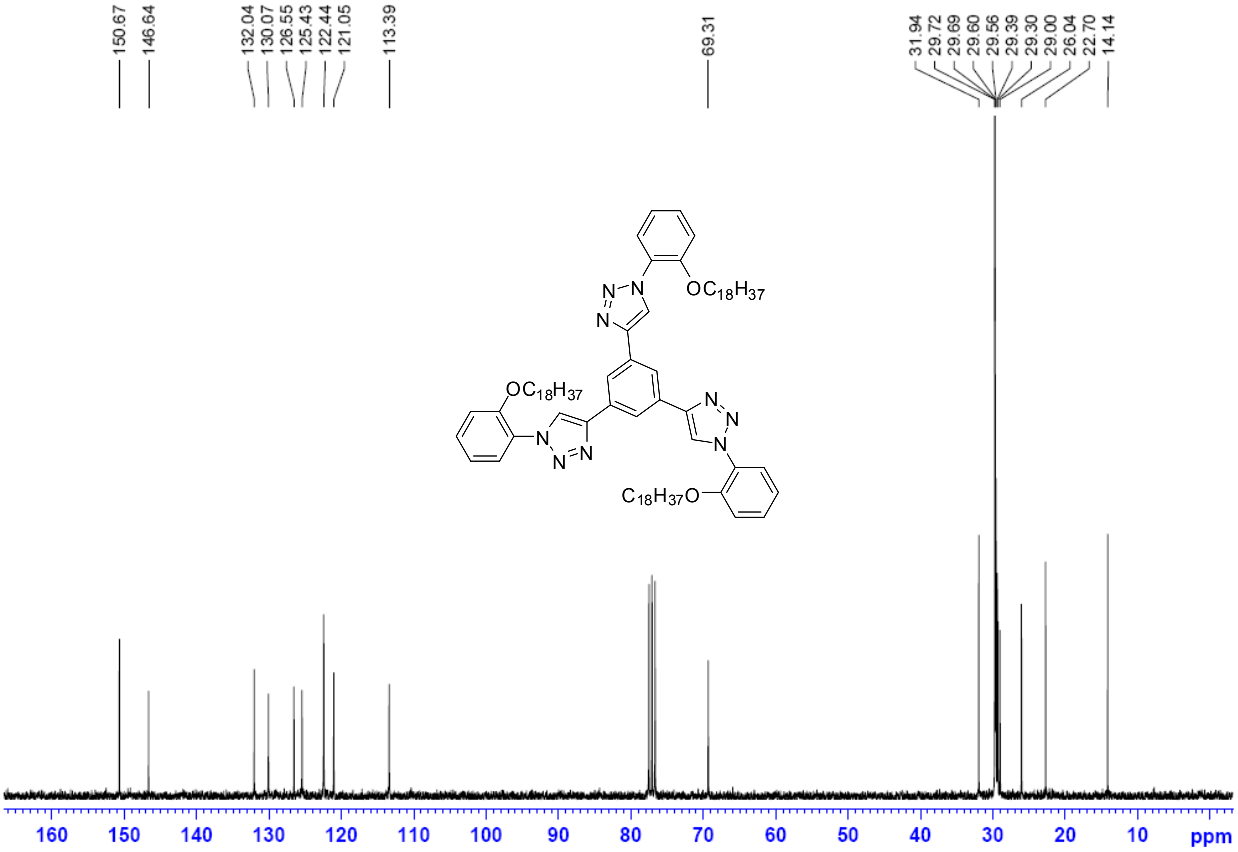
150.67
146.64
132.04
130.07
126.55
125.43
122.44
121.05
113.39
69.31
31.94
29.72
29.69
29.60
29.56
29.39
29.30
29.00
26.04
22.70
14.14
N
N
N
OC18H37
OC18H37
N
N
N
N
N
N
C18H37O
160
150
140
130
120
110
100
90
80
70
60
50
40
30
20
10
ppm

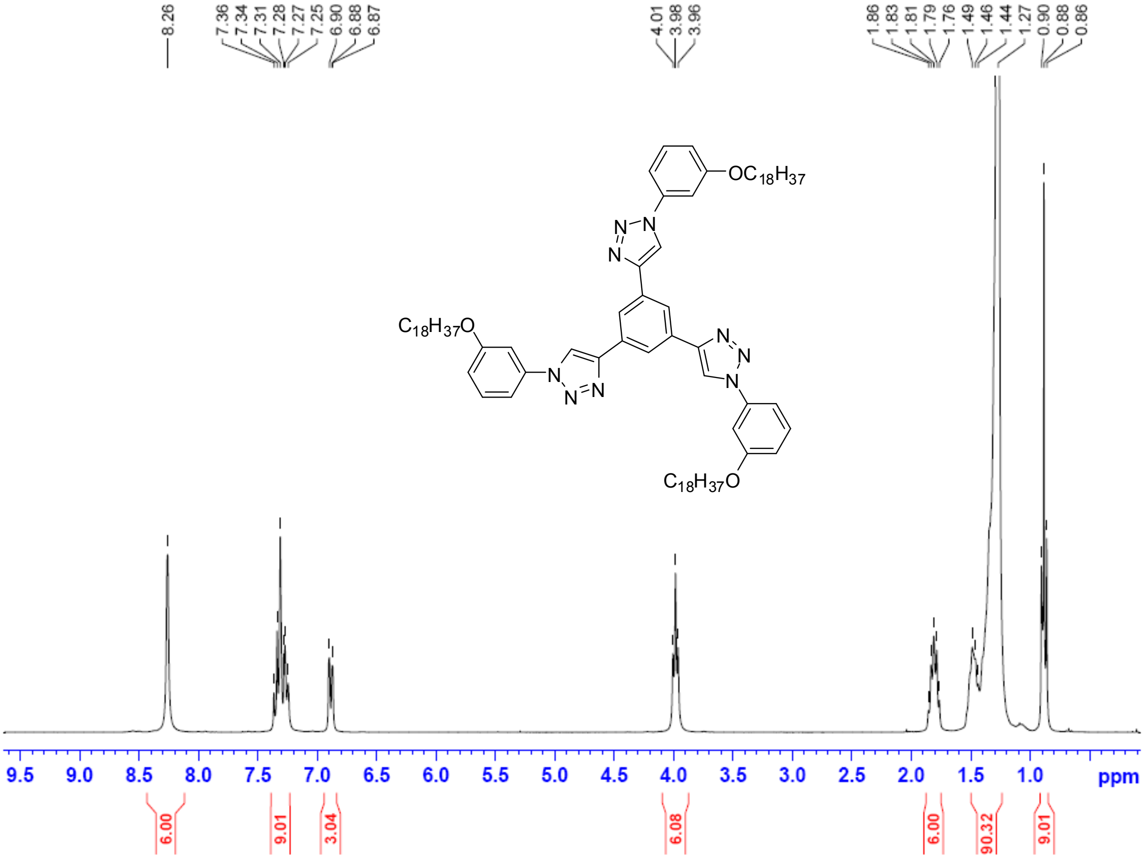
8.26
7.36
7.34
7.31
7.28
7.27
7.25
6.90
6.88
6.87
4.01
3.98
3.96
1.86
1.83
1.81
1.79
1.76
1.49
1.46
1.44
1.27
0.90
0.88
0.86
OC18H37
C18H37O
C18H37O
N
N
N
9.5
9.0
8.5
8.0
7.5
7.0
6.5
6.0
5.5
5.0
4.5
4.0
3.5
3.0
2.5
2.0
1.5
1.0
ppm
6.00
9.01
3.04
6.08
6.00
90.32
9.01

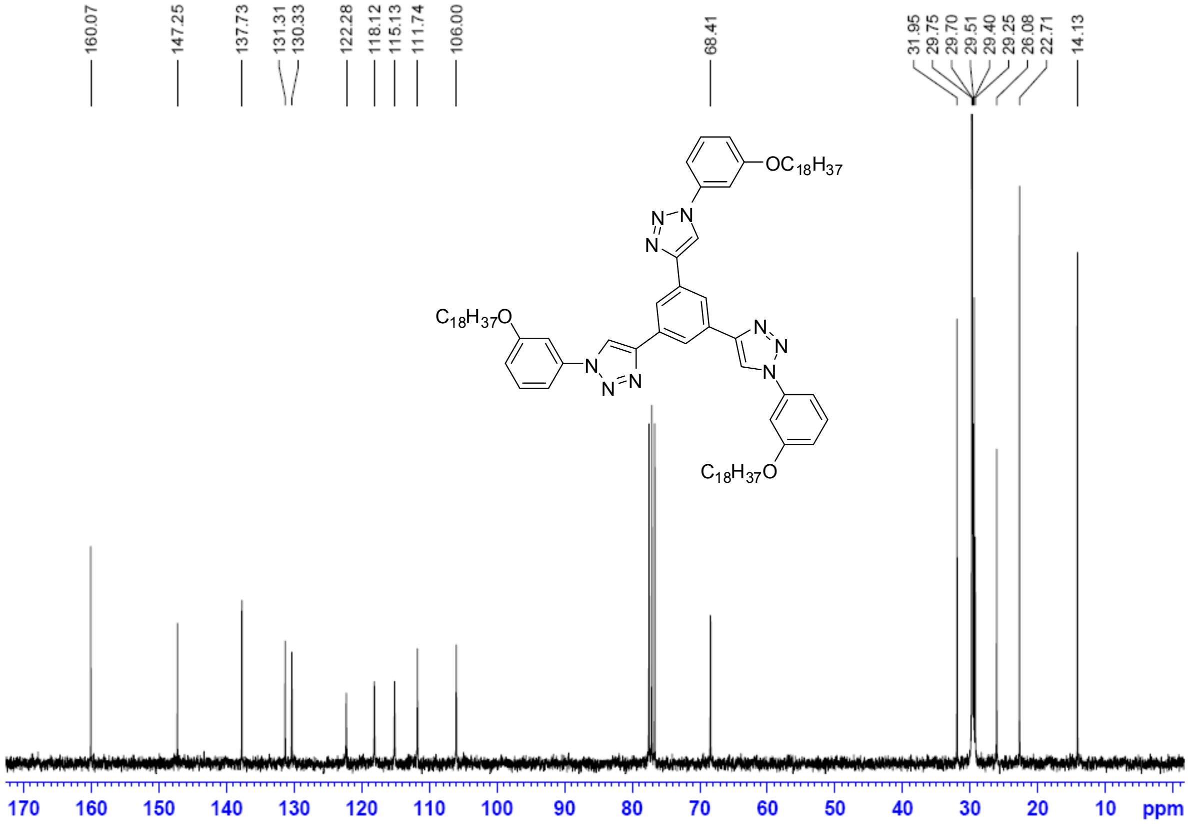
160.07
147.25
137.73
131.31
130.33
122.28
118.12
115.13
111.74
106.00
68.41
31.95
29.75
29.70
29.51
29.40
29.25
26.08
22.71
14.13
OC18H37
C18H37O
C18H37O
N
N
N
170
160
150
140
130
120
110
100
90
80
70
60
50
40
30
20
10
ppm

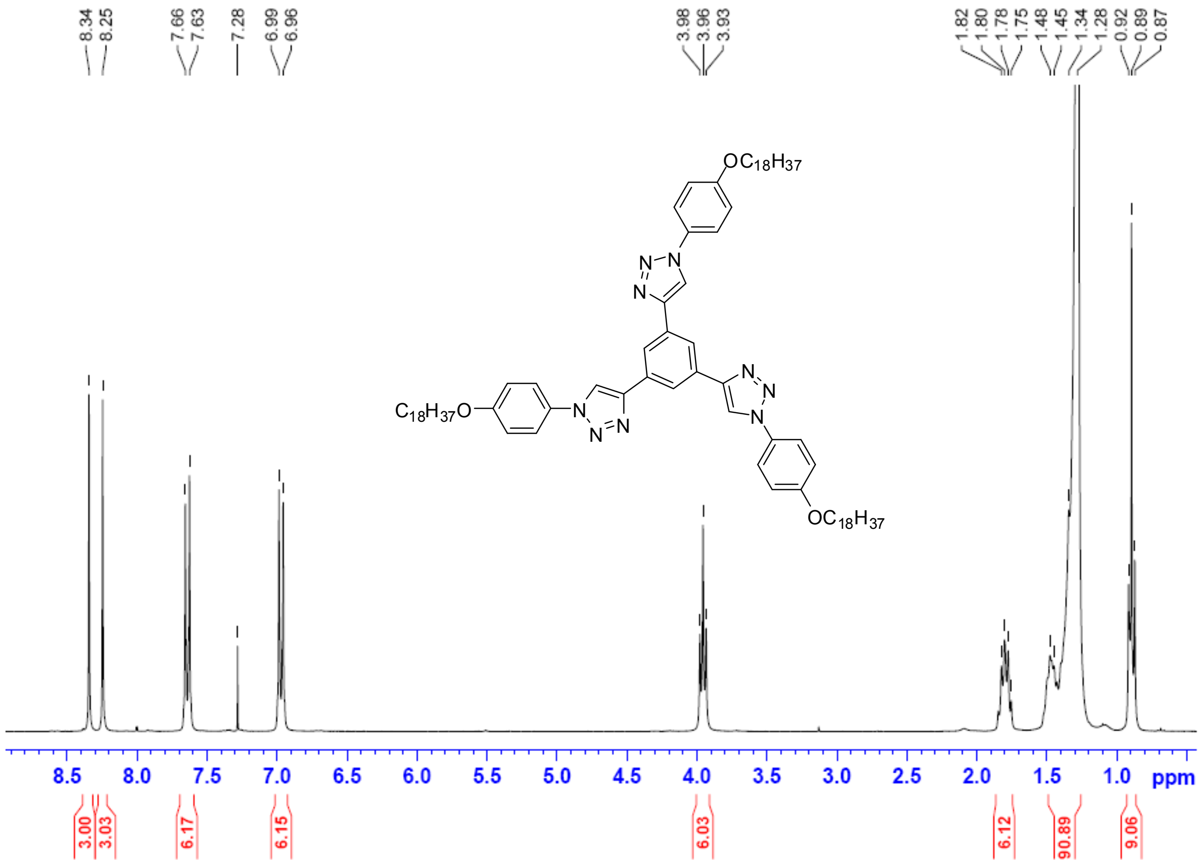
8.34
8.25
7.66
7.63
7.28
6.99
6.96
3.98
3.96
3.93
1.82
1.80
1.78
1.75
1.48
1.45
1.34
1.28
0.92
0.89
0.87
OC18H37
N
N
N
C18H37O
N
N
N
N
N
N
OC18H37
8.5
8.0
7.5
7.0
6.5
6.0
5.5
5.0
4.5
4.0
3.5
3.0
2.5
2.0
1.5
1.0
ppm
3.00
3.03
6.17
6.15
6.03
6.12
90.89
9.06

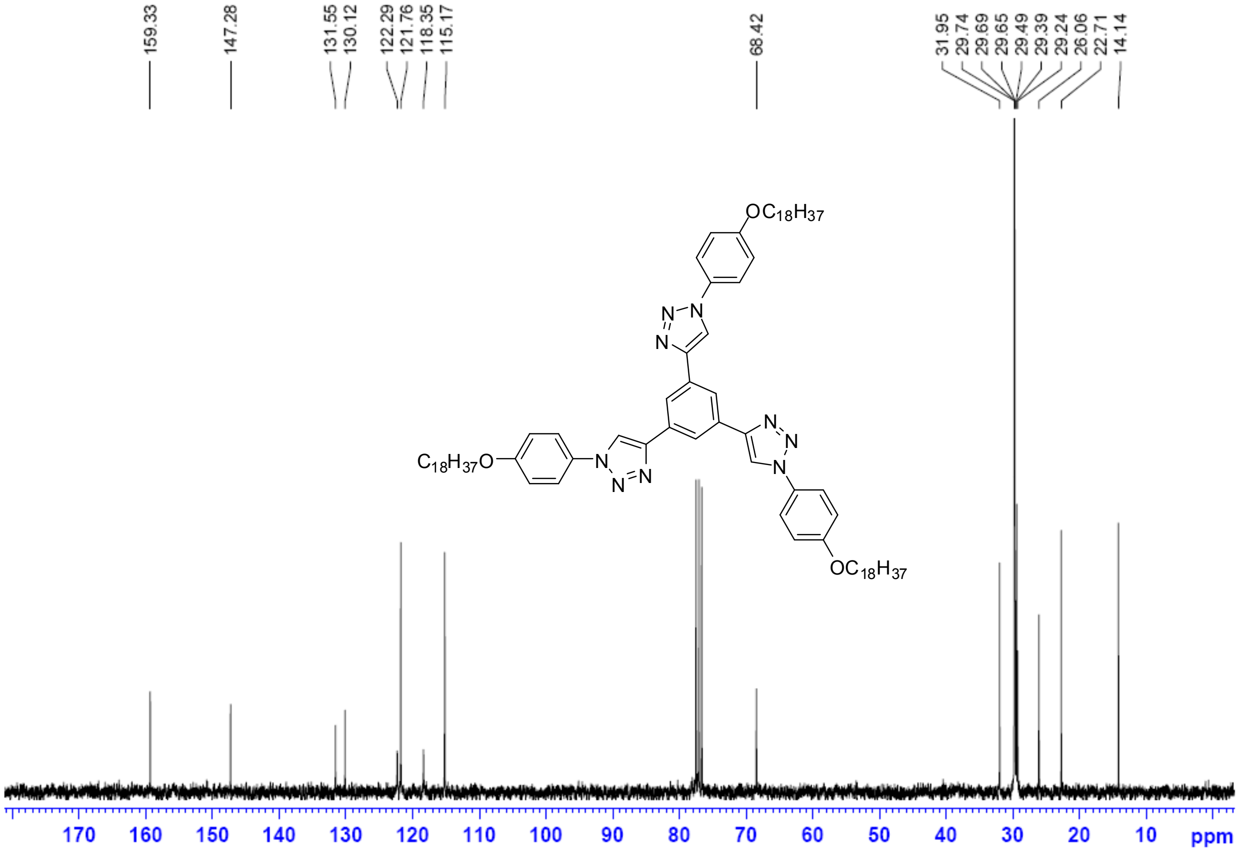
159.33
147.28
131.55
130.12
122.29
121.76
118.35
115.17
68.42
31.95
29.74
29.69
29.65
29.49
29.39
29.24
26.06
22.71
14.14
OC18H37
N
N
N
C18H37O
N
N
N
N
N
N
OC18H37
170
160
150
140
130
120
110
100
90
80
70
60
50
40
30
20
10
ppm

Annex 3: synthesis of SCs

General methods

All reagents were analytical grade and used as received. The solvents were carefully dried and freshly distilled prior to use according to common laboratory practice. All reactions were performed under dry Argon atmosphere using standard Schlenk techniques. Flash chromatography was performed with silica gel 60 (particle size 63 – 200 µm, 230 – 400 mesh, Merck®). ^{1}H NMR spectra were recorded at 295 K using a Bruker Avance 400 spectrometer at 400 MHz. The chemical shifts (∂) are given in ppm and the residual solvent peak was used as reference for calibration. Peaks are described as singlet (s), doublet (d), triplet (t), quartet (q), and multiplet (m), broad (br).

Synthesis of sc9

5-(Dodec-1-ynyl)pyrimidin-2-amine (sc9) was prepared from 2-amino-5-iodopyrimidine by a Sonogashira coupling, according with the reported procedure.[i]

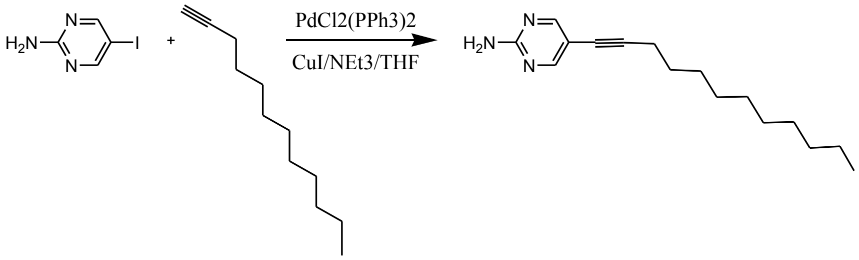

Scheme S1. Synthesis of sc9.

To a mixture of 2-amino-5-iodopyrimidine (0.8 g, 3.6 mmol), PdCl2(PPh3)2 (0.13 g, 0.18 mmol) and CuI (0.034 g, 0.18 mmol) in Et3N (10 mL) and THF (10 mL) under nitrogen atmosphere was added 1-dodecyne (1.5 ml, 7.2 mmol), then heated at reflux for 36 h. After removal of the solvent, the residue was purified by column chromatography (silica gel, CHCl3) and recrystallized from hexane to give sc9 as yellow solid (0.726 g, 78%).

1H-NMR (CDCl3, 400 MHz) ∂: 0.91 (3H, t, CH3), 1.27-1.37 (12H, m, CH2), 1.42-1.48 (2H, m, CH2), 1.57-1.64 (2H, m, CH2), 2.41 (2H, t, CH2), 5.29 (2 H, br s, NH2), 8.34 (2

H, s, ArH) ppm. MS (m/z) $[M]^+$: 236.

Synthesis of sc10 (5)

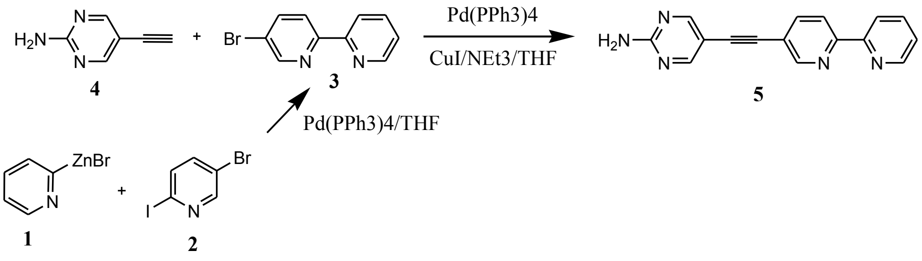

Scheme S1. Synthesis of sc10.

Commercially available 5-brome-2-aminopyrimidine was treated with TMS-acetylene under Sonogashira conditions followed by cleavage of the terminal silane, yielding alkynylpyrimidine 4.[ii] 5-Bromo-2,2'-bipyridine (3) was prepared by palladium catalyzed coupling reaction of a stable 2-pyridylzinc bromide (1) with 2-Bromo-5-iodopyridine (2), according with the reported procedure.[iii] The obtained Bromo-bipyridine was then coupled with 2-amino-5-iodopyrimidine (4) under Sonogashira coupling condition to give 5-(Dec-1-ynyl)pyrimidin-2-amine (5).

Synthesis of 4. Into a 250 mL round-bottom flask were placed 2-amino-5-iodopyrimidine (2.0 g, 13 mmol), acetonitrile (40 mL), triethylamine (10 mL), TMS-acetylene (2.6 g, 27 mmol), PdCl2(PPh3)2 (0.437 g, 0.06 mmol), and CuI (0.115 g, 0.06 mmol). The vessel was filled with argon and allowed to stir at room temperature for 12 h. The solvent was evaporated and the product was purified via flash chromatography on silica with a mixture of CHCl3 and EtOAc 9:1. The resulting product was in dry methanol (100ml). Excess potassium carbonate (2 equiv) was added, and the mixture was stirred overnight at room temperature. Activated charcoal was added and the mixture was filtered through Celite. The filtrate was concentrated under reduced pressure to afford a tan solid, which was added to a solution of 10% methanol in water (50 mL). The resulting precipitate was isolated by filtration and dried in a vacuum oven to constant mass to afford 4 (0.9 g, 57%): 1H NMR (400 MHz, CDCl3): 3.21 (1H, s), 5.33 (2H, br s), 8.43 (2H, s) ppm.

Synthesis of 3. In a 50mL round-bottomed flask, Pd[P(Ph)3]4 (0.10g,1mol%) was placed. Next, 20mL of 0.5M solution of 2-pyridylzinc bromide(1) in THF was added into the flask at rt. 2-Bromo-5-iodopyridine (2) (2.26g, 8mmol) dissolved in 5.0mL of THF was added via a syringe. The resulting mixture was stirred at rt for 24h. Quenched with saturated NH4Cl solution, then extracted with CH2Cl2(30mL x 3). Combined organics were washed with saturated Na2S2O3 solution and brine. Dried over anhydrous Na2SO4. A flash column chromatography(Hexane: EtOAc = 9:1) and recrystallization of the product from hot hexane gave 1.3g of 5-bromo-2,2'-bipyridine(4b) as a white solid in 72% isolated yield. 1H-NMR (CDCl3, 400 MHz) ∂: 7.33-7.36 (1H, m), 7.84 (1H, td), 7.96 (1H, dd), 8.34 (1H, d),8.39 (1H, d), 8.69 (1H, d), 8.74 (1H, d) ppm.

Synthesis of 5. To a mixture of 5-Bromo-2,2'-bipyridine (3) (152 mg, 0.65 mmol), Pd(PPh3)4 (38 mg, 0.032 mmol) and CuI (6.1 mg, 0.032 mmol) in Et3N (3 mL) and THF (3 mL) under nitrogen atmosphere was added 5-ethynylpyrimidin-2-amine (80 mg, 0.68 mmol), then heated at reflux for 48 h. After removal of the solvent, the residue was extracted with dichloromethane and water. The organic layer was collected, dried over $MgSO_4$ and evaporated. PPh3 was precipitated and filtrated from ethyl acetate. The solvent was evaporated and the residue recrystallized from ethanol to give sc10 as white solid (80 mg, 20%).

1H-NMR (DMSO, 400 MHz) ∂: 5.29 (2H, br s), 7.37 (1H br s), 7.87 (1H, t), 7.95 (1H, d), 8.47 (2H br s), 8.53 (2H, s), 8.33-8.83 (2H, br m) ppm.

---

[i] Yosuke Hisamats, Naohiro Shirai, Shin-ichi Ikeda, and Kazunori Odashima, Org.Lett., 11, 2009, 4342
[ii] Victor J. Cee et al., J. Med. Chem. 2007, 50, 627-640.
[iii] Seung-Hoi Kim, Reuben D. Rieke, Tetrahedron Letters 50 (2009) 5329–5331.

Annex 4 – synthesis and characterization of porphyrins

Synthesis & Characterization

4'-(5,5-dimethyl-1,3,2-dioxaborinan-2-yl)-2,2':6',2''-terpyridine

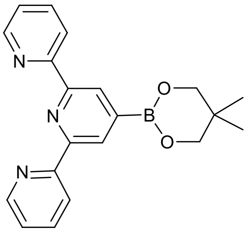

Chemical Formula: $C_{20}H_{20}BN_3O_2$
Molecular Weight: 345.20 g.mol^{-1}
The synthesis was achieved according to the described procedure[12]. Under argon, a solution of bis(neopentyl glycolato)boron (542 mg, 2.4 mmol, 1.5 eq), 4'-bromoterpyridine (500 mg, 1.6 mmol, 1 eq), dry KOAc (471 mg, 4.8mmol, 3 eq) and Pd(dppf)Cl_2 (35 mg, 0.048 mmol, 0.03 eq) in dry DMSO (12 mL) was heated a 80 °C for 6h. The solution was cooled to room temperature and diluted with toluene (100 mL). The organic layer was washed with water (3 x 100 mL), dried over $MgSO_4$, filtered, and the solvent was removed under reduced pressure. The beige solid was washed with ethanol (2 x 10 mL) and dried to afford the product as a tan solid (250 mg, 45 %)

^{1}H-NMR (300 MHz, $CDCl_3$) δ: 1.04 (s, 6H, H_1), 3.60 (s, 4H, H_2), 7,32 (ddd, J = 7.5, 4.8 and 1.1 Hz, 2H, H_6), 7.85 (ddd, J = 7.9, 7.5 and 1.8 Hz, 2H, H_5), 8.61 (dd, J = 7.9 and 1.1 Hz, 2H, H_4), 8.73 (m, 2H, H_7), 8.80 (s, 2H, H_3).

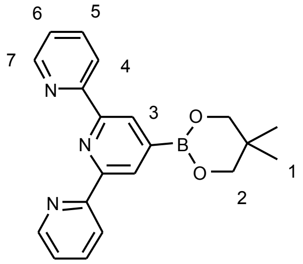

5,15-dimesityl-10-(pyridin-4-yl)-20-(4-(2,2',6,2-terpyridyl))porphyrin (1)

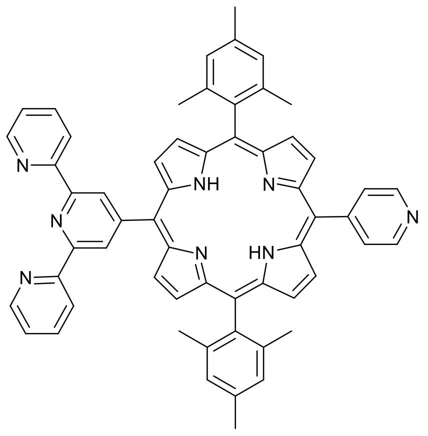

Chemical Formula: $C_{58}H_{46}N_8$
Molecular Weight: 855.04 g.mol^{-1}

5,15-dimesityl-10-(pyridin-4-yl)-20-bromoporphyrin **9** (50 mg, 0.071 mmol, 1eq), 4'-(5,5-dimethyl-1,3,2-dioxaborinan-2-yl)-2,2':6',2''-terpyridine (40 mg, 0.11 mmol, 1.6 eq) and caesium carbonate (21 mg, 0.064 mmol, 0.9 eq) were dissolved in dry DMF (80 mL) and flushed with argon for 30 minutes. $Pd(PPh_3)_4$ (8.5 mg, 0.007 mmol, 0.1 eq) was added and the mixture was heated at 110 °C for 20h. The solvent was evaporated under reduced pressure and the dark mixture was dissolved in $CHCl_3$ (40 mL) and washed with water (3 x 40 mL). The organic phase was dried over $MgSO_4$, filtered and evaporated under reduced pressure. The product was purified by column chromatography (silica gel, CH_2Cl_2/acetone 85:15). The pure product was obtained as a purple solid (50 mg, 82 %).

^{1}H-NMR (300 MHz, $CDCl_3$) δ: -2.58 (s, br, 2H, NH), 1.90 (s, 12H, CH_{3ortho}), 2.65 (s, 6H, CH_{3para}), 7.32 (s, 4H, $H_{méta}$), 7.40 (ddd, *J* = 7.5, 4.8 and 1.3 Hz, 2H, H_6), 8.01 (dd, *J* = 7.5, 7.5 Hz, 2H, H_5), 8.23, (dd, *J* = 4.4 and 1.5 Hz, 4H, H_2), 8.73 (d, *J* = 4.8 Hz, 2H, H_7), 8.77 (d, *J* = 4.8 Hz, 2H, $H_{\beta pyrrol}$), 8.81 (s, 4H, $H_{\beta pyrrol}$), 8.94 (d, *J* = 4.8 Hz, 2H, $H_{\beta pyrrol}$), 8.97-9.07 (m, 4H, H_1 et H_4), 9.38 (s, 2H, H_3).

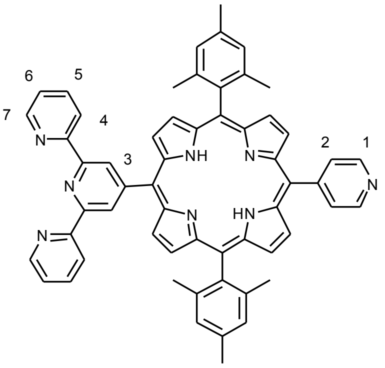

^{13}C-NMR (90 MHz, $CDCl_3$) δ: 21.49 (CH_3), 21.68 (CH_3), 116.00 (C), 117.21 (C), 119.08 (C), 121.87 (CH), 124.05 (CH), 126.28 (CH), 127.85 (CH), 129.45 (CH), 137.05 (CH), 137.94 (CH), 138.11 (C), 139.37 (C), 148.19 (CH), 149.34 (CH), 150.44 (C), 152.27 (C), 153.88 (C), 156.26 (C).

λ_{max} (CH_2Cl_2)/nm (ε x 10^4/L mol^{-1} cm^{-1}) 419 (47.21), 514 (1.84), 548 (0.57), 589 (0.54), 645 (0.28).

ν_{max} (ATR)/cm^{-1} 2962, 1583, 1566, 1542, 1467, 1439, 139, 1343, 1262, 1200, 1185, 1117, 1089, 1072, 1016, 973, 948, 913, 882, 851, 800, 741, 666, 659.

m/z (HRM$^+$) $[M+H^+]_{calc}$ = 855.392, $[M+H^+]_{found}$ = 855.389.

5,15-dimesityl-10-(pyridin-4-yl)-20-bromoporphyrinato Ni(II)

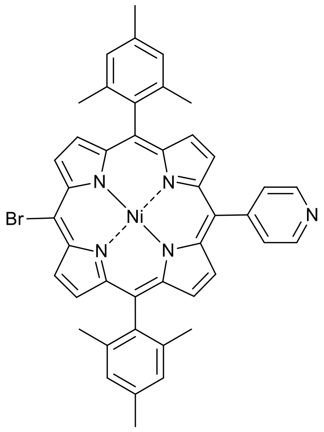

Chemical Formula: $C_{43}H_{34}BrN_5Ni$
Molecular Weight: 759.36 $g.mol^{-1}$
5,15-dimesityl-10-(pyridin-4-yl)-20-bromoporphyrin **9** (200 mg, 0.28 mmol, 1 eq) and nickel acetate tetrahydrate (250 mg, 1 mmol, 3.6 eq) in DMF (50 mL) were heated at 120 °C for 3h. The solvent was evaporated under reduced pressure and the dark solid was dissolved in $CHCl_3$ (100 mL) and washed with water (2 x 100 mL). The organic phase was dried over $MgSO_4$, filtered and evaporated under reduced pressure to afford the compound as a purple/red solid (205 mg, 95 %).

^{1}H-NMR (300 MHz, $CDCl_3$) δ: 1.80 (s, 12H, CH_{3ortho}), 2.58 (s, 6H, CH_{3para}), 7.22 (s, 4H, $H_{méta}$), 8.00 (br, 2H, H_2), 8.61 (s, 4H, $H_{\beta pyrrol}$), 8.67 (d, *J* = 4.9 Hz, 2H, $H_{\beta pyrrol}$), 9.01 (br, 2H, H_1), 9.52 (d, *J* = 5.1 Hz, 2H, $_{\beta pyrrol}$).

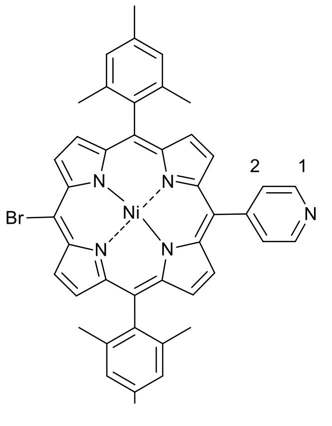

^{13}C-NMR (90 MHz, $CDCl_3$) δ: 21.36 (CH_3) 21.44 (CH_3), 102.63 (CBr), 118.43 (C), 127.89 (CH), 132.22 (CH), 132.42 (CH), 132.76 (CH), 134.07 (CH), 136.60 (C), 138.04 (C), 138.93 (C), 142.86 (C), 142.96 (C), 143.52 (C).

λ_{max} (CH_2Cl_2)/nm (ε x 10^4/L mol^{-1} cm^{-1}) 415 (25.88), 530 (1.82), 564 (0.39).

ν_{max} (ATR)/cm^{-1} 2921, 1605, 1457, 1437, 1329, 1264, 1232, 1205, 1072, 1003, 990, 855, 831, 790, 719, 668

m/z (HRM$^+$) $[M+H^+]_{calc}$ = 759.146 $[M+H^+]_{found}$ = 759.141.

5,15-dimesityl-10-(pyridin-4-yl)-20-(4-ethynylterpyridine) porphyrinato Ni(II) (3)

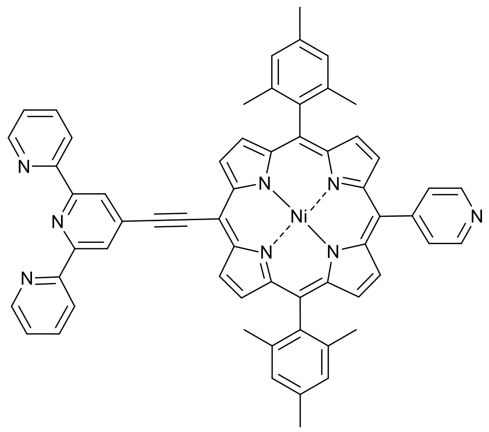

Chemical Formula: $C_{60}H_{44}N_8Ni$
Molecular Weight: 935.74 g.mol^{-1}

In a schlenck tube, a solution of 5,15-dimesityl-10-(pyridin-4-yl)-20-bromoporphyrin **Ni-9** (108 mg, 0.143 mmol, 1 eq), 4-etyhnil terpyridine[13] (74.2 mg, 0.28 mmol, 2 eq), $Pd(PPh_3)_2Cl_2$ (9.8 mg, 0.014 mmol, 0,1 eq) and CuI (4 mg, 0.021 mmol, 0.1 5eq) were added. Degassed triethylamine (3 mL) and dry THF (7 mL) was added and the mixture was heated at 75 °C for 1h. The mixture was cooled to room temperature and the solvent was evaporated under reduced pressure. The product was washed with methanol (3 x 10 mL) and purified by column chromatography (Al_2O_3, CH_2Cl_2) to afford the pure compound as a purple/green solid (100 mg, 97%).

^{1}H-NMR (300 MHz, $CDCl_3$) δ: 1.82 (s, 12H, CH_{3ortho}), 2.58 (s, 6H, CH_{3para}), 7.23 (s, 4H, $H_{méta}$), 7.36-7.42 (m, 2H, H_6), 7.90 (ddd, *J* = 7.5, 7.5 and 1.3 Hz, 2H, H_5), 7.98 (d, *J* = 4.2 Hz, 2H, H_2), 8.55-8.60 (m, 4H, $H_{\beta pyrrol}$), 8.65-8.75 (m, 4H, $H_{\beta pyrrol}$ and H_7), 8.79 (d, *J* = 4.2 Hz, 2H, H_1), 8.94 (s, 2H, H_3), 8.99 (br, 2H, H_4), 9.68 (d, *J* = 4.9 Hz, 2H, $H_{\beta pyrrol}$).

^{13}C-NMR (90 MHz, $CDCl_3$) δ: 21.37 (CH_3), 21.47 (CH_3), 97.85 (C), 118.97 (C), 121.25 (CH), 121.44 (CH), 122.71 (CH), 123.53 (CH), 124.18 (CH), 127.93 (CH), 128.66 (CH), 131.82 (CH), 132.12 (CH), 132.46 (CH), 132.70 (CH), 136.64 (CH), 136.94 (CH), 137.06 (CH), 138.03, 138.92 (C), 141.60 (C), 142.83 (C), 143,47 (C), 145.38 (C), 148.29 (C), 149.29 (CH), 155.83 (C).

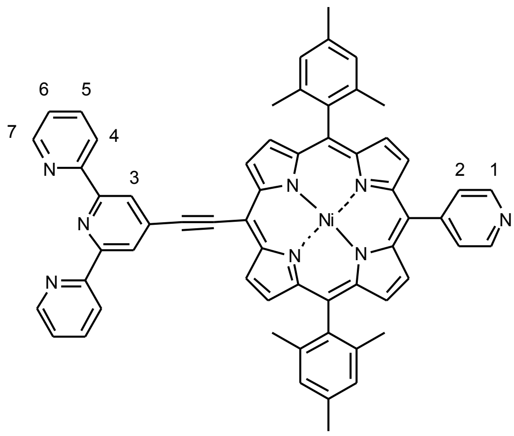

λ_{max} (CH_2Cl_2)/nm (ε x 10^4/L mol^{-1} cm^{-1}) 432 (20.15), 544 (1.31), 581 (1.42).

ν_{max} (ATR)/cm^{-1} 3326, 2327, 2201, 1594, 1581, 1537, 1467, 1391, 1347, 1262, 1203, 1117, 1073, 1040, 1003, 880, 850, 795, 745, 731, 705.

m/z (HRM$^+$) $[M+H^+]_{calc}$ = 935.312 $[M+H^+]_{found}$ = 935.312.

5,15-dimesityl-10-bromoporphyrinato Ni(II)

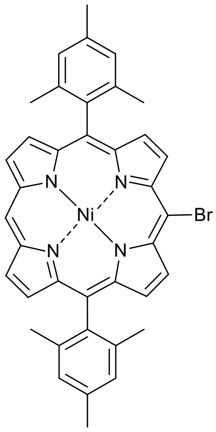

Chemical Formula: $C_{38}H_{31}BrN_4Ni$
Molecular Weight: 682.28 g.mol^{-1}
A solution of 5,15-dimesityl-10-bromoporphyrin **7** (100 mg, 0.16 mmol, 1 eq) and nickel acetate tetrahydrate (125 mg, 0.5 mmol, 3,1 eq) in DMF (30 mL) was refluxed for 3h. The solvent was evaporated under reduced pressure and the dark solid was dissolved in $CHCl_3$ (100 mL) and washed with water (2 x 100 mL). The organic phase was dried over $MgSO_4$, filtered and evaporated under reduced pressure to afford the compound as a purple/red solid (105 mg, 95 %).

^{1}H-NMR (300 MHz, $CDCl_3$) δ: 1.85 (s, 12H, CH_{3ortho}), 2.64 (s, 6H, CH_{3para}), 7.29 (s, 4H, $H_{méta}$), 8.73 (d, *J* = 4.5 Hz, 4H, $H_{βpyrrol}$), 9.06 (d, *J* = 4.7 Hz, 2H, $H_{βpyrrol}$), 9.59 (d, *J* = 4.7 Hz, 2H, $H_{βpyrrol}$), 9.76 (s, 1H, $H_{méso}$).

^{13}C-NMR (90 MHz, $CDCl_3$) δ: 21.37 (CH_3), 21.44 (CH_3), 102.59 ($CBr_{méso}$), 104.84 (CH), 117.63 (C), 127.83 (CH), 131.91 (CH), 132.04 (CH), 132.84 (CH), 133.44 (CH), 136.89 (C), 137.88 (C), 138.99 (C), 142.28 (C), 142.82 (C), 143.26 (C), 143.34 (C).

$λ_{max}$ (CH_2Cl_2)/nm (ε x 10^4/L mol^{-1} cm^{-1}) 409 (23.46), 524 (1.66), 555 (0.41).

$ν_{max}$ (ATR)/cm^{-1} 2963, 2915, 2359, 1608, 1559, 1471, 1404, 1374, 1333, 1261, 1195, 1147, 1093, 1049, 1018, 966, 855, 846, 817, 793, 785, 738, 719, 689.

m/z (HRM$^+$) $[M+H^+]_{calc}$ = 680.108, $[M+H^+]_{found}$ = 680.112.

5,15-dimesityl-10-(pyridin-4-ylethynyl)porphyrinato Ni(II)

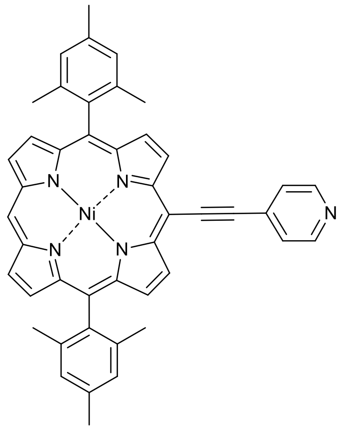

Chemical Formula: $C_{45}H_{35}N_5Ni$
Molecular Weight: 704.49 g.mol^{-1}

In a schlenck tube, a solution of Nickel 5,15-dimesityl-10-bromoporphyrin **Ni 7** (110 mg, 0.16 mmol, 1 eq), 4-ethynyl pyridine (24.3 mg, 0.23 mmol, 1.5 eq), $Pd(PPh_3)_2Cl_2$ (10.9 mg, 0.016 mmol, 0,1 eq) and CuI (4.5 mg, 0.023 mmol, 0.15 eq) and degassed triethylamine (10 mL) was heated at 75 °C for 4h. The mixture was cooled to room temperature and the solvent was evaporated under reduced pressure. The product was purified by column chromatography (SiO_2, $CHCl_3$/Cyclohexane 1:1 then $CHCl_3$) to afford the pure compound as a purple solid (80 mg, 70 %).

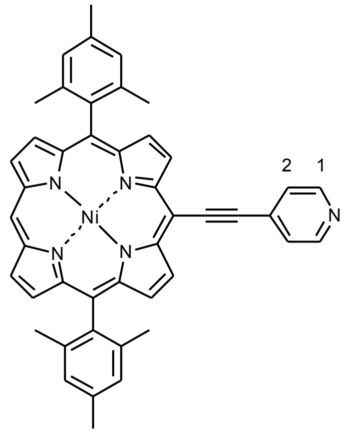

^{1}H-NMR (300 MHz, $CDCl_3$) δ: 1.81 (s, 12H, $CH_{3\text{ortho}}$), 2.61 (s, 6H, $CH_{3\text{para}}$), 7.25 (s, 4H, $H_{\text{méta}}$), 7.79 (d, *J* = 3,7 Hz, 2H, H_2), 8.68 (d, *J* = 4.5 Hz, 2H, $H_{\beta\text{pyrrol}}$), 8.75 (d, *J* = 4.5 Hz, 4H, $H_{\beta\text{pyrrol}}$), 8.80 (d, *J* = 3,7 Hz, 2H, H_1), 9.58 (d, *J* = 4.5 Hz, 2H, $H_{\beta\text{pyrrol}}$), 9.78 (s, 1H, $H_{\text{méso}}$).

^{13}C-NMR (90 MHz, $CDCl_3$) δ: 21.36 (CH_3), 21.46 (CH_3), 77.25 (C), 106.37 (CH), 118.38 (C), 125.59 (CH), 127.89 (CH), 131.47 (CH), 131.67 (CH), 132.29 (CH), 133.09 (CH), 136.85 (C), 137.98 (C), 138.99 (CH), 142.71 (C), 143.01 (C), 143.56 (C), 144.79 (C), 149.95 (CH).

λ_{max} (CH_2Cl_2)/nm (ε x 10^4/L mol^{-1} cm^{-1}) 424 (16.51), 537 (1.14), 573 (0.96).

ν_{max} (ATR)/cm^{-1} 1597, 1558, 1464, 1440, 1334, 1270, 1244, 1218, 1193, 1174, 1072, 997, 961, 844, 796, 784, 736, 750, 696.

m/z (HRM$^+$) $[M+H^+]_{calc}$ = 704.232, $[M+H^+]_{found}$ = 704.236.

5,15-dipentylporphyrin

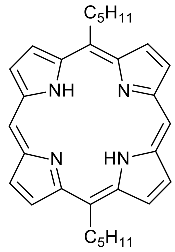

Chemical Formula: $C_{30}H_{34}N_4$
Molecular Weight: 450.62 $g.mol^{-1}$
A solution of dipyrrométhane **4** (1.46 g, 10 mmol, 1 eq) and hexanal (1.22 mL, 10 mmol, 1 eq) in $CHCl_2$ (1.9 L) was flushed with argon for 5 min and treated with TFA (74 µL, 1 mmol, 0.1 eq) at room temperature for 16h under argon. DDQ (3.41 g, 15 mmol, 1.5 eq) was added, and the mixture was stirred for 2 h. Triethylamine (135 µL, 1 mmol, 0.1 eq) was added, the mixture was filtered over an alumina pad and solvent was evaporated under reduced pressure. The product was purified by column chromatography (silica, CH_2Cl_2/petroleum ether 7:3) to afford a purple solid (480 mg, 21 %).

^{1}H-NMR (300 MHz, $CDCl_3$) δ: -2.93 (s, br, 2H, NH), 0.99 (t, 6H, *J* = 7.3 Hz, H_1), 1.54-1.62 (m, 4H, H_2), 1.75-1.85 (m, 4H, H_3), 2.50-2.60 (m, 4H, H_4), 4.99 (t, 4H, *J* = 8.1 Hz, H_5), 9.39 (d, *J* = 4.6Hz, 4H, $H_{\beta\text{pyrrol}}$), 9.56 (d, *J* = 4.6Hz, 4H, $H_{\beta\text{pyrrol}}$), 10.15 (s, 2H, $H_{\text{méso}}$).

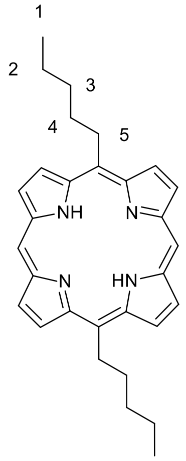

^{13}C-NMR (90 MHz, $CDCl_3$) δ: 14.16 (CH_3), 22.80 (CH), 32.73 (CH), 34.60 (CH), 38.31 (CH), 104.24 (CH), 118.81 (C), 127.79 (CH), 131.86 (CH), 144.18 (C), 147.46 (C).

λ_{max} (CH_2Cl_2)/nm (ε x 10^4/L mol^{-1} cm^{-1}) 404 (32.93), 504 (1.45), 535 (0.34), 578 (0.44), 633 (0.14).

ν_{max} (ATR)/cm^{-1} 2954, 2932, 2857, 1533, 1497, 1471, 1249, 1241, 1169, 1159, 1112, 1057, 1041, 977, 970, 919, 894, 842, 832, 785, 728, 685.

m/z (HRM$^+$) $[M+H^+]_{calc}$ = 451.286 $[M+H^+]_{found}$ = 451.291.

5,15-dipentyl-10,20-dibromoporphyrin

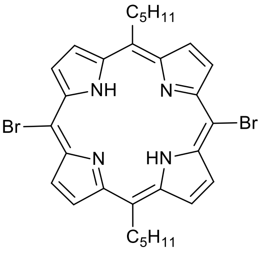

Chemical Formula: $C_{30}H_{32}Br_2N_4$
Molecular Weight: 608.41 g.mol^{-1}
A solution of 5,15-dipentylporphyrin **18** (100 mg, 0.22 mmol, 1 eq) in $CHCl_3$ (75 mL) and pyridine (0.1 mL) was treated with NBS (83 mg, 0.47 mmol, 2.1 eq) at 0 °C. After 1h, the reaction was quenched with acetone (4.2 mL). The solvent was evaporated under reduced pressure and the poorly soluble product was washed with methanol (3 x 10 mL). The product was obtained as a purple solid (130 mg, 96 %).

^{1}H-NMR (300 MHz, $CDCl_3$) δ: -2.76 (s, br, 2H, NH), 0.97 (t, 6H, *J* = 7.4 Hz, H_1), 1.50-1.58 (m, 4H, H_2), 1.70-1.80 (m, 4H, H_3), 2.50-2.60 (m, 4H, H_4), 4.84 (t, 4H, *J* = 8.1 Hz, H_5), 9.38 (d, *J* = 4.9 Hz, 4H, $H_{\beta pyrrol}$), 9.65(d, *J* = 4.9 Hz, 4H, $H_{\beta pyrrol}$).

^{13}C-NMR: Owing to the low solubility of the compound, no ^{13}C spectra could be acquired.

ν_{max}(ATR)/cm^{-1} 2973, 2916, 2852, 2359, 2332, 1471, 1241, 1159, 1089, 1049, 993, 977, 953, 921, 880, 832, 780, 775, 729, 682.

λ_{max} (CH_2Cl_2)/nm (ε x 10^4/L mol^{-1} cm^{-1}) 420 (35.63), 524 (1.28), 559 (1.10), 606 (0.35), 665 (0.75).

m/z (HRM$^+$) $[M+H^+]_{calc}$ = 609.105 $[M+H^+]_{found}$ = 609.107

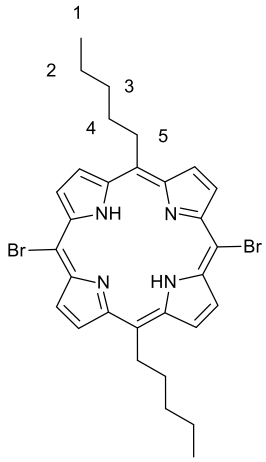

5,15-dipentyl-10,20-(pyridin-4-ylethynyl)porphyrin (4)

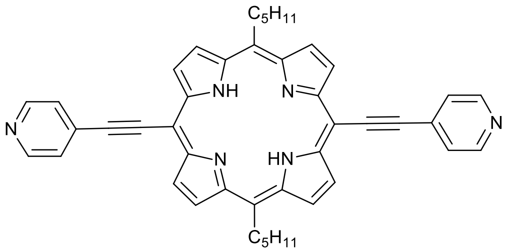

Chemical Formula: $C_{44}H_{40}N_6$
Molecular Weight: 652.83 g.mol^{-1}
In a schlenck tube, a solution of 5,15-dipentyl-10,20-dibromoporphyrin **18** (100 mg, 0.16 mmol, 1 eq), 4-ethynyl pyridine (42 mg, 0.41 mmol, 2.5 eq), $Pd(PPh_3)_2Cl_2$ (11 mg, 0.016 mmol, 0.1 eq) and CuI (4.5 mg, 0.024 mmol, 0.15 eq) in degassed triethylamine (4 mL) and dry THF (13 mL) was heated at 75 °C for 1h. The mixture was cooled to room temperature and the solvent was evaporated under reduced pressure. The product was washed with methanol (3 x 10 mL). The compound was obtained as a green solid (80 mg, 80 %).

^{1}H-NMR (300 MHz, $CDCl_3$) δ: -1.99 (s, br, 2H, NH), 0.98 (t, 6H, *J* = 7.3 Hz, H_1), 1.50-1.58 (s, br, 4H, H_2), 1.70-1.85 (s, br, 4H,

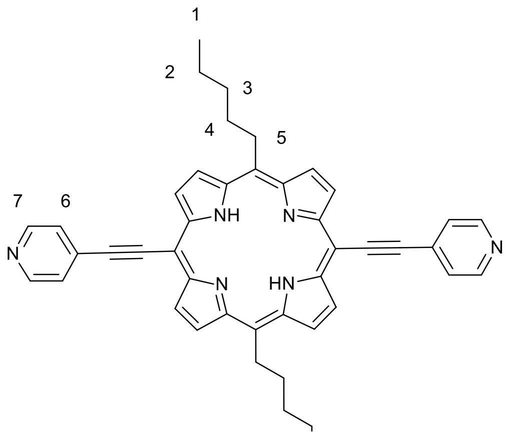

H_3), 242 2.57 (s, br, 4H, H_4), 4.80-4.95 (s, br 4H, H_5),7.90 (d, 4H, *J* = 5.5 Hz, H_6), 8.85 (d, 4H, *J* = 5.5 Hz, H_7) 9.43 (d, *J* = 4.0 Hz, 4H, $H_{\beta pyrrol}$), 9.70 (d, *J* = 4.0 Hz, 4H, $H_{\beta pyrrol}$).

^{13}C-NMR: Owing to the low solubility of the compound, no ^{13}C spectra could be acquired.

ν_{max}(ATR)/ cm^{-1} 2955, 2928, 2869, 2852, 2359, 2332, 2198, 2198, 1590, 1533, 1471, 1404, 1363, 1337, 1282, 1262, 1241, 1212, 1159, 1057, 993, 921, 830, 785, 725, 668.

λ_{max} (CH_2Cl_2)/nm (ε x 10^4/L mol^{-1} cm^{-1}) 440 (42.25), 550 (0.07), 597 (3.41), 632 (1.15), 694 (2.83).

m/z (HRM$^+$) $[M+H^+]_{calc}$ = 653.339 $[M+H^+]_{found}$ = 653.339.